Study on field-effect transistors and superconductors with phenacene molecules

2013, August

Xuexia He

Graduate School of Natural Science and Technology
(Doctor's Course)
OKAYAMA UNIVERSITY

Contents

Abstract

Field-effect transistors (FETs) with organic molecules have been extensively studied owing to their many advantages such as flexibility, large-area coverage, low-cost / low-energy fabrication processes and ease of design. Most of these FETs were fabricated with thin films of organic molecules towards future practical applications. However, defects, grain boundaries and impurities formed in thin films masked the intrinsic properties in FETs with organic materials. Furthermore, the FET performance of organic thin film FETs was still lower than that of Si metal-oxide-semiconductor (MOS) FET [1]. Recently, the organic single crystal FETs have attracted much attention from not only basic scientists but also engineers in electronics because the single crystals have fewer extrinsic factors lowering the FET performance. The intrinsic nature of FETs with organic materials may be obtained in using single crystals instead of thin films. This is one of the most important motivations to use single crystals in organic FETs.

Phenacene takes a W-shaped molecular structure with fused benzene rings. The molecules are termed as picene for five benzene rings, [6]phenacene for six and [7]phenacene for seven. A picene thin film FET device was fabricated for the first time by our group [2], and its field-effect mobility, μ, was > 1.0 $cm^2\ V^{-1}\ s^{-1}$. The O_2 gas-sensing property that the O_2 gas increases the FET performance was confirmed in the picene thin film FET [3,4]. Subsequently, the [6]phenacene and [7]phenacene thin film FETs showed the μ values of 3.7 $cm^2\ V^{-1}\ s^{-1}$ [5] and 7.5 × 10^{-1} $cm^2\ V^{-1}\ s^{-1}$ [6], respectively. In particular, the μ value for [6]phenacene thin film FET presently reaches 7.4 $cm^2\ V^{-1}\ s^{-1}$ [7]. Therefore, the studies on phenacene single crystal FETs have been strongly desired because of the expectation of the higher FET performance than that in thin film FETs.

The metal intercalated picene solids showed superconductivity with a superconducting transition temperature, T_c, as high as 18 K [8]. The T_c commands considerable attention because of its higher T_c than the highest T_c (= 14.2 K [9]) in organic superconductors discovered so far. Furthermore, our group succeeded in an

observation of superconductivity in metal intercalated [6]phenacene and [7]phenacene solids. The emergence of superconductivity in phenacene solids was realised by a donation of high density of electrons to phenacene molecules, stimulating our idea that electrostatic carrier accumulation in channel region of phenacene crystals may produce superconductivity without any chemical doping with metal atoms. Therefore, it is important to fabricate single crystal FETs with high-*k* gate dielectrics and electric-double-layer (EDL) capacitors, because of their high capacitance.

Based on the background described above, the author has systematically studied the FET properties of phenacene single crystal FETs. Various types of phenacene single crystal FET devices have been fabricated, and their characteristics have been systematically and quantitatively studied. In this Doctor thesis, the author describes on the background of this study in chapter 1, the growth of single crystals in chapters 2, the electronic structures of phenacene molecules and solids in chapter 3, and the theoretical background in chapter 4. From chapter 5 to 11, the author describes the FET characteristics found in phenacene single crystal FETs. The description on phenacene single crystal FETs occupies eleven chapters in this Doctor thesis (chapters 1 - 11 in part 1).

In chapter 5, the fundamental FET properties of phenacene single crystal FETs are reported. The FET shows p-channel FET properties, and a large concave behaviour for output curve at low absolute drain voltage, $|V_D|$, caused by large contact resistance between single crystal and source / drain electrodes is raised as a serious problem in the FETs. In chapter 6, an interface modification with insertion materials is tested to solve the problem raised in chapter 5. In particular, the variation of output curves is fully investigated by an insertion of electron acceptor or donor between single crystal and electrodes. Actually, the interface modification lowers the concave behaviour found in output curves at low absolute drain voltage, $|V_D|$, range. The μ value drastically increases by the interface modification. The highest μ reaches 6.9 $cm^2 V^{-1} s^{-1}$ in [7]phenacene single crystal FET with the Au electrodes modified with 2,5-diethyl-7,7,8,8-tetracyano-p-quinodimethane (Et2TCNQ). Thus, the interface

modification by electron acceptors / donors enabled ones to reduce the contact resistance and thereby increase the μ value. The interface modification decreases the concave behaviour in the output curves, from which a decrease in the hole-injection barrier height, ϕ_h, is quantitatively evaluated in chapter 7. The effect of electron acceptor / donor on barrier height is well scaled by the redox potential, E_{redox}, of insertion material. The relation between FET parameters (μ and absolute threshold voltage, $|V_{TH}|$) and E_{redox} is also tried to be scaled by E_{redox}, and a clear correlation between $|V_{TH}|$ and E_{redox} is confirmed.

In chapter 8, the utilization of high-*k* gate dielectrics is investigated for low-voltage operation, and the $|V_{TH}|$ is reduced to 2.6 V in [7]phenacne FET with HfO_2 gate dielectric in which tetrafluoro-7,7,8,8-tetracyano-p-quinodimethane (F4TCNQ) is inserted between single crystal and source / drain electrodes. This is too low in comparison with the $|V_{TH}|$ (= 18 V) in [7]phenacene single crystal FET with SiO_2 gate dielectric and F4TCNQ. Thus, both the usage of high-*k* gate dielectric and the interface modification cause the low-voltage operation. As a result, the strategy for realisation of ideal FET exhibiting the high μ and low $|V_{TH}|$ can be proposed based on the study described in chapters 5 - 8.

In chapter 9, the bias stress and O_2 gas-sensing properties are investigated in [7]phenacene single crystal FET. The bias stress may be caused by the trap formed by an application of strong electric-field to [7]phenacene single crystal under presence of H_2O. The O_2 gas-sensing property that the O_2 gas enhances the FET performance in [7]phenacene single crystal FET have not been observed, showing that the channel region is not affected by O_2 molecules because the single crystal may have no grain boundaries in which O_2 molecules can penetrate. In chapter 10, the author describes on the characteristics of [7]phenacene single crystal FET with EDL capacitor, which can operate at very low voltage ($|V_{TH}|$ = 2.3 V). Here, the ionic liquid gel and polymer-sheet are used as EDL capacitor to accumulate carriers. The possibility of high density carrier accumulation to control physical properties (or induce superconductivity) is also discussed. Finally, in chapter 11, the author describes temperature dependence of FET parameters in [7]phenacene single crystal FET. The temperature dependence of μ shows

two different behaviours in low and high temperature ranges. The channel transport can be explained by band-transport model; thermal phonon governs the transport in high temperature range, while impurity scattering dominates it in low temperature range. The contact resistance may also affect the μ in low temperature range.

The author reports a study on picene superconductor in chapters S-1 and S-2 of part 2. In chapter S-1, an introduction to hydrocarbon superconductors is provided. K doped picene, K_3picene, showed two different superconducting phases with T_c = 7 and 18 K [8]. Subsequently, new superconductors, $K_x$phenanthrene and K_xDBP (DBP: 1,2:8,9-dibenzopentacene) were discovered [10,11]. In particular, the T_c is 33 K in K_xDBP [11]. The purposes of this study are to clarify (1) the number of electrons in $K_x$picene and Rb_xpicene by Raman scattering, (2) the pressure dependence of 18 K phase, and (3) a new synthesis route for superconducting $K_x$picene by solution process.

As seen from chapter S-2, Raman scatterings of $K_x$picene and Rb_xpicene allow the determination of the number of electrons transferred from metal to a picene molecule. As a result, it has been found that $K_x$picene shows superconductivity only for x = 3. Second, the pressure dependence of T_c in two superconducting phases in K_3picene is found. One superconducting phase with T_c = 7 K shows a negative pressure dependence of T_c. In contrast, the other phase with T_c = 18 K exhibits a positive pressure dependence which cannot be understood with the simple conventional BCS mechanism. Finally, a new synthesis method for superconducting K_3picene by a solution process with monomethylamine, CH_3NH_2, is developed. The method enables a selective preparation of K_3picene with T_c = 18 K. The structure for 18 K phase is also suggested. Finally, the author mentions the discovery of new organic hydrocarbon superconductor, K_3coronene, with T_c = 7 K. This study clarifies fundamental properties of superconducting phases, and it will contribute to a development of new superconductors based on a diverse of hydrocarbon molecules.

References

[1] J. P. Colinge and C. A. Colinge, Physics of Semiconductor Devices (Springer, Massachusetts, 2006).

[2] H. Okamoto, N. Kawasaki, Y. Kaji, Y. Kubozono, A. Fujiwara, and M. Yamaji, *J. Am. Chem. Soc.* **130**, 10470 (2008).

[3] X. Lee, Y. Sugawara, A. Ito, S. Oikawa, N. Kawasaki, Y. Kaji, R. Mitsuhashi, H. Okamoto, A. Fujiwara, K. Omote, T. Kambe, N. Ikeda, and Y. Kubozono, *Org. Electron.* **11**, 1394 (2010).

[4] N. Kawasaki, W. L. Kalb, T. Mathis, Y. Kaji, R. Mitsuhashi, H. Okamoto, Y. Sugawara, A. Fujiwara, Y. Kubozono, and B. Batlogg, *Appl. Phys. Lett.* **96**, 113305 (2010).

[5] N. Komura, H. Goto, X. He, H. Mitamura, R. Eguchi, Y. Kaji, H. Okamoto, Y. Sugawara, S. Gohda, K. Sato, and Y. Kubozono, *Appl. Phys. Lett.* **101**, 083301 (2012).

[6] Y. Sugawara, Y. Kaji, K. Ogawa, R. Eguchi, S. Oikawa, H. Gohda, A. Fujiwara, and Y. Kubozono, *Appl. Phys. Lett.* **98**, 013303 (2011).

[7] R. Eguchi, *unpublished data*.

[8] R. Mitsuhashi, Y. Suzuki, Y. Yamanari, H. Mitamura, T. Kambe, N. Ikeda, H. Okamoto, A. Fujiwara, M. Yamaji, N. Kawasaki, Y. Maniwa, and Y. Kubozono, *Nature* **464**, 76 (2010).

[9] H. Taniguchi, M. Miyashita, K. Uchiyama, K. Satoh, N. Môri, H. Okamoto, K. Miyagawa, K. Kanoda, M. Hedo, and Y. Uwatoko, *J. Phys. Soc. Jpn.* **72**, 468 (2003).

[10] X. F. Wang, R. H. Liu, Z. Gui, Y. L. Xie, Y. J. Yan, J. J. Ying, X. G. Luo, and X. H. Chen, *Nature Commun*. **2**, 507 (2011).

[11] M. Xue, T. Cao, D. Wang, Y. Wu, H. Yang, X. Dong, J. He, F. Li, and G. F. Chen, *Sci. Rep.* **2**, 389 (2012).

Part 1

Chapter 1. Introduction to recent organic field-effect transistors and aim of this study

Through chapter 1, some textbooks on transistors and electronic devices [1-10] are used as references. These textbooks have been most commonly read by the scientists and engineers in research fields of electronics. Actually, the textbooks have been very useful for the auther to describe the Doctor thesis, in particular chapters 1 and 4. Chapter 1 relates to the introduction to transistors, the background and motivation of her Doctor thesis, and the aim of her study, while chapter 4 relates to the theoretical background of transistor. The author sometimes checked these textbooks to confirm her own knowledge and understanding on transistors. Furthermore, they contributed to build up new strategy of her study, *i.e.*, experiences and knowledge on transistor integrated during past 60 years, which are described in the textbooks, supported her study together with many papers cited in this Doctor thesis.

1-1.Basic principle of field-effect transistor

A transistor, whose term is derived from 'transfer resistor' is a three-terminal electronic device controlling the electric current. In this device, the electric current flowing between two terminals is controlled by the third terminal, *i.e.*, the electric current flowing between terminals can be enhanced (amplified) by other terminal.

A field-effect transistor (FET) is one of the transistors, in which electric field controls the conductivity in a semiconductor material. As seen from schematic picture of FET device shown in Figure 1-1, the electric current flows through the active layer between two electrodes where the bias voltage is applied. The active layer is made of semiconductors such as Si, inorganic materials and organic materials. The active layer and two electrodes are named as channel, source and drain electrodes. The source and drain electrodes are indistinguishable in the device, but the source electrode is always grounded in applying the bias voltage. The bias voltage is applied to the drain electrode, and the voltage is expresses as V_D. The electric current is modulated / controlled by the

different bias voltage which is applied to the third electrode called as gate electrode. The voltage is called as gate voltage which is expressed as V_G.

As seen from Figure 1-1, the V_G is applied to the gate electrode which is attached to the opposite side for active layer across the gate dielectric. Generally SiO_2 is used as gate dielectric in FET because of its strong protection for leakage of gate current induced in applying V_G and easy fabrication of SiO_2. SiO_2 can be easily made by thermal oxidation of Si. When the V_G is applied to gate electrode, the electric charges are separated to positive and negative. Consequently, the charge-enriched region of active layer which corresponds to channel region is produced underneath the gate electrode. The charge-enriched region can be easily recognised as the low-resistance region in which the electric current can flow. Strictly speaking, the negative charge is electron, while the positive charge is hole. They are light, and easily move through the channel region between source and drain electrodes by applying V_D. Based on the polarity of applied V_G, the enriched charges should change to negative or positive *i.e.*, electron or hole. In applying negative V_G, the enriched charge is hole, while in applying positive V_G, the charge is electron. In the former case, hole has a responsibility for electric-current flow which is called as p-channel operation, while in the latter case electron has a responsibility for electric-current flow which is called as n-channel. These charges are called as 'carrier' because electric current is carried by these charges (hole and electron).

1-2. Transistor operation in Si MOS field-effect transistor

In Si metal-oxide-semiconductor (MOS) FET which is the central device of recent electronics, Si is an active layer. In this FET, the Si crystals contain element located in either column III (B) or column V (P or As). The former dopant can accept electron from Si atom, while the latter can donate electron to Si atom. Therefore, the hole concentration is higher in the former than non-doped Si crystals; this is p-type semiconductor. On the other hand, the electron concentration is higher in the latter than non-doped Si crystals; this is n-type semiconductor. The actual dopant concentration is 1 per 10^6 Si atoms. Thus, the semiconductor (active layer) used in Si MOS FET is called as an extrinsic

semiconductor. In Si MOS FET, the hole (electron) enriched region in Si semiconductor should be formed when applying negative (positive) V_G. However, the p-channel operation is observed in only Si MOS FET with n-type Si semiconductor, whereas the n-channel operation is observed in Si MOS FET with p-type Si semiconductor. In other words, the carrier with higher concentration (majority carrier) cannot carry the electric current even if applying the suitable V_G but carrier with lower concentration (minority carrier) can carry the electric current. Namely, the hole (electron) concentration increases in the channel region when applying the negative (positive) V_G to n-type (p-type) semiconductor through the gate dielectric. Therefore, the channel is formed by minority carrier which is called as an inversion layer. Thus Si MOS FET is a unipolar device. The formation of inversion layer is shown in energy diagram drawn in Figure 1-2. The theoretical background of FET operation are fully described in chapter 4.

1-3. History of development of field-effect transistor

The first FET device was proposed by Lilienfeld [11], and he received the first patent in 1926. The second was granted in 1931 [12]. The patents have never attracted attention from most of scientists because of non-reliability of the devices [13-15]. However, the advancement of materials-processing technology, *i.e.*, development of technology to fabricate pure Si crystals opened an avenue for application of FET devices towards electronics. In 1960, Atalla and Kahng succeeded in fabrication of the first practical FET [16,17].

The FET device is a very effective electric-current amplifier because they can increase electric current by 10^7 - 10^{12} times. Furthermore, FET can realise a lower noise-level than the other type of transistor such as bipolar junction transistor (BJT), which means the high stability in operation. From view of manufacture, FET device has more advantage than BJT, because FET requires fewer steps to build up than BJT and other transistors. In addition, FETs can be integrated into an electronic circuit, *i.e.*, many FET chips can be integrated in one substrate. The integration can lead to low-power consumption and high-speed operation. Based on the nature of active layer, FET device

can be categorized into some types. We list only recent typical FET devices with references as follows: carbon nanotube FET [18-21], DNA FET [22-24], and graphene FET [25-28]. The study on these FETs is one of the most significant research-subjects because of the expectation to future application. In particular, graphene FET attracts much attention from view of not only potential application based on high operation-speed but also fundamental physics, because its transport properties directly reflect relativistic quantum physics [25-28]. Our group also has investigated a new type of graphene FET [29] and fundamental physics of graphene FET [30,31].

1-4. Fundamental principle of organic field-effect transistor

Organic FET implies the FET device with organic materials as active layer. The study on organic FET presently attracts a great deal of interest from scientists and engineers because of the flexibility, light weight, large area coverage and ease of design [32-45]. Also organic FET device can be fabricated with low-cost and low-energy processes because the active layer can be easily formed by solution process. In contrast to organic FETs, the high-temperature process is indispensable for a fabrication of Si MOS FET since the temperature greater than 1000 °C is required to obtain the pure single crystals of Si. The application of organic FET towards a variety of equipments such as identification tags, driver of active matrix display and smart card is presented owing to its flexibility and light weight. Furthermore, organic FET has a high compatibility with plastic substrates and it can be integrated to the flexible plastic substrates. The concept is a ubiquitous electronics that people can use them easily without any barrier at any time and any place.

Typical structure of organic FET is shown in Figure 1-3. The structure is the same as other FET devices such as Si MOS FET. The FET consists of three electrodes (source, drain and gate), gate dielectric and active layer. The active layer is an organic material instead of Si or other inorganic materials. As described later, thin films or single crystals of organic materials are used as the active layer. The most important issue is that organic materials form van-der-Waals crystals, which is different from Si and other inorganic

materials. Si crystals are formed by the covalent bond which can produce a wide band owing to the strong transfer integral between Si atoms. On the other hand, in the organic crystals, the band is very narrow because of the weak transfer integral between organic molecules. These results affect the operation speed in FET. The operation speed can be evaluated by one important FET parameter, field-effect mobility, μ. The FET has the larger μ, the faster the operation becomes. In the Si MOS FET, the typical μ value is > 1000 $cm^2 V^{-1} s^{-1}$ [1-10], while the μ value in organic FETs is still lower than 10 $cm^2 V^{-1} s^{-1}$ [32-45]. The reason why the μ of organic FET is low can be easily explained by the narrow band described above. The increase in μ value is one of the most important studies in organic FET research. Many studies other than those relating to increase in μ are developed [32-45]. The low voltage operation is also significant in organic FET. For this purpose, the SiO_2 with dielectric constant ε (= 3.9) can be replaced by other gate dielectrics with high ε (high-*k* gate dielectrics) such as HfO_2 and Ta_2O_5. The effectiveness of high-*k* gate dielectrics is described in chapter 8 in detail.

Here, it is important to say that the mechanism of FET operation in organic FET is quite different from that of Si MOS FET. In section 1-2, the mechanism of transistor operation in Si MOS FET was briefly described. In Si MOS FET, the inversion layer in which minority carriers are enriched is formed in extrinsic-doped Si semiconductor. Therefore, Si MOS FET operates with minority carrier and it is in principle a unipolar transistor. In organic FET, impurity is not doped to the active layer. Therefore, in organic FET, carriers are accumulated to intrinsic (pure) organic semiconductor without any majority carriers. Consequently, the transistor operation is not explained based on the formation of the inversion layer. Such a difference can lead to a unique and interesting physics different from Si MOS FET. These problems are fully discussed in chapter 4 and other related chapters.

1-5. A brief history of organic field-effect transistor

The first description on organic FET has to be back to the beginning of 1970s. Barbe and Westgate reported field-effect measurements on single crystals of metal-free

phthalocyanine (Figure 1-4) in some different atmospheric conditions. The modification of channel conductance induced by a variation of gate potential was observed in this system [46]. The paper clarified the surface parameters of phthalocyanine single crystal using this technique. This may be the first FET device. The realistic organic FET device was fabricated by Tsumura *et al*. in 1986 [47]. In this study, they used polythiophene in the active layer. The schematic structure of the polythiophene FET fabricated by Tsumura *et al*. is shown in Figure 1-5. This device showed normally-off type FET characteristics. The drain current, I_D, increased by two - three orders of magnitude by applying V_G. The μ was at most ~ 10^{-5} $cm^2 V^{-1} s^{-1}$ [47]. The same group improved the μ value to 0.22 $cm^2 V^{-1} s^{-1}$ using polythienylenevinylene FET in 1993 [48].

In 1992, Horowitz *et al*. reported a series of organic thin-film FETs using various π-conjugated oligomers, such as oligothiophene series and two linear-polyacenes (tetracene and pentacene) [49]. This is the first application of pentacene molecule to FET device. Presently, pentacene is extensively used for study on organic FET because of its potential application. The structures of tetracene and pentacene are shown in Figure 1-6. Dodabalapur *et al*. successfully made FET device with thiophene-type oligomer (α-hexathienylene). The on/off ratio of drain current I_D reached $>10^6$ [44]. The current density and switching speed realised in this device were sufficient for practical electronic circuits. Subsequently, Dimitrakopoulos *et al*. fabricated pentacene thin film FET in which thin film was made using molecular beam deposition method [50]. A maximum μ of FET recorded 0.038 $cm^2 V^{-1} s^{-1}$. Furthermore, Lin *et al*. reported pentacene thin film FETs with the μ values as high as 1.5 $cm^2 V^{-1} s^{-1}$ [51]. These pentacene FETs operated in p-channel, *i.e.*, hole carries electric current in the FETs. In 2004, Yasuda *et al*. reported an impressive result that pentacene FET can operate in both p and n-channels [52]. The source and drain electrodes were formed with Ca in the FET device. The Fermi level of Ca is close to lowest occupied molecular orbital (LUMO); the LUMO orbital is related to the conduction of electron (n-channel). The μ value in p-channel (hole mobility) was 4.5×10^{-4} $cm^2 V^{-1} s^{-1}$, while the μ in n-channel (electron mobility) was 2.7×10^{-5} $cm^2 V^{-1} s^{-1}$. This result shows clearly that the operation of organic FET is based on the active layer of intrinsic (no-doped) semiconductor, *i.e.*, organic FET operates in Mott-Schottky

limit.

These organic FETs are made of thin films of organic materials. The FET device with organic single crystal was fabricated for the first time with rubrene by Podzorov *et al*. in 2003 [53]. The molecular structure of rubrene is shown in Figure 1-7. The single crystal of rubrene was grown by physical vapour transport, where hydrogen gas was flowed. The FET device demonstrated p-channel characteristics exhibiting the μ more than 1 $cm^2 V^{-1} s^{-1}$ and the on/off ratio ~ 10^4. The FET devices fabricated with pentacene single crystal exhibited p-channel FET characteristics with the μ as high as 0.30 $cm^2 V^{-1} s^{-1}$ and on/off ratio as high as 5×10^6 [54]. Further, the tetracene single crystal FETs was also fabricated, with the μ being as high as 0.4 $cm^2 V^{-1} s^{-1}$ [55]. Takeya *et al*. reported a very high μ value in rubrene single crystal FET [56]. The maximum μ value reached 18 $cm^2 V^{-1} s^{-1}$ at two-terminal measurement mode and 40 $cm^2 V^{-1} s^{-1}$ at four-terminal measurement mode. Presently, the highest μ value is 94 $cm^2 V^{-1} s^{-1}$ for κ-(BEDT-TTF)$_2$Cu[N(CN)$_2$]Br (BEDT-TTF=bis(ethylenedithio)tetrathiafulvalene) in organic single crystal FETs at four-terminal measurement mode [57].

1-6. A new type of organic field-effect transistor with phenacene molecules

In 2008, our group fabricated thin film FET with new type of organic molecule, picene [58], which showed the μ ~ 1.0 $cm^2 V^{-1} s^{-1}$. This FET device showed clear O_2 gas sensing properties, in which the μ and absolute I_D increased under O_2 atmospheric condition [58,59]. The molecular structure of picene is shown in Figure 1-8. As seen from Figure 1-8, picene molecule is W-shaped, with it consisting of five fused benzene rings. Such an organic molecule is called as 'phenacene'. As fully described in chapter 3, picene molecule is more stable than pentacene, which is closely associated with armchair-edge structure. Subsequently, our group fabricated and characterised [6]phenacene and [7]phenacene thin film FETs [60,61]. The highest μ value is 7.4 $cm^2 V^{-1} s^{-1}$ in [6]phenacene thin film FET [62]. Many FET works with phenacene thin films are reported during past 5 years [63-67]. The FETs with single crystals of phenacene

were reported by Kawai *et al.* [68], and the μ value recorded 1.3 $cm^2 V^{-1} s^{-1}$ at two-terminal measurement mode. The μ is not higher than that, ~ 3 $cm^2 V^{-1} s^{-1}$, of picene thin film FETs [59], regardless of the fewer defects, grain-boundaries and impurities expected in single crystals. The reason why the μ is lower in single crystal FET was explained based on the O_2 sensing properties of picene FET [59]. The details of characteristics of phenacene FET are fully described in introduction of each chapter based on the necessity.

1-7. Interesting physical properties of phenacene molecules

Recently, it was found that chemical doping of alkali metal atoms into picene solids resulted in superconductivity [69]. The observed superconducting transition temperature, T_c, is as high as 7 K or 18 K in K_3picene [69,70]. The superconductivity of metal intercalated picene solids attracted much attention since the T_c (= 18 K) was higher than the highest T_c (= 14.2 K) in other organic molecular superconductors [71]. Thus, picene has very attractive properties from view of solid state physics. It was found that the phenacene molecules other than picene also show the superconductivity [72,73]. Furthermore, electrostatic carrier doping into some inorganic materials realised the superconductivity [74-76]. Namely, electron accumulation into ZrNCl single crystal using FET structure resulted in emergence of superconductivity [75]. Actually, electron or hole-enriched channel region is formed in inorganic materials to modify the electronic structure.

Based on this background, we may expect an emergence of superconductivity through the electrostatic accumulation of hole or electron into the channel region of phenacene solids. The high-density carrier accumulation using FET structure requires the suitable capacitor with high capacitance ($C \equiv \frac{\varepsilon_0 \varepsilon}{d}$), which is realised by high dielectric constant, ε, or thin dielectric thickness, d. The electric double layer (EDL) capacitor is based on the separation of anions and cations. Since the EDL formed by anions or cations has thickness below 1 nm, the extremely high capacitance may be produced, which enables ones to accumulate high density of carriers in the channel region. To pursue the

electrostatically induced superconductivity, EDL FETs with phenacene single crystal using ionic liquids have been prepared. In this FET, using single crystals as active layer may be crucial because they have few traps (defects, grain boundaries and impurities) and the accumulated carriers are mobile. In chapter 10, the fabrication and characterization of [7]phenacene single crystal EDL FET are described.

1-8. Motivation and aim of this study

This Doctor thesis focusses on the clarification of FET properties of phenacene single crystal FETs. Various types of FET devices are fabricated and characterised in order to analyse the FET characteristics systematically and quantitatively.

The first purpose of this study is to identify the fundamental properties of phenacene molecules because the molecules have never been obtained. For this purpose, we fabricate high-quality single crystals of phenacene molecules and FET devices with single crystals because intrinsic nature can be obtained without any artificial perturbation in single crystal FET. In chapters 2 and 3, the author shows the method to make high-quality single crystals and the electronic structures of phenacene solids, respectively. The theoretical background to discuss FET characteristics is described in chapter 4. The fundamental FET characteristics are discussed in chapter 5. The O_2 sensing properties which are clearly observed in phenacene thin film FETs are investigated in single crystal FETs. In addition, the bias stress effects of FET characteristics are studied. These are discussed in chapter 9. Temperature dependence of phenacene single crystal FET was fully investigated to clarify the mechanism of transport in the FETs. This is described in chapter 11.

The second purpose is to show the effectiveness of phenacene molecules towards future practical electronics. Further, the effectiveness of device modification has also been evaluated in this FET. In this study, high-performance single crystal FETs exhibiting high-μ and low-voltage operation have been fabricated with electron acceptors / donors for reducing contact resistance and with high-*k* gate dielectrics for effective

carrier accumulation, suggesting the effectiveness of phenacene molecules for future electronics. The author designs various types FETs and evaluates the effects of device modification on FET characteristics. The interface control of FET device is successfully applied to phenacene single crystal FETs to obtain the high FET performance. The interface control is fully described in chapters 6 and 7. Furthermore, the study on low-voltage operation is discussed in chapter 8. The μ value is comparable to 6.9 $cm^2 V^{-1} s^{-1}$. Thus, excellent performance of the phenacene single crystal FET is obtained by the device modifications.

The third purpose of this study is to accumulate high-density of carriers into channel region. The author tries to accumulate carriers into channel region of single crystals by the FET with EDL capacitor. This study is closely related to the expectation of emergence of superconductivity. Through this study, various FET devices are designed. For instance, the ionic liquid gel and the ionic liquid polymer-sheet are used for EDL capacitor. The description is supplied in chapter 10.

Through this study, the author clarified high potentiality of phenacene molecules towards future electronics. Moreover, she found that the device modification can be successfully applied to the FET devices. In other words, the device modification could extract the potential ability of phenacene for transistor.

References

[1] H. T. Grahn, Introduction to Semiconductor Physics (World science publishing Co. Pte. Ltd., Singapore, 1999).

[2] J. P. Colinge and C. A. Colinge, Physics of Semiconductor Devices (Springer, Massachusetts, 2006).

[3] D. K. Schroder, Semiconductor Material and Device Characterization (John Wiley & Sons. Inc., New Jersey, 2006).

[4] S. M. Sze, Physics of Semiconductor Devices (John Wiley & Sons. Inc., New Jersey, 2007).

[5] U. K. Mishra and J. Singh, Semiconductor Device Physics and Design (Springer, Dordrecht, 2008).

[6] J. J. Liou, A. O. Conde, and F. G. Sanchez, Analysis and Design of MOSFETs: Modeling, Simulation, and Parameter Extraction (Kluwer Academic publishers, Massachusetts, 1998).

[7] I. Kymissis, Organic Field Effect Transistors: Theory, Fabrication and Characterization (Springer, New York, 2009).

[8] Z. Bao and J. Locklin, Organic Field-Effect Transistors (CRC press, Taylor & Francis Group, Boca Raton, 2007).

[9] R. E. Hummel, Electronic Properties of Materials (Springer, New York, 2012).

[10] Y. Singh and S. Agnihotri, Semiconductor Devices (I. K. International Publishing House Pvt. Ltd., New Delhi, 2009).

[11] J. E. Lilienfeld, "Method and apparatus for controlling electric currents" US patent 1, 745, 175, filed October 8, 1926, granted January 28, 1930.

[12] J. E. Lilienfeld, "Device for controlling electric current" US patent 1, 900, 018, filed March 28, 1928, patented March 7, 1933.

[13] J. Bardeen and W. H. Brattain, Phys. Rev. **74**, 230 (1948).

[14] W. Shockley, Bell Syst. Tech. J. **28**, 435 (1949).

[15] W. Shockley, M. Sparks, and G. K. Teal, Phys. Rev. **83**, 151 (1951).

[16] D. Kahng, "Electric field controlled semiconductor device" US Patent 3, 102, 230, filed May 31, 1960, issued August 27, 1963.

[17] S.M. Sze, Semiconductor Devices: physics and Technology (John Wiley & Sons. Inc., New York, 2002)

[18] J.-P. Cleuziou, W. Wernsdorfer, V. Bouchiat, T. Ondarçuhu, and M. Monthioux, Nature Nanotech. **1**, 53 (2006).

[19] V. V. Deshpande, B. Chandra, R. Caldwell, D. S. Novikov, J. Hone, and M. Bockrath, Science **323**, 106 (2009).

[20] W. Liang, M. Bockrath, D. Bozovic, J. H. Hafner, M. Tinkham, and H. Park, Nature **411**, 665 (2001).

[21] S. Sahoo, T. Kontos, J. Furer, C. Hoffmann, M. Gräber, A. Cottet, and C. Schönenberger, Nature Phys. **1**, 99 (2005).

[22] D. Porath, A. Bezryadin, S. de Vries, and C. Dekker, Nature **403**, 635 (2000).

[23] K.-H. Yoo, D. H. Ha, J.-O. Lee, J. W. Park, J. Kim, J. J. Kim, H.-Y. Lee, T. Kawai, and H. Y. Choi, Phys. Rev. Lett. **87**, 198102 (2001).

[24] J. S. Hwang, K. J. Kong, D. Ahn, G. S. Lee, D. J. Ahn, and S. W. Hwang, Appl. Phys. Lett. **81**, 1134 (2002).

[25] K. S. Novoselov, A. K. Geim, S. V. Morozov, D. Jiang, M. I. Katsnelson, I. V. Grigorieva, S. V. Dubonos, and A. A. Firsov, Nature **438**, 197 (2005).

[26] Y. Zhang. Y.-W. Tan, H. L. Stormer, and P. Kim, Nature **438**, 201 (2005).

[27] A. F. Young, and P. Kim, Nature Phys. **5**, 222 (2009).

[28] H. B. Heersche, P. J. Herrero, J. B. Oostinga, L. M. K. Vandersypen, and A. F. Morpurgo, Nature **446**, 56 (2007).

[29] H. Goto, E. Uesugi, R. Eguchi, A. Fujiwara, and Y. Kubozono, Nano Lett. **13**, 1126 (2013).

[30] E. Uesugi, H. Goto, R. Eguchi, A. Fujiwara, and Y. Kubozono, Sci. Rep. **3**, 1595 (2013).

[31] H. Goto, E. Uesugi, R. Eguchi, and Y. Kubozono, unpublished data.

[32] Y. Sun, Y. Liu, and D. Zhu, J. Mater. Chem. **15**, 53 (2005).

[33] A. R. Murphy and J. M. J. Frèchet, Chem. Rev. **107**, 1066 (2007).

[34] J. E. Anthony, Angew. Chem. Int. Ed. **47**, 452 (2008).

[35] S. Allard, M. Forster, B. Souharce, H. Thiem, and U. Scherf, Angew. Chem. Int. Ed. **47**, 4070 (2008).

[36] S. Liu, W. M. Wang, A. L. Briseno, S. C. B. Mannsfeld, and Z. Bao, Adv. Mater. **21**, 1217 (2009).

[37] S. Wang, M. Kappl, I. Liebewirth, M. Müller, K. Kirchhoff, W. Pisula, and K. Müllen, Adv. Mater. **24**, 417 (2012).

[38] Y. Ie, M. Ueta, M. Nitani, N. Tohnai, M. Miyata, H. Tada, and Y. Aso, Chem. Mater. **24**, 3285 (2012).

[39] M. Cavallini, P. D'Angelo, V. V. Criado, D. Gentili, A. Shehu, F. Leonardi, S. Milita, F. Liscio, and F. Biscarini, Adv. Mater. **23**, 5091 (2011).

[40] C. Keil and D. Schlettwein, Org. Electron. **12**, 1376 (2011).

[41] A. Lv, S. R. Puniredd, J. Zhang, Z. Li, H. Zhu, W. Jiang, H. Dong, Y. He, L. Jiang, Y. Li, W. Pisula, Q. Meng, W. Hu, and Z. Wang, Adv. Mater. **24**, 2626 (2012).

[42] Z. Bao, A. J. Lovinger, and A. Dodabalapur, Appl. Phys. Lett. **69**, 3066 (1996).

[43] H. T. Yi, M. M. Payne, J. E. Anthony, and V. Podzorov, Nature Commun. **3**, 1259 (2012).

[44] A. Dodabalapur, L. Torsi, and H. E. Katz, Science **268**, 270 (1995).

[45] U. Zschieschang, M. J. Kang, K. Takimiya, T. Sekitani, T. Someya, T. W. Canzler, A. Werner, J. B. Nimoth, and H. Klauk, J. Mater. Chem. **22**, 4273 (2012).

[46] D. F. Barbe and C. R. Westgate, J. Phys. Chem. Solids **31**, 2679 (1970).

[47] A. Tsumura, H. Koezuka, and T. Ando, Appl. Phys. Lett. **49**, 1210 (1986).

[48] H. Fuchigami, A. Tsumura, and H. Koezuka, Appl. Phys. Lett. **63**, 1372 (1993).

[49] G. Horowitz, X.-Z. Peng, D. Fichou, and F. Garnier, Synth. Met. **51**, 419 (1992).

[50] C. D. Dimitrakopoulos, A. R. Brown, and A. Pomp, J. Appl. Phys. **80**, 2501 (1996).

[51] Y.-Y. Lin, D. J. Gundlach, S. F. Nelson, and T. N. Jackson, Electron Device Lett. **18**, 606 (1997).

[52] T. Yasuda, T. Goto, K. Fujita, and T. Tsutsui, Appl. Phys. Lett. **85**, 2098 (2004).

[53] V. Podzorov, V. M. Pudalov, and M. E. Gershenson, Appl. Phys. Lett. **82**, 1739 (2003).

[54] V. Y. Butko, X. Chi, D. V. Lang, and A. P. Ramirez, Appl. Phys. Lett. **83**, 4773 (2003).

[55] R. W. I. de Boer, T. M. Klapwijk, and A. F. Morpurgo, Appl. Phys. Lett. **83**, 4345 (2003).

[56] J. Takeya, M. Yamagishi, Y. Tominari, R. Hirahara, Y. Nakazawa, T. Nishikawa, T. Kawase, T. Shimoda, and S. Ogawa, Appl. Phys. Lett. **90**, 102120 (2007).

[57] Y. Kawasugi, H. M. Yamamoto, M. Hosoda, N. Tajima, T. Fukunaga, K. Tsukagoshi, and R. Kato, Appl. Phys. Lett. **92**, 243508 (2008).

[58] H. Okamoto, N. Kawasaki, Y. Kaji, Y. Kubozono, A. Fujiwara, and M. Yamaji, J. Am. Chem. Soc. **130**, 10470 (2008).

[59] N. Kawasaki, Y. Kubozono, H. Okamoto, A. Fujiwara, and M. Yamaji, Appl. Phys. Lett. **94**, 043310 (2009).

[60] N. Komura, H. Goto, X. He, H. Mitamura, R. Eguchi, Y. Kaji, H. Okamoto, Y. Sugawara, S. Gohda, K. Sato, and Y. Kubozono, Appl. Phys. Lett. **101**, 083301 (2012).

[61] Y. Sugawara, Y. Kaji, K. Ogawa, R. Eguchi, S. Oikawa, H. Gohda, A. Fujiwara, and Y. Kubozono, Appl. Phys. Lett. **98**, 013303 (2011).

[62] 7.4 $cm^2 V^{-1} s^{-1}$ by R. Eguchi *et al*., unpublished data.

[63] X. Lee, Y. Sugawara, A. Ito, S. Oikawa, N. Kawasaki, Y. Kaji, R. Mitsuhashi, H. Okamoto, A. Fujiwara, K. Omote, T. Kambe, N. Ikeda, and Y. Kubozono, Org. Electron. **11**, 1394 (2010).

[64] N. Kawasaki, W. L. Kalb, T. Mathis, Y. Kaji, R. Mitsuhashi, H. Okamoto, Y. Sugawara, A. Fujiwara, Y. Kubozono, and B. Batlogg, Appl. Phys. Lett. **96**, 113305 (2010).

[65] Y. Sugawara, K. Ogawa, H. Goto, S. Oikawa, K. Akaike, N. Komura, R. Eguchi, Y. Kaji, S. Gohda, and Y. Kubozono, Sens. Actuators B : Chem. **171-172**, 544 (2012).

[66] Y. Kaji, K. Ogawa, R. Eguchi, H. Goto, Y. Sugawara, T. Kambe, K. Akaike, S. Gohda, A. Fujiwara, and Y. Kubozono, Org. Electron. **12**, 2076 (2011).

[67] Y. Kaji, N. Kawasaki, X. Lee, H. Okamoto, Y. Sugawara, S. Oikawa, A. Ito, H. Okazaki, T. Yokoya, A. Fujiwara, and Y. Kubozono, Appl. Phys. Lett. **95**, 183302 (2009).

[68] N. Kawai, R. Eguchi, H. Goto, K. Akaike, Y. Kaji, T. Kambe, A. Fujiwara, and Y. Kubozono, J. Phys. Chem. C **116**, 7983 (2012).

[69] R. Mitsuhashi, Y. Suzuki, Y. Yamanari, H. Mitamura, T. Kambe, N. Ikeda, H. Okamoto, A. Fujiwara, M. Yamaji, N. Kawasaki, Y. Maniwa, and Y. Kubozono, Nature **464**, 76 (2010).

[70] Y. Kubozono, H. Mitamura, X. Lee, X. He, Y. Yamanari, Y. Takahashi, Y. Suzuki, Y. Kaji, R. Eguchi, K. Akaike, T. Kambe, H. Okamoto, A. Fujiwara, T. Kato, T. Kosugi, and H. Aoki, Phys. Chem. Chem. Phys. **13**, 16476 (2011).

[71] H. Taniguchi, M. Miyashita, K. Uchiyama, K. Satoh, N. Môri, H. Okamoto, K. Miyagawa, K. Kanoda, M. Hedo, and Y. Uwatoko, J. Phys. Soc. Jpn. **72**, 468 (2003).

[72] X. F. Wang, R. H. Liu, Z. Gui, Y. L. Xie, Y. J. Yan, J. J. Ying, X. G. Luo, and X. H. Chen, Nature Commun. **2**, 507 (2011).

[73] X. F. Wang, Y. J. Yan, Z. Gui, R. H. Liu, J. J. Ying, X. G. Luo, and X. H. Chen, Phys. Rev. B **84**, 214523 (2011).

[74] K. Ueno, S. Nakamura, H. Shimotani, A. Ohtomo, N. Kimura, T. Nojima, H. Aoki, Y. Iwasa, and M. Kawasaki, Nature Mater. **7**, 855 (2008).

[75] J. T. Ye, S. Inoue, K. Kobayashi, Y. Kasahara, H. T. Yuan, H. Shimotani, and Y. Iwasa, Nature Mater. **9**, 125 (2010).

[76] K. Ueno, S. Nakamura, H. Shimotani, H. T. Yuan, N. Kimura, T. Nojima, H. Aoki, Y. Iwasa, and M. Kawasaki, Nature Nanotech. **6**, 408 (2011).

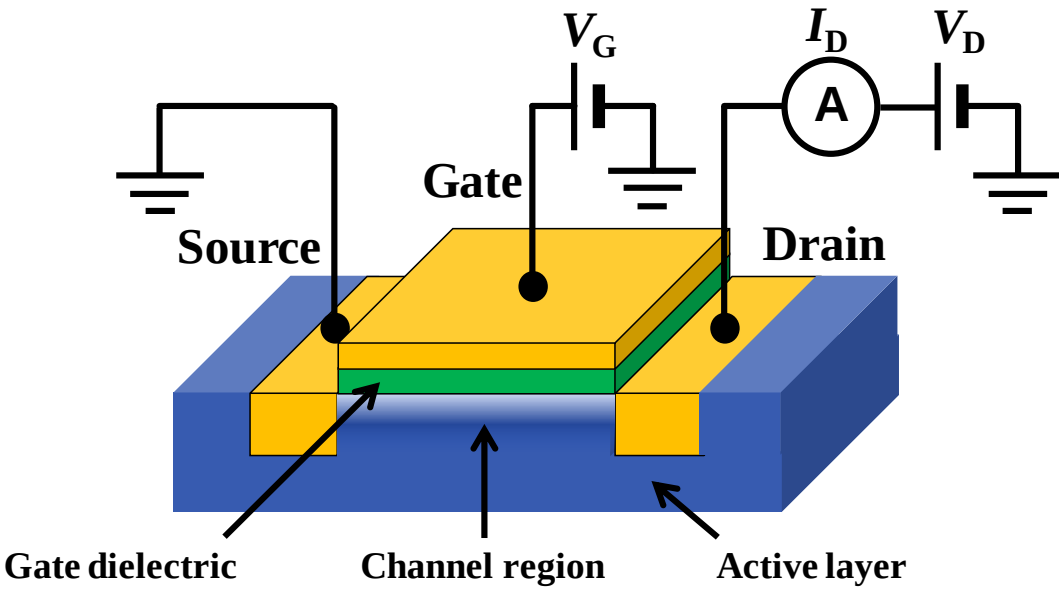

Figure 1-1. Typical structure of FET devices.

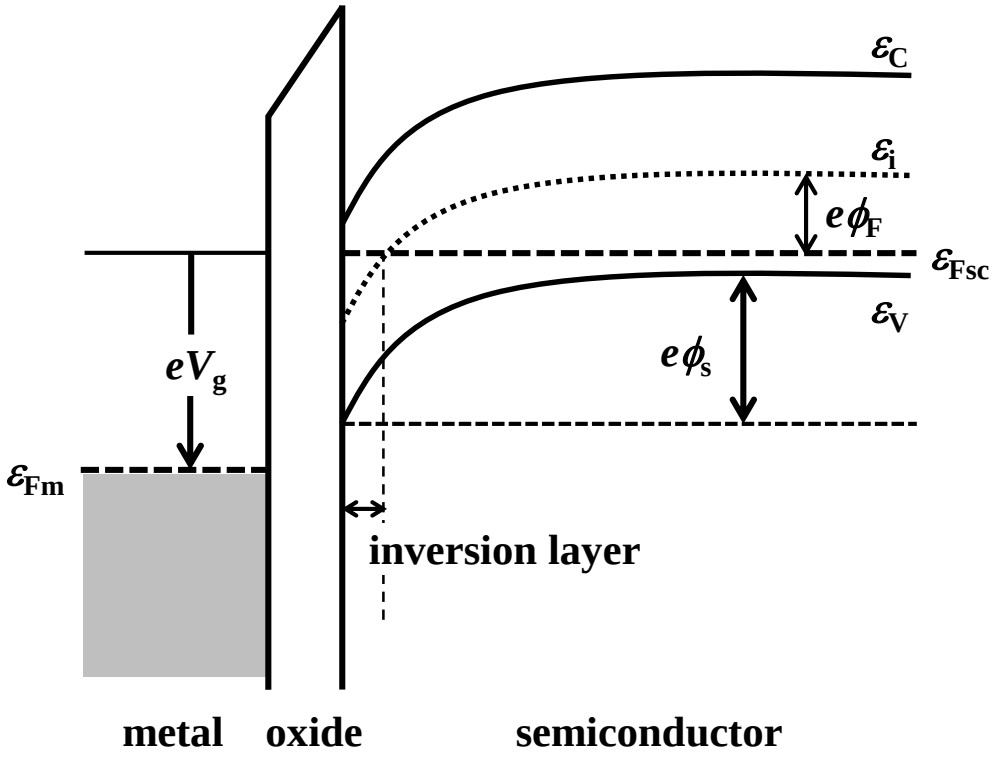

Figure 1-2. Formation of inversion layer in a typical MOS FET. When a large positive voltage, V_g, is applied to the metal in a metal / oxide / p-type semiconductor junction, the energy bands are bent as shown in the figure and the inversion layer is formed. Consequently, the holes are repelled from the surface, while the electron concentration increases. The operation mechanism is described in section 4-1-2 in detail.

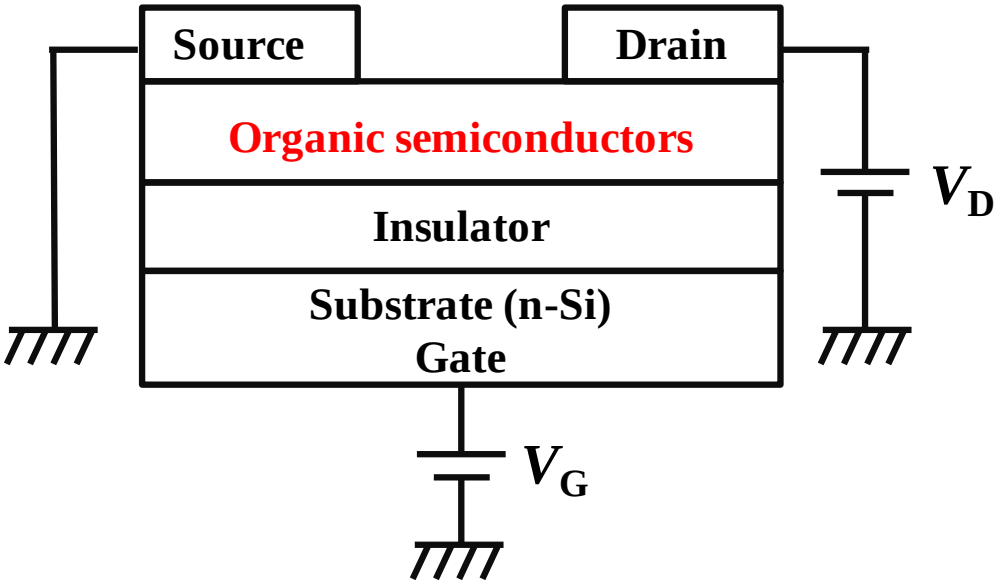

Figure 1-3. Structure of an organic FET device.

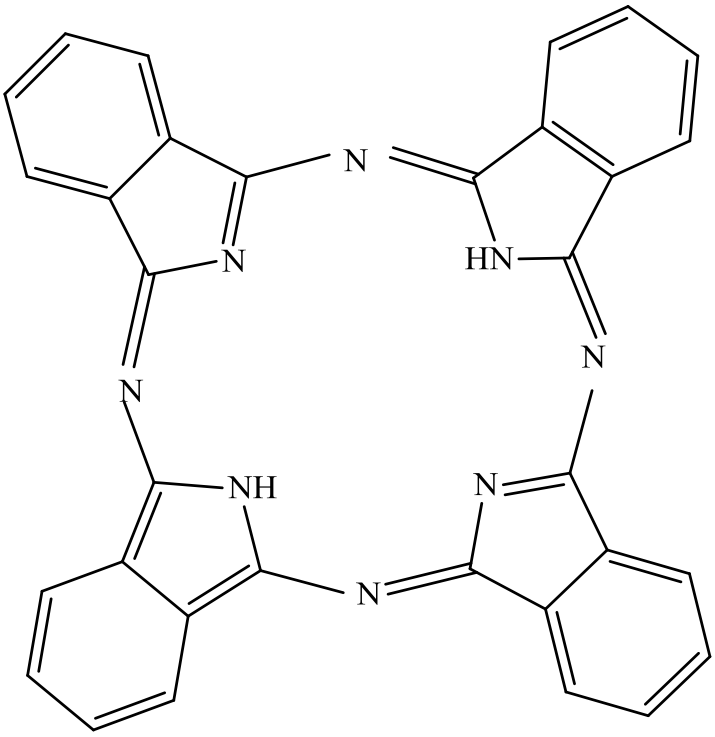

phthalocyanine

Figure 1-4. Molecular structure of phthalocyanine used in the first orgainc FET.

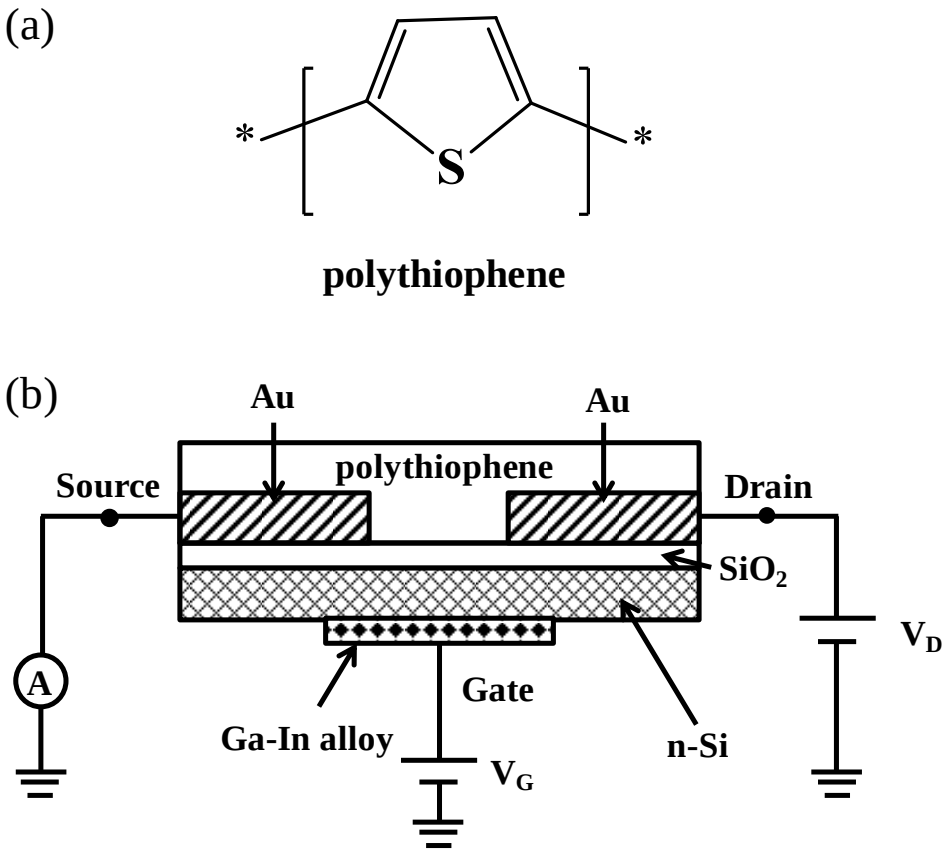

Figure 1-5. (a) Molecular structure of polythiophene. (b) Device structure of the first realistic organic FET using polythiophene in active layer.

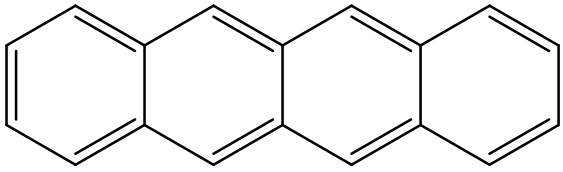

tetracene

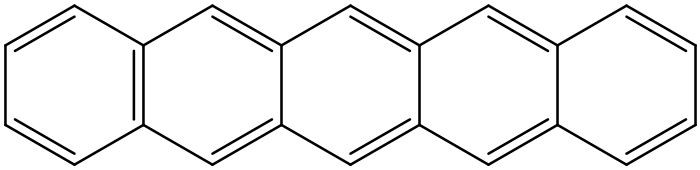

pentacene

Figure 1-6. Molecular structures of tetracene and pentacene.

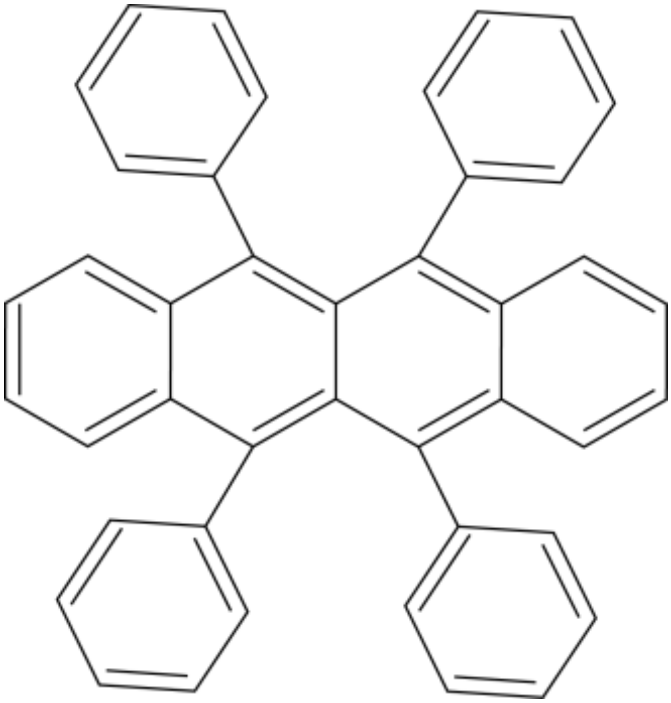

rubrene

Figure 1-7. Molecular structure of rubrene.

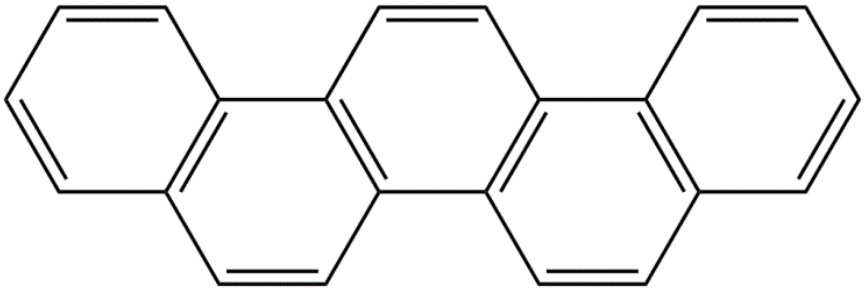

picene

Figure 1-8. Molecular structure of picene.

Chapter 2. Crystal growth of phenacene molecules and topological images of crystals

2-1. Growth of phenacene single crystals

Organic semiconductors are very attractive from view of potential application for future electronics owing to the many advantages such as flexibility, light weight, large-area coverage and ease of design as well as low-temperature / low-cost device-fabrication process [1-15]. The advantages of low-temperature / low-cost fabrication of transistor enable us to form active layers without any thermal treatment, for example, by using solution process. Large-area coverage with active layers is possible with various techniques such as solution casting [16], inkjet printing [17,18], stamping [19] and spin coating [20]. The other advantage of flexibility comes from the weak interaction between organic molecules. The solids of organic materials are formed by van der Waals force, which is a weak intermolecular interaction in comparison with covalent bonds and ionic bonds which are the main interactions of inorganic materials. Therefore, flexibility and large-area coverage can be easily produced in organic materials [21,22].

The different interaction produces different physical properties between solids of organic and inorganic materials. As described in chapter 1, the band width of organic solids is very narrow because of the small transfer integral originating from weak van der Waals interaction, while that of inorganic solids is generally broad because of the large transfer integral originating from strong covalent or ionic bonds. From view point of application towards electronics, the former is effective for flexible electronics, while the latter can provide high carrier mobility leading to high-speed transistor devices. Actually, the operation speed of organic FET is much lower than that of FETs with inorganic materials. The highest μ value is still < 10 $cm^2 V^{-1} s^{-1}$ in thin film organic FET [23, whereas that is 18 $cm^2 V^{-1} s^{-1}$ in organic single crystal FET [24]; the values correspond to the μ recorded at two-terminal measurement mode. The μ value is higher in single crystal FET than that of thin film FET because of few defects, few grain boundaries and few impurities. Since organic single crystal FET is not affected by the extrinsic factors, intrinsic nature of organic materials determines the characteristics of the FET device,

leading to high FET performance without any factors which lower the device performance. Furthermore, four-terminal measurement mode provides higher μ value than two-terminal measurement mode because the contact resistance between an active layer and electrodes is included in two-terminal measurement; the μ of 18 $cm^2 V^{-1} s^{-1}$increased to 40 $cm^2 V^{-1} s^{-1}$ by changing the measurement mode from two-terminal to four-terminal [24]. Consequently, the study on organic single crystal FETs is important not only to obtain high-performance FET device but also to clarify the intrinsic nature of organic materials.

For producing high-performance organic single crystal FETs, the most important issue is to make high-quality single crystals which are used as active layers. The high-quality in single crystals implies no presence of defects, grain boundaries and impurities. Larger transfer integral between molecules leads to larger conductance and higher μ. However, the design of crystal structure to produce large transfer integral may be difficult. It means the crystal engineering but it is not still established. On the other hand, making crystals without defects, grain boundaries and impurities may be possible by precisely controlling the growth condition. Generally, there are some approaches for growth of single crystals; Czochralski method [25], Bridgman method [26], hydrothermal method [27], chemical vapour deposition (CVD) method [28] and physical vapour transport (PVT) method [29]. In this chapter, the techniques for crystal growth are introduced.

2-2. Melt growth method for single crystal growth

The melt growth technique has been applied only for single crystal growth of inexpensive organic molecules because large amount of initial sample is required. The initial / source sample is heated and melted, and cooled to low temperature to obtain single crystals. This technique is applied for the crystal growth of pyrene [30], naphthalene [31], anthracene [32], phenanthrene [33], tetracene [34] and stilbene [35]. These molecules are stable at the melting temperature but they may be often polymerized or decomposed by a long-time heating or an irradiation of intense light. The single crystal

growth using this method is not widely used because of difficulty in crystallization.

2-3. Solution process for single crystal growth

Organic molecules are dissolved in organic solvents under various pressures and temperatures. The single crystals can be formed from the solution in which organic materials are dissolved. This technique is normally used for crystal growth of organic molecules with large molecular weight because of difficulty in sublimation. The molecules with large molecular weight may be decomposed by sublimation. Based on the nature of corresponding organic molecules, various solution processes such as slow cooling [36], solvent evapouration [37], liquid-liquid interface control [38] and dissolution with supercritical solvent [39] may be available for making high-quality single crystals.

2-4. Physical vapour transport method for single crystal growth

Organic single crystals can be grown from gas phase. Firstly, the initial organic sample is heated / sublimed at high-temperature zone and the sublimed sample is moved under dynamical or static condition [40], as seen from Figure 2-1. The sublimed sample is often moved under a gas flow. The single crystals can be formed at lower temperature zone shown in Figure 2-1. Figure 2-1(a) shows the 'open system' of PVT method in which the sublimed sample is moved with flow-gas under the dynamical condition, while Figure 2-1(b) shows the 'closed system' in which the sublimed sample is moved based on the difference of temperature. The flow gas which assists the flow of the sublimed material is called as 'carrier gas'. The PVT method often provides single crystals with higher quality than those obtained using other techniques [40]. The high quality means few defects, few grain boundaries and few impurities. The single crystals obtained from this technique never contain solvent, leading to a decrease in scatterers in channel region. In making single crystals for FET devices, the PVT method is one of the most effective techniques for crystal growth.

In the open system (Figure 2-1(a)), the speed of sublimation is controlled by the flow gas. The zone 1 and zone 2 correspond to high-temperature and low-temperature regions, respectively. The source material is placed in the zone 1, and it is sublimed. The sublimed material moves to the zone 2 under the carrier gas. The crystals can be obtained in the zone 2. Actually, for collecting the crystals, the small glass tube is placed in the zone 2. The impurities which are sublimed more easily than the material are collected in lower reach. The carrier gas plays an important role not only to prevent source / sublimed materials from oxidizing, but also to move the sublimed material to the zone 2 effectively. It is well known that this method provides organic single crystals suitable for the active layer of FET devices. Actually, the good single crystals of anthracene [41], tetracene [42], pentacene [43] and rubrene [44] are produced with this method.

In the closed system shown in Figure 2-1(b), the source material is sealed in glass tube under vacuum. The source materials are in the zone 1 and the crystals can be made in zone 2. The sublimation of source materials may be more effective in this system than open system because of reduced pressure. The crystal growth is only based on the temperature difference. The source and sublimed materials are not oxidized under high vacuum condition. This method was used not only for purification of organic materials [45,46] and C_{60} [47], but for the crystal growth of naphthalene, tetrancene, pyrene, pentancene, anthracene and fullerenes [40].

The various experimental conditions such as the temperatures of zones 1 and 2, the flowing rate of carrier gas, the vacuum level, the weight of source material and the size (volume) of system are important for the ideal crystal growth. Therefore, the experimental conditions have to be controlled precisely.

2-5. Physical vapour transport method used in this study

In this study, the PVT method with the open system was used for the single crystal growth. The equipment is shown in Figure 2-1(a). In this study, the picene, [6]phenacene and [7]phenacene single crystals were made. Picene, [6]phenacene and [7]phenacene were purchased from NARD Co. Ltd. The purity of these materials was 99.9%. For

instance, the single crystals of [7]phenacene were prepared as follows. The source sample was placed on zone 1, and the carrier gas was flowed in the system with the flowing rate of 50 ml / min. In this study, Ar gas was used as carrier gas. The temperature of zone 1 was maintained to 673 K, while the temperature of zone 2 was regulated to 493 K. The single crystals were obtained in zone 2 where the small tube was placed for collecting the crystals. Some of impurities were found in the down reach of zone 2. The single crystals of picene, [6]phenacene and [7]phenacene obtained were transparent and plate-like, as described in subsequent sections. The typical crystals size of picene, [6]phenacene and [7]phenacene were 2.0 mm × 0.7 mm. Their flat side was parallel to the *ab*-plane, and their thickness was ~1 μm along the *c*-axis. Here, it should be noticed that the *a* and *b* directions of [6]phenacene are different from those of picene and [7]phenacene as described in section 2-8. The experimental condition for crystal growth for picene, [6]phenacene and [7]phenacene single crystals is listed in Table 2-1.

2-6. Optical microscope images of phenacene single crystals

Optical microscope images of typical picene single crystal are shown in Figure 2-2. Although some defects are observed in the crystals, large area of crystal surface is flat and defect-free. The shape of single crystals is plate-like and very flat, suggesting that the crystal exactly consists of one single crystal. Optical microscope images of [6]phenacene single crystals are shown in Figure 2-3. Different from the images of picene single crystals, the optical microscope images of [6]phenacene show rawboned shapes and rough surfaces, which means the overlap of some single crystals. Thus, [6]phenacene single crystals are also flat and plate-like, but they are frequently overlapped and the size of flat area is small. In this study, the wide, flat and plate-like single crystals were not easily formed for [6]phenacene.

Optical microscope images of typical [7]phenacene single crystals are shown in Figure 2-4. The optical microscope images show the similar ones to those of picene single crystals, *i.e.*, plate-like and wide. The surface of single crystals is very flat and defect-free. The overlap of some single crystals is not found in the image of [7]phenacene

single crystals. The optical microscope images show that the wideness of flat and plate-like single crystals for [7]phenacene is the best, and that for picene is intermediate between [6]phenacene and [7]phenacene.

The flat parts of these single crystals were used as active layers of FET devices. From the microscope images, the quality of [7]phenacene single crystals is probably best among three kinds of phenacene molecules. The quality of [6]pehenacene single crystal is worst from view of application for active layers; active layers require the wide, flat and plate-like single crystal.

The optical microscope images in Figures 2-2 – 2-4 show single crystals placed on parylene coated SiO_2 / Si substrates, where the thickness of parylene is 30 nm. Figure 2-5 shows the optical microscope images of phenacene single crystals which were covered with 50 nm thick Au. The image was taken for evaluating the real situation of single crystals because the Au electrodes were deposited on the single crystals in the top-contact type single crystal FET. The quality of single crystals can be more clearly observed in Figure 2-5 than the images in Figures 2-2 – 2-4, because the contrast of the images of single crystals covered with Au (Figure 2-5) is clear, and defects and overlap of some crystals are observed as black images. From the images, the defect-free / flat surface and no-overlap of crystals are clearly recognised in [7]phenacene single crystal. Consequently, the high-quality single crystals are obtained in [7]phenacene. As described above based on Figures 2-2 – 2-5, the quality of picene single crystal is intermediate between [6]phenacene and [7]phenacene. [6]phenacene single crystal consists of some overlapped crystals.

2-7. Atomic force microscope (AFM) images of phenacene single crystals

AFM image can provide the topological characters in more fine scale than optical microscope image. The roughness of surface can also be obtained from the AFM image in angstrom scale (1 Å = 0.1 nm). Figure 2-6 shows typical AFM images of the topological structures of picene, [6]phenacene and [7]phenacene single crystals. The AFM image of surface of single crystal is obtained in 10 μm × 10 μm scale. Many

images of the randomly selected areas were recorded, and the typical images are shown in Figure 2-6.

The root mean square roughness, R_{rms}, of single crystal is 2.2 nm for picene, 3.7 nm for [6]phenacene and 3.6 nm for [7]phenacene in 10 μm × 10 μm area. The R_{rms}s of 0.07 and 0.09 nm in 1 μm × 1 μm area are observed in [6]phenacene and [7]phenacene single crystal FETs, respectively. The AFM image shown in Figure 2-6 shows a presence of steps. The difference in height between two teraces (step height) is 1.7 nm, suggesting that the thickness of a single crystal is different in nanometer scale.

2-8. X-ray diffraction patterns for [6]phenacene and [7]phrnacene single crystals

X-ray diffraction patterns of [6]phenacene and [7]phenacene crystalline powder samples were measured using an X-ray diffractometer (RIGAKU RINT-TTR III). The unit cell parameters for the phenacene solids were determined by the LeBail analysis program in the GSAS package [48]. X-ray diffraction patterns for [6]phenacene and [7]phenacene crystalline powder samples are shown in Figures 2-7(a) and (b), respectively; the powder samples were obtained by grinding the single crystals obtained. The lattice parameters were determined by LeBail fit. In the Figure 2-7, the experimental X-ray diffraction patterns are plotted together with the patterns calculated based on LeBail fit. The space groups of the [6]phenacene and [7]phenacene crystals were the same, $P2_1$, based on the X-ray diffraction patterns, but different molecular symmetries (C_{2h} for [6]phenacene and C_{2v} for [7]phenacene) led to different lattice constants, *a*, *b*, *c* and β; the directions of *a* and *b* are different between [6]phenacene and [7]phenacene crystals. The directions of *a* and *b* axes are the same between picene [49] and [7]phenacene. The *a*, *b*, *c* and β values were 12.130(1) Å, 7.9416(7) Å, 15.401(1) Å and 93.161(8)° for the [6]phenacene solids, respectively, while those for the [7]phenacene solids were 8.4381(8) Å, 6.1766(6) Å, 17.829(2) Å and 93.19(1)°; a = 8.472(2), b = 6.170(2), c = 13.538(7) Å and β = 90.81(4)° for picene (X-ray diffraction pattern is not

shown) [49]. Figure 2-8 shows the 'herringbone' crystal structure in the picene single crystal [49]. The same structure is taken in all phenacene single crystals.

These lattice parameters are listed in Table 2-2 together with those of picene [49]. Notably, since the *a* and *b* for [7]phenacene were close to the *a* and *b* for picene, probably because of their identical molecular symmetry (C_{2v}), their molecular arrangement and orientation can be assumed to be the same. The molecular arrangement and orientation of [6]phenacene in the *ab*-plane cannot be predicted, but the difference in lattice constants between [6]phenacene and [7]phenacene suggests a difference in the molecular stacking in the *ab*-plane. Rietveld refinements for these X-ray diffraction patterns are now in progress to determine the precise crystal structures.

The *c* values, 15.401(1) Å for [6]phenacene and 17.829(2) Å for [7]phenacene, can be reasonably interpreted based on the length of the long axis of the molecules, as the *c* value increases with the length of the long axis. These values are consistent with those reported previously for thin films, 15.55(1) Å for [6]phenacene [50] and 18.1(2) Å for [7]phenacene [51]. The expansion of the unit cell volume, *V*, in phenacene crystals—picene, [6]phenacene and [7]phenacene—depends on the increase in *c*. The thickness direction of the single crystals corresponds to the *c*-direction because *c* is larger than *a* and *b* in all phenacene crystals; the direction of large lattice constant corresponds to the direction of weak growth in single crystal. In plate-like phenacene single crystals, the thickness direction normal to the wide (flat-surface) area can be associated with the *c*. In the real picene, [6]phenacene and [7]phenacene single crystal FETs fabricated in this study, the *ab*-plane (the flat surface of the single crystals) is oriented parallel to the SiO_2 surface. This arrangement is preferable for fabrication of lateral FET structures because channel conduction in [6]phenacene and [7]phenacene single crystals occurs in the *ab*-plane judging from the larger *c* than *a* and *b*. Conduction is thus concluded to occur along the *b*-axis for [7]phenacene by analogy with picene, which had a large transfer integral between the molecules along *b* [52]. The direction of conduction in the *ab*-plane may not be specified for [6]phenacene.

References

[1] Y. Sun, Y. Liu, and D. Zhu, J. Mater. Chem. **15**, 53 (2005).

[2] A. R. Murphy and J. M. J. Fréchet, Chem. Rev. **107**, 1066 (2007).

[3] J. E. Anthony, Angew. Chem. Int. Ed. **47**, 452 (2008).

[4] S. Allard, M. Forster, B. Souharce, H. Thiem, and U. Scherf, Angew. Chem. Int. Ed. **47**, 4070 (2008).

[5] S. Liu, W. M. Wang, A. L. Briseno, S. C. B. Mannsfeld, and Z. Bao, Adv. Mater. **21**, 1217 (2009).

[6] S. Wang, M. Kappl, I. Liebewirth, M. Müller, K. Kirchhoff, W. Pisula, and K. Müllen, Adv. Mater. **24**, 417 (2012).

[7] Y. Ie, M. Ueta, M. Nitani, N. Tohnai, M. Miyata, H. Tada, and Y. Aso, Chem. Mater. **24**, 3285 (2012).

[8] M. Cavallini, P. D'Angelo, V. V. Criado, D. Gentili, A. Shehu, F. Leonardi, S. Milita, F. Liscio, and F. Biscarini, Adv. Mater. **23**, 5091 (2011).

[9] C. Keil and D. Schlettwein, Org. Electron. **12**, 1376 (2011).

[10] A. Lv, S. R. Puniredd, J. Zhang, Z. Li, H. Zhu, W. Jiang, H. Dong, Y. He, L. Jiang, Y. Li, W. Pisula, Q. Meng, W. Hu, and Z. Wang, Adv. Mater. **24**, 2626 (2012).

[11] Z. Bao, A. J. Lovinger and A. Dodabalapur, Appl. Phys. Lett. **69**, 3066 (1996).

[12] A. Tsumura, H. Koezuka, and T. Ando, Appl. Phys. Lett. **49**, 1210 (1986).

[13] A. Dodabalapur, L. Torsi, and H. E. Katz, Science **268**, 270 (1995).

[14] H. Fuchigami, A. Tsumura, and H. Koezuka, Appl. Phys. Lett. **63**, 1372 (1993).

[15] C. Reese and Z. Bao, Materials Today **10**, 20 (2007).

[16] M. M.-Torrent, M. Durkut, P. Hadley, X. Ribas, and C. Rovira, J. Am. Chem. Soc. **126**, 984 (2004).

[17] H. Sirringhaus, T. Kawase, R. H. Friend, T. Shimoda, M. Inbasekaran, W. Wu, and

E. P. Woo, Science **290**, 2123 (2000).

[18] J. Zhang, Y. Zhao, Z. Wei, Y. Sun, Y. He, C. Di, W. Xu, W. Hu, Y. Liu, and D. Zhu, Adv. Funt. Mater. **21**, 786 (2011).

[19] E. Menard, V. Podzorov, S.-H. Hur, A. Gaur, M. E. Gershenson, and J. A. Rogers, Adv. Mater. **16**, 2097 (2004).

[20] D. J. Lipomi, B. C.-K. Tee, M. Vosgueritchian, and Z. Bao. Adv. Mater. **23**, 1771 (2011).

[21] Y. Zhao, C. Di, X. Gao, Y. Hu, Y. Guo, L. Zhang, Y. Liu, J. Wang, W. Hu, and D. Zhu, Adv. Mater. **23**, 2448 (2011).

[22] H. T. Yi, M. M. Payne, J. E. Anthony, and V. Podzorov, Nature Comm. **3**, 1259 (2012).

[23] M. J. Kang, I. Doi, H. Mori, E. Miyazaki, K. Takimiya, M.Ikeda, and H. Kuwabara, Adv. Mater. **23**, 1222 (2011).

[24] J. Takeya, M. Yamagishi, Y. Tominari, R. Hirahara, Y. Nakazawa, T. Nishikawa, T. Kawase, T. Shimoda, and S. Ogawa, Appl. Phys. Lett. **90**, 102120 (2007).

[25] J. Aleksic, P. Zielke, and J. A. Szymczyk, Ann. N. Y. Acad. Sci. **972**, 158 (2002).

[26] P. Rudolph and F.-M. Kiessling, Cryst. Res. Tec. **23**, 1207 (1988).

[27] X. Yu, H. Wang, Y. Liu, X. Zhou, B. Li, L. Xin, Y. Zhou, and H. Shen, J. Mater. Chem. A **1**, 2110 (2013).

[28] C. Yan, Y. K. Vohra, H. Mao, and R. J. Hemley, Proc. Natl. Acad. Soc. **99**, 12523 (2002).

[29] R. A. Laudise, C. Kloc, P. G. Simpkins, and T. Siegrist, J. Cryst. Growth **187**, 449 (1998).

[30] H. Inokuchi, Bull. Chem. Soc. Jpn. **29**, 131 (1956).

[31] S. Selvakumar, K. Sivaji, A. Arulchakkaravarthi, N. Balamurugan, S. Sankar, and P. Ramasamy, J. Cryst. Growth, **282**, 370 (2005).

[32] K.H. Probst and N. Karl, Phys. Status Solidi (a) **27**, 499 (1975).

[33] B. J. McArdle, J. N. Sherwood, and A. C. Damask, J. Cryst. Growth **22**, 193 (1974).

[34] J. Niemax and J. Pflaum, Appl. Phys. Lett. **87**, 241921 (2005).

[35] A. Arulchakkaravarthi, P. Santhanaraghavan, and P. Ramasamy, J. Cryst. Growth **224**, 89 (2001).

[36] S. A. Odom, M. M. Caruso, A. D. Finke, A. M. Prokup, J. A. Ritchey, J. H. Leonard, S. R. White, N. R. Sottos, and J. S. Moore, Adv. Funct. Mater. **20**, 1721 (2010).

[37] D. Nanova, S. Beck, A. Fuchs, T. Glaser, C. Lennartz, W. Kowalsky, A. Pucci, and M. Kroeger, Org. Electron. **13**, 1237 (2012).

[38] T. Wakahara, P. D'Angelo, K. Miyazawa, Y. Nemoto, O. Ito, N. Tanigaki, D. D. C. Bradley, and T. D. Anthopoulos, J. Am. Chem. Soc. **134**, 7204 (2012).

[39] C. N. Field, P. A. Hamley, J. M. Webster, D. H. Gregory, J. J. Titman, and M. Poliakoff, J. Am. Chem. Soc. **122**, 2480 (2000).

[40] H. Jiang and C. Kloc, MRS Bull. **38**, 28 (2013).

[41] A. N. Aleshin, J. Y. Lee, S. W. Chu, J. S. Kim, and Y. W. Park, Appl. Phys. Lett. **84**, 5383 (2004).

[42] R. W. I. de Boer, T. M. Klapwijk, and A. F. Morpurgo, Appl. Phys. Lett. **83**, 4345 (2003).

[43] V. Y. Butko, X. Chi, D. V. Lang, and A. P. Ramirez, Appl. Phys. Lett. **83**, 4773 (2003).

[44] J. Takeya, M. Yamagishi, Y. Tominari, R. Hirahara, Y. Nakazawa, T. Nishikawa, T. Kawase, T. Shimoda, and S. Ogawa, Appl. Phys. Lett. **90**, 102120 (2007).

[45] O. D. Jurchescu, J. Baas, and T. T. M. Palstra, Appl. Phys. Lett. **84**, 3061 (2004).

[46] R. Zeis, C. Besnard, T. Siegrist, C. Schlockermann, X. Chi, and C. Kloc, Chem.

Mater. **18**, 244 (2006).

[47] W. Gang, X. S.-Shen, L. Wei, F. C.-Sheng, L. C.-Rong, W. C.-Qing, L. Nan, Q. S.-Fa, Z. Z.-Bo, Y. Y.-De, and Z. W.-Ya, Acta Physca Sinca **3**, 360 (1994).

[48] A. C. Larson and R. B. Von Dreele, "General Structure Analysis System (GSAS)", Los Alamos National Laboratory Report LAUR, 86 (2004).

[49] R. Mitsuhashi, Y. Suzuki, Y. Yamanari, H. Mitamura, T. Kambe, N. Ikeda, H. Okamoto, A. Fujiwara, M. Yamaji, N. Kawasaki, Y. Maniwa, and Y. Kubozono, Nature **464**, 76 (2010).

[50] N. Komura, H. Goto, X. He, H. Mitamura, R. Eguchi, Y. Kaji, H. Okamoto, Y. Sugawara, S. Gohda, K. Sato, and Y. Kubozono, Appl. Phys. Lett. **101**, 083301 (2012).

[51] Y. Sugawara, Y. Kaji, K. Ogawa, R. Eguchi, S. Oikawa, H. Gohda, A. Fujiwara, and Y. Kubozono, Appl. Phys. Lett. **98**, 013303 (2011).

[52] Y. Kubozono, H. Mitamura, X. Lee, X. He, Y. Yamanari, Y. Takahashi, Y. Suzuki, Y. Kaji, R. Eguchi, K. Akaike, T. Kambe, H. Okamoto, A. Fujiwara, T. Kato, T. Kosugi, and H. Aoki, Phys. Chem. Chem. Phys. **13**, 16476 (2011).

Table 2-1. Experimetal condition for crystal growth for picene, [6]phenacene and [7]phenacene single crystals used in this study.

	picene	[6]phenacene	[7]phenacene
Temperature in zone 1	573 K	653 K	673 K
Temperature in zone 2	438 K	453 K	493 K
Ar flow speed	70 ml / min	70 ml / min	50 ml / min

Table 2-2. Lattice parameters of picene, [6]phenacene and [7]phenacene single crystals.

	picene[a]	[6]phenacene	[7]phenacene
a (Å)	8.472(2)	12.130(1)	8.4381(8)
b (Å)	6.170(2)	7.9416(7)	6.1766(6)
c (Å)	13.538(7)	15.401(1)	17.829(2)
β (°)	90.81(4)	93.161(8)	93.19(1)
V (Å^3)	707.59	1481.4(1)[b]	927.8(1)

[a] Lattice parameters of picene are taken from Ref. 49.

[b] $V/2$ (= 740.7(1) Å) for [6]phenacene can be compared with the V for picene and [7]phenacene, because the molecular arrangement and orientation of [6]phenacene are different from those of picene and [7]phenacene.

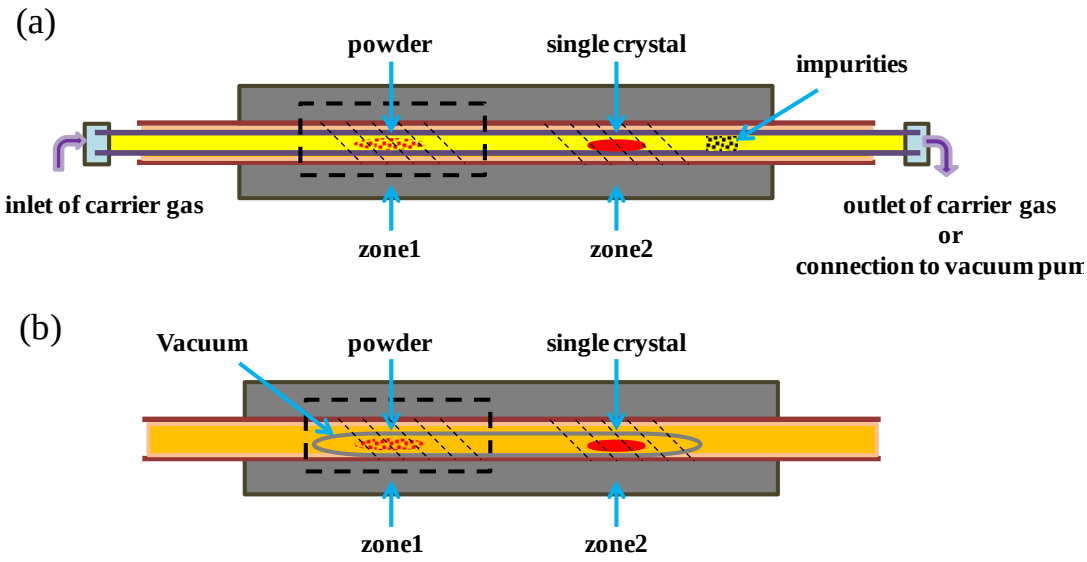

Figure 2-1. Schematics of the physical vapor transport method in (a) open system and (b) closed system. In the actual setup of open system (a), a small glass tube is placed in the zone 2 to collect the single crystals.

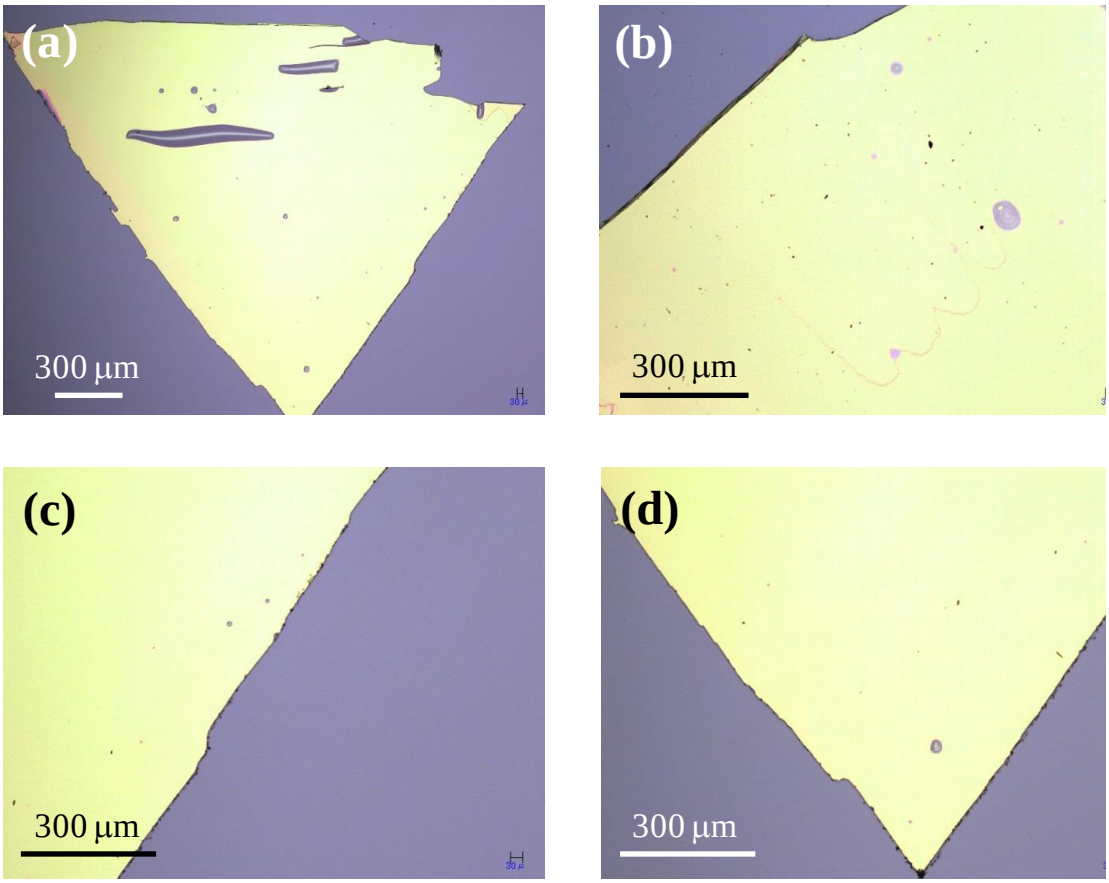

Figure 2-2. Optical microscope images of typical picene single crystals on SiO_2 substrates.

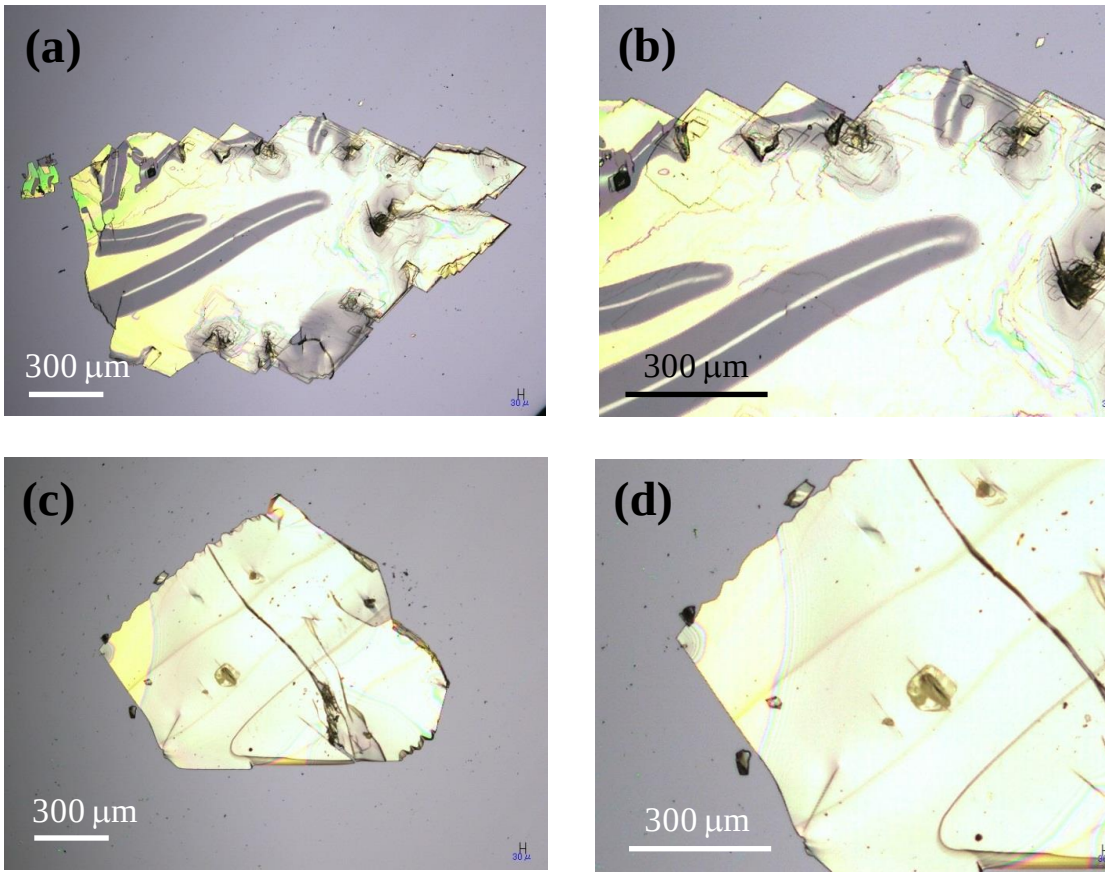

Figure 2-3. Optical microscope images of typical [6]phenacene single crystals on SiO_2 substrates.

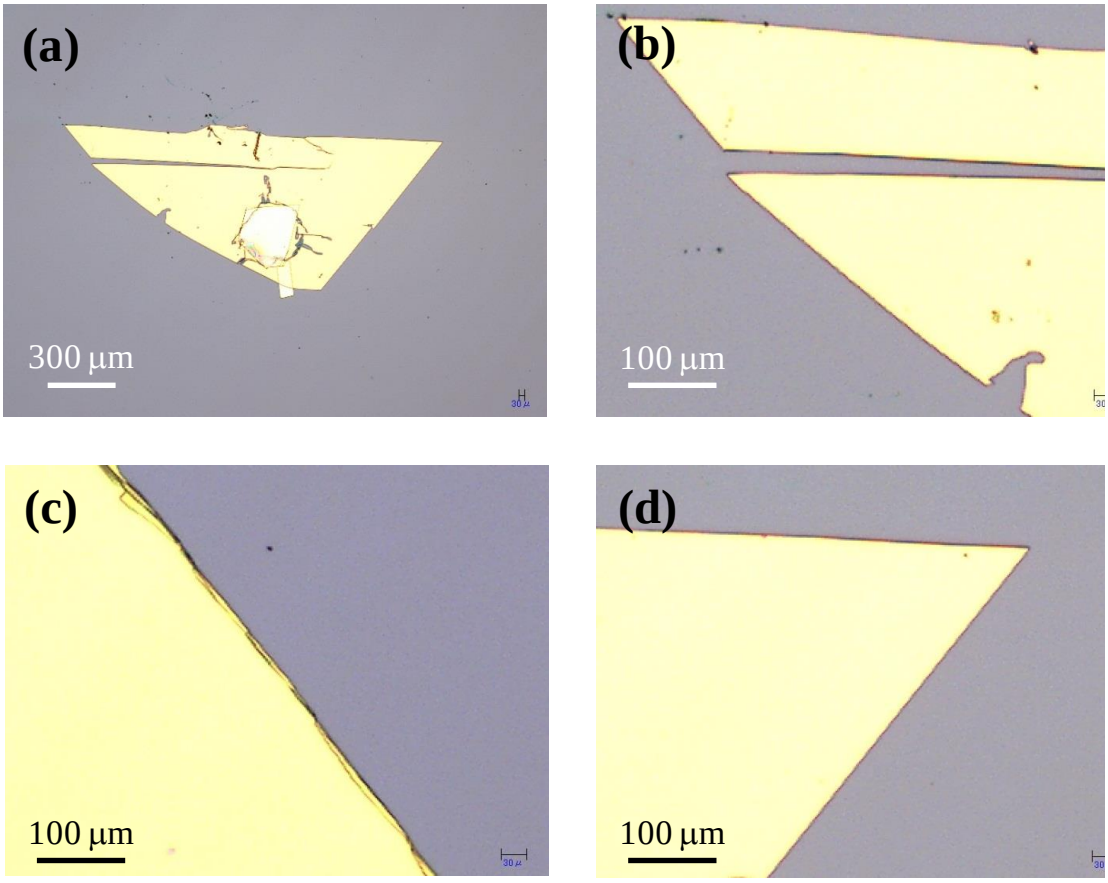

Figure 2-4. Optical microscope images of typical [7]phenacene single crystals on SiO_2 substrates.

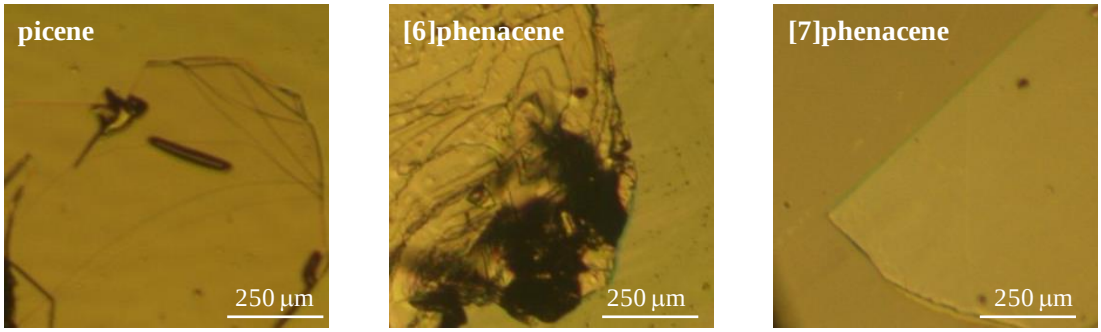

Figure 2-5. Optical microscope images of picene, [6]phenacene and [7]phenacene single crystals covered with 50 nm thick Au.

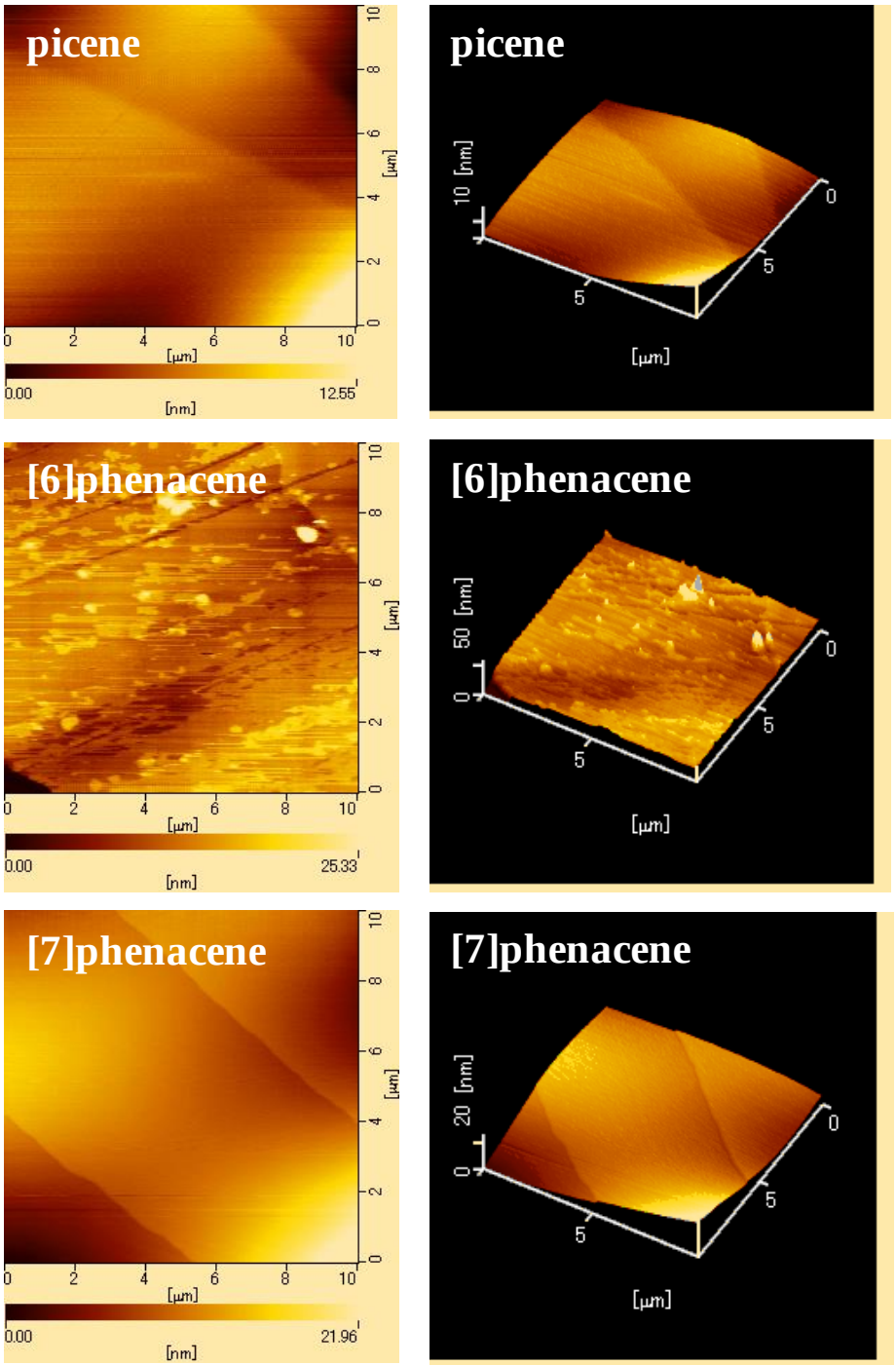

Figure 2-6. AFM images of picene, [6]phenacene and [7]phenacene single crystals.

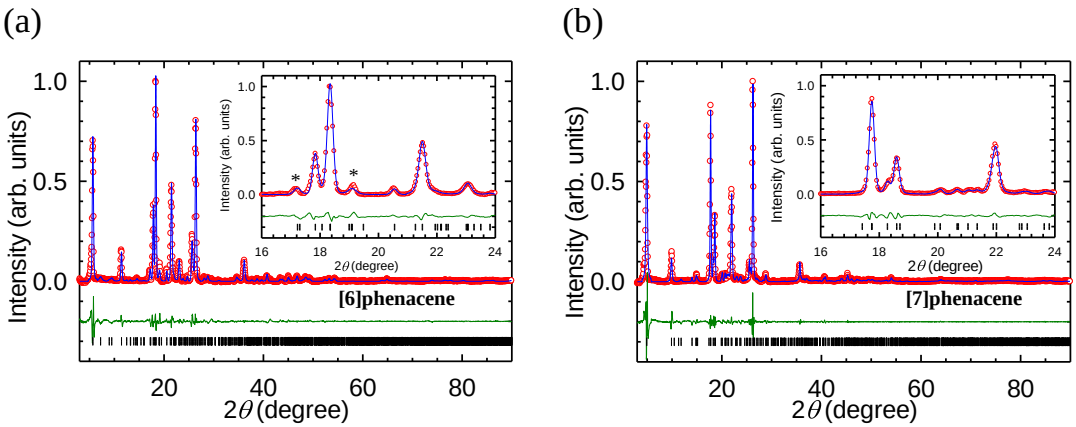

Figure 2-7. X-ray diffraction patterns of (a) [6]phenacene and (b) [7]phenacene powders. In (a) and (b), circles (red) and solid lines (blue) refer to the experimental and calculated (LeBail fit) patterns. The difference between the experimental and calculated patterns and the predicted reflections are shown as lines (green) and ticks (black), respectively. The peaks denoted by an asterisk in (a) reflect the large differences in *a* and *b* between [6]phenacene and [7]phenacene.

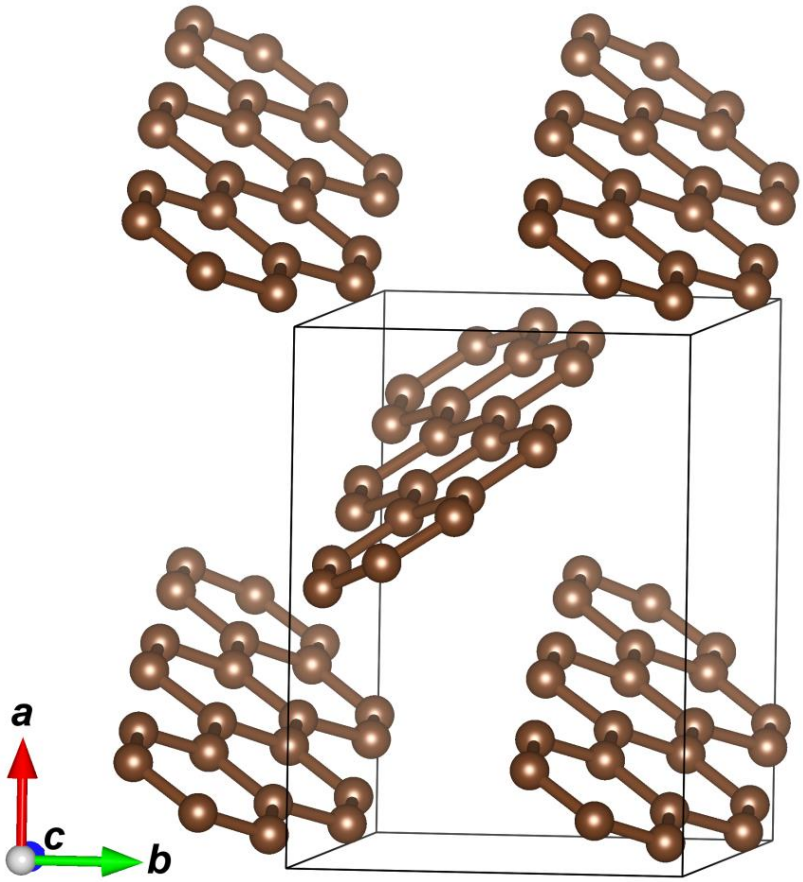

Figure 2-8. Herringbone crystal structure in picene single crystal.

Chapter 3. Electronic structures of phenacene single crystals

This chapter fully describes the electronic structures of phenacene molecules clarified so far. The electronic structures of phenacene molecules have been extensively elucidated based on the studies performed by our groups, inclusive of unpublished data [1-5]. In particular, the review paper reported by Kubozono *et al.* reports details of electronic structures of phenacene molecules and solids [2]. The author of this Doctor thesis is one of co-authors of the review paper [2]. Therefore, this chapter is described based on this review paper [2] and some other studies performed by our group [1,3-5].

Phenacene molecule takes a W-shaped fused configuration of benzene rings, which is quite different from the structure of acene molecule exhibiting a liner fused configuration of benzene rings. Therefore, phenacene molecule has the electronic structure characteristic of the molecular structure.

3-1. Electronic structures of phenacene molecules determined by photoelectron yield spectroscopy and optical absorption under atmospheric condition

As seen from Figure 3-1 [6], the optical absorption bands of [*n*]acenes and [*n*]phenacenes vary with respect to the number of benzene rings. The first absorption band originating from the energy difference between the highest occupied molecular orbital (HOMO) and the lowest unoccupied molecular orbital (LUMO) rapidly shifts to longer wavelengths when the number of benzene rings increases for acenes, suggesting that larger acene molecules exhibit smaller HOMO-LUMO gaps.

On the other hand, the first absorption band of phenacene molecules hardly changes even when the number of benzene rings increases, and the HOMO-LUMO gap is in the UV region. This experimental result also supports the stability of phenacene molecules, *i.e.*, the large HOMO-LUMO gap should suppress the chemical reaction. Figure 3-2 shows the energy diagram for pentacene and picene, for comparing the energy levels of HOMO and LUMO between acene and phenacene. These energy levels are determined

from the photoelectron yield and optical absorption spectra measured under atmospheric conditions [1,2,7]. In pentacene ([5]acene), the HOMO-LUMO gap is 1.8 eV with the HOMO level located at −5.0 eV [7], while picene has a much larger gap of 3.3 eV with the HOMO level at −5.5 eV [1,2]. Figure 3-3 shows the energy diagram of [6]phenacene and [7]phenacene. The energy levels of LUMO and HOMO are located at −2.4 and −5.5 eV for [6]phenacene, and −2.6 and −5.7 eV for [7]phenacene, respectively [3-4]. The HOMO-LUMO gap, or band gap, is 3.1 eV for both molecules. These values are consistent with those for picene. The comparison of FET characteristics among picene, [6]phenacene and [7]phenacene single crystal FETs is of interest because of their similar electronic structure. In the energy diagrams in Refs. 1-4, the Fermi level of Au is drawn together with the energy levels of molecules to explain the well p-channel conduction. Further, the Fermi levels of Ca, Sr and Eu as well as those of HOMO and LUMO of [6]phenacene and [7]phenacene are drawn in Figure 3-4, to discuss the possibility of the n-channel operation [5]; the author does not describe ambipolar property in this Doctor thesis but has already reported it in Ref. 5.

3-2. Electronic structures of phenacene molecules determined by ultra-high vacuum photoemission spectroscopy

The electronic structures of picene and [7]phenacene under ultra-high vacuum condition were obtained with photoemission spectroscopy (PES) and inverse-photoemission spectroscopy (IPES) [8]. PES directly determines HOMO levels, while IPES determines LUMO levels. These experiments were performed under ultra-high vacuum, at 10^{-9} - 10^{-10} Torr. The picene and [7]phenacene thin films were evapourated onto Au / Indium tin oxide substrates in high vacuum. The HOMO and LUMO levels relative to the Fermi level on Au films were determined by in-situ PES and IPES under high-vacuum conditions.

As seen from Figure 3-5, the HOMO and LUMO levels are −1.8 eV and 1.4 eV, respectively, in picene, while the HOMO and LUMO levels are −1.7 eV and 1.4 eV in [7]phenacene, which means that the Fermi level on Au is located around the centre of the

HOMO-LUMO gap. The structures and the energy positions of the PES spectrum in picene are consistent with those of previous reports [9,10]. However, it is suggested that this electronic structure is quite different from those obtained under atmospheric conditions described in section 3-1. Under atmospheric conditions, the Fermi level of Au is near the HOMO levels in picene, [6]phenacene and [7]phenacene (see Figure 3-4), indicating that picene and [7]phenacene tend to become hole-doped (p-type) semiconductors under atmospheric conditions, contrary to their behaviour (intrinsic semiconductor) in a high vacuum. Recently, Okazaki *et al.* reported PES spectra of K doped picene thin films and observed the new state near Fermi level, suggesting metallic behaviour [11]. The band structure could not be explained by simple rigid band picture.

3-3. Angle-resolved photoemission spectroscopy (ARPES) of picene solids

Band dispersions in organic thin films and single crystals have been extensively measured with angle-resolved ultraviolet photoemission spectroscopy (ARUPS). Koch *et al*. succeeded in observing the energy band dispersion in well-oriented pentacene thin films formed on a highly oriented pyrolytic graphite (HOPG) substrate, which showed a band width of 0.19 eV at room temperature [12]. The energy dispersion in pentacene thin films using various metal substrates, such as Cu (110), Bi (001) and $\sqrt{3}\times\sqrt{3}$ Bi-Si(111), were also reported [13-15].

Recently, Xin *et al*. reported ARPES spectra of picene single crystals [10]. The report showed the electronic structure and band dispersion along π-stacking direction. The hole effective mass, m, of picene was determined to be $2.24m_0$, where m_0 is the rest mass of electron. As the m is not so large, in this study the m was taken to be $1.0m_0$ when the m is required in the analysis (Chapter 7). The dispersion width of valence band (HOMO) was 0.18 eV along $\Gamma - Y$ direction, which is much smaller than that of theoretically predicted one, 0.51 eV [16]. The band dispersion of 0.18 eV is consistent with that, 0.25 eV, along Γ- X determined from ARPES for rubrene single crystals [17]. The fact that ARPES could be observed in picene single crystals clearly shows that the molecular orbitals of picene forms band in single crystals, suggesting that the channel

transport takes place based on the band-transport mechanism in picene single crystal FET.

References

[1] H. Okamoto, N. Kawasaki, Y. Kaji, Y. Kubozono, A. Fujiwara, and M. Yamaji, J. Am. Chem. Soc. **130**, 10470 (2008).

[2] Y. Kubozono, H. Mitamura, X. Lee, X. He, Y. Yamanari, Y. Takahashi, Y. Suzuki, Y. Kaji, R. Eguchi, K. Akaike, T. Kambe, H. Okamoto, A. Fujiwara, T. Kato, T. Kosugi, and H. Aoki, Phys. Chem. Chem. Phys. **13**, 16476 (2011).

[3] Y. Sugawara, Y. Kaji, K. Ogawa, R. Eguchi, S. Oikawa, H. Gohda, A. Fujiwara, and Y. Kubozono, Appl. Phys. Lett. **98**, 013303 (2011).

[4] N. Komura, H. Goto, X. He, H. Mitamura, R. Eguchi, Y. Kaji, H. Okamoto, Y. Sugawara, S. Gohda, K. Sato, and Y. Kubozono, Appl. Phys. Lett. **101**, 083301 (2012).

[5] X. He, R. Eguchi, H. Goto, E. Uesugi, S. Hamao, Y. Takabayashi, and Y. Kubozono, Org. Electron. **14**, 1673 (2013).

[6] Based on Ref. 2, Prof. Okamoto newly made figures.

[7] T. Yasuda, T. Goto, K. Fujita, and T. Tsutsui, Appl. Phys. Lett. **85**, 2098 (2004).

[8] R. Eguchi, Abstract of 7th International Conference on Organic Electronics, Roma, June 2011. R. Eguchi, N. Kawai, Y. Kaji, K. Ogawa, A. Fujiwara, and Y. Kubozono, unpublished.

[9] F. Roth, M. Gatti, P. Cudazzo, M. Grobosch, B. Mahns, B. Büchner, A. Rubio, and M. Knupfer, New J. Phys. **12**, 103036 (2010).

[10] Q. Xin, S. Duhm, F. Bussolotti, K. Akaike, Y. Kubozono, H. Aoki, T. Kosugi, S. Kera, and N. Ueno, Phys. Rev. Lett. **108**, 226401 (2012).

[11] H. Okazaki, T. Wakita, T. Muro, Y. Kaji, X. Lee, H. Mitamura, N. Kawasaki, Y. Kubozono, Y. Yamanari, T. Kambe, T. Kato, M. Hirai, Y. Muraoka, and T. Yokoya, Phys. Rev. B **82**, 195114 (2010).

[12] N. Koch, A. Vollmer, I. Salzmann, B. Nickel, H. Weiss, and J. P. Rabe, Phys. Rev. Lett. **96**, 156803 (2006).

[13] H. Yamane, E. Kawabe, D. Yoshimura, R. Sumii, K. Kanai, Y. Ouchi, N. Ueno, and K. Seki, Phys. Stat. Sol. (b) **245**, 793 (2008).

[14] H. Kakuta, T. Hirahara, I. Matsuda, T. Nagao, S. Hasegawa, N. Ueno, and K. Sakamoto, Phys. Rev. Lett. **98**, 247601 (2007).

[15] M. Ohtomo, T. Suzuki, T. Shimada, and T. Hasegawa, Appl. Phys. Lett. **95**, 123308 (2009).

[16] T. Kosugi, T. Miyake, S. Ishibashi, R. Arita, and H. Aoki, J. Phys. Soc. Jpn. **78**, 113704 (2009).

[17] H. Ding, C. Reese, A. J. Mäkinen, Z. Bao, and Y. Gao, Appl. Phys. Lett. **96**, 222106 (2010).

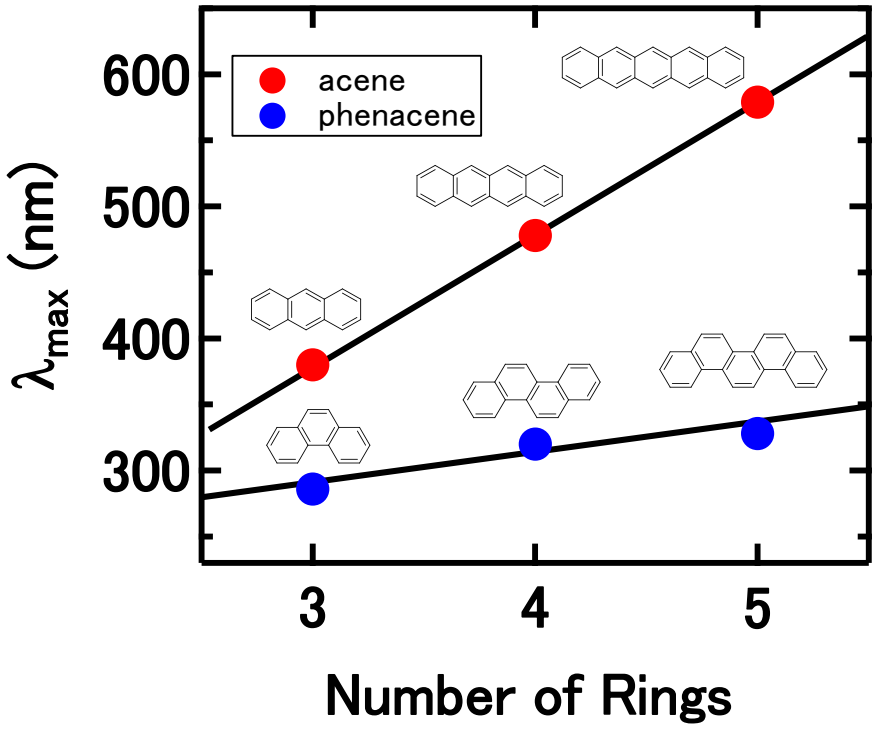

Figure 3-1. Optical absorption bands of [*n*]acenes and [*n*]phenacenes with different number of benzene rings.

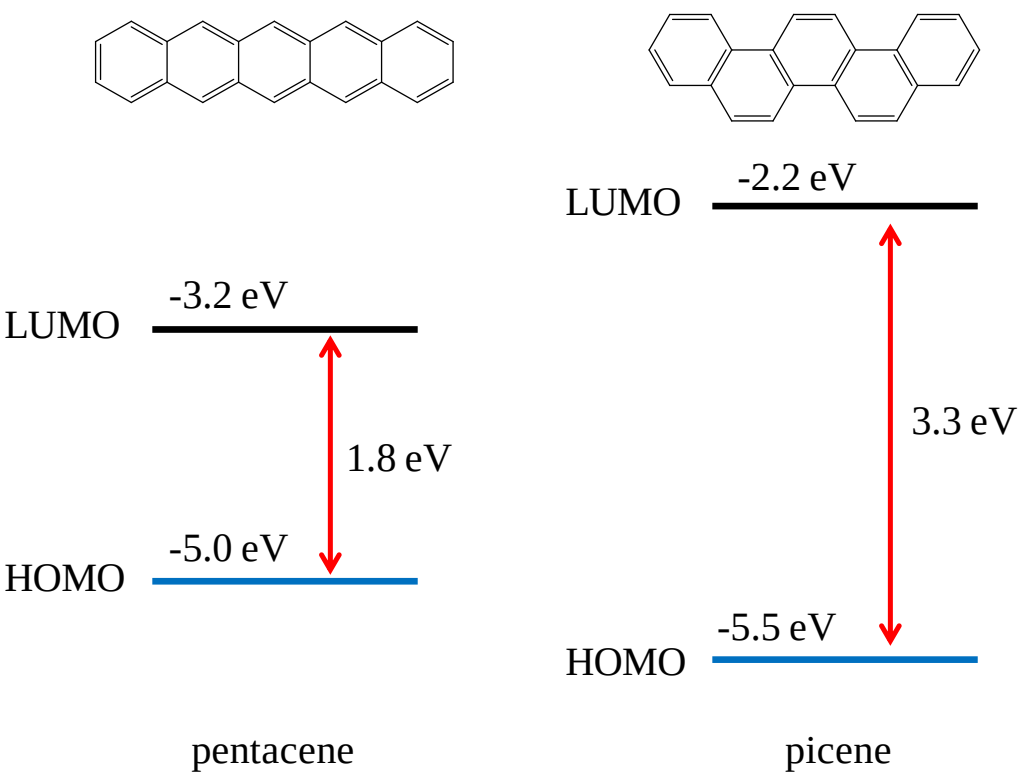

Figure 3-2. Energy diagrams of pentacene (left) and picene (right). HOMO-LUMO gaps are indicated by red arrows.

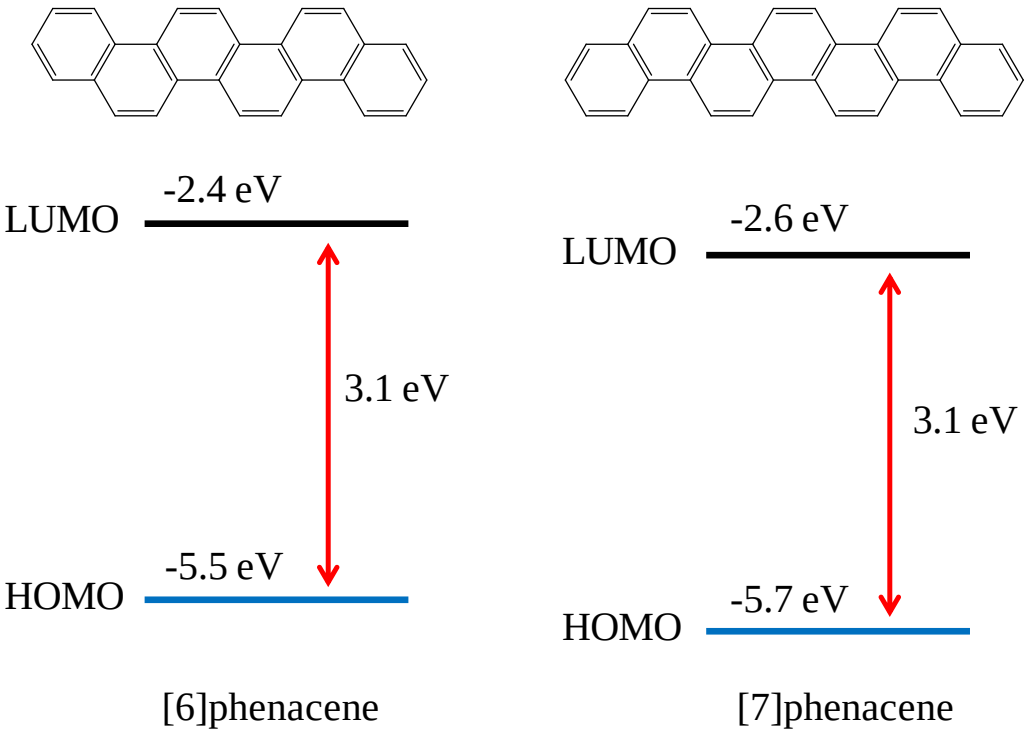

Figure 3-3. Energy diagrams of [6]phenacene (left) and [7]phenacene (right). HOMO-LUMO gaps are indicated by red arrows.

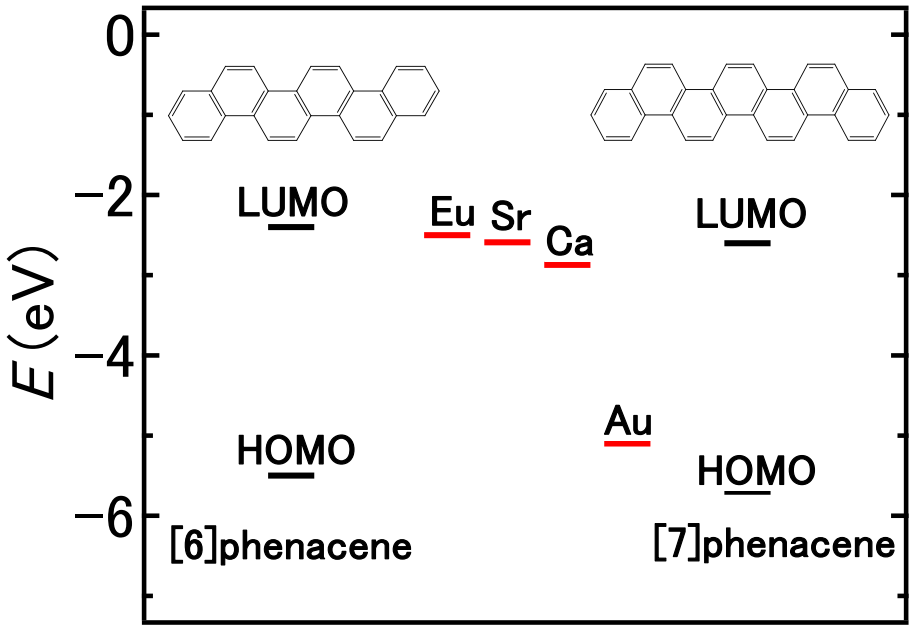

Figure 3-4. Energy diagrams of [6]phenacene and [7]phenacene, and the work functions of metals used for electrodes of FET devices in this study and Ref. 5.

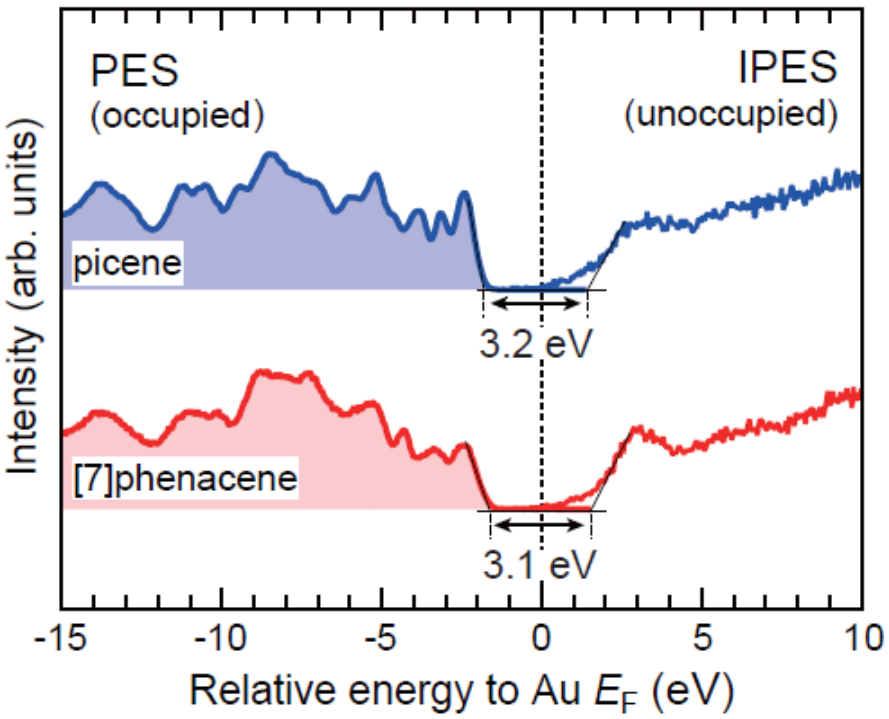

Figure 3-5. Electronic structures of picene and [7]phenacene obtained by PES and IPES. HOMO-LUMO gaps are determined from the edge energies of PES and IPES spectra.

Chapter 4. Theoretical bases for FET

The FET device enables ones to amplify the drain current between sources and drain electrodes using gate voltage. The fundamental principle of FET operation was introduced in chapter 1. In this chapter, the author fully describes the operation mechanism in FET devices with mathematical formulae. Actually, the description in this chapter refers to the operation mechanism of Si MOS FET. As described in chapter 1, strictly speaking the operation of organic FET is different from that of Si MOS FET. The operation in the former FET is based on the accumulation of carrier, and the active layer is substantially recognised as intrinsic semiconductor, while the operation of the latter FET is explained with the formation of inversion layer. In the latter FET, n-type or p-type Si semiconductor is used as active layer of FET, *i.e.*, the extrinsic semiconductor is a key material for the Si MOS FET. The description of this chapter is mainly made based on some text books [1-10], in the same manner as chapter 1.

4-1. Explanation of technical terms in FET

Technical terms necessary for understanding FET operation are explained in this section. In this section, no mathematical formulae are used for the explanation of the technical terms. The terms are explained based on the mathematical formulae in section 4-2.

4-1-1. Field-effect mobility

The field-effect mobility, μ, shows how strongly hole or electron is influenced in the channel region of FET when applying V_D. Actually, the channel is formed by applying V_G. If the carrier responsible for channel conduction in FET is hole (electron), the field-effect mobility is called as 'hole (electron) field-effect mobility'. Thus, the mobility in the FET is named as 'field-effect mobility', while the word 'mobility' is generally used as the parameter which shows how strongly carriers in semiconductor are influenced by electric field. Therefore, the field-effect mobility can be determined from the FET characteristics,

and the value is always given in units of $cm^2\ V^{-1}\ s^{-1}$. In the organic FET device, the field-effect mobility is affected from not only intrinsic nature of channel material such as formation of effective π-conduction network but also extrinsic factors such as defects, grain boundaries, impurities and contact resistance. The defects, grain boundaries and impurities are formed extrinsically in channel region, and the contact resistance relates to the carrier injection between active layer and source / drain electrodes. Therefore, the field-effect mobility is a device parameter representing the device performance.

4-1-2. Threshold voltage and on-off ratio

In Si MOS FET, the 'strong' inversion layer can be formed by applying V_G so that the band curvature at surface (interface between active layer and gate dielectric) becomes equal to the twice value, $2e\phi_F$ (= $2|\varepsilon_{Fsc} - \varepsilon_i|$), of the Fermi potential energy, $e\phi_F$, where ε_{Fsc} and ε_i refer to Fermi energy and intrinsic energy, respectively (see Figure 1-2). The V_G is called as 'threshold voltage'. In Si MOS FET, the channel starts to open at the V_{TH}. In the organic FET, the threshold voltage, V_{TH}, is the voltage indispensable to accumulate the carriers enough to form accumulation layer. Actually, the $|V_{TH}|$ is strongly influenced by the interface states such as trap states formed in channel region, *i.e.*, the $|V_{TH}|$ increases with an increase in trap states. Consequently, from view of practical application, the $|V_{TH}|$ must be decreased.

The 'on-off ratio' is the ratio of switch-on drain current to the off-current. The minimum absolute-current below $|V_{TH}|$ is taken as the off-current, while the maximum absolute-current is taken as the on-current. On-off ratio is important in the integration of FETs, *i.e.*, the formation of logic gate circuits. Suppressing the off-current is significant to decrease the power consumption. For high-power FET which is required for mobile communication system, communication moon relay, and compact radar, the enhancement of on-drain current is indispensable.

4-1-3. Subthreshold swing

The 'subthreshold swing', *S*, is the parameter how much V_G is required to increase I_D by a factor of 10. This value is normally called as '*S* factor' because another name of subthreshold swing is also 'subthreshold slope'. The value is given in V decade^{-1}. The smaller *S* provides more efficient / rapid switching. The lowest *S* is theoretically 60 mV decade^{-1} at 300 K. For the organic FET in which accumulation layer forms the channel region, the minimum *S* is theoretically evaluated to be more than 60 mV decade^{-1} [4].

4-2. Theoretical background of FET

Figure 4-1 shows the device structure of typical organic FET. The I_D can be controlled by applying the V_G. A positive V_G attracts electrons to the interface between the gate dielectric and the organic active layer, while a negative V_G attracts holes to the interface between the gate dielectric and the organic active layer. These electrons or holes form a conducting channel between the source and the drain. Typical I_D - V_D curves under different V_G in FET devices is shown in Figure 4-2. The curves are called as 'output cuves', and the I_D - V_D at low V_D range ($V_D << V_G - V_{TH}$) is called as 'liner regime', while the I_D - V_D at high V_D range ($V_D > V_G - V_{TH}$) is called as 'saturation regime'. The I_D is constant in this range. Figure 4-3 shows the I_D - V_G curve at fixed V_D. The curve is called as 'transfer curve'. The theoretical formula for I_D - V_G curve is different between linear and saturation regimes. The μ, V_{TH}, on-off ratio and *S* are evaluated from the transfer curve. Normally, in the FET experiments, the output curves are measured to determine the linear and saturation regimes in advance of measurements of transfer curves.

In the Si MOS FET, the channel can be formed by minority carriers, which is called as 'inversion layer'. However, in organic FET, the channel is formed by accumulated carriers in the accumulation layer. The formulae based on the formation of inversion layer in Si MOS FET must be modified in organic FET because the I_D in Si MOS FET is directly related to the inversion charge $Q_{inv}(y)$ modified by depletion charge $Q_{dep}(y)$.

Nevertheless, the basic conceptual issues are applicable to the organic FETs. The I_D in inversion layer is given by the following equation [1]:

$$\int_0^L I_D dy = -\mu W \int_{V_S}^{V_D} Q_{inv}(y) dV(y), \quad (4\text{-}1)$$

where W and L is channel width and length, respectively, as shown in Figure 4-1. $V(y)$ is the local electrostatic potential satisfying boundary conditions, $V(0) = V_S$ and $V(L) = V_D$. Here, the general theory which covers nonzero V_S is presented. $Q_{inv}(y)$ induced by V_G is estimated from the parallel-plate capacitor model, and then, Eq. 4-1 is expressed as

$$I_D = \mu C_{ox} \frac{W}{L} \int_{V_S}^{V_D} (V_G - [V_{THo} + nV(y)]) dV(y), \quad (4\text{-}2)$$

where C_{ox}, V_{THo}, n and $V(y)$ refer to capacitance per area for gate dielectric, non-ideal threshold voltage, body factor and voltage at y, respectively. This equation can also be applied to the organic FET in which the channel is formed through carrier accumulation. By considering the dependence of threshold voltage on source voltage V_s,

$$V_{TH} = V_{THo} + nV_s. \quad (4\text{-}3)$$

Therefore, the Eq. 4-2 reduces to

$$I_D = \frac{\mu C_{ox} W}{L} \left\{ (V_G - V_{TH}) V_{DS} - \frac{n V_{DS}^2}{2} \right\}. \quad (4\text{-}4)$$

Here, $V_{DS} \equiv V_D - V_S$. In the linear region, as $V_{DS} << V_G - V_{TH}$, the second term can be neglected. Consequently, we can obtain the following equation:

$$I_D = \frac{\mu C_{ox} W}{L} \{ (V_G - V_{TH}) V_{DS} \}. \quad (4\text{-}5)$$

In the saturation regime, $dI_D / dV_{DS} = 0$ in Eq. 4-4. Therefore, the V_D in saturation regime is expressed as follows:

$$V_D = \frac{V_G - V_{TH}}{n} + V_s. \quad (4\text{-}6)$$

The Eq. 4-6 is substituted into Eq. 4-4. Consequently, the I_D in the saturation regime can be derived,

$$I_D = \mu C_{ox} W \frac{1}{L} \frac{(V_G - V_{TH})^2}{2n}. \quad (4\text{-}7)$$

Generally, n = 1. This leads to the following equation.

$$I_{\mathrm{D}} = \mu C_{\mathrm{ox}} W \frac{1}{L} \frac{(V_{\mathrm{G}} - V_{\mathrm{TH}})^2}{2}. \quad (4\text{-}8)$$

This formula is generally used to evaluate the μ value from the I_{D} -V_{G} curve in saturation regime.

The S factor can be expressed as

$$S = \frac{dV_{\mathrm{G}}}{d\log I_{\mathrm{D}}}. \quad (4\text{-}9)$$

Therefore, the S factor can be evaluated from the log I_{D} - V_{G} curve. The S factor is related to the density of trap. If the trap states are few in the active layer, the S factor decreases [1]. The S factor in accumulation region is fully discussed in Ref. 11.

4-3. Evaluation of carrier injection barrier height

The Schottky barrier is formed in the contact between metal and semiconductor. Figure 4-4 shows the energy diagram of metal and semiconductor, in which the $\varepsilon_{\mathrm{Fsc}}$ is higher than that of metal, ε_{m}. After contact of semiconductor and metal (Figure 4-5), the Fermi level alignment produces the band curvature in semiconductor region. Further, the presence of depletion layer in semiconductor produces the strong electric field to fix the band curvature. Here the potential barrier height in semiconductor, V_{i}, can be expressed as

$$eV_{\mathrm{i}} = e(\phi_{\mathrm{m}} - \phi_{\mathrm{sc}}), \quad (4\text{-}10)$$

where ϕ_{m} and ϕ_{sc} correspond to the work functions of metal and semiconductor, respectively. In this energy diagram (Figure 4-5), $e\phi_{\mathrm{B}}$ is called as 'Schottky barrier height'; e is taken as positive. When applying the bias voltage V_{a} to metal, the band bending is drastically modified. In $V_{\mathrm{a}} > 0$, the energy diagram shown in Figure 4-6(a) is formed. In $V_{\mathrm{a}} < 0$, the energy diagram shown in Figure 4-6(b) is formed. In the case of

positive (negative) V_a, the potential barrier in semiconductor decreases (increases), but $e\phi_B$ is constant. In this case, the current density J (current per junction area) flowing between metal and semiconductor is expressed as

$$J = A^* T^2 \exp\left(\frac{-e\phi_B}{k_B T}\right)\left[\exp\left(\frac{eV_a}{k_B T}\right) - 1\right]. \qquad (4\text{-}11)$$

In Eq. 4-11, A^* is 'Richardson constant', k_B is the Boltzmann constant and T is temperature. In this model, the Schottky barrier is formed at the interface between metal and semiconductor, which prevents the effective carrier injection across the interface. On the other hand, the Ohmic contact must be formed in semiconductor side for the ideal measurement of carrier transport. The Eq. 4-11 provides the rectifying behaviour in J - V_a curve as shown in Figure 4-7. In chapter 7, single Schottky barrier model described in this section is expanded to double Schottky barrier model. The double Schottky barrier model, in which the formation of two Schottky barriers is assumed, is used for evaluating the potential barrier height between single crystals and source / drain electrodes. The details of the formula of double Schottky barrier height model is described in chapter 7.

References

[1] H. T. Grahn, Introduction to Semiconductor Physics (World scientific publishing Co. Pte. Ltd., Singapore, 1999).

[2] J. P. Colinge and C. A. Colinge, Physics of Semiconductor Devices (Springer, Massachusetts, 2006).

[3] D. K. Schroder, Semiconductor Material and Device Characterization (John Wiley & Sons. Inc., New Jersey, 2006).

[4] S. M. Sze, Physics of Semiconductor Devices (John Wiley & Sons. Inc., New Jersey, 2007).

[5] U. K. Mishra and J. Singh, Semiconductor Device Physics and Design (Springer, Dordrecht, 2008).

[6] J. J. Liou, A. O. Conde, and F. G. Sanchez, Analysis and Design of Mosfets: Modeling, Simulation, and Parameter Extraction (Kluwer Academic Publishers, Massachusetts, 1998).

[7] I. Kymissis, Organic Field Effect Transistors: Theory, Fabrication and Characterization (Springer, New York, 2009).

[8] Z. Bao and J. Locklin, Organic Field-Effect Transistors (CRC press, Taylor & Francis Group, Boca Raton, 2007).

[9] R. E. Hummel, Electronic Properties of Materials (Springer, New York, 2012).

[10] Y. Singh and S. Agnihotri, Semiconductor Devices (I. K. International Publishing House Pvt. Ltd., New Delhi, 2009).

[11] N. Kawasaki, Y. Ohta, Y. Kubozono, A. Konishi, and A. Fujiwara, Appl. Phys. Lett. **92**, 163307 (2008).

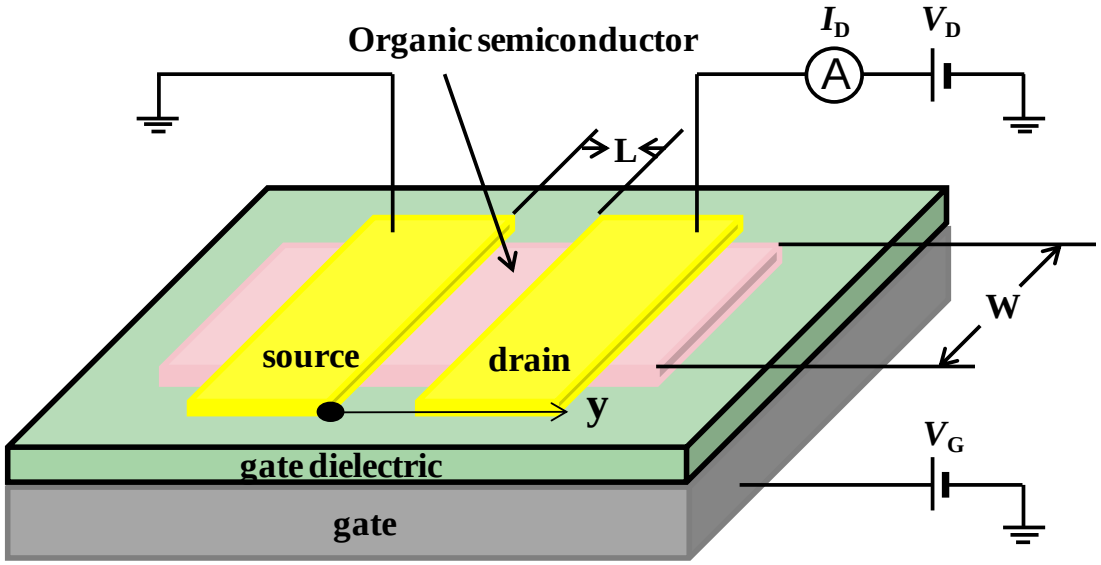

Figure 4-1. Typical organic FET device structure.

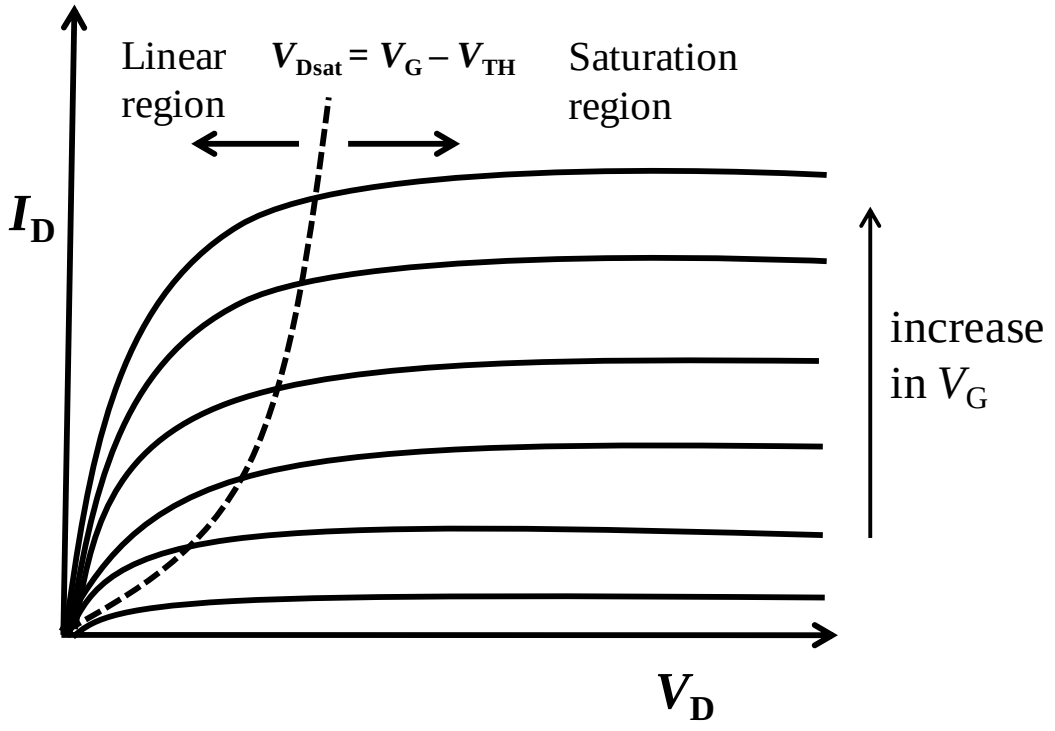

Figure 4-2. I_D - V_D characteristics (output curves) for different V_G. The dashed parabolic line separates the linear regime and the saturation regime.

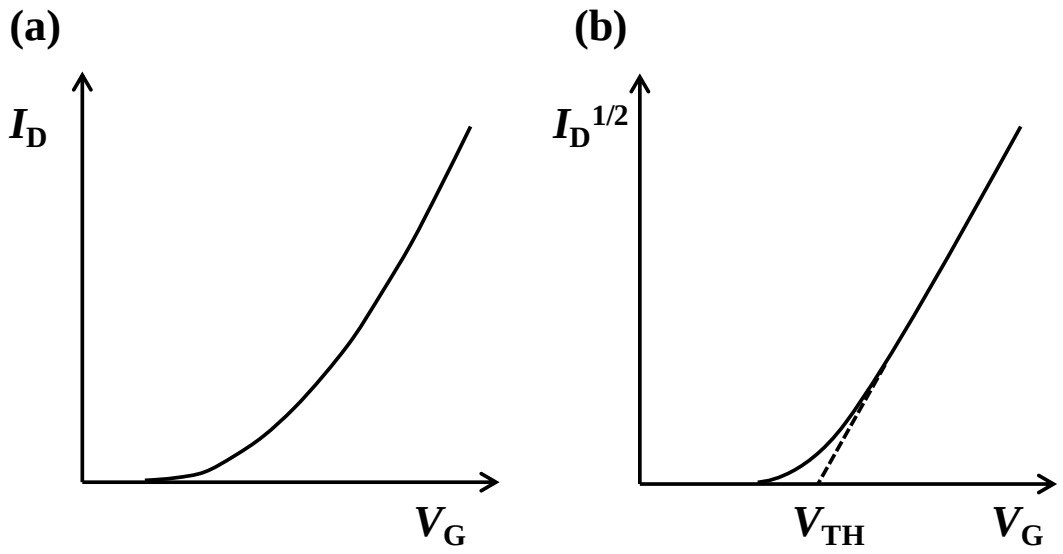

Figure 4-3. (a) I_D - V_G characteristic (transfer curve) measured in a saturation region. (b) The saturation drain current is proportional to $(V_G - V_{TH})^2$, indicating a linear relation between $I_D^{1/2}$ and V_G.

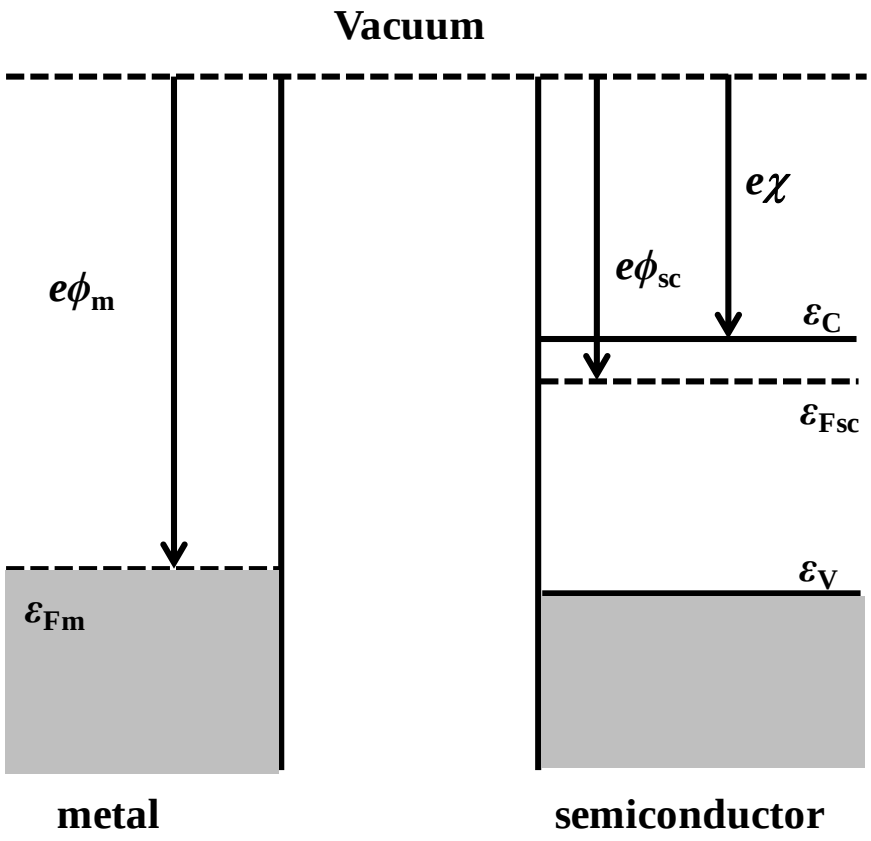

Figure 4-4. Energy bands in a metal and an n-type semiconductor.

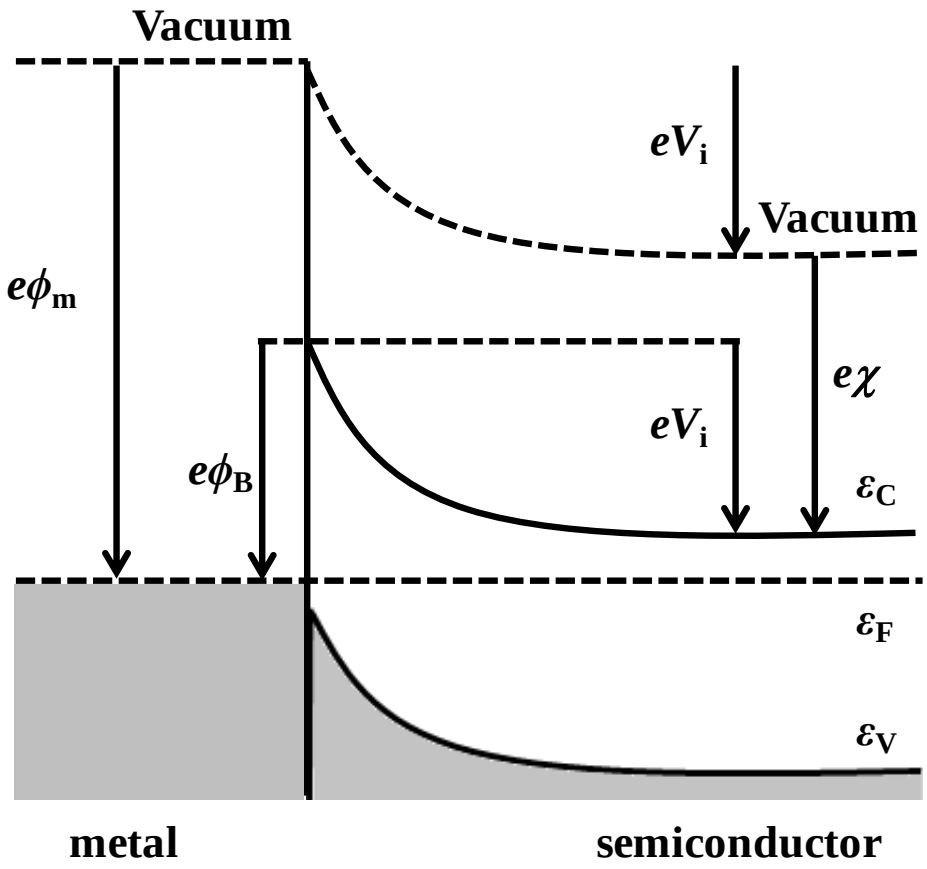

Figure 4-5. Energy band diagram modified by the contact of a metal and a semiconductor. The Schottky barrier is formed at the interface.

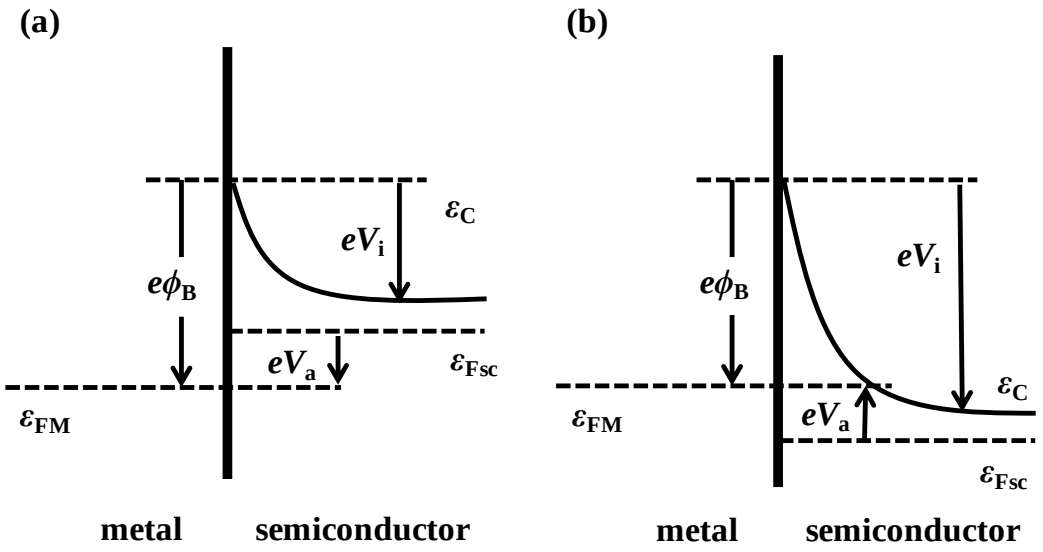

Figure 4-6. Energy band diagrams of the Shottky contact under (a) forward bias ($V_a > 0$) and (b) reverse bias ($V_a < 0$), where V_a is the bias voltage applied to the metal.

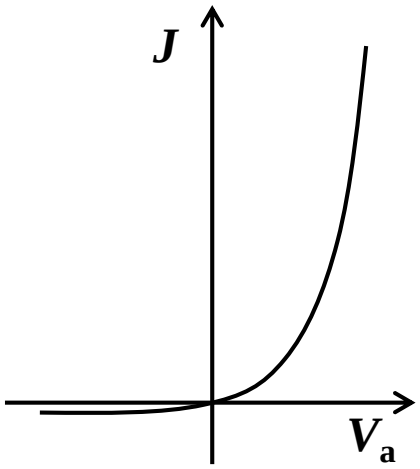

Figure 4-7. Current-voltage characteristic of the Schottky contact.

Chapter 5. Fundamental FET characteristics of phenacene single crystal FETs

In this chapter, the author describes the fundamental FET characteristics of normal phenacene single crystal FETs; three phenacene molecules, picene, [6]phenacene and [7]phenacene, are used in this work. The results are of significance to understand deeply the whole FET characteristics of various types of phenacene single crystal FETs fabricated in this study. From the fundamental FET characteristics, we can know the exciting and interesting properties of the phenacene single crystal FETs as well as the potential application of the FETs towards practical electronics. The experimental techniques used in this FET study are described in the section 5-1. In this Doctor thesis, only a study described in section 5-2 is performed by our Laboratory member other than the auther, and it is not original work of the author; the experimental results are reported in Ref. 1. However, for the comparison with the study performed by the author (all parts other than section 5-2), the experimental results are significant. Therefore, based on the data stored in our Laboratory, the experimental results are described and discussed by author in section 5-2.

5-1. Common experimental techniques used in chapters 5 to 11

The single crystal growth of phenacene molecules is described in chapter 2. The cleaning process of substrates of SiO_2 / Si substrates is shown in Figure 5-1.

The commercially available SiO_2 / Si substrates were used in this study. The surface of a SiO_2 (300 or 400 nm) / Si substrate was washed with acetone, methanol, H_2O_2 / H_2SO_4 (1 volume / 4 volume) and distilled water. The washing of all substrates including SiO_2 / Si substrate was performed in an ultrasonic bath.

The Ta_2O_5 (50 nm) / Si and HfO_2 (50 nm) / Si substrates were prepared from magnetron RF sputtering method. Commercially available Ta_2O_5 (50 nm) / Si and HfO_2 (50 nm) / Si substrates were used in this study. These substrates were washed with methanol and isopropanol in the same manner as the cleaning process of SiO_2 / Si; the

solvents used for washing are different between SiO_2 / Si and Ta_2O_5 (50 nm) or HfO_2 (50 nm) / Si substrates.

The surfaces of SiO_2, Ta_2O_5 and HfO_2 were coated with parylene (*i.e.*, parylene (30 nm) / SiO_2 / Si). The phenacene single crystals were placed on the substrates coated with parylene. Parylene-coated surface can provide a hydrophobic environment and suppress a leakage of the gate current [1]. The parylene-coating process is shown in Figure 5-2. In parylene-coating, the precursor material, dichloro[2,2]paracyclophane, was sublimed at 120°C and thermally-polymerized at 680°C. The polymerized material is named as parylene-C. During parylene-coating, the vacuum level of the parylene-coating system was maintained at 10^{-2} Torr. As shown in Figure 5-2, the SiO_2 / Si substrate was placed on the vacuum chamber. The parylene-C is reported to be mechanically stable from -200 to +150 °C.

In this study, the phenacene single crystal FETs are prepared on parylene-coated gate-dielectric surface formed according to the procedures (substrate cleaning and parylene-coating) described above. The single crystal was placed on the parylene-coated gate dielectric substrate (SiO_2 / Si or Ta_2O_5 / Si or HfO_2 / Si), as shown in Figure 5-3. The channel was formed on the single crystal by a thermal deposition of Au using tungsten-wire as a shadow mask. The deposition process is shown in Figure 5-4. In Figure 5-4, the deposition chamber used in this study is schematically drawn. In the deposition chamber, the substrate was put under the sample holder, and the sample holder was kept at room temperature; strictly speaking the sample holder were not heated or cooled but the temperature of sample holder during deposition was not monitored. The thickness monitor was placed near the sample holder, and during deposition of sample the thickness was checked carefully. The heating for evapouration of sample was performed by applying the electric power to the evapourators containing samples. The base pressure in the deposition chamber was maintained to ~ 10^{-7} Torr before the start of thermal deposition. The thickness of Au source / drain electrodes was 50 nm for all FET devices. In the subsequent sections and chapters, the author does not describe the process shown above.

The experimental capacitance per area, C_o, for each gate dielectric was obtained by extrapolating the capacitance recorded at 20 Hz - 200 kHz to 0 Hz with an AC amplitude of 1 V using an LCR meter (Agilent E4980A). The C_o values were determined to be 11 nF cm^{-2} for parylene (30 nm) / SiO_2 (300 nm), 9.1 nF cm^{-2} for parylene (30 nm) / SiO_2 (400 nm), 49 nF cm^{-2} for parylene (50 nm) / Ta_2O_5 (300 nm), and 49 nF cm^{-2} for parylene (30 nm) / HfO_2 (50 nm).

The FET characteristics were measured using a probe system (HiSOR HMP-400) and a semiconductor parametric analyser (Agilent B1500A). The source electrode was always grounded. The V_D was applied to drain electrode and V_G was directly applied to the Si substrates; the Si substrate is a heavily doped Si and it is metallic. They were measured in an Ar-filled glove box, except for temperature dependence of FET characteristics in chapters 7 and 11; the details of measurement for temperature dependence are described in each chapter. Two-terminal measurement mode was used in measuring FET characteristics.

The FET parameters were determined from the forward transfer curves in the saturation regime for single crystal FETs with a simple MOS formula (Eqs. 4-5 and 4-8 in chapter 4).

5-2. Fundamental FET characteristics of picene single crystal FET

5-2-1. Introduction

The characteristics of FETs have been extensively studied with thin films of phenacene type molecules, which consist of W-shape fused benzene ring network, or armchair-edge structure [2-13]. These FETs showed excellent p-channel FET characteristics with the μ being higher than 1 $cm^2 V^{-1} s^{-1}$ [8-11]. The picene thin film FET was fabricated by our group for the first time [7]. It was found from the subsequent studies that the picene FET was one of the most promising FET devices from the point of view of practical application, because of its high μ (> 1.0 $cm^2 V^{-1} s^{-1}$) , a clear O_2 gas sensing effect, and high stability in atmosphere [8-10]. Furthermore, we succeeded in

fabrication of [6]phenacene and [7]phenacene thin film FETs [10-13], and the μ as high as 7.4 $cm^2 V^{-1} s^{-1}$ was recorded in [6]phenacene thin film FET [11]. Kawai *et al*. fabricated picene single crystal FET for the first time, and the μ as high as 1.3 $cm^2 V^{-1} s^{-1}$ was recorded in the picene single crystal FET [1]. Although the μ value is not higher than that of picene thin film FET [8], the μ more than 1 $cm^2 V^{-1} s^{-1}$ attracts interest in the study aiming for the future application. Furthermore, the study on picene single crystal is of significance from view of fundamental physics and chemistry that clarify the intrinsic properties of picene solids. Since in particular alkali-metal intercalated solids (or electron accumulated picene solids) showed the superconductivity, the study on picene solids accumulated carriers is exciting.

Kawai *et al*. reported previously the FET characteristics of picene single crystal FET with some gate dielectrics, and the improvement of FET characteristics (increase in μ) through a reduction of contact resistance using 7,7,8,8-tetracyano-p-quinodimethane (TCNQ) was fully discussed [1]. In chapter 6, the author describes the FET characteristics of picene single crystal FET, in which the interface between single crystal and source / drain electrodes is modified using the 2,3,5,6-tetrafluoro-7,7,8,8-tetracyano-p-quinodimethane (F4TCNQ) which is the stronger electron acceptor than TCNQ. In the section 5-2, the fundamental FET characteristics of picene single crystal FET without any interface control are reported with two different gate dielectrics, SiO_2 and Ta_2O_5.

5-2-2. Experimental section

The picene single crystal FETs with SiO_2 / Si and Ta_2O_5 / Si substrates were fabricated according the experimental process described in the section 5-1; thickness of SiO_2 was 400 nm and that of Ta_2O_5 was 50 nm. The FET device structure is shown in Figure 5-5. The channel length *L* and width *W* of channel were 30 μm and 250 μm for picene single crystal FET with SiO_2 / Si substrate, respectively, and 30 μm and 2000 μm for picene single crystal FET with Ta_2O_5 / Si substrate.

5-2-3. Results and discussion

Transfer and output curves of the picene single crystal FET with 400 nm thick SiO_2 gate dielectric are shown in Figures 5-6(a) and (b), respectively. In this device, any materials are not inserted into the space between single crystal and source / drain electrodes. These curves were recorded in two-terminal measurement mode, and the transfer curves were recorded in the saturation regime (V_D = −150 V). As seen from Figure 5-6(b), clear p-channel FET characteristics are observed. The hysteresis between the forward and reverse transfer curves is observed; the hysteresis originates in the bias stress effect, which is probably related to a presence of H_2O in the interface between single crystals and the SiO_2 surface.

The large concave behaviour in output curves at low $|V_D|$ range is found, as seen from Figure 5-6(b). The result suggests that the large contact resistance is present between single crystal and source / drain electrodes. Namely, the large potential barrier for hole produces such a concave behaviour. In chapter 6, the improvement of this concave behaviour is fully discussed based on the FET characteristics of picene single crystal FET in which F4TCNQ is inserted into the interface between single crystal and electrodes. The μ and $|V_{TH}|$ were 4.7×10^{-1} $cm^2 V^{-1} s^{-1}$ and 96 V, respectively. The low μ value is assigned to the difficulty in hole injection caused by large potential barrier in this device.

The transfer and output curves of the picene single crystal FET with 50 nm thick Ta_2O_5 gate dielectric are shown in Figures 5-7(a) and (b), respectively. These FET characteristics also show p-channel FET properties, and the large concave behaviour is observed in the output curves at low $|V_D|$ range, which is larger than that of the picene single crystal FET with SiO_2 gate dielectric (Figure 5-6(b)). The μ and $|V_{TH}|$ were 3.4×10^{-2} $cm^2 V^{-1} s^{-1}$ and 26 V. Thus, the large concave behaviour is observed owing to the large injection barrier height.

5-3. Fundamental FET characteristics of [6]phenacene and [7]phenacene single crystal FETs

5-3-1. Introduction

The highest μ value of [6]phenacene thin film FET recorded so far is 7.4 $cm^2 V^{-1} s^{-1}$in two terminal measurement at room temperature [11]. The μ value is much higher than that, 1.4 $cm^2 V^{-1} s^{-1}$, evaluated from the transfer curve in picene thin film FET [8]. Thus [6]phenacene thin films provide the excellent FET performance. Therefore, we may expect excellent FET characteristics in [6]phenacene single crystal FET. Recently, our group observed superconductivity in K intercalated [6]phenacene solids [14], which showed T_c as high as 5 K. This suggests a possibility of electric-field-induced superconductivity in [6]phenacene, as in picene.

The [7]phenacene thin film FET showed the μ as high as 0.75 $cm^2 V^{-1} s^{-1}$ [12]. The μ value is not so high in comparison with those of picene (1.4 $cm^2 V^{-1} s^{-1}$) and [6]phenacene (7.4 $cm^2 V^{-1} s^{-1}$) thin film FETs. Our group reported [7]phenacene thin film FET with ionic liquid gate dielectrics (EDL FET), which showed clear p-channel FET operation [13]. The low-voltage operation is achieved in [7]phenacene thin film EDL FET, and the electrochemical reaction occurs in the FET.

The high-performance may be expected in [7]phenacene single crystal FET since the good quality of [7]phenacene single crystals is confirmed, as described in chapter 2. Judging from a viewpoint of quality of single crystals, we may not expect high-performance in [6]phenacene single FET, in contrast to the performance in [6]phenacene thin film FET. In the section 5-3, the fundamental FET characteristics are fully discussed for these single crystal FETs.

5-3-2. Experimental section

The growth of single crystals of [6]phenacene and [7]phenacene is done based on the procedure described in chapter 2. The washing of substrates, parylene-coating of gate dielectric surface, and fabrication of FET devices are made according to the procedures

described in the section 5-1. The L and W were 30 μm and 200-2000 μm, respectively, for both [6]phenacene and [7]phenacene single crystal FETs.

5-3-3. Results and discussion

Transfer and output curves of [6]phenacene single crystal FET with SiO_2 (300 nm) gate dielectric are shown in Figures 5-8(a) and (b). Clear p-channel characteristics are observed in Figure 5-8. The output curves show concave behaviour at low $|V_D|$ range and a saturation behaviour at high $|V_D|$ range. The concave behaviour suggests that the large potential barrier exists in the interface between single crystal and source / drain electrodes. The μ, $|V_{TH}|$ and on-off ratio were estimated to be 7.6×10^{-2} $cm^2 V^{-1} s^{-1}$, 47 V and 3.9×10^7, respectively. The low μ value probably originates from the large hole-injection barrier. As seen from Figure 5-8, the large hysteresis between forward and reverse transfer curves still exists regardless of hydrophobic treatment of the SiO_2 surface by parylene-coating, suggestive of presence of H_2O near channel region, as described below.

Transfer and output curves of [7]phenacene single crystal FET with 400 nm thick SiO_2 gate dielectric are shown in Figures 5-9(a) and (b). As in [6]phenacene single crystal FET, clear p-channel FET characteristics are observed for the [7]phenacene single crystal FET. The concave behaviour at low $|V_D|$ range and saturation behaviour at high $|V_D|$ range are observed in output curves shown in Figure 5-9(b), suggesting the presence of a large hole-injection barrier between single crystal source / drain electrodes. Notably, hysteresis between the forward and reverse transfer curves is still observed. The hysteresis is probably associated with the bias stress effect, which closely relates to H_2O in the interface between the single crystals and the SiO_2 surface. Previously, we succeeded in a disappearance of hysteresis in the forward and reverse transfer curves in picene thin film FET by using strongly hydrophobic gate dielectric [9]; complete disappearance was obtained in 1 μm thick parylene gate dielectric. This result strongly suggests that the hysteresis is correlated with the presence of H_2O, and the 30 nm thick parylene-coating cannot provide hydrophobic surface enough to remove hysteresis. The μ,

$|V_{TH}|$ and on-off ratio values were 2.6×10^{-2} cm^2 V^{-1} s^{-1}, 91 V and 3.0×10^6, respectively. This μ value is lower than that, 7.6×10^{-2} cm^2 V^{-1} s^{-1}, of [6]phenacene single crystal FET. To increase the FET characteristics, an interface modification to reduce the hole-injection barrier height is indispensable in [6]phenacene and [7]phenacene single crystal FETs.

5-4. Conclusion on fundamental FET characteristics

The output curves of all phenacene single crystal FETs (picene, [6]phenacene and [7]phenacene) without any interface control suggested the presence of large hole-injection barrier. The large barrier lowers the properties of these single crystal FETs. The μ values obtained for these single crystal FETs are much lower than those of the corresponding thin film FETs. The low μs shown in chapter 5 probably originates from the large hole-injection barrier. In chapters 6 and 7, the electron acceptors and donors are inserted into the space between single crystals and electrodes to reduce hole-injection barrier height. In chapter 6, the author describes the typical FET characteristics of phenacene single crystal FET in which the interface control is carried out by the insertion of electron acceptors and donors. In chapter 7, the quantitative study is performed using 14 electron acceptors and donors.

References

[1] N. Kawai, R. Eguchi, H. Goto, K. Akaike, Y. Kaji, T. Kambe, A. Fujiwara, and Y. Kubozono, J. Phys. Chem. C **116**, 7983 (2012).

[2] X. He, R. Eguchi, H. Goto, E. Uesugi, S. Hamao, Y. Takabayashi, and Y. Kubozono, Org. Electron. **14**, 1673 (2013).

[3] Y. Kaji, N. Kawasaki, X. Lee, H. Okamoto, Y. Sugawara, S. Oikawa, A. Ito, H. Okazaki, T. Yokoya, A. Fujiwara, and Y. Kubozono, Appl. Phys. Lett. **95**, 183302 (2009).

[4] Y. Kaji, R. Mitsuhashi, X. Lee, H. Okamoto, T. Kambe, N. Ikeda, A. Fujiwara, M. Yamaji, K. Omote, and Y. Kubozono, Org. Electron. **10**, 432 (2009).

[5] X. Lee, Y. Sugawara, A. Ito, S. Oikawa, N. Kawasaki, Y. Kaji, R. Mitsuhashi, H. Okamoto, A. Fujiwara, K. Omote, T. Kambe, N. Ikeda, and Y. Kubozono, Org. Electron. **11**, 1394 (2010).

[6] Y. Sugawara, K. Ogawa, H. Goto, S. Oikawa, K. Akaike, N. Komura, R. Eguchi, Y. Kaji, S. Gohda, and Y. Kubozono, Sens. Actuators B **171-172**, 544 (2012).

[7] H. Okamoto, N. Kawasaki, Y. Kaji, Y. Kubozono, A. Fujiwara, and M. Yamaji, J. Am. Chem. Soc. **130**, 10470 (2008).

[8] N. Kawasaki, Y. Kubozono, H. Okamoto, A. Fujiwara, and M. Yamaji, Appl. Phys. Lett. **94**, 043310 (2009).

[9] N. Kawasaki, W. L. Kalb, T. Mathis, Y. Kaji, R. Mitsuhashi, H. Okamoto, Y. Sugawara, A. Fujiwara, Y. Kubozono, and B. Batlogg, Appl. Phys. Lett. **96**, 113305 (2010).

[10] N. Komura, H. Goto, X. He, H. Mitamura, R. Eguchi, Y. Kaji, H. Okamoto, Y. Sugawara, S. Gohda, K. Sato, and Y. Kubozono, Appl. Phys. Lett. **101**, 083301 (2012).

[11] 7.4 $cm^2 V^{-1} s^{-1}$by R. Eguchi *et al*., unpublished data.

[12] Y. Sugawara, Y. Kaji, K. Ogawa, R. Eguchi, S. Oikawa, H. Gohda, A. Fujiwara, and Y. Kubozono, Appl. Phys. Lett. **98**, 013303 (2011).

[13] Y. Kaji, K. Ogawa, R. Eguchi, H. Goto, Y. Sugawara, T. Kambe, K. Akaike, S. Gohda, A. Fujiwara, and Y. Kubozono, Org. Electron. **12**, 2076 (2011).

[14] Y. Sakai *et al*., unpublished data.

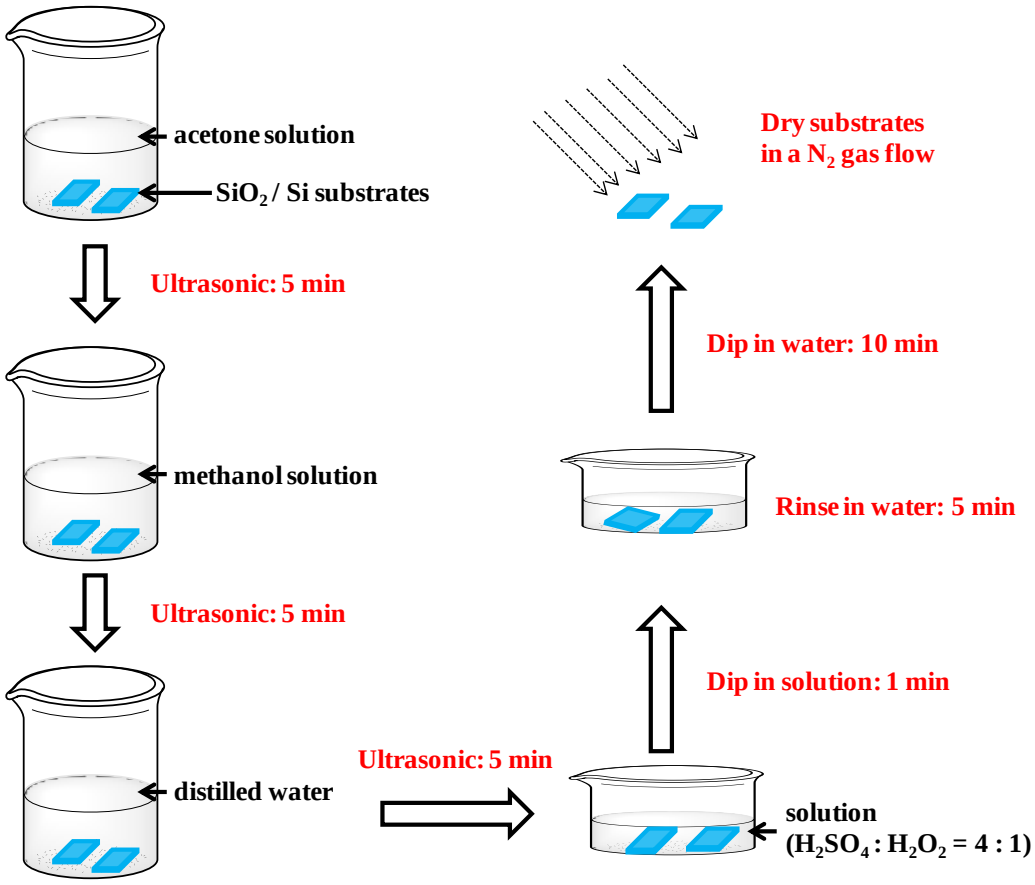

Figure 5-1. Schematics of a cleaning process for SiO_2 / Si substrates.

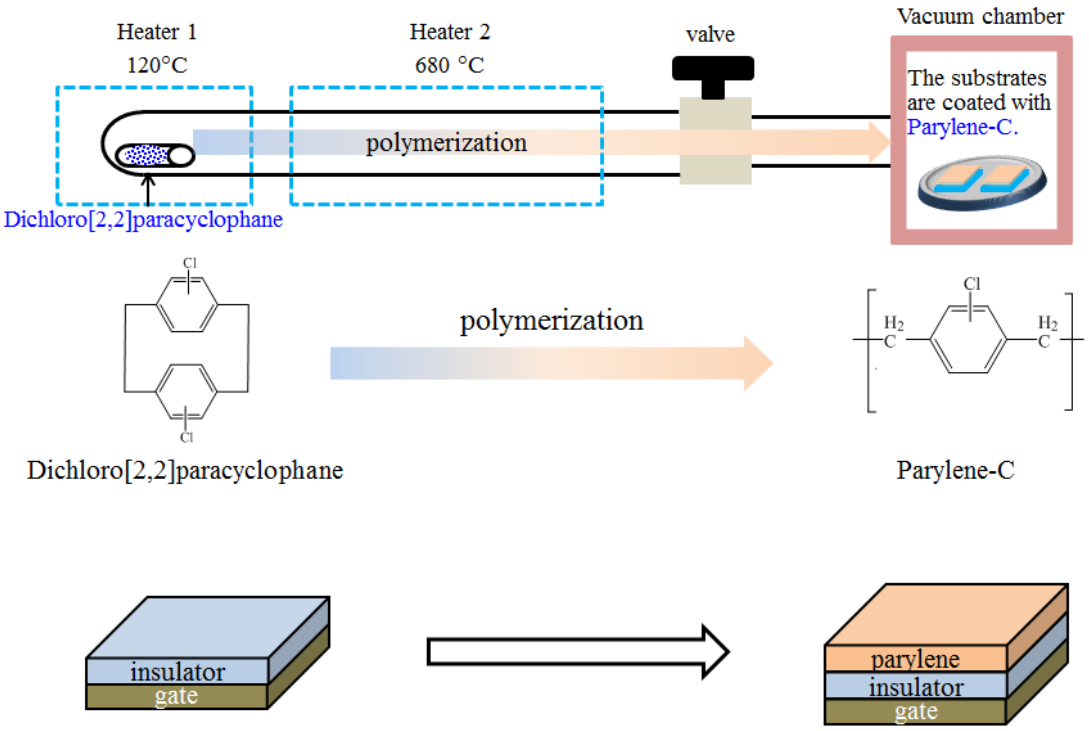

Figure 5-2. Schematics of a parylene coating process.

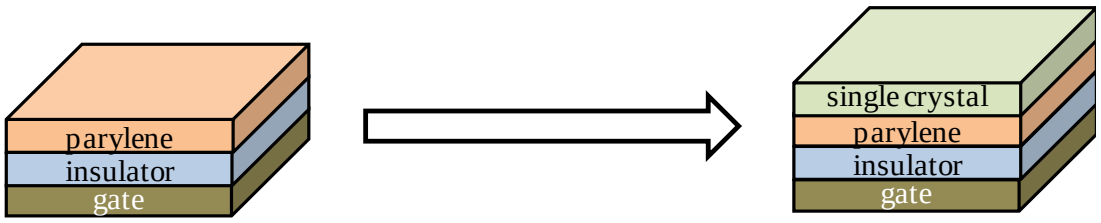

Figure 5-3. Schematics of a single crystal placed on the parylene-coated gate dielectric substrate.

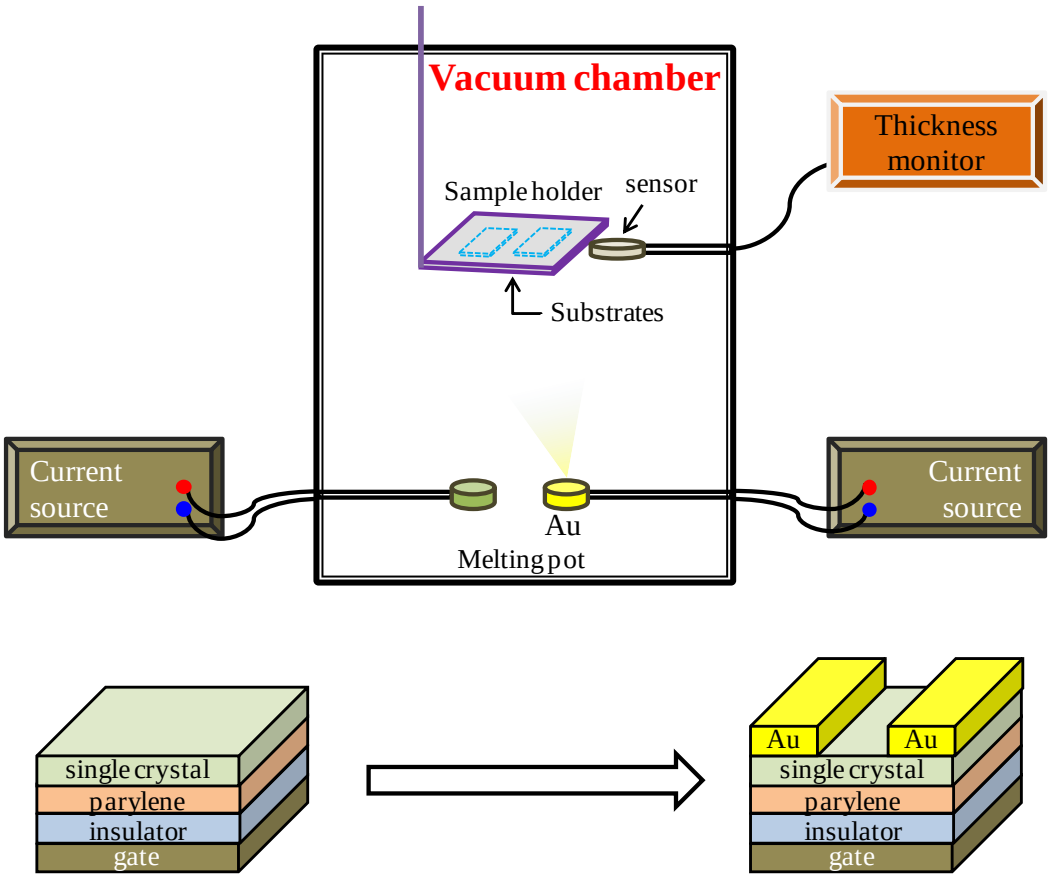

Figure 5-4. Schematics of a deposition chamber and an Au deposition process.

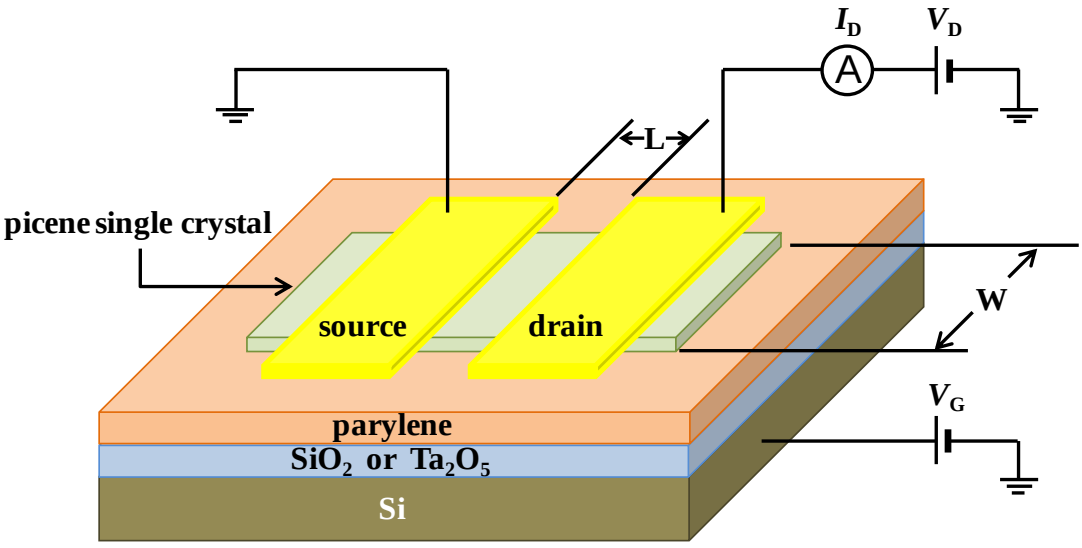

Figure 5-5. Device structure of a picene single crystal FET.

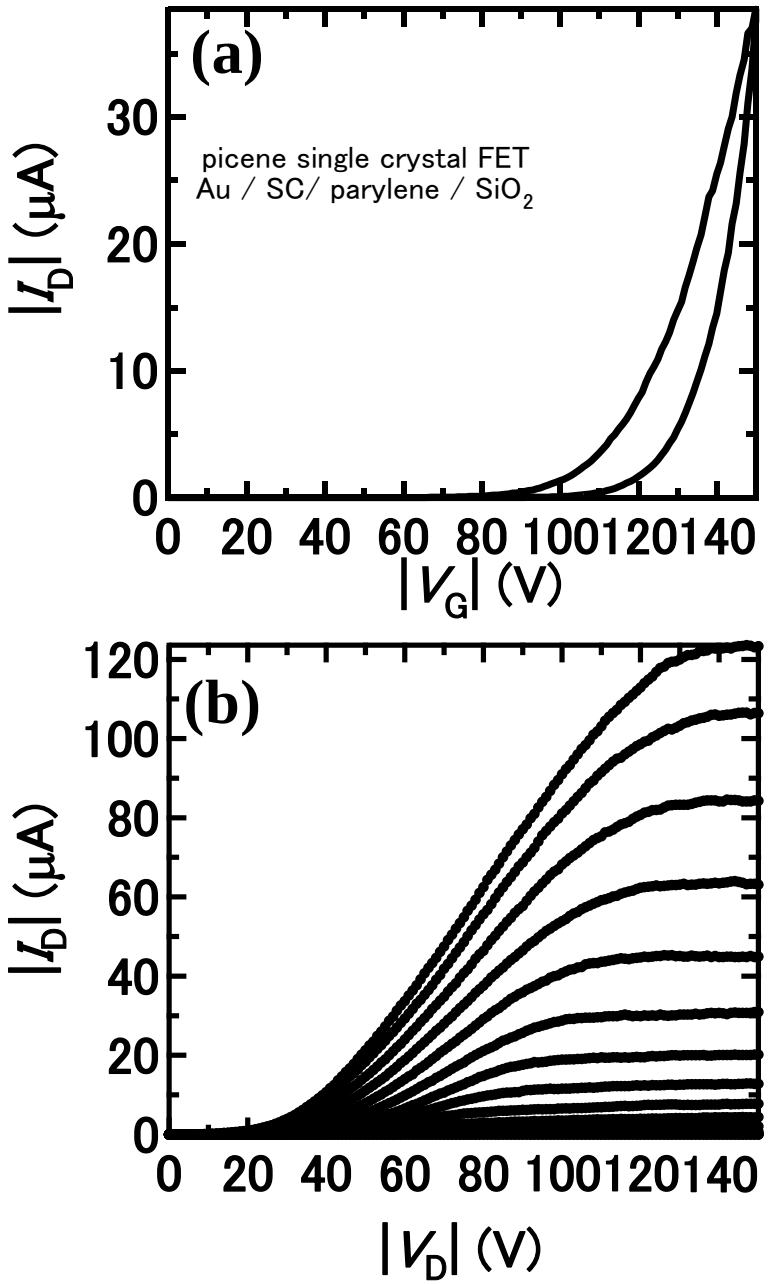

Figure 5-6. (a) Transfer and (b) output curves for picene single crystal FET with a SiO_2 gate dielectric.

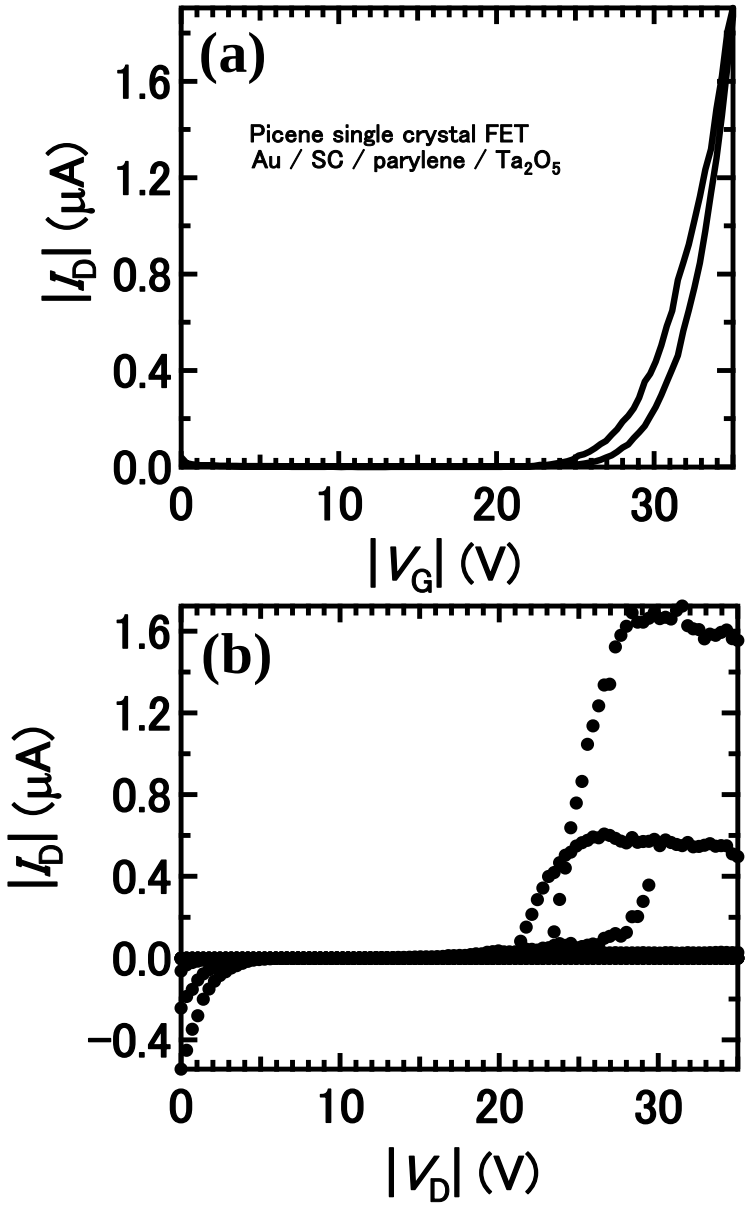

Figure 5-7. (a) Transfer and (b) output curves for picene single crystal FET with a Ta_2O_5 gate dielectric.

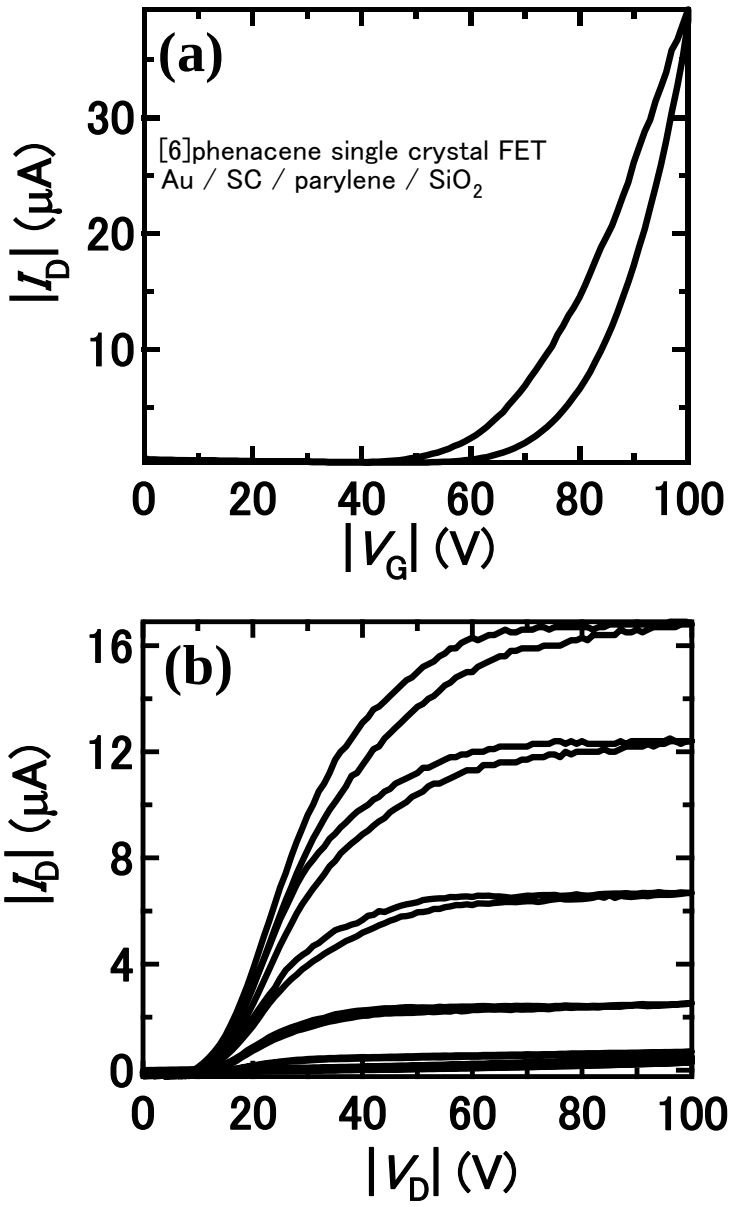

Figure 5-8. (a) Transfer and (b) output curves for [6]phenacene single crystal FET with a SiO_2 gate dielectric.

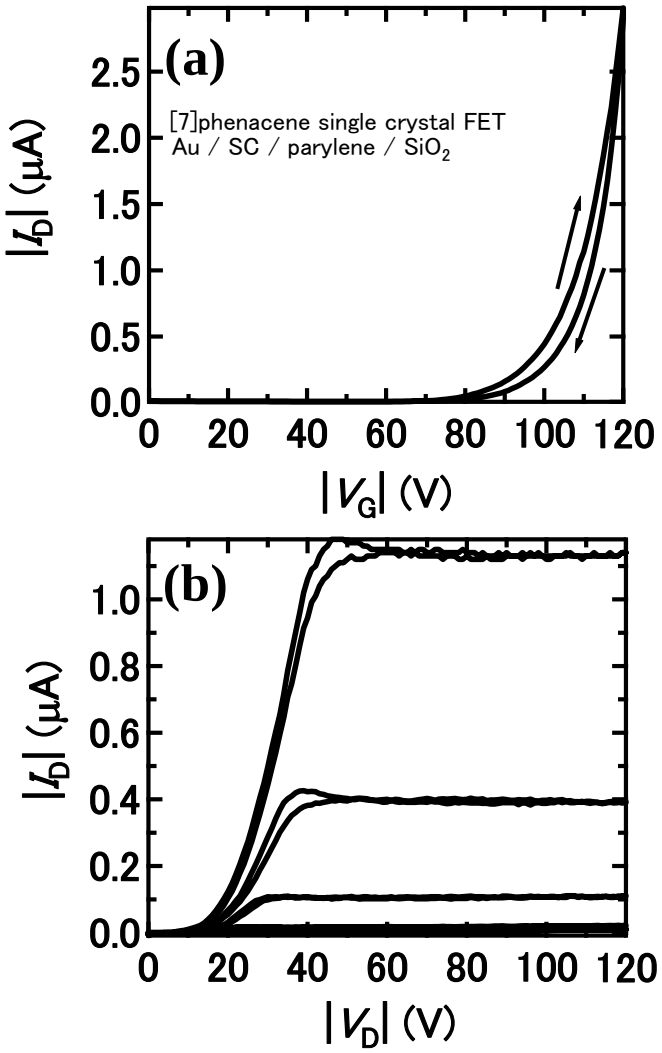

Figure 5-9. (a) Transfer and (b) output curves for [7]phenacene single crystal FET with a SiO_2 gate dielectric.

Chapter 6. Interface modification with electron acceptor and donor in phenacene single crystal FETs

In chapter 6, the author describes the FET characteristics of [7]phenacene single crystal FETs in which the strongest electron acceptor, F4TCNQ, or the strongest electron donor, 2,5-dihydroxy-p-benzoquinone (Q(OH)2), is inserted into the space between single crystal and source / drain electrodes. The strength of electron acceptor and donor is scaled by redox potential, E_{redox}; the E_{redox} values are 0.60 V for F4TCNQ and −0.38 eV for Q(OH)2; the redox potential values for the electron acceptors and donor used in this study are taken from Refs. 1 and 2 and they are shown in Table 6-1. Thus, the material with positive (negative) E_{redox} corresponds to electron acceptor (electron donor). Furthermore, the FET characteristics of [7]phenacene FET device exhibiting the highest μ value in this study, in which 2,5-diethyl-7,7,8,8-tetracyano-p-quinodimethane (Et2TCNQ) (E_{redox} = 0.15 V) is inserted, are also discussed in chapter 6. In addition, in this chapter the FET characteristics of picene and [6]phenacene single crystal FETs are also discussed; the former FET device is modified by F4TCNQ, while the latter device is modified by TCNQ.

In particular, how FET characteristics of these three phenacene single crystal FETs change between chapter 5 and chapter 6 is the most important research theme in this chapter. Namely, it is the most important to investigate the effect of interface modification on FET properties. The effect is quantitatively studied in chapter 7, while in chapter 6 the FET characteristics after interface modification are directly compared with those before interface modification.

6-1. FET characteristics of phenacene single crystal FETs in which electron acceptor or donor is inserted

6-1-1. Introduction

Blochwitz *et al*. investigated the properties of metal - organic interfaces by ultraviolet and X-ray photoemission spectroscopy (UPS and XPS) and transport

experiments [3]. They used electron acceptors, F4TCNQ and zinc-phthalocyanine (ZnPc), to modify the interface. The UPS showed that the Fermi surface shifted to HOMO level to cause upward band bending and the space charge layer reduced with doping of the electron acceptors, producing a reduction of potential barrier. Therefore, the insertion of electron acceptor into the space between single crystal and source / drain Au electrodes may be effective for a decrease in Schottky barrier height.

The μ value as high as 1.3 $cm^2 V^{-1} s^{-1}$ was recently recorded in the picene single crystal FET with HfO_2 gate dielectric [4]. Here, the interface between single crystals and source / drain electrodes was modified by TCNQ with E_{redox} = 0.22 V, which is a typical electron acceptor material. This led to a significant improvement of FET properties. In particular, a concave behaviour in output curves at a low $|V_D|$ range changed to linear, suggesting a lowering of hole-injection barrier height. This is consistent with the above results obtained by UPS and XPS [3]. In section 6-1, we have investigated FET properties of three phenacene single crystal FETs in which electron acceptor or donor is inserted into the space between single crystal and electrodes. The output curves at a low $|V_D|$ range have been compared with those without insertion materials described in chapter 5.

6-1-2. Experimental

The fabrication process of FET devices is described in chapter 5. The thickness of SiO_2 gate dielectric is 400 nm for picene single crystal FETs and 300 nm for [6]phenacene single crystal FETs. The thickness of SiO_2 gate dielectric in [7]phenacene single crystal FETs is 300 nm for TCNQ, Q(OH)2, and Et2TCNQ-modified electrodes, and 400 nm for F4TCNQ-modified electrodes. In the devices described in this chapter, 3 nm thick electron acceptor or donor was deposited on the single crystals, and the Au source / drain electrodes were formed subsequently without exposing the devices to air. We inserted F4TCNQ for picene single crystal FET, TCNQ for [6]phenacene single crystal FET, and F4TCNQ, Et2TCNQ and Q(OH)2 for [7]phenacene single crystal FETs. The device structure is shown in Figure 6-1. Furthermore, the molecular structures of TCNQ, F4TCNQ, Q(OH)2 and Et2TCNQ are shown in Figure 6-2.

6-1-3. Results and discussion

6-1-3-1. FET characteristics of picene single crystal FET (F4TCNQ insertion)

In order to improve the contact between single crystal and source / drain electrodes in picene single crystal FET, Kawai *et al*. inserted 1 nm thick TCNQ into the space between single crystal and source / drain electrodes [4]. The concave behaviour in the output curve was drastically improved in picene single crystal FET with Ta_2O_5 gate dielectric after TCNQ insertion. The μ and $|V_{TH}|$ for the picene single crystal FET were determined to be 3.4×10^{-2} cm^2 V^{-1} s^{-1} and 26 V, respectively, for no insertion, while the μ and $|V_{TH}|$ were determined to be 4.0×10^{-1} cm^2 V^{-1} s^{-1} and 27 V, respectively, for TCNQ insertion [4].

We newly inserted F4TCNQ into the space between single crystal and source / drain electrodes in picene single crystal FET with SiO_2 gate dielectric. The transfer and output curves are shown in Figure 6-3(a) and (b), respectively. The output curves of picene single crystal FET (Figure 6-3(b)) still shows the concave behaviour at low $|V_D|$ range. However, the concave behaviour is improved by using F4TCNQ in comparison with that (Figure 5-6) in picene single crystal FET without any insertion materials described in chapter 5. The μ, $|V_{TH}|$ and on-off ratio of picene single crystal FET with SiO_2 gate dielectric and F4TCNQ insertion are 7.3×10^{-1} cm^2 V^{-1} s^{-1}, 11 V and 4.4×10^8, respectively. The μ value is slightly higher than that of 4.7×10^{-1} cm^2 V^{-1} $s^{-1}$for picene single crystal FET without any insertion materials (Figure 5-6) described in chapter 5. Although the μ did not drastically increase, the $|V_{TH}|$ significantly decreased from 96 to 11 V by an insertion of F4TCNQ.

We further fabricated picene single crystal FET with Ta_2O_5 gate dielectric in which F4TCNQ was inserted between single crystal and electrodes. The results are shown in Figures 6-4(a) and (b). The output curves of picene single crystal FET (Figure 6-4(b)) shows the small concave behaviour at low $|V_D|$ range, suggestive of a decrease in hole-injection barrier height. The μ, $|V_{TH}|$ and on-off ratio were determined to be 6.8×10^{-1} cm^2 V^{-1} s^{-1}, 11 V and 9.8×10^6, respectively. The μ value is slightly higher than that

of 4.7×10^{-1} $cm^2 V^{-1} s^{-1}$ for picene single crystal FET without any insertion materials (Figure 5-6) described in chapter 5.

6-1-3-2. FET characteristics of [6]phenacene single crystal FET (TCNQ insertion)

The transfer and output curves of [6]phenacene single crystal FET with SiO_2 gate dielectric, in which TCNQ is inserted, are shown in Figure 6-5 (a) and (b). The transfer curves are recorded in saturation regime (V_D = −100 V). Clear p-channel FET characteristics are observed. Hysteresis between forward and reverse transfer curves still exists in spite of 30 nm thick parylene-coating of the SiO_2 surface. The μ was 5.6×10^{-1} $cm^2 V^{-1} s^{-1}$ for [6]phenacene single crystal FET with TCNQ, which is higher than that, 7.6×10^{-2} $cm^2 V^{-1} s^{-1}$, for [6]phenacene single crystal FET (no insertion, see Figure 5-8). The $|V_{TH}|$ and the on-off ratio were determined to be 36 V and 6.2×10^8 for [6]phenacene single crystal FET with electrodes modified with TCNQ, while $|V_{TH}|$ and the on-off ratio were 47 V and 3.9 x 10^7 for [6]phenacene single crystal FET (no insertion, see Figure 5-8) as described in chapter 5. Thus, insertion of 3nm thick TCNQ is effective to improve the FET properties. The concave behaviour in output curves at a low $|V_D|$ range is still observed in [6]phenacene single crystal FET with electrodes modified with TCNQ. However, the concavity is a little suppressed, *i.e.*, the hole-injection barrier is exactly lowed by the insertion of TCNQ.

6-1-3-3. FET characteristics of [7]phenacene single crystal FET (F4TCNQ and Q(OH)2 insertion)

We fabricated [7]phenacene single crystal FET with an SiO_2 gate dielectric, in which F4TCNQ was inserted between single crystal and source / drain electrodes. The transfer and output curves are shown in Figures 6-6(a) and (b), respectively. Clear p-channel FET characteristics can be observed in Figure 6-6. The concave behaviour in output curves at a low $|V_D|$ range is much smaller than that in [7]phenacene single crystal FET without any insertion (see Figure 5-9) described in chapter 5, suggestive of a lowering of

hole-injection barrier by insertion of F4TCNQ. Nevertheless, a slight concave behaviour in the low $|V_D|$ region is still observed in the [7]phenacene single crystal FET with F4TCNQ (Figure 6-6(b)). Therefore, the concave behaviour could not be completely removed, even by the insertion of F4TCNQ.

The μ, $|V_{TH}|$ and on-off ratio were 4.7 $cm^2 V^{-1} s^{-1}$, 18 V and 2.2×10^9, respectively, for the [7]phenacene single crystal FET with F4TCNQ (Figure 6-6(a)). Another [7]phenacene single crystal FET device with the same device structure (F4TCNQ and SiO_2) showed a μ as high as 6.7 $cm^2 V^{-1} s^{-1}$. If we compare FET parameters between F4TCNQ and other electron acceptor TCNQ, the μ value, 4.7 – 6.7 $cm^2 V^{-1} s^{-1}$, for F4TCNQ was twice as high as that, 2.3 $cm^2 V^{-1} s^{-1}$, for the [7]phenacene single crystal FET with TCNQ, whereas the $|V_{TH}|$ of 18 V was much smaller than that with TCNQ (54 V). The on-off ratio was 2.2×10^9, which was slightly higher than that with TCNQ (1.6×10^9). From the viewpoint of device performance, the insertion of F4TCNQ may be more effective than TCNQ.

We next fabricated [7]phenacene single crystal FET with an SiO_2 gate dielectric, in which electron donor, Q(OH)2, was inserted between single crystal and source / drain electrodes. The transfer and output curves are shown in Figures 6-7(a) and (b), respectively. Clear p-channel FET characteristics are observed in Figure 6-7. The μ, $|V_{TH}|$ and on-off ratio were determined to be 1.2 $cm^2 V^{-1} s^{-1}$, 79 V and 4.9×10^8, respectively for the [7]phenacene single crystal FET with Q(OH)2 insertion (Figure 6-7(a)). The μ value (= 1.2 $cm^2 V^{-1} s^{-1}$) is much higher than that, 2.6×10^{-2} $cm^2 V^{-1} s^{-1}$, for the [7]phenacene single crystal FET without any insertion materials (see Figure 5-9), while the $|V_{TH}|$ of 79 V was smaller than that of 91 V in FET without insertion, indicating an effectiveness of electron donor materials for an improvement of FET performance. Furthermore, the concave behaviour in output curves at low $|V_D|$ range is much smaller than that in [7]phenacene single crystal FET without any insertion (see Figure 5-9) described in chapter 5, suggestive of a lowering of hole-injection barrier by insertion of electron donor. In chapter 7, a systematic study on the effect of electron acceptors and donors on FET properties including hole-injection barrier height is provided

6-2. FET characteristics of [7]phenacene single crystal FETs in which Et2TCNQ is inserted: the observation of excellent FET characteristics

The transfer and output curves of the [7]phenacene FET, in which Et2TCNQ is inserted into the interface between single crystal and source / drain electrodes, are shown in Figure 6-8(a) and (b), respectively. Clear p-channel FET properties that the switch-on drain current is observed by applying negative V_G are observed in these curves. The values of μ, $|V_{TH}|$, on-off ratio and S were determined to 6.9 $cm^2 V^{-1} s^{-1}$, 50 V, 1.0×10^9 and 9.3×10^{-1} V $decade^{-1}$, resepctively. The μ (= 6.9 $cm^2 V^{-1} s^{-1}$) is the highest in the [7]phenacene single crystal FETs reported so far. The μ is higher than the highest μ value, 6.7 $cm^2 V^{-1} s^{-1}$, in the [7]phenacene single crystal FET in which F4TCNQ was inserted into the interface between single crystal and source / drain electrodes, described in section 6-1-3-3.

The $|V_{TH}|$ (= 50 V) is higher than that, ~ 18 V, for [7]phenacene single crystal FET with F4TCNQ. Thus, the insertion of Et2TCNQ to interface between single crystal and electrodes results in the high μ value. The value of E_{redox} for Et2TCNQ is 0.15 V, which is smaller than that, 0.60 V, for F4TCNQ, suggesting that Et2TCNQ is a week electron acceptor. The correlation between μ and E_{redox} is also discussed in chapter 7.

6-3. Conclusion

Interface control with electron donor and acceptors for picene, [6]phenacene and [7]phenacene single crystal FETs provided a significant improvement in FET performance. First the concave behaviour in output curves at low $|V_D|$ range was improved. Second the FET parameters (μ, $|V_{TH}|$ and on-off ratio) were improved. In particular, the insertion of Et2TCNQ led to a very high μ value as high as 6.9 $cm^2 V^{-1} s^{-1}$ in [7]phenacene single crystal FET with SiO_2 gate dielectric. The reason why μ value increases and hole-injection barrier height (concave behaviour in output curves) decreases by an insertion of electron acceptor and donor is fully discussed in chapter 7.

References

[1] G. Saito, H. Sasaki, T. Aoki, Y. Yoshida, A. Otsuka, H. Yamochi, O. O. Drozdova, K. Yakushi, H. Kitagawa, and T. Mitani, J. Mater. Chem. **12**, 1640 (2002).

[2] Unpublished data from Dr. Yukihiro Yoshida and Prof. Gunzi Saito of Meijo University.

[3] J. Blochwitz, T. Fritz, M. Pfeiffer, K. Leo, D. M. Alloway, P. A. Lee, and N. R. Armstrong, Org. Electron. **2**, 97 (2001).

[4] N. Kawai, R. Eguchi, H. Goto, K. Akaike, Y. Kaji, T. Kambe, A. Fujiwara, and Y. Kubozono, J. Phys. Chem. C **116**, 7983 (2012).

Table 6-1. Redox potentals of electron donors and accepters used in this chapter.

material	redox potential (V)
Q(OH)2	-0.38
Et2TCNQ	0.15
TCNQ	0.22
F4TCNQ	0.60

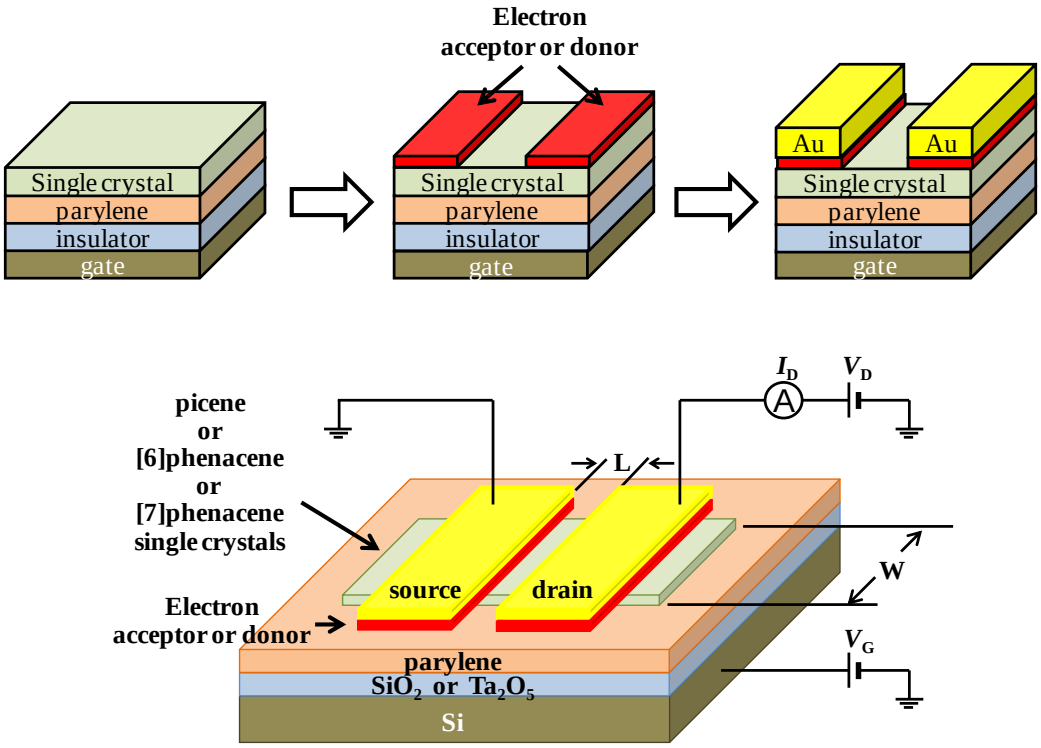

Figure 6-1. Device structure of single crytal FETs with electron acceptor or donor inserted into the space between single crystal and source/drain electrodes.

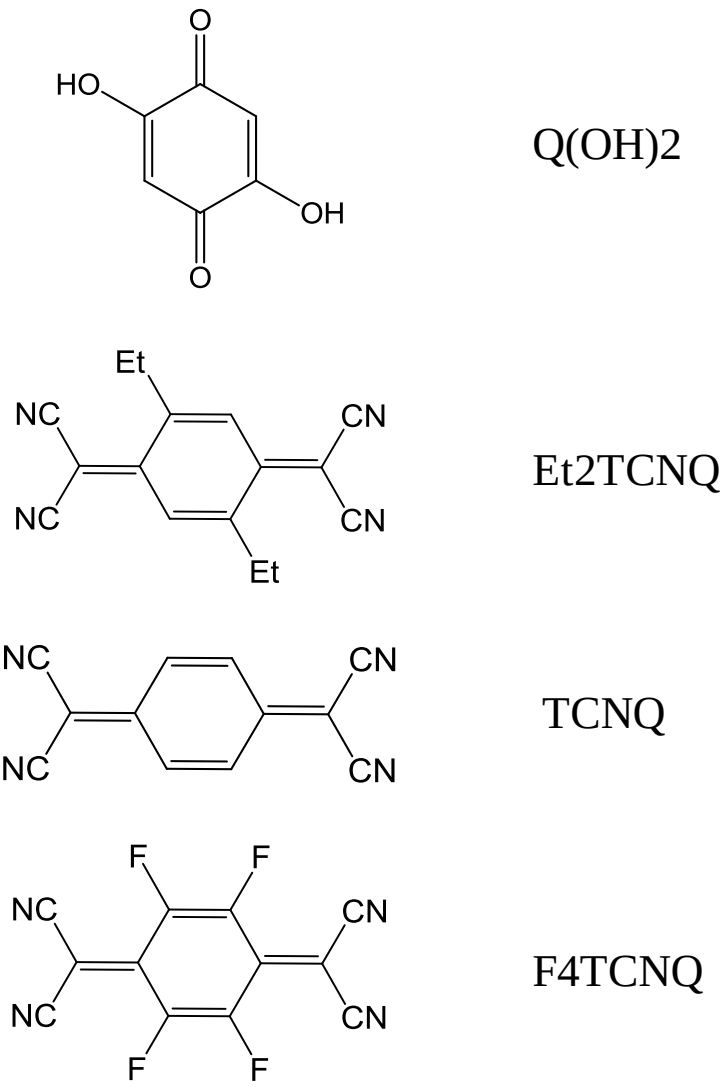

Figure 6-2. Moleculer structures of Q(OH)2, Et2TCNQ, TCNQ and F4TCNQ.

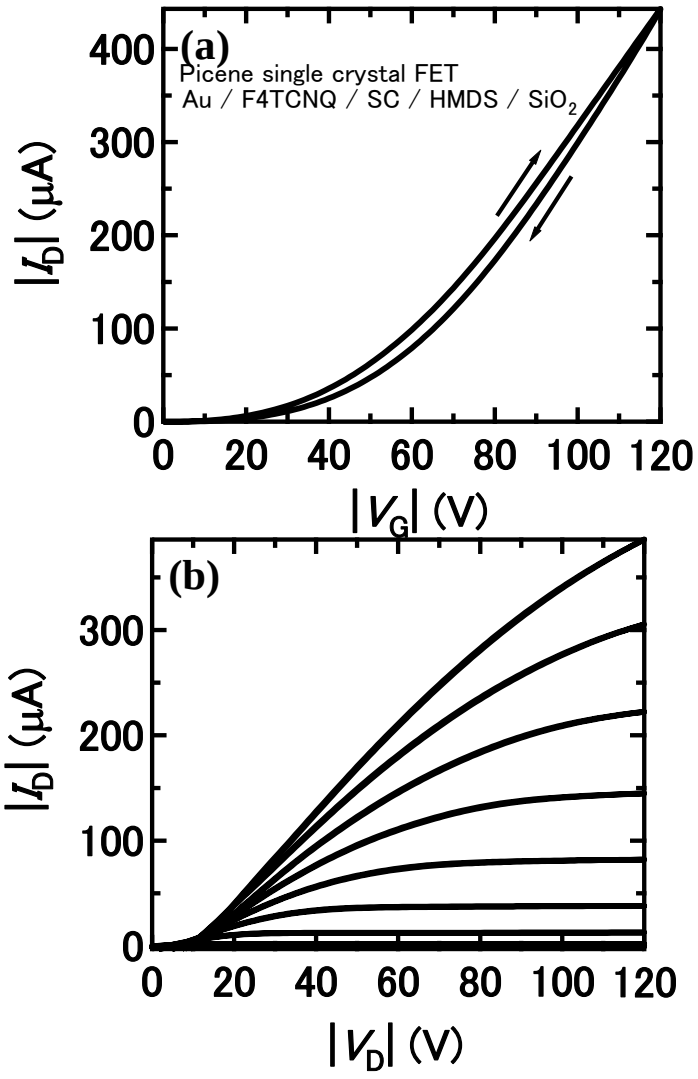

Figure 6-3. (a) Transfer and (b) output curves of picene single crystal FET with SiO_2 gate dielectric, in which F4TCNQ is inserted into the space between single crystal and electrods.

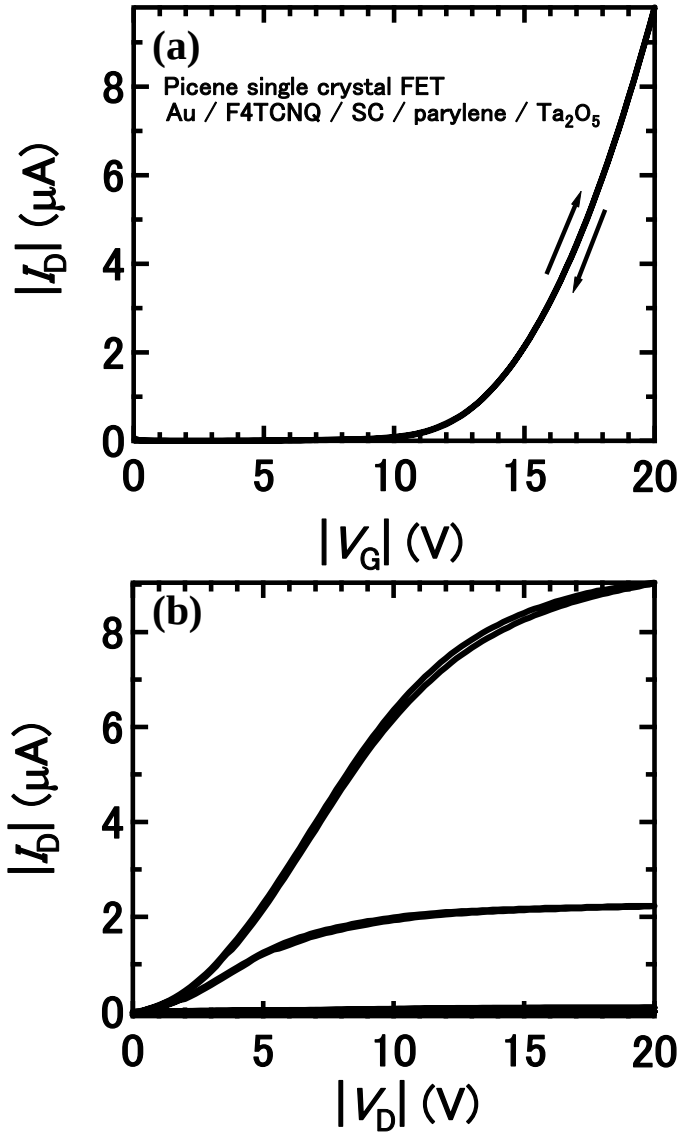

Figure 6-4. (a) Transfer and (b) output curves of picene single crystal FET with Ta_2O_5 gate dielectric, in which F4TCNQ is inserted into the space between single crystal and electrods.

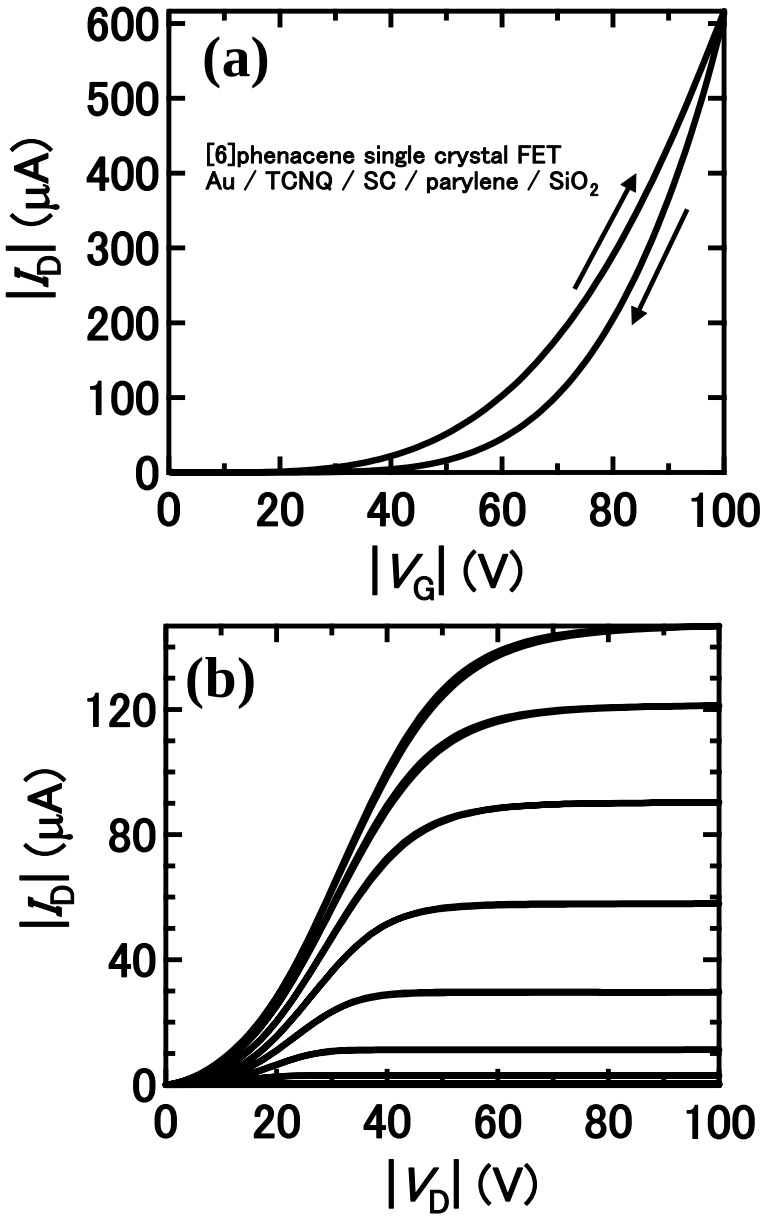

Figure 6-5. (a) Transfer and (b) output curves of [6]phenacene single crystal FET with SiO_2 gate dielectric, in which TCNQ is inserted into the space between single crystal and electrods.

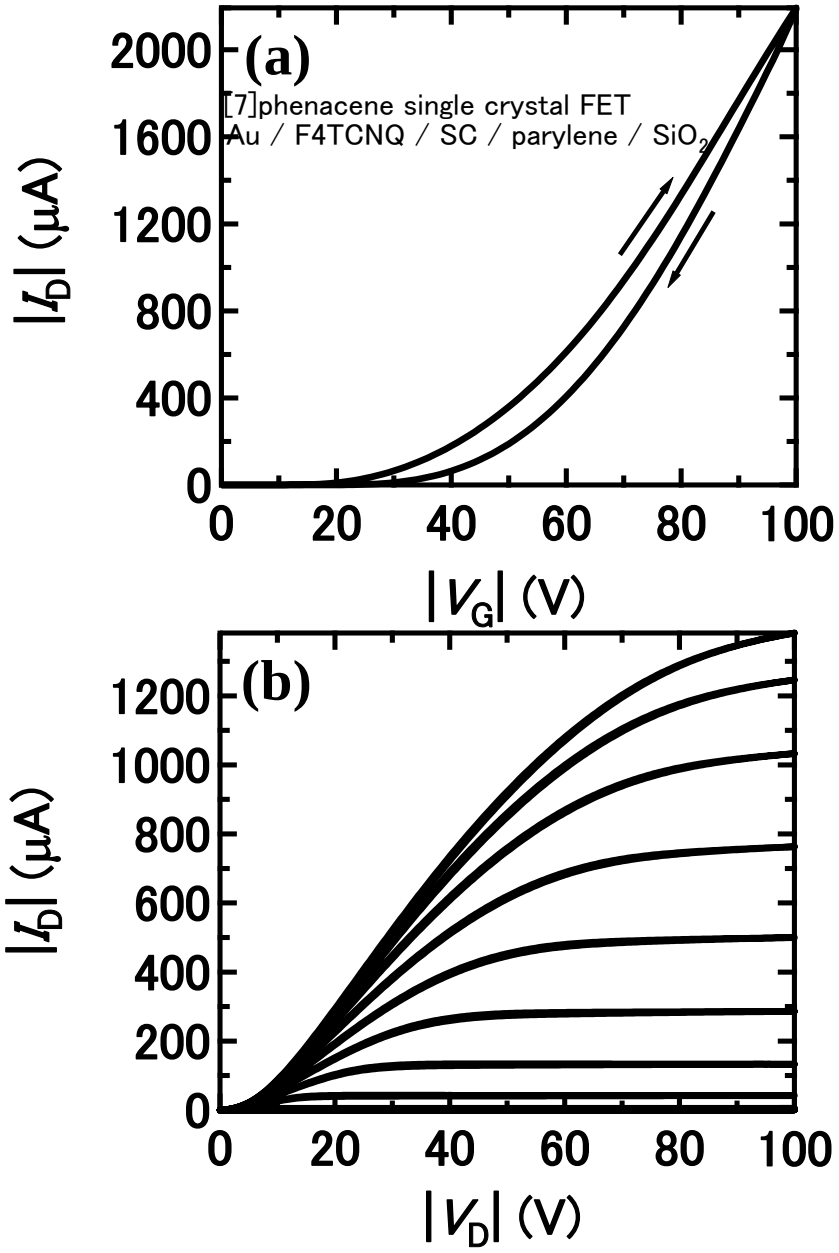

Figure 6-6. (a) Transfer and (b) output curves of [7]phenacene single crystal FET with SiO_2 gate dielectric, in which F4TCNQ is inserted into the space between single crystal and electrods.

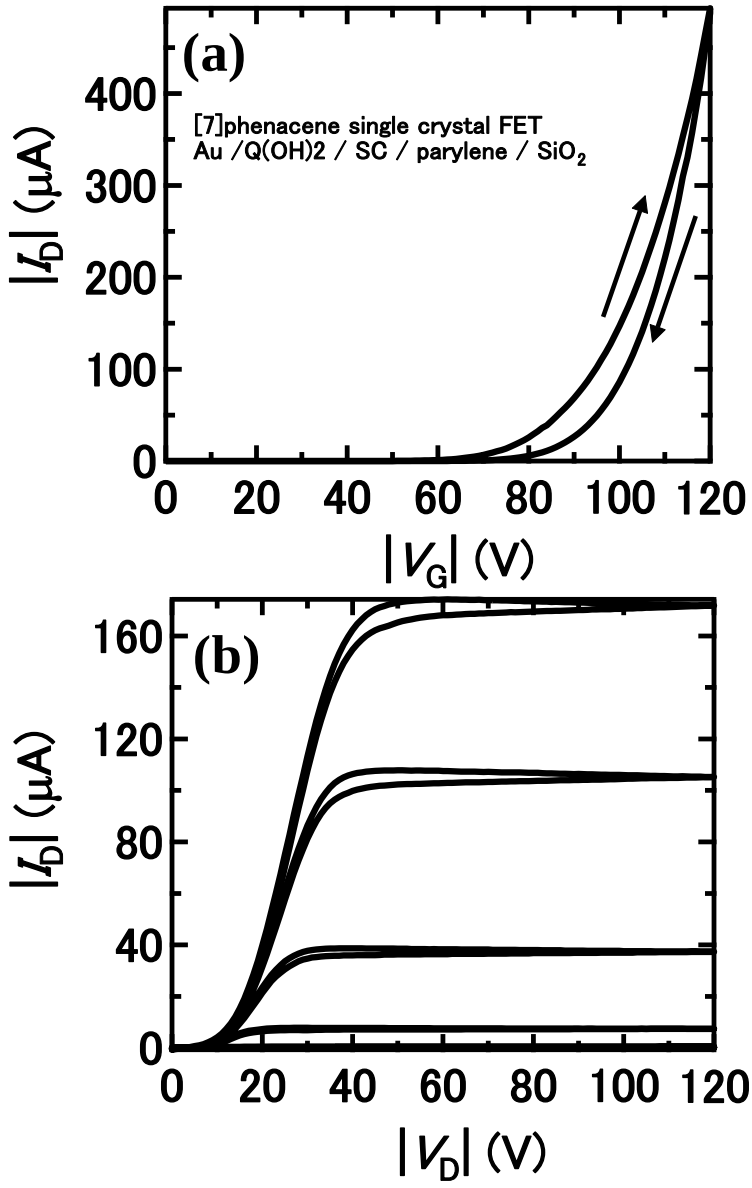

Figure 6-7. (a) Transfer and (b) output curves of [7]phenacene single crystal FET with SiO_2 gate dielectric, in which Q(OH)2 is inserted into the space between single crystal and electrods.

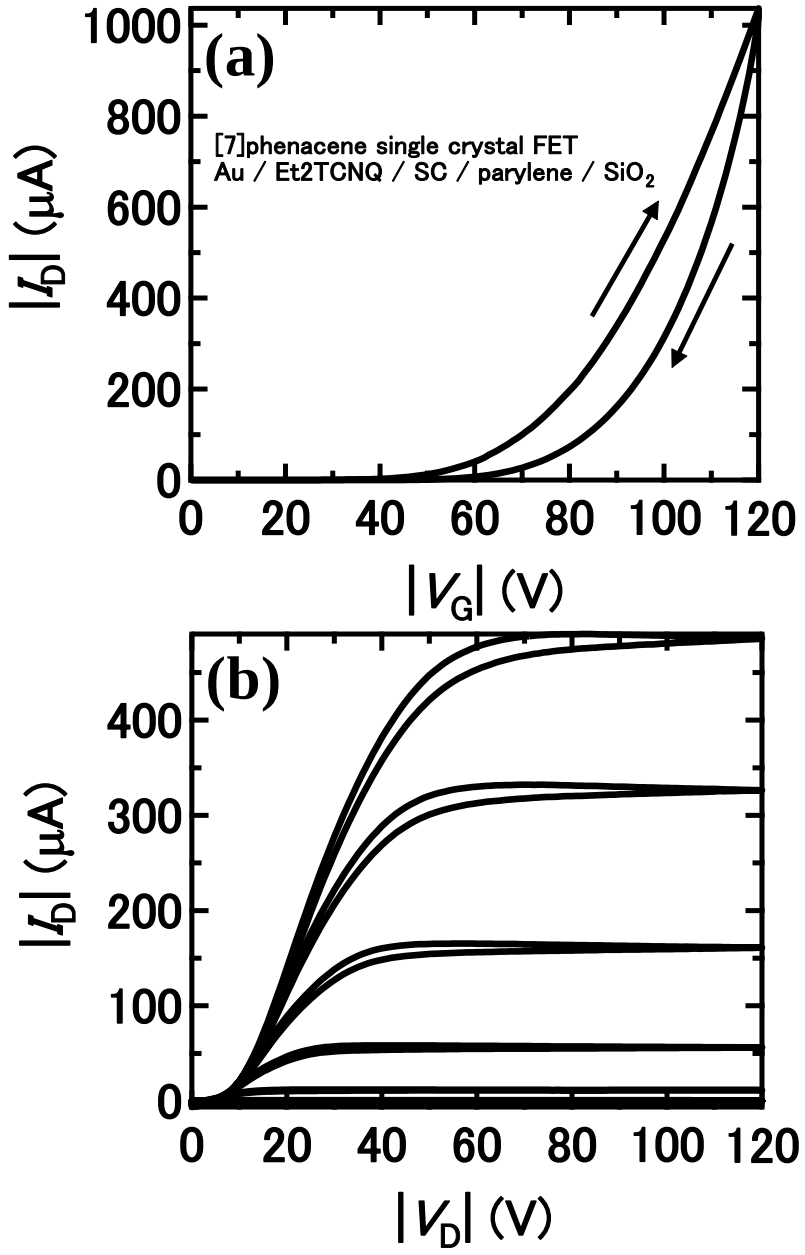

Figure 6-8. (a) Transfer and (b) output curves of [7]phenacene single crystal FET with SiO_2 gate dielectric, in which Et2TCNQ is inserted into the space between single crystal and electrods.

Chapter 7. Systematic control of hole-injection barrier height with electron donors and acceptors in [7]phenacene single crystal EFTs

In this chapter, the author describes a systematic study on contacts between single crystal and source / drain electrodes in single crystal FET. For this study, we selected [7]phenacene single crystal because the FET showed the excellent FET properties as described in chapters 5 and 6. In chapter 6, the FET characteristics in [7]phenacene single crystal FET in which the representative electron acceptor or donor is inserted into the space between single crystal and source / drain electrodes are discussed, and a decrease in concave behaviour in output curves is confirmed. In this chapter, the author has evaluated the effective hole-injection barrier-heights, ϕ_h^{eff}s, formed between single crystal and source / drain electrodes in [7]phenacene single crystal FETs in which various electron acceptors and donors (insertion materials) are inserted. The ϕ_h^{eff} obtained was correlated with redox potential, E_{redox}. In this chapter, the E_{redox} of insertion material is a key parameter to discuss not only the ϕ_h^{eff} but also FET parameters such as μ, $|V_{TH}|$, S and on-off ratio.

7-1. Introduction

During the past decade, the organic FETs have been extensively investigated since high-performance FET characteristics can be obtained owing to few extrinsic factors in the active layer, and the intrinsic nature of organic materials can be investigated [1-8]. The phenacene single crystal FET was first fabricated with picene by our group [9], which provides the μ as high as 1.3 $cm^2 V^{-1} s^{-1}$. In this device, electron acceptor, TCNQ, was inserted into the space between single crystal and source / drain electrodes. The insertion of TCNQ led to a significant improvement of FET properties. In particular, a concave behaviour observed in output curves at a low $|V_D|$ range decreased drastically, suggesting a lowering of hole-injection barrier height.

In chapters 5 and 6, the decrease in concave behaviour by an insertion of strong electron acceptor, F4TCNQ, is confirmed in [7]phenacene single crystal FET. As described in ch. 6, the μ as high as 6.9 $cm^2 V^{-1} s^{-1}$ is obtained in [7]phenacene single crystal FET in which Et2TCNQ is inserted into the space between single crystal and source / drain electrodes. Thus an interface control with electron acceptor is found to be effective to reduce the ϕ_h, or contact resistance. Therefore, it is of interest to evaluate quantitatively the ϕ_h in organic single crystal FETs with not only electron acceptors but also electron donors. This should lead to a deep understanding on the control of the hole-injection barrier. We have to establish a technique of interface control because this technique can improve not only contact between single crystals and source / drain electrodes but also FET properties such as μ, V_{TH}, S and on-off ratio. In this chapter, FET properties of [7]phenacene single crystal FETs with 14 insertion materials (electron acceptors and donors) are investigated systematically / quantitatively. The hole-injection barrier height and FET parameters have been obtained and correlated with the E_{redox} of insertion materials.

7-2. Experimental

The [7]phenacene single crystal FETs with SiO_2 (300 nm) gate dielectric were fabricated according to the procedure described in chapter 5; 400 nm thick SiO_2 gate dielectric was used only for the FETs corresponding to Figures 7-6 and 7-7 (c). 3 nm thick electron acceptor (or donor) was inserted into the space between single crystal and source / drain electrodes. The device structure is the same as that shown in Figure 6-1 in chapter 6. The L and W of the channel in the single crystal FET devices fabricated in this study were 30 μm and 200 - 2000 μm, respectively. The molecular structures of insertion materials are shown in Figure 7-1. The exact name of insertion materials and their abbreviation are shown in Table 7-1. The densities of insertion materials, which are required for evaluation of thickness of thin films (electron acceptor / donor films) formed by thermal deposition, are listed in Table 7-2. Most of the electron-acceptor and the electron-donor materials were synthesized according to the procedures reported

elsewhere [10]. Only four materials (TCNQ, FTCNQ, F2TCNQ and F4TCNQ) were purchased from either Sigma-Aldrich Co. LLC or Tokyo Chemical Industry Co., Ltd.

The hole-injection barrier height can be evaluated from output curves of FETs with thermionic emission model for double Schottky barriers [11], as we discussed in chapter 4. However, two Schottky barriers are formed in the FET device, as seen from its device structure, *i.e.*, source electrode - single crystal and drain electrode - single crystal. Therefore, the formula (Eq. 4-11) developed in chapter 4 has to be expanded to double Schottky model. The FET parameters are determined with a conventional MOS FET formula [11]. The E_{redox} values of electron acceptors and donors used in this study are listed in Table 7-3. Here a positive E_{redox} refers to the nature of electron acceptor (EA), while a negative E_{redox} refers to the nature of electron donor (ED). The 'EA' and 'ED' shown in Figure 7-1 refer to electron acceptors and donors, respectively. As a reference, the [7]phenacene single crystal FET without interface control (no insertion) is also fabricated and characterised; the transfer and output curves are shown in Figure 5-9 in chapter 5.

7-3. Results and Discussion

7-3-1. Evaluation of $<\phi_{\mathrm{h}}^{\mathrm{eff}}>$ in [7]phenacene single crystal FETs with / without insertion materials

The output curves at $|V_{\mathrm{D}}|$ = 0 - 20 V and $|V_{\mathrm{G}}|$ = 120 V are shown in Figure 7-2. The $|I_{\mathrm{D}}|$s of each output curves are normalized at $|V_{\mathrm{D}}|$ = 20 V, so that the $|I_{\mathrm{D}}|$ at $|V_{\mathrm{D}}|$ = 20 V is consistent. In this graph, only output curves for five FET devices with four insertion materials (Q(OH)2, Et2TCNQ, FTCNQ and F4TCNQ) and without insertion materials (no insertion) are plotted for a convenience of finding the difference. The difference in concavity can be clearly recognised in these output curves. The highest concavity implying the largest hole-injection barrier is observed in FET without insertion materials, and the concavity decreases with an increase in E_{redox} from negative to positive in the four FET devices modified with insertion materials, suggesting that the insertion of electron acceptors with positive E_{redox} is effective for lowering the concavity.

The hole-injection barrier, which produces the contact resistance between single crystal and source / drain electrodes, corresponds approximately to the Schottky barrier which is formed by the energy difference between HOMO and Fermi level, ε_F, of Au electrodes. As the [7]phenacene single crystal FET operates in p-channel (or operation by holes), the energy level of HOMO, ε_{HOMO}, is associated with hole conduction. The energy levels, ε_{HOMO} (−5.7 eV) of [7]phenacene and ε_F (−5.1 eV) of Au [12], are systematically drawn in Figure 7-3(a). The fact that the ε_F is higher by 0.6 eV than ε_{HOMO} can produce the Schottky barrier. The energy difference (= 0.6 eV) substantially corresponds to the Schottky barrier height, *i.e.*, the potential barrier height from Au to [7]phenacene; this barrier height is defined as ϕ_h. When the [7]phenacene comes into contact with Au electrodes, the alignment of Fermi levels between Au and [7]phenacene must take place to form band curvature shown in Figure 7-3(b). The curvature is strictly maintained owing to the formation of the depletion region through the movement of hole to Au due to the alignment of Fermi level. Here the Fermi level of [7]phenacene is assumed to be located between ε_F of Au and HOMO, *i.e.*, ε_F is near HOMO, although the Fermi level of [7]phenacne is unclear. This assumption seems to be reasonable because [7]phenacene is a p-type semiconductor. Actual FET device has two Schottky barriers as shown in Figure 7-3(b). When the negative V_D is applied to drain electrode, the new band bending shown in Figure 7-3(c) should take place, showing that the hole-injection barrier is produced only at source electrode. Namely, the ϕ_h at drain electrode does not act as an effective barrier for hole, but only ϕ_h at source electrode is significant.

Not only such an electronic band bending but also a tunnelling barrier between single crystal and electrodes may contribute to the formation of an actual potential barrier. The tunnelling barrier is probably due to the insulating region produced owing to the difficulty in formation of ideal contact between organic single crystal and gold electrodes. Namely, the ϕ_h^{eff} value can be expressed as [11],

$$\phi_h^{eff} = \phi_h + k_B T\beta l \qquad (7\text{-}1)$$

where T, k_B, β and l refer to temperature, Boltzmann constant, tunnelling efficiency and length of tunnelling barrier, respectively. Namely, the first and second terms are

contributions from the electronic band bending (Schottky barrier) and the tunnelling barrier, respectively.

We determined the ϕ_h^{eff} values by a least-square fitting to the output curves at $|V_G|$ = 120 V with the formula based on the thermionic emission model for double Shottky barriers [11]. The formula is expressed as

$$|I_D| = W\ t\ A^*\ T^2\ \exp\left(\frac{-\phi_h^{eff}}{k_B T}\right)\left[\frac{\frac{\sinh(eV)}{2k_B T}}{\frac{\cosh(eV)}{2nk_B T}}\right] \qquad (7\text{-}2)$$

where W, t, A^*, e and n are the channel width, the thickness of the carrier accumulated region, the Richardson constant, elementary charge and ideality factor, respectively; T = 300 K. This equation is expanded from Eq. (4-11) for single Schottky barrier. The t was fixed to the lattice constant c (= 1.78 nm) of [7]phenacene (see Table 2-2), *i.e.*, the thickness of herringbone layer (*ab*-layer). The A^* ($\equiv 4\pi e m_h^* k_B^2/h^3$) was also fixed to 1.2 × 10^2 A cm^{-2} K^{-2}, where the effective mass, m_h^*, is assumed to be equal to the rest mass, m_0. Since the $1.55m_0$ is previously used for pentacene [13], the above assumption is probably reasonable, in chapter 3, we showed the exact m_h of picene as $2.24m_0$, which is near $1.0m_0$. From the fitting, the ϕ_h and n values can be definitely determined for each FET device. As typical examples of fitting, the experimental and fitting curves for F4TCNQ and Q(OH)2 are shown in Figures 7-4(a) and (b). The ϕ_h^{eff} values are evaluated from at least two FET devices for each insertion material, and the average value, $<\phi_h^{eff}>$, is used in a discussion described in section 7-3-2.

7-3-2. Variation of $<\phi_h^{eff}>$ for insertion materials with different redox potentials

Figure 7-5 shows the $<\phi_h^{eff}>$ plot as a function of E_{redox} of each insertion material. The highest $<\phi_h^{eff}>$ (= 0.40(4) eV) is obtained for the [7]phenacene single crystal FET without any insertion materials, *i.e.*, an insertion of either electron acceptors or donors is at least effective to reduce the $<\phi_h^{eff}>$. The $<\phi_h^{eff}>$ in the FET without any insertion materials (no insertion) cannot be scaled by the E_{redox}. On the other hand, the strongest electron acceptor, F4TCNQ, can provide the smallest $<\phi_h^{eff}>$ in the insertion materials

used in this study. The $<\phi_h^{eff}>$ decreases substantially with an increase in E_{redox}, *i.e.*, the $<\phi_h^{eff}>$ in the FETs with insertion materials can be scaled by E_{redox}. However, the slope of the $<\phi_h^{eff}>$ - E_{redox} plot is steeper in negative E_{redox} range, *i.e.*, in electron donors.

These results may present the following scenarios for the effect of insertion materials on $<\phi_h^{eff}>$. (1) The $<\phi_h^{eff}>$ may be associated with two barriers, Schottky barrier and tunnelling barrier, as suggested in section 7-3-1. (2) Both of electron acceptors and donors can reduce the tunnelling barrier through an improvement of contact between single crystal and electrodes; the contribution to the $<\phi_h^{eff}>$ from the tunnelling barrier may be independent of the E_{redox}. (3) The $<\phi_h^{eff}>$ decreases exactly with an increase in E_{redox}, and the E_{redox} dependence of $<\phi_h^{eff}>$ may be the same between electron acceptors and donors. These scenarios are verified in section 7-3-3.

The mechanism of a lowering of Schottky barrier height can be well explained based on the band bending shown in Figure 7-3(c). As seen from Figure 7-3(c), the electron acceptor produces the charge separation of negative and positive charges to reduce the potential barrier near drain electrode. The dipole moment formed between electron acceptor and [7]phenacene single crystal can maintain the new band bending which lowers potential barrier height. However, the interface between electron acceptor and Au drain electrode cannot produce the depletion layer because of an enrichment of electrons both in electron acceptor and Au, stimulating a destruction of the Schottky barrier. These effects cooperate to reduce the Schottky barrier. On the other hand, the electron donor may provide the opposite band bending (not shown), where the higher potential barrier height must be formed owing to band bending caused by electron donor. To establish the mechanism presented above, we have to determine the pure Schottky barrier heights, ϕ_hs, in the [7]phenacene single crystal FETs with / without insertion materials. In particular, for investigating the effect of insertion material they must be absolutely determined.

7-3-3. Temperature dependence of $<\phi_h^{eff}>$ and the distinction of Schottky barrier and tunnelling barrier

To distinguish the contributions to potential barrier height from Schottky barrier and tunnelling barrier, we plotted temperature dependence of $<\phi_h^{eff}>$ for [7]phencene single crystal FET without any insertion materials. The ϕ_h should be definitely determined by an extrapolation of the $<\phi_h^{eff}>$ - T plot to 0 K since the ϕ_h^{eff} is expressed with Eq. 7-1. Furthermore, the tunnelling barrier can be quantitatively evaluated from the slope of $<\phi_h^{eff}>$ - T plot, because the slope corresponds to tunnelling barrier term, $k_B\beta l$. The $<\phi_h^{eff}>$ - T plot of [7]phenacene single crystal FETs without any insertion materials (no insertion) is shown in Figure 7-6. However, the $<\phi_h^{eff}>$ - T plot does not show a linear relationship but almost constant. This is inconsistent with the prediction that the clear linear relationship is obtained. The result shown in Figure 7-6 suggests that the tunnelling barrier is not formed between single crystals and electrodes. When the tunnelling barrier is not formed, the large $<\phi_h^{eff}>$ recorded in [7]phenacene single crystal FET without insertion materials may be contributed only from the Schottky barrier. If it is the case, it must be concluded that the $<\phi_h^{eff}>$ in the FET without insertion material is not scaled by E_{redox}, which is different from the behaviour of $<\phi_h^{eff}>$ in other FETs with insertion materials. At the present stage, we cannot answer reason why all the $<\phi_h^{eff}>$ cannot be scaled in [7]phenacene single crystal FET. Consequently, we have to recognise the $<\phi_h^{eff}>$ without insertion materials as the specials case, which is different from the $<\phi_h^{eff}>$ with insertion materials.

7-3-4. V_G dependence of $<\phi_h^{eff}>$ and influence of accumulated holes in channel range

Here we investigated the V_G dependence of $<\phi_h^{eff}>$ in order to clarify the effect of accumulated holes in channel region on potential barrier. Simply considering the Schottky barrier height formed in source electrodes, an enrichment of carriers by applying V_G may destroy the Schottky barrier which is formed through the contact of the semiconductor and the metal. The carriers enriched in the semiconductor may result in the Ohmic-like contact with metal, because of the decrease in the depletion region (area of low concentration of carriers). This implies that the $<\phi_h^{eff}>$ decreases gradually with an

increase in $|V_G|$. The $<\phi_h^{eff}>$ - $|V_G|$ plots for [7]phenacene single crystal FETs with Q(OH)2 and F4TCNQ, and without any insertion materials are shown in Figure 7-7. The $<\phi_h^{eff}>$ only for the F4TCNQ inserted FET linearly decreases with an application of negative V_G. The accumulation of holes in the [7]phenacene single crystal FET changes the $<\phi_h^{eff}>$ from 0.40(9) eV at $V_G = -15$ V to 0.41(5) eV at $V_G = -120$ V for no insertion materials, the $<\phi_h^{eff}>$ from 0.16(2) eV at $V_G = -15$ V to 0.12(1) eV at $V_G = -120$ V for F4TCNQ, and the $<\phi_h^{eff}>$ from 0.36(2) eV at $V_G = -30$ V to 0.32(6) eV at $V_G = -120$ V for Q(OH)2. Because of difficulty in fitting for the output curve at $V_G = -15$ V in [7]phenacene single crystal FET with Q(OH)2, the $<\phi_h^{eff}>$ at $V_G \geq -30$ V is shown in Figure 7-7(a). The slope, $d<\phi_h^{eff}> / d|V_G|$, estimated from $<\phi_h^{eff}>$ - $|V_G|$ plots shown in Figures 7-7(a), (b) and (c) are determined to be -4.1×10^{-4} for Q(OH)2, -5.0×10^{-3} for F4TCNQ and 9.8×10^{-5} without insertion materials. Namely, the slope is negative for insertion, and positive (too small) for no insertion. The results imply that the lowering of the potential barrier caused by the hole accumulation through an application of V_G is different between FETs with and without insertion materials, and that the lowering of $<\phi_h^{eff}>$ by hole accumulation is small.

7-3-5. A correlation between FET parameters and E_{redox}

Figure 7-8(a) shows the plot of the averaged μ, $<\mu>$, as a function of E_{redox} in the [7]phenacene single crystal FET with / without insertion materials. From the plots, we cannot find the clear correlation between μ and E_{redox}. The μ value should reflect not only channel conductance but also contact resistance (or injection barrier) since the measurement of FET characteristics is performed at two-terminal measurement mode. Therefore, it is first assumed that the μ increase monotonously with increasing E_{redox} because of the decreases in ϕ_h^{eff}. From the plot shown in Figure 7-8(a), except for the $<\mu>$ for no insertion, the $<\mu>$ seems to increase with an increase in E_{redox} in the low E_{redox} range from negative to 0.15 V. This is easily understood based on the decrease in ϕ_h^{eff}. Actually, the μ for the [7]phenacene single crystal FET without insertion materials (no

insertion) is too low, as seen from the plot (Figure 7-8(a)), which is also explained based on the extremely high ϕ_h^{eff}. However, the $<\mu>$ values appear to much scatter in the E_{redox} range above 0.15 V. The $<\mu>$ values indicate the broad maximum (~ 4 $cm^2 V^{-1} s^{-1}$) at around E_{redox} = −0.1 - 0.15 V; as described in chapter 6, the highest μ value (= 6.9 $cm^2 V^{-1} s^{-1}$) is recorded in one device of the [7]phenacene single crystal FETs with source / drain electrodes modified with Et2TCNQ (E_{redox} = 0.15 V). The $<\mu>$ value for the [7]phenacene single crystal FET with Et2TCNQ shown in Figure 7-8(a) is also approximately the maximum.

The scattering of $<\mu>$ found in the positive E_{redox} range cannot simply be explained based on the contact resistance since the $<\phi_h^{eff}>$ substantially decreases with an increase in E_{redox} in the positive E_{redox} range above 0.15 V. The μ values for F2TCNQ (E_{redox} = 0.41 V) and F4TCNQ (E_{redox} = 0.6 V) are almost consistent with the maximum value. This may be interpreted by the scenario that the channel conductance dominates the μ value, instead of the contact resistance. In other words, by inserting high E_{redox} materials the contact resistance is minimized but the channel of [7]phenacene single crystal probably remains unchanged, so that the channel conductance governs the μ in the devices providing the low ϕ_h^{eff} (or high E_{redox} materials), which should show the saturation of μ. However the reason why the $<\mu>$ values for some insertion materials with the E_{redox} of 0.2 to 0.45 V are too low is still unclear.

Figure 7-8(b) shows the plots of average $|V_{TH}|$, $<|V_{TH}|>$, as a function of E_{redox} in the [7]phenacene single crystal FETs with / without insertion materials; all V_{TH} values were negative. Except for $<|V_{TH}|>$ for the [7]phenacene single crystal FET without insertion materials (no insertion), all $<|V_{TH}|>$s substantially lie on the straight line, showing a monotonanous decrease in $|V_{TH}|$ with an incerase in E_{redox}. This is closely related to the decrease in ϕ_h^{eff} with increasing E_{redox}, *i.e.*, the smooth hole-injection from the source electrode to the [7]phenacene single crystal should cause the rapid switch-on (or the small $|V_{TH}|$), because the V_{TH} (or switch-on voltage) in the transfer curve is affected from two factors, trap-filling by carrier-accumulation (main / direct factor) and carrier-injection (indirect factor) from electrode, at two-terminal measurement mode.

Recently, we found a clear lowering of $|V_{TH}|$ by an insertion of electron acceptor between single crystal and gate dielectric in [7]phenacene single crystal FET [14]. This implies the additional negative-voltage application by electron acceptor, causing the trap-filling by application of low $|V_G|$. This study is now in progress.

Thus, the correlation between $|V_{TH}|$ and E_{redox} is closely associated with that between ϕ_h^{eff} and E_{redox}. The $<|V_{TH}|>$ in the [7]phenacene single crystal FET without insertion materials (no insertion), which is not on the linear relationship shown in Figure 7-8(b), can be explained by the fact that the ϕ_h^{eff} in [7]phencene single crystal FET without insertion materials is too large to be scaled by E_{redox}. The large ϕ_h^{eff} without insertion materials, which deviates from the linear relationship in ϕ_h^{eff} - E_{redox} plot (Figure 7-5) must make it difficult to inject holes effectively, increasing the $|V_{TH}|$. Thus, the $|V_{TH}|$ relates directly to ϕ_h^{eff}.

7-3-6. Effect of crystal thickness on hole-injection barrier height

We have found a clear correlation of ϕ_h^{eff} and V_{TH} *versus* E_{redox} of insertion materials. To confirm the validity of this correlation, we have to take into account various problems that may affect to ϕ_h^{eff} and V_{TH}. In this study, the [7]phenacene single crystals with thickness of 200 - 1000 nm were used for an evaluation of FET parameters including ϕ_h^{eff}. Therefore, the effect of thickness of single crystal on ϕ_h^{eff} should be fully investigated. As an example, the plot of ϕ_h^{eff} as a function of thickness of single crystal in the [7]phenacene single crystal FET with source / drain electrodes modified with F2TCNQ is shown in Figure 7-9; the $<\phi_h^{eff}>$ value (= 0.17(2) eV) for F2TCNQ shown in Figure 7-5 is evaluated from the ϕ_h^{eff} values plotted in Figure 7-9. The plot shown in Figure 7-9 shows the independence of ϕ_h^{eff} of crystal thickness, *i.e.*, the thickness of single crystal does not affect the ϕ_h^{eff} or contact resistance within the thickness range of 200 to 1000 nm. This implies that the variation of FET characteristics clarified in this study is produced exclusively by the change of insertion materials. In other words, this study evaluates evidently FET characteristics caused by an insertion of electron acceptors and donors.

7-4. Conclusion

The hole injection from electrodes has been precisely controlled by an insertion of various materials (electron acceptors an donors) into the space between [7]phenacene single crystal and source / drain electrodes. The hole-injection barrier formed between single crystal and electrodes has closely been correlated with redox potential of the insertion materials. No insertion of electron acceptors and donors suggested the presence of large tunnelling barrier, because the ϕ_h^{eff} was much larger than the ϕ_h^{eff} - E_{redox} plot for the FETs with electron acceptors and donors. However, the Schottky barrier height and the tunnelling barrier height could not be distinguished from the temperature dependence of ϕ_h^{eff} for [7]phenacene single crystal FETs. Consequently, the evidence of formation of tunnelling barrier could not clearly be obtained. At the present stage, we must conclude that all ϕ_h^{eff}s with insertion materials can be scaled by E_{redox}.

The $|V_{TH}|$ could also be correlated with E_{redox}, except for $|V_{TH}|$ in FET without insertion materials. This result may be reasonable because the decrease in ϕ_h^{eff} through an increase in E_{redox} should cause the smooth hole-injection to result in a decrease in $|V_{TH}|$. In addition, the large ϕ_h^{eff} without insertion materials produces large $|V_{TH}|$. In other words, the $|V_{TH}|$ can be absolutely correlated with ϕ_h^{eff}. Thus, this study not only shows an effectiveness of interface control with electron acceptors and donors but also leads to its quantitative understanding. Furthermore, the interface control with insertion materials realised the very high μ value (= 6.9 $cm^2 V^{-1} s^{-1}$) in [7]phenacene single crystal FET, which is the highest in the phenacene single crystal FETs.

References

[1] A. R. Murphy and J. M. J. Fréchet, Chem. Rev. **107**, 1066 (2007).

[2] S. Liu, W. M. Wang, A. L. Briseno, S. C. B. Mannsfeld, and Z. Bao, Adv. Mater. **21**, 1217 (2009).

[3] S. Wang, M. Kappl, I. Liebewirth, M. Müller, K. Kirchhoff, W. Pisula, and K. Müllen, Adv. Mater. **24**, 417 (2012).

[4] Y. Ie, M. Ueta, M. Nitani, N. Tohnai, M. Miyata, H. Tada, and Y. Aso, Chem. Mater. **24**, 3285 (2012).

[5] A. Lv, S. R. Puniredd, J. Zhang, Z. Li, H. Zhu, W. Jiang, H. Dong, Y. He, L. Jiang, Y. Li, W. Pisula, Q. Meng, W. Hu, and Z. Wang, Adv. Mater. **24**, 2626 (2012).

[6] Z. Bao, A. J. Lovinger, and A. Dodabalapur, Appl. Phys. Lett. **69**, 3066 (1996).

[7] A. Dodabalapur, L. Torsi, and H. E. Katz, Science **268**, 270 (1995).

[8] H. Fuchigami, A. Tsumura, and H. Koezuka, Appl. Phys. Lett. **63**, 1372 (1993).

[9] N. Kawai, R. Eguchi, H. Goto, K. Akaike, Y. Kaji, T. Kambe, A. Fujiwara, and Y. Kubozono, J. Phys. Chem. C **116**, 7983 (2012).

[10] G. Saito, H. Sasaki, T. Aoki, Y. Yoshida, A. Otsuka, H. Yamochi, O. O. Drozdova, K. Yakushi, H. Kitagawa, and T. Mitani, J. Mater. Chem. **12**, 1640 (2002).

[11] T. Nagano, M. Tsutsui, R. Nouchi, N. Kawasaki, Y. Ohta, Y. Kubozono, N. Takahashi, and A. Fujiwara, J. Phys. Chem. C **111**, 7211 (2007).

[12] Y. Sugawara, Y. Kaji, K. Ogawa, R. Eguchi, S. Oikawa, H. Gohda, A. Fujiwara, and Y. Kubozono, Appl. Phys. Lett. **98**, 013303 (2011).

[13] N. Kawasaki, Y. Ohta, Y. Kubozono, and A. Fujiwara, Appl. Phys. Lett. **91**, 123518 (2007).

[14] T. Mikami, Y. Shimo, X. He, S. Hamao, R. Eguchi, H. Goto, Y. Kubozono. Unpublished data.

Table 7-1. Name of insertion materials and their abbreviations.

Name of insertion material	Abbreviation
2,5-dihydroxy-p-benzoquinone	Q(OH)2
2,5-dichloro-3,6-dihydroxy-p-benzoquinone	QCl2(OH)2
2,5-dibromo-3,6-dihydroxy-p-benzoquinone	QBr2(OH)2
2,3,5,6-tetraiodo-p-benzoquinone	QI4
2,3,5,6-tetrachloro-p-benzoquinone	QCl4
2,5-diethyl-7,7,8,8-tetracyano-p-quinodimethane	Et2TCNQ
2,5-dimethyl-7,7,8,8-tetracyano-p-quinodimethane	Me2TCNQ
7,7,8,8-tetracyano-p-quinodimethane	TCNQ
9,9,10,10-tetracyano-2,6-naphthoquinodimethane	TNAP
9-(dicyanomethylene)-2,4,5,7-tetranitrofluorene	DTENF
2-fluoro-7,7,8,8-tetracyano-p-quinodimethane	FTCNQ
2,5-difluoro-7,7,8,8-tetracyano-p-quinodimethane	F2TCNQ
trifluoromethyl-7,7,8,8-tetracyanoquinodimethane	CF3TCNQ
2,3,5,6-tetrafluoro-7,7,8,8-tetracyano-p-quinodimethane	F4TCNQ

Table 7-2. Density of insertion materials used in this chapter in units of g cm^{-3}.

Insertion material	Density	Reference
Q(OH)2	1.65	D. Semmingsen, Acta Chem. Scand. B **31**, 11 (1977).
QBr2(OH)2	2.53	C. Robl, Z. Kristallogr. **180**, 249 (1987).
QCl2(OH)2	1.96	N. Biliškov *et al*., J. Phys. Chem. A **115**, 3154 (2011).
QI4	3.86	H. Kobayashi *et al*., Bull. Chem. Soc. Jpn. **47**, 2333 (1974).
QCl4	2.02	Y. Kubozono *et al*., J. Phys. Chem. Solids **58**, 1375 (1997).
Et2TCNQ	1.18	Database of SciFinder
Me2TCNQ	1.25	Database of SciFinder
TCNQ	1.33	R. E. Long *et al*., Acta Cryst. **18**, 932 (1965).
TNAP	1.34	Database of SciFinder
DTENF	1.82	Database of SciFinder
FTCNQ	1.42	F. M. Wiygul *et al*., Mol. Cryst. Liq. Cryst. **71**, 303 (1981).
F2TCNQ	1.52	F. M. Wiygul *et al*., Mol. Cryst. Liq. Cryst. **78**, 279 (1981).
CF3TCNQ	1.50	Database of SciFinder
F4TCNQ	1.65	T. J. Emge *et al*., Mol. Cryst. Liq. Cryst. **65**, 161 (1981).

Table 7-3. Redox potential, E_{redox}, of insertion materials used in this chapter in units of V. These E_{redox} values are taken from Ref. 10 except for Q(OH)2, the E_{redox} of Q(OH)2 is taken from Ref. 2 in p. 99.

No.	Insertion material	E_{redox}
1	Q(OH)2	-0.38
2	QCl2(OH)2	-0.13
3	QBr2(OH)2	-0.12
4	QI4	-0.02
5	QCl4	0.05
6	Et2TCNQ	0.15
7	Me2-TCNQ	0.15
8	TCNQ	0.22
9	TNAP	0.23
10	DTENF	0.23
11	FTCNQ	0.32
12	F2TCNQ	0.41
13	CF3TCNQ	0.44
14	F4TCNQ	0.60

Q(OH)2	R_1, R_3 = H, R_2, R_4 = OH	ED
QCl2(OH)2	R_1, R_3 = Cl, R_2, R_4 = OH	ED
QBr2(OH)2	R_1, R_3 = Br, R_2, R_4 = OH	ED
QI4	R_1, R_2, R_3, R_4 = I	ED
QCl4	R_1, R_2, R_3, R_4 = Cl	EA
Et2TCNQ	R_1, R_3 = Et, R_2, R_4 = H	EA
Me2TCNQ	R_1, R_3 = Me, R_2, R_4 = H	EA
TCNQ	R_1, R_2, R_3, R_4 = H	EA
FTCNQ	R_1 = F, R_2, R_3, R_4 = H	EA
F2TCNQ	R_1, R_3 = F, R_2, R_4 = H	EA
CF3TCNQ	R_1 = CF3, R_2, R_3, R_4 = H	EA
F4TCNQ	R_1, R_2, R_3, R_4 = F	EA
DTENF		EA
TNAP		EA

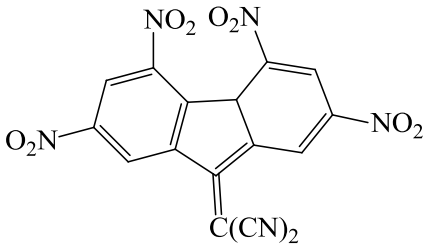

DTENF

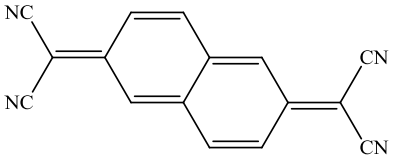

TNAP

Figure 7-1. Molecular structures of insertion materials used in this chapter. The ‘EA’ and ‘ED’ refer to electron acceptor and donor, respectively.

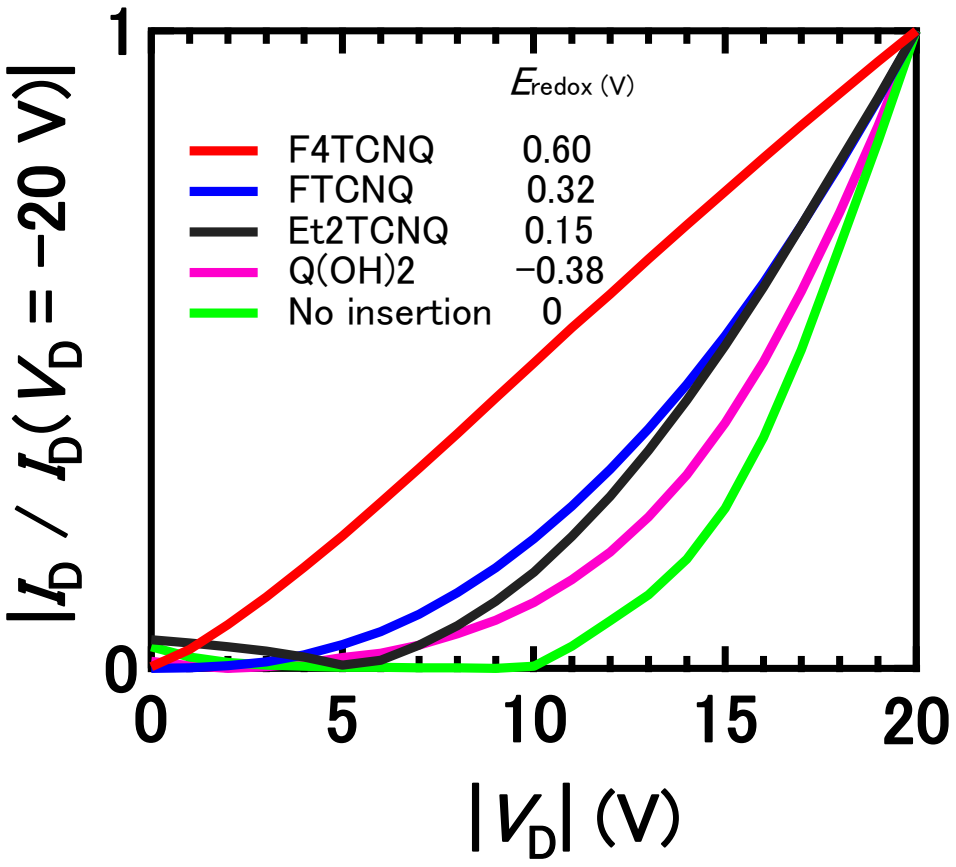

Figure 7-2. Output curves at V_G = –120 V of [7]phenacene single crystal FETs with four insertion materials (Q(OH)2, Et2TCNQ, FTCNQ and F4TCNQ) and without insertion materials (no insertion). The $|I_D|$ is normalized at V_D = –20 V.

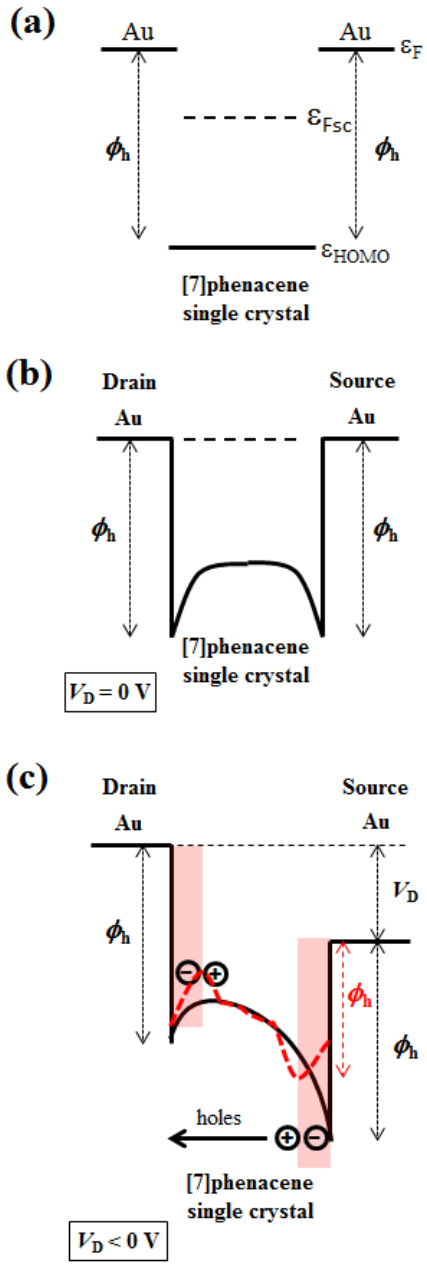

Figure 7-3. Energy diagrams of Au and [7]phenacene (a) before and (b) after thier contact, where V_D = 0 V. (c) Energy diagram of Au and [7]phenacene after thier contact, in which negative V_D is applied. In (c), the source electrode is grounded. Schematic of the band bending with / without insertion materials is shown in (c). The solid and dashed lines refer to the band bending without insertion materials and with electron acceptor / donor, respectively.

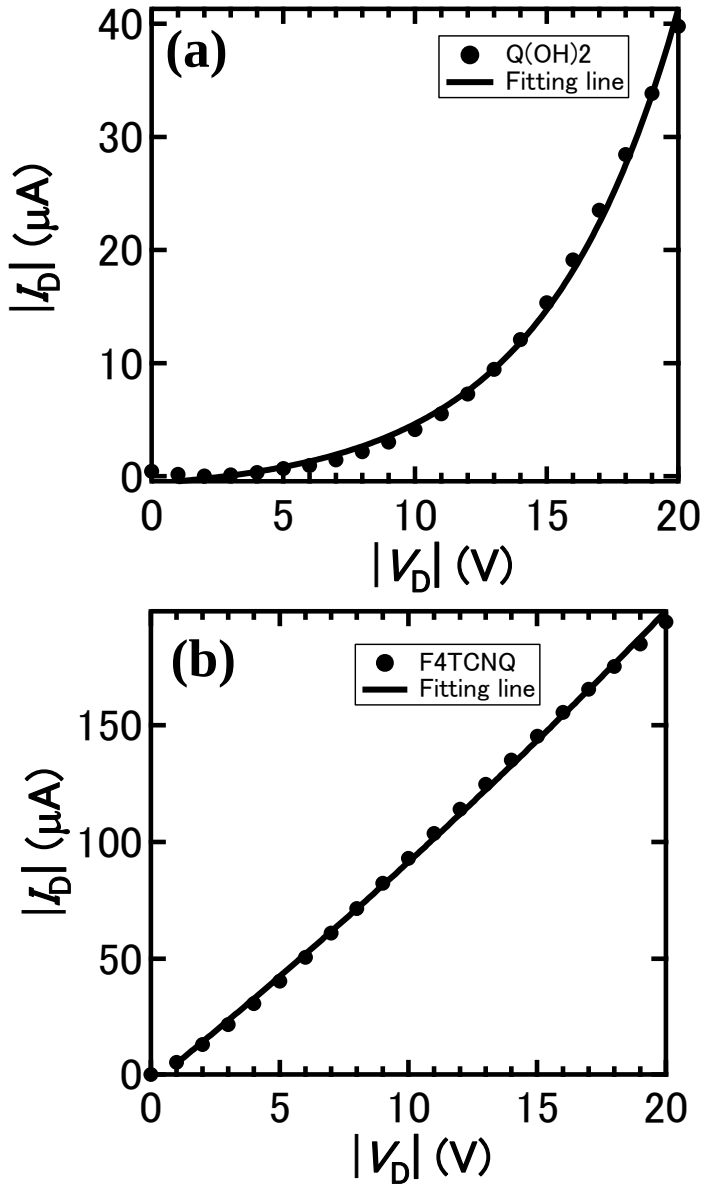

Figure 7-4. Output curves of [7]phenacene single crystal FETs with (a) Q(OH)2 and (b) F4TCNQ insertion. The fitting curves are shown by solid lines.

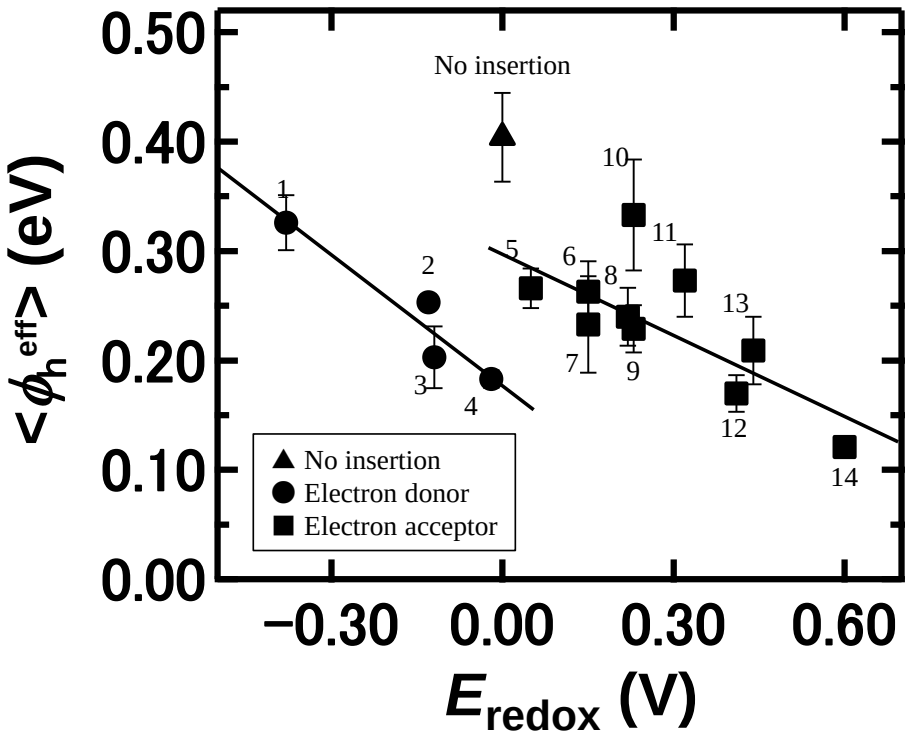

Figure 7-5. $<\phi_h^{eff}>$ plots as a function of E_{redox} of each insertion material, as well as that of no insertion. Numbers indicate the name of the insertion materials; 1 = Q(OH)2, 2 = QCl2(OH)2, 3 = QBr2(OH)2, 4 = QI4, 5 = QCl4, 6 = Et2TCNQ, 7 = Me2TCNQ, 8 = TCNQ, 9 = TNAP, 10 = DTENF, 11 = FTCNQ, 12 = F2TCNQ, 13 = CF3TCNQ and 14 = F4TCNQ.

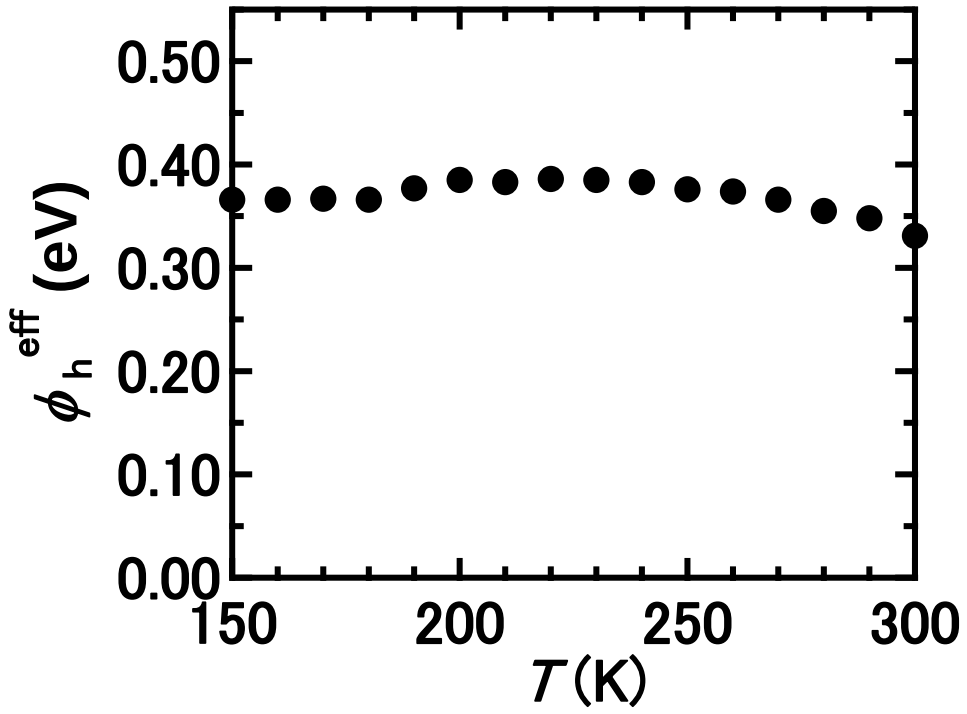

Figure 7-6. ϕ_h^{eff} vs T plots of [7]phenacene single crystal FET without any insertion materials (no insertion).

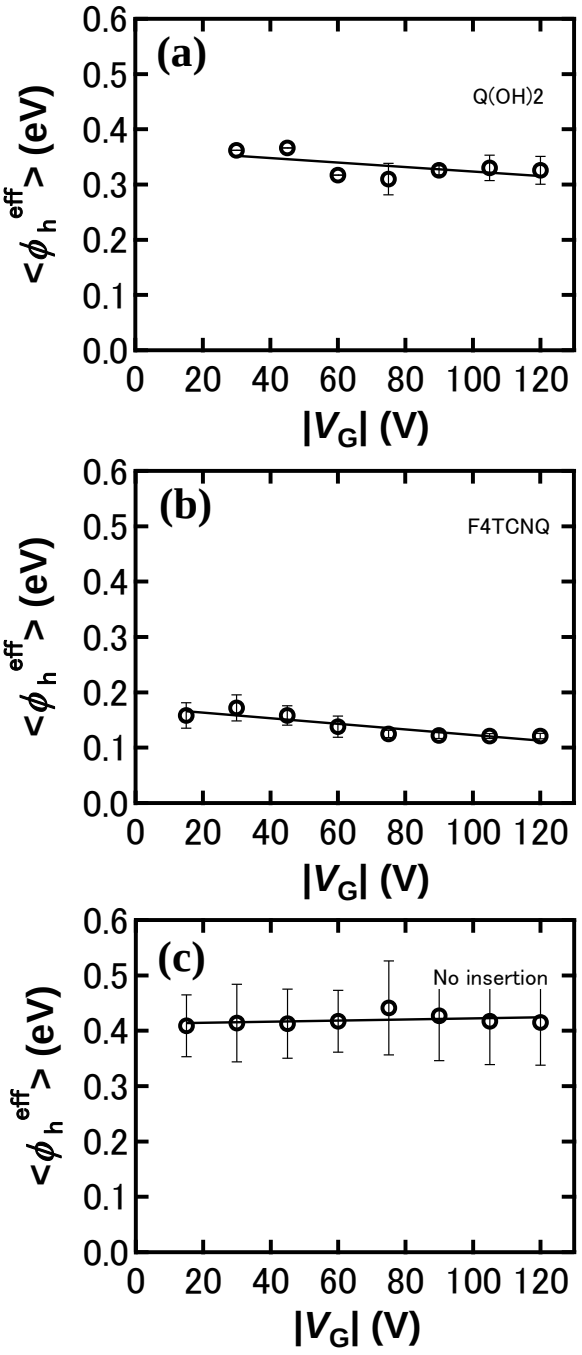

Figure 7-7. $<\phi_h^{eff}>$ vs $|V_G|$ plots for [7]phenacene single crystal FETs with (a) Q(OH)2 and (b) F4TCNQ, and (c) without any insertion materials (no insertion).

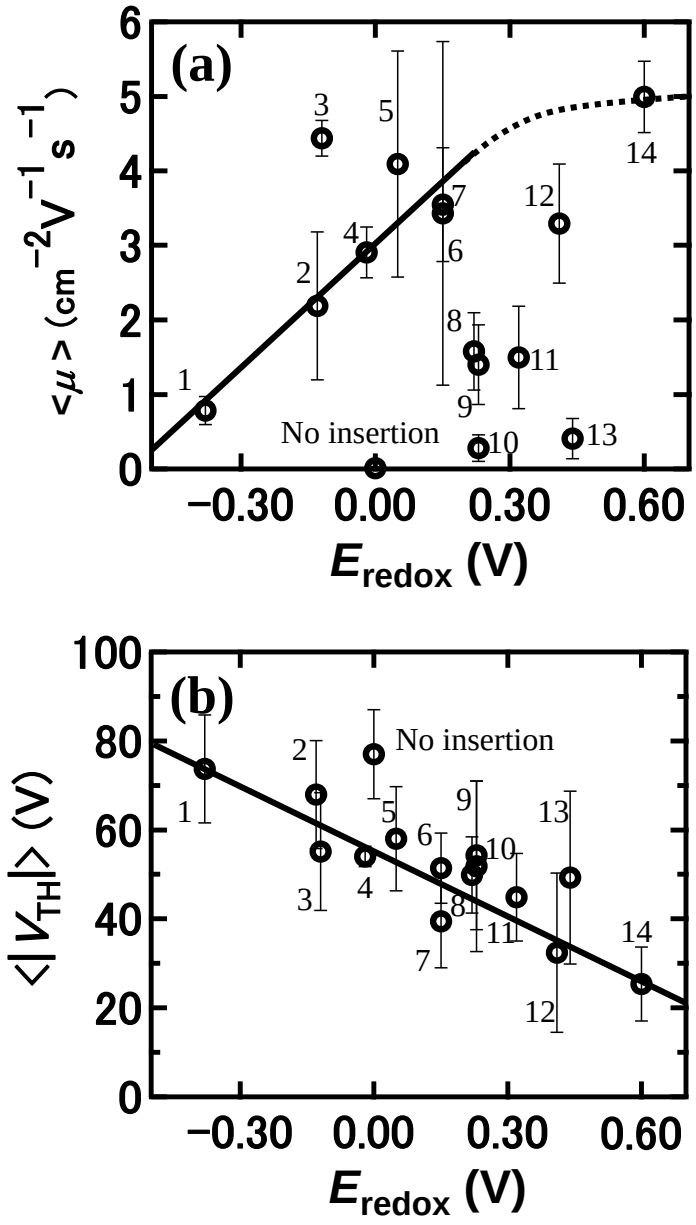

Figure 7-8. (a) <μ> and (b) <|V_{TH}|> as a function of E_{redox} in [7]phenacene single crystal FETs with / without insertion materials. Arabic numbers indicate the name of insertion materials in the same number as Figure 7-5.

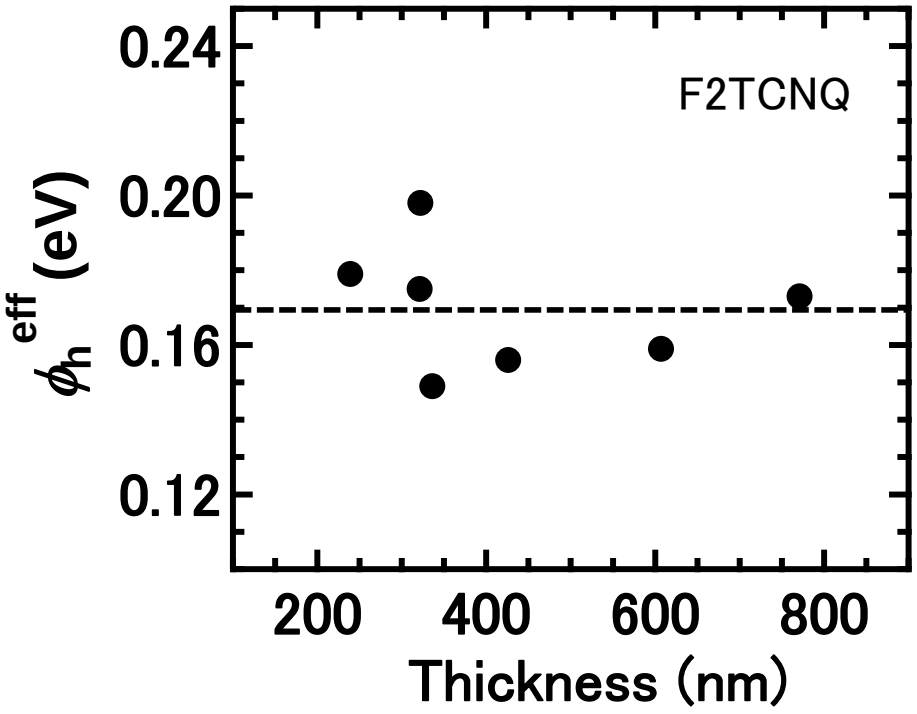

Figure 7-9. ϕ_h^{eff} as a function of thickness of [7]phenacene single crystal in the [7]phenacene single crystal FETs with F2TCNQ insertion.

Chapter 8. Low voltage operation in [7]phenacene single crystal FETs using high-*k* gate dielectrics

In this chapter, the author describes the study on low-voltage operation of [7]phenacene single crystal FET using high-*k* gate dielectrics. The low-voltage operation is quite important in view of practical application. The author showed the $|V_{TH}|$ of [7]phenacene single crystal FET with 400 nm thick SiO_2 gate dielectric (see Figure 5-9). The $|V_{TH}|$ (= 91 V) is too large to be utilized for practical devices. Therefore, decreasing $|V_{TH}|$ is one of the most significant works in research on organic transistor. We have three different approaches for decreasing $|V_{TH}|$, as described in section 8-1. The first approach is to decrease the thickness of gate dielectric, the second is using electron acceptors and donors to modify the interface between single crystals and source / drain electrodes, and the third is to use dielectrics with high relative permittivity, ε (called as 'high-*k* gate dielectric'). In this chapter, the author applies both the second and the third approaches to [7]phenacene single crystal FET in order to realise low-voltage FET operation.

8-1. Introduction

In chapters 5 and 6, fundamental FET characteristics are shown for [6]phenacene and [7]phenacene single crystal FETs with source / drain electrodes without any modifications (chapter 5) and with electrodes modified with either electron acceptors or donors (chapter 6). In particular, the μ value for [7]phenacene single crystal FET with electrodes modified with Et2TCNQ shows 6.9 $cm^2 V^{-1} s^{-1}$. However, the $|V_{TH}|$ value is as high as 50 V. The lowest $|V_{TH}|$ value in [7]phenacene single crystal FETs with SiO_2 gate dielectric reported in chapters 5 - 7 is 18 V for the FET with electrodes modified with F4TCNQ (Chapter 6); the average $|V_{TH}|$ is 30 V (Chapter 7) and one FET device with F4TCNQ provided 18 V (Chapter 6). In chapter 7, it has been found that the $|V_{TH}|$ can be reduced by interface control using high E_{redox} insertion materials (see Figure 7-8(b)). This is the second approach for decreasing $|V_{TH}|$.

However, the $|V_{TH}|$ is still high from view of the practical application. In fact, SiO_2 gate dielectric is used in most of organic thin film and single crystal FETs [1-15], but bias-voltages required for FET operation cannot be reduced owing to the small ε value (= 3.9). In particular, the $|V_{TH}|$ of FETs with phenacene thin films [16-19] and single crystal [20, chapters 5 - 7 in this Doctor thesis] is high in comparison with other organic FETs [1-15]. Therefore, the study on the low voltage operation is indispensable for phenacene FETs.

The capacitance per area C_o is given in

$$C_o = \frac{\varepsilon\varepsilon_0}{d}, \qquad (8\text{-}1)$$

where ε_0 is the permittivity in vacuum (= 8.85418×10^{-14} F cm^{-1}), and d is thickness of gate dielectric. The C_o is included as C_{ox} in the MOS FET formulae shown in chapter 4. The carrier density, n, which can be accumulated by applying V_G is expressed as

$$n = \frac{C_o V_G}{e}, \qquad (8\text{-}2)$$

where elemental charge, e, is 1.620218×10^{-19} C. From Eqs. 8-1 and 8-2, the smaller d can produce the larger n, and the higher ε can produce the larger n. Several attempts with high-k gate dielectrics (the third approach) for lowering the $|V_{TH}|$ were done for organic single crystal FETs [20-23]. In this study, the second and third approaches are applied to [7]phenacene single crystal FET, and the low-voltage operation is realised.

8-2. Experimental

In this study, 50 nm thick Ta_2O_5 or 50 nm thick HfO_2 gate dielectric was used for device fabrication. The device fabrication processes are described in chapter 5. The surface is coated with 30 nm thick parylene. In all devices fabricated, 3 nm thick TCNQ or F4TCNQ was inserted into the space between source / drain electrodes and single crystal. The channel length, L, and channel width, W, were 30 μm and 200 - 2000 μm, respectively. The device structure is shown in Figure 8-1. The C_o values determined

experimentally were described in chapter 5; the C_o is 49 nF cm^{-2} for both Ta_2O_5 and HfO_2.

8-3. Results and Discussion

The transport and output curves for [7]phenacene single crystal FET with Ta_2O_5 gate dielectric, in which 3nm thick TCNQ was inserted into the space between single crystal and source / drain electrodes, are shown in Figure 8-2. As seen from Figure 8-2, clear p-channel FET characteristics are observed with the low-voltage operation. The μ and $|V_{TH}|$ were determined to be 3.2 cm^2 V^{-1} s^{-1} and 6.3 V, respectively. The $|V_{TH}|$ is much smaller than the lowest $|V_{TH}|$ value (= 18 V) realised in [7]phenacene single crystal FET with SiO_2 gate dielectric. The on-off ratio was 3.6×10^8, which is close to that ($\sim 10^9$) for FET with SiO_2 gate dielectric. Furthermore, it can be pointed out that the μ value is also quite high.

As seen from Figure 8-2, no hysteresis is observed in the forward and reverse transfer / output curves. Thus the [7]phenacene single crystal FET with a Ta_2O_5 gate dielectric exhibits excellent FET characteristics accompanied with high μ and low $|V_{TH}|$. The μ, 3.2 cm^2 V^{-1} s^{-1}, is higher than the best record of μ, 1.3 cm^2 V^{-1} s^{-1}, for picene single crystal FET with HfO_2 gate dielectric [20]. The low-voltage operation in [7]phenacene single crystal FET with Ta_2O_5 gate dielectric may originate from not only a usage of high-k gate dielectric (Ta_2O_5) but also TCNQ insertion. Namely, the combination of the second and the third approaches may lead to a lowering of $|V_{TH}|$. This is discussed later in this section.

Furthermore, [7]phenacene single crystal FETs with HfO_2 gate dielectric were fabricated, in which 3 nm thick F4TCNQ was inserted into the interface between single crystal and source / drain electrodes. The transfer and output curves are shown in Figures 8-3(a) and (b), respectively. The μ value for the [7]phenacene single crystal FET with HfO_2 gate dielectric was estimated to be 3.0 cm^2 V^{-1} s^{-1}, in comparable to that, 3.2 cm^2 V^{-1} s^{-1}, for FET with Ta_2O_5 and TCNQ (Figure 8-2), and the $|V_{TH}|$ value was as low as

2.6 V. The on-off ratio was 2.3×10^8 which is comparable to that, 3.6×10^8, in FET with Ta_2O_5 and TCNQ. The hysteresis in the transfer and output curves was also small, as seen from Figure 8-3. Thus, the lower voltage-operation ($|V_{TH}|$ = 2.6 V) is achieved in [7]phenacene single crystal FET with HfO_2 than FET device with Ta_2O_5 ($|V_{TH}|$ = 6.3 V).

Here, it should be noticed that the C_o is the same between Ta_2O_5 and HfO_2. This should result in the same $|V_{TH}|$ value because the accumulated hole-density should be the same at the same V_G as seen from Eq. 8-2. Nevertheless, a significant difference in $|V_{TH}|$ is obtained between Ta_2O_5 and HfO_2. Therefore, the origin of the difference in $|V_{TH}|$ may be attributed to the difference of insertion material: TCNQ for Ta_2O_5, and F4TCNQ for HfO_2. These insertion materials have different E_{redox} values (0.22 V for TCNQ and 0.60 V for F4TCNQ). As described in section 8-1, the larger E_{redox} is effective for the lowering of $|V_{TH}|$, which is evidenced in chapter 7. As a consequence, we have concluded that the second (high E_{redox}-insertion materials) and third (high-k gate dielectrics) approaches effectively decrease the $|V_{TH}|$ in [7]phenacene single crystal FET. In [7]phenacene single crystal FET, the lowest $|V_{TH}|$ was realised in the combination of HfO_2 and F4TCNQ in the case of solid gate dielectrics.

8-4. Conclusion

The author fabricated [7]phenacene single crystal FET with high-k gate dielectrics, Ta_2O_5 and HfO_2, in which TCNQ and F4TCNQ was inserted, respectively. The high μ values (~ 3 $cm^2 V^{-1} s^{-1}$) were realised and the low $|V_{TH}|$ values (2.6 - 6.3 V) were obtained. It has been found from the difference in $|V_{TH}|$ between two devices that not only the usage of high-k gate dielectrics but also the insertion of high E_{redox} materials are significant for the low-voltage operation.

References

[1] A. F. Stassen, R. W. I. de Boer, N. N. Iosad, and A. F. Morpurgo, Appl. Phys. Lett. **85**, 3899 (2004).

[2] Q. Tang, H. Li, M. He, W. Hu, C. Liu, K. Chen, C. Wang, Y. Liu, and D. Zhu, Adv. Mater. **18**, 65 (2006).

[3] H. E. Romero, N. Shen, P. Joshi, H. R. Gutierrez, S. A. Tadigadapa, J. O. Sofo, and P. C. Eklund, ACS Nano **2**, 2037 (2008).

[4] F. Xue, Z. Liu, Y. Su, and K. Varahramyan, Microelectron. Eng. **83**, 298 (2006).

[5] L. Li, Q. Tang, H. Li, X. Yang, W. Hu, Y. Song, Z. Shuai, W. Xu, Y. Liu, and D. Zhu, Adv. Mater. **19**, 2613 (2007).

[6] H. Tada, H. Touda, M. Takada, and K. Matsushige, Appl. Phys. Lett. **76**, 873 (2000).

[7] Z. Chen, Y. Zheng, H. Yan, and A. Facchetti, J. Am. Chem. Soc. **131**, 8 (2009).

[8] H. Ebata, T. Izawa, E. Miyazaki, K. Takimiya, M. Ikeda, H. Kuwabara, and T. Yui, J. Am. Chem. Soc. **129**, 15732 (2007).

[9] B. Yoo, B. A. Jones, D. Basu, D. Fine, T. Jung, S. Mohapatra, A. Facchetti, K. Dimmler, M. R. Wasielewski, T. J. Marks, and A. Dodabalapur, Adv. Mater. **19**, 4028 (2007).

[10] Th. B. Singh, N. Marjanović, P. Stadler, M. Auinger, G. J. Matt, S. Günes, N. S. Sariciftci, R. Schwödiauer, and S. Bauer, J. Appl. Phys. **97**, 083714 (2005).

[11] J. Jang, J. W. Kim, N. Park, and J.-J. Kim, Org. Electron. **9**, 481 (2008).

[12] H.-C. Tiao, Y.-J. Lee, Y.-S. Liu, S.-H. Lee, C.-H. Li, and M.-Y. Kuo, Org. Electron. **13**, 1004 (2012).

[13] L. Jiang, J. Gao, E. Wang, H. Li, Z. Wang, W. Hu, and L. Jiang, Adv. Mater. **20**, 2735 (2008).

[14] D. H. Kim, D. Y. Lee, H. S. Lee, W. H. Lee, Y. H. Kim, J. I. Han, and K. Cho, Adv. Mater. **19**, 678 (2007).

[15] H. Ebata, E. Miyazaki, T. Yamamoto, and K. Takimiya, Org. Lett. **9**, 4499 (2007).

[16] H. Okamoto, N. Kawasaki, Y. Kaji, Y. Kubozono, A. Fujiwara, and M. Yamaji, J. Am. Chem. Soc. **130**, 10470 (2008).

[17] N. Kawasaki, Y. Kubozono, H. Okamoto, A. Fujiwara, and M. Yamaji, Appl. Phys. Lett. **94**, 043310 (2009).

[18] N. Komura, H. Goto, X. He, H. Mitamura, R. Eguchi, Y. Kaji, H. Okamoto, Y. Sugawara, S. Gohda, K. Sato, and Y. Kubozono, Appl. Phys. Lett. **101**, 083301 (2012).

[19] Y. Sugawara, Y. Kaji, K. Ogawa, R. Eguchi, S. Oikawa, H. Gohda, A. Fujiwara, and Y. Kubozono, Appl. Phys. Lett. **98**, 013303 (2011).

[20] N. Kawai, R. Eguchi, H. Goto, K. Akaike, Y. Kaji, T. Kambe, A. Fujiwara, and Y. Kubozono, J. Phys. Chem. C **116**, 7983 (2012).

[21] N. Hiroshiba, R. Kumashiro, K. Tanigaki, T. Takenobu, Y. Iwasa, K. Kotani, I. Kawayama, and M. Tonouchi, Appl. Phys. Lett. **89**, 152110 (2006).

[22] R. W. I. de Boer, N. N. Iosad, A. F. Stassen, T. M. Klapwijk, and A. F. Morpurgo, Appl. Phys. Lett. **86**, 032103 (2005).

[23] W. Ou-Yang, T. Uemura, K. Miyake, S. Onish, T. Kato, M. Katayama, M. Kang, K. Takimiya, M. Ikeda, H. Kuwabara, M. Hamada, and J. Takeya, Appl. Phys. Lett. **101**, 223304 (2012).

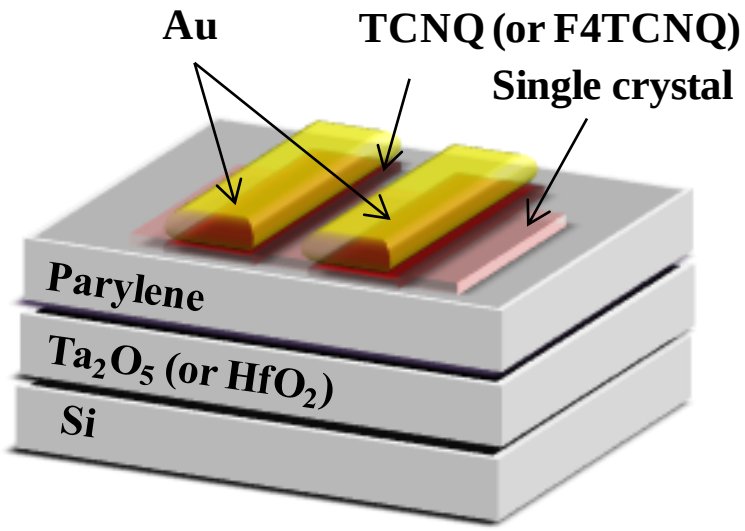

Figure 8-1. Device structure of a [7]phenacene single crystal FET with a high-*k* gate dielectric.

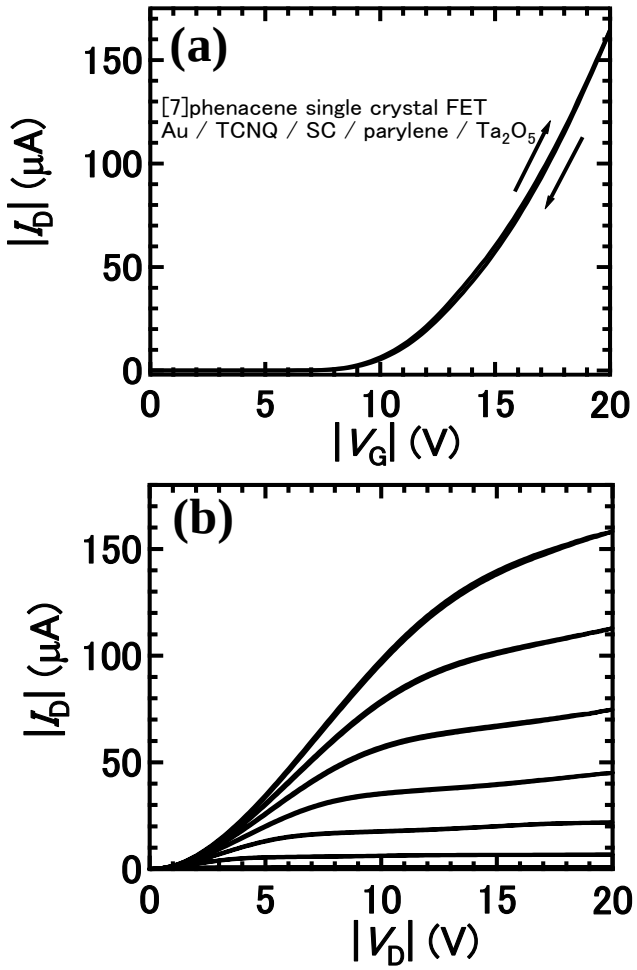

Figure 8-2. (a) Transfer and (b) output curves for [7]phenacene single crystal FET with a Ta_2O_5 gate dielectric.

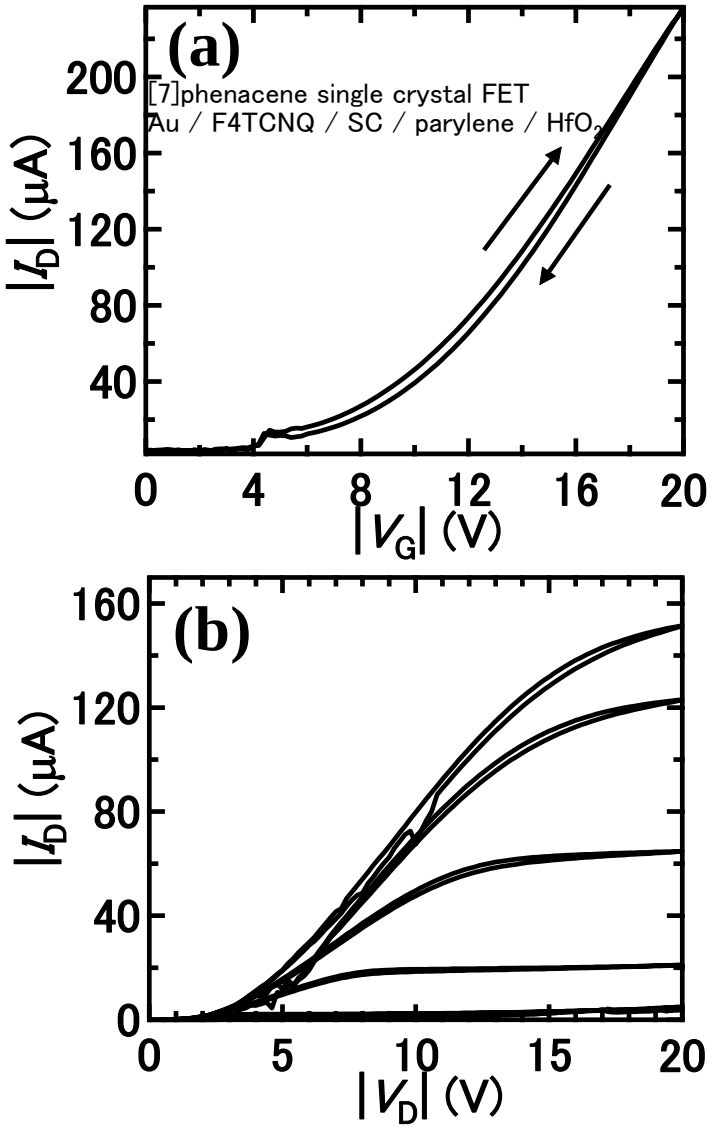

Figure 8-3. (a) Transfer and (b) output curves for [7]phenacene single crystal FET with a HfO_2 gate dielectric.

Chapter 9. Bias stress effect and O_2 gas sensing properties in [6]phenacene and [7]phenacene single crystal FETs

In this chapter, the author describes the bias stress effect and O_2 gas sensing properties of phenacene single crystal FETs. Here, the bias stress effect means the drastic decrease in $|I_D|$ observed when applying bias voltages (V_D and V_G) to the phenacene FET devices, *i.e.*, the effect that the bias stress causes for the FETs. This effect probably relates to the hysteresis observed in the forward and reverse transfer / output curves. Such a bias stress effect was found in picene thin film FET by Sugawara *et al*. [1]. This is closely associated with the presence of H_2O in the channel region [1]. On the other hand, it was found that the exposure of picene thin film FET device to O_2 gas increased the $|I_D|$ and μ [2-4]. This implies that the picene thin film FET has the O_2 sensing ability. Subsequently, the O_2 sensing ability of [6]phenacene and [7]phenacene thin film FETs was fully evaluated [5,6]. These studies aim at the practical gas sensors based on phenacene thin film FETs. In this chapter, the author reports two properties (bias stress effect and O_2 gas sensing ability) characteristic of phenacene FETs.

9-1. Introduction

A large hysteresis in forward and reverse transfer curves was observed in picene thin film FET [2-4]. The hysteresis was suppressed by making hydrophobic surface on gate dielectric or using hydrophobic gate dielectric [4]. Therefore, the hysteresis was discussed based on the presence of H_2O at the interface between single crystal and gate dielectric [4]. This hysteresis always provides the lower $|I_D|$ in the reverse transfer curve than the forward transfer curve [2-4]. Namely, the hysteresis seems to closely relate to the bias stress effect. Recently, Sugawara *et al*. discussed the bias stress effect in picene thin film FETs [1]. The $|I_D|$ of the picene thin film FET with SiO_2 gate dielectric was continuously measured at $V_G = V_D = -100$ V, showing a rapid decrease with time; the SiO_2 surface was not coated with parylene but hexamethyldisilazane (HMDS). Furthermore, the $|I_D|$ of picene thin film FET with Ta_2O_5 gate dielectric coated with 35

nm thick parylene was continuously measured at $V_D = V_G = -10$, -8 and -6 V. The rapid decrease in $|I_D|$ was suppressed with decreasing $|V_D|$ and $|V_G|$, suggesting that bias stress effect (or decrease in $|I_D|$ by the continuous voltage operation) is supressed by decreasing the bias voltage. Also the bias stress effect was the largest in the FET device with SiO_2 gate dielectric in which the surface of SiO_2 may contain large amounts of H_2O because of no parylene-coating. These results show that bias stress effect is closely correlated with both the bias voltage and the presence of H_2O. Such properties were also observed in [6]phenacene thin film FET [5]. As described later, the bias stress effect causes the suppression of O_2 sensing ability in picene thin film FETs.

The phenacene thin film FETs have a clear O_2 sensing ability that the maximum $|I_D|$ ($|I_D|^{max}$) measured at the highest applied $|V_D|$ and $|V_G|$ as well as the μ value increases under O_2 atmosphere and decreases by removal of O_2 [1-6]. On the other hand, the picene single crystal FET recorded highest μ value, 1.3 $cm^2 V^{-1} s^{-1}$, under O_2-free atmosphere, *i.e.*, in Ar-filled glove box, and the O_2 sensing effect has not yet been confirmed [7]. In this chapter, the author reports the O_2 sensing properties of [6]phenacene and [7]phenacene single crystal FETs. Furthermore, the comparison of O_2 sensing properties between thin film and single crystal FETs are discussed.

Although the O_2 sensing properties are characteristic of phenacene thin film FETs [1-6], Sugawara *et al.* reported that the properties were not observed by continuous bias application. Namely, the bias - voltage application suppresses the O_2 sensing ability in these FETs. This seems to be related to the bias stress effect. Actually, Sugawara *et al.* measured $|I_D|$ in continuous application of $V_G = V_D = -10$ V under O_2 atmosphere and O_2-free condition, which showed the monotonous decrease in $|I_D|$ even under O_2 atmosphere. Thus bias stress effect produced a serious problem for the O_2 sensing ability of phenacene thin film FET. In this chapter, the bias stress effect is also studied in [6]phenacene and [7]phenacene single crystal FETs in connection with the O_2 sensing ability.

9-2. Experimental

The structure of FET device used in this chapter is the same that as in chapters 6 and 7: The SiO_2 was used for gate dielectric; 300 nm for [6]phenacene and 400 nm for [7]phenacene single crystal FETs. TCNQ was inserted for the interface modification between single crystal and source / drain electrodes. For the study on bias stress effect, the transfer curves were measured repeatedly at intervals of 1 min or 1 h, and time evolution of $|I_D|^{max}$ was plotted for both phenacene single crystal FETs; $|I_D|^{max}$ means $|I_D|$ at $|V_G| = |V_D| = 100$ V. For study on O_2 sensing properties, the $|I_D|$ is measured for both phenacene single crystal FETs before / after O_2-exposure.

9-3. Results and Discussion

9-3-1. Observation of bias stress effect and its mechanism

Figure 9-1(a) shows the transfer curves for [6]phenacene single crystal FET measured at 1 min interval. The transfer curves are plotted at 5 times step. The $|I_D|$ in transfer curve decreases with an increase in number of measurement cycle. The large hysteresis is observed in the transfer curves at the first cycle of measurement, but it disappears rapidly and no hysteresis is observed in the 30th transfer curve. The time evolution of $|I_D|^{max}$ is shown in Figure 9-1(b). As seen from Figure 9-1(b), the $|I_D|^{max}$ decreases exponentially with an increase in time; the $|I_D|^{max}$ evolution is plotted with the $|I_D|^{max}$ in the transfer curve measured at 1 min interval (Figure 9-1(a)). It is found that the $|I_D|^{max}$ in picene and [6]phenacene thin film FET rapidly decrease in applying V_G and V_D continuously [1,2,3,5]. Such a behaviour originates from bias-stress effect, which may be related to an emergence of trap associated closely with presence of H_2O are discussed later [8-13]. The O_2 sensing ability for the picene and [6]phenacene thin film FETs disappears by the bias stress effect [1,5], *i.e.*, even in exposure of FET to 760 Torr of O_2, the $|I_D|^{max}$ does not increase under a continuous application of V_G and V_D. The exponential decay of $|I_D|^{max}$ shown in Figure 9-1(b) is the same phenomenon as that observed in picene and [6]phenacene thin film FETs, *i.e.*, it originates from the bias stress effect.

Figure 9-2(a) shows the transfer curves for [6]phenacene single crystal FET measured at 1 h interval. The transfer curves hardly decrease with an increase in number of measurement cycle, contrary to the transfer curves measured at 1 min interval. The time evolution of $|I_D|^{max}$ plotted with $|I_D|^{max}$ in the transfer curves measured at 1 h interval is shown in Figure 9-2(b). The $|I_D|^{max}$ is almost constant during 33 h. Thus, the measurement at 1 h interval does not substantially induce the bias stress effect, although very small fluctuation of $|I_D|^{max}$ is observed. Furthermore, the hysteresis between forward and reverse transfer curves is hardly observed in Figure 9-2(a), which means that the hysteresis is closely related to the bias stress, *i.e.*, the hysteresis is induced by the bias stress effect.

Figures 9-3(a) and (b) show the transfer curves and $|I_D|^{max}$ evolution measured for [7]phenacene single crystal FET at 1 min interval, which show the decrease in transfer curves and $|I_D|^{max}$ with an increase in number of measurement cycle; the $|I_D|^{max}$ evolution is plotted with the $|I_D|^{max}$ in the transfer curves. The $|I_D|^{max}$ decreases monotonously with an increase in time, but the rate of decrease is smaller than that for [6]phenacene single crystal FET (Figure 9-1). As seen from the transfer curves measured at 1 h interval (Figure 9-4(a)), the transfer curves do not change despite increasing number of measurement cycle. Figure 9-4(b) shows the plot of $|I_D|^{max}$ recorded at 1 h interval, which is constant during 30 h. This behaviour is almost the same as that for [6]phenacene single crystal FET. Actually, the bias stress effect observed at 1 min interval (Figure 9-3) is smaller than that for [6]phenacene single crystal FET (Figure 9-1), and [7]phenacene single crystal FET in the measurement at 1 h interval showed no bias stress effect, *i.e.*, no fluctuation of $|I_D|^{max}$. As a consequence, we can stress that [7]phenacene single crystal FETs operate more stably than [6]phenacene single crystal FETs. It can be conclude that the bias stress effect can be removed by the measurement of transfer curves at 1 h interval.

It is found in our previous study that the bias stress effect is closely related to H_2O [1,2], and the hydrophobic surface does not show the reduction of $|I_D|$ [2]. Therefore we will discuss bias stress effect by considering presence of H_2O on gate dielectrics in this chapter. This discussion is clearly described in our group's paper [1]. When the H_2O

molecule is aligned so as to bound H atoms with dielectrics surface by applying strong negative V_G, *i.e.*, when O atoms are faced to [7]phenacene single crystal, this should produce an additional negative voltage to decrease $|V_{TH}|$ because of polarized O atoms ($O^{\delta-}$). This suggests the enhancement of $|I_D|$ by application of a strong negative bias voltage under presence of H_2O. Such a V_{TH} shift is observed in using polarized self-assembly monolayer (SAM) (the F-terminated SAM), which stands on gate dielectric to push out negatively polarized F ($F^{\delta-}$) to active layer, shifted V_{TH} to positive direction, *i.e.*, caused a reduction of $|V_{TH}|$ [14]. Therefore, the bias stress effect may not be explained based on the dipole moment of H_2O aligned by a negative voltage. The presence of H_2O related trap for explaining the bias stress effect is considered under high gate voltage [8-12]. The discrete trap states of 2×10^{12} cm^{-2} in pentacene FET [10] are observed at 430 meV [12] above the valence band edge. The discrete trap states are formed only in the first monolayer of pentacene under negative bias application [12]. Furthermore, it is found that the bias-voltage application for 5 h in pentacene FET causes the saturation of total density of H_2O related trap states [10]. The formation and filling of the H_2O related trap states should increase the $|V_{TH}|$ to directly decrease $|I_D|$, producing the experimental results that the $|I_D|$ decreases with time (Figures 9-1 and 9-3) or the $|I_D|$ in the reverse transfer curve is smaller than that in the forward transfer curve (Figures 9-1, 9-3 and 9-5). Thus, the H_2O aligned by bias voltage application must play an important role in the formation-process of trap states [9,10,12,13]. As a consequence, the H_2O related trap states produced in [6]phenacene and [7]phenacene single FET under short-time-step (1 min interval) voltage application must cause the reduction of $|I_D|$, as in [7]phenacene thin film FET under continuous bias voltage operation [1].

9-3-2. O_2 sensing ability in phenacene single crystal FETs

To investigate the O_2 senising effect in [6]phenacene and [7]phenacene single crystal FETs, we measured the transfer curves in [6]phenacene and [7]phenacene single crystal FETs before / after O_2-exposure. The transfer curves in [6]phenacene single crystal FET which are measured in Ar-filled glove box are shown in Figure 9-5(a). The transfer

curves described as 'before O_2-exposure' were measured in Ar-filled glove box just after making the FET device. The transfer curves, described as 'after O_2-exposure' were measured in Ar-filled glove box after the FET was stored under 760 Torr of dried O_2 for 6 days.

As seen from Figure 9-5(a), the transfer curves after O_2-exposure decrease in comparison with those before O_2-exposure, implying no O_2-induced $|I_D|$-enhancement in [6]phenacene single crystal FET. The μ and on-off ratio are 9.2×10^{-2} $cm^2 V^{-1} s^{-1}$and 1.6×10^8, respectively, before O_2-exposure and those are 5.0×10^{-2} $cm^2 V^{-1} s^{-1}$ and 9.6×10^7 after O_2-exposure. The $|V_{TH}|$ values before and after O_2-exposure are 19 and 21 V, respectively, suggesting that $|V_{TH}|$ is hardly affected by O_2.

The transfer curves in [7]phenacene single crystal FET before / after O_2-exposure are shown in Figure 9-5(b); the measurement condition is the same as those for [6]phenacene single crystal FET described above. The transfer curves after O_2-exposure decrease in comparison with those before O_2-exposure. This result implies no O_2-induced enhancement of $|I_D|$ in [7]phenacene single crystal FET, as in [6]phenacene single crystal FET. The μ and on-off ratio are 8.2×10^{-1} $cm^2 V^{-1} s^{-1}$ and 2.7×10^8, respectively, before O_2-exposure and those are 6.3×10^{-1} $cm^2 V^{-1} s^{-1}$ and 1.9×10^8 after O_2-exposure. The $|V_{TH}|$ values before and after O_2-exposure are 52 and 54 V, respectively. Thus, the response for O_2 is almost the same between [6]phenacene and [7]phenacene single crystal FETs, *i.e.*, the μ and on-off ratio decrease after O_2-exposure of single crystal FETs, which is contrary to that for [6]phenacene and [7]phenacene thin film FETs [5,6]. The O_2 response in [6]phenacene and [7]phenacene single crystal FETs is consistent with that in picene single crystal FET [7]. The result that the μ and $|I_D|^{max}$ do not increase by O_2-exposure may originate from that O_2 cannot effectively penetrate into the channel region because of few grain boundaries and defects in single crystals in comparison with thin films.

9-4. Conclusion

The bias stress effect and O_2 sensing properties have been investigated for [6]phenacene and [7]phenacene single crystal FET devices, which show that the bias stress can be removed in transfer-curve measurements at 1 h interval. The mechanism of bias stress effect has been discussed based on the formation of trap states produced by the presence of H_2O in the interface between single crystal and gate dielectric under strong electric-filed. The phenacene single crystal FETs do not cause the enhancement of μ and $|I_D|^{max}$ by O_2-exposure, the reason may be that O_2 may not effectively penetrate into the channel region in single crystal FET because of few grain boundaries and defects.

References

[1] Y. Sugawara, K. Ogawa, H. Goto, S. Oikawa, K. Akaike, N. Komura, R. Eguchi, Y. Kaji, S. Gohda, and Y. Kubozono, Sens. Actuators, B **171 /172**, 544 (2012).

[2] X. Lee, Y. Sugawara, A. Ito, S. Oikawa, N. Kawasaki, Y. Kaji, R. Mitsuhashi, H. Okamoto, A. Fujiwara, K. Omote, T. Kambe, N. Ikeda, and Y. Kubozono, Org. Electron. **11**, 1394 (2010).

[3] N. Kawasaki, W. L. Kalb, T. Mathis, Y. Kaji, R. Mitsuhashi, H. Okamoto, Y. Sugawara, A. Fujiwara, Y. Kubozono, and B. Batlogg, Appl. Phys. Lett. **96**, 113305 (2010).

[4] N. Kawasaki, Y. Kubozono, H. Okamoto, A. Fujiwara, and M. Yamaji, Appl. Phys. Lett. **94**, 043310 (2009).

[5] N. Komura, H. Goto, X. He, H. Mitamura, R. Eguchi, Y. Kaji, H. Okamoto, Y. Sugawara, S. Gohda, K. Sato, and Y. Kubozono, Appl. Phys. Lett. **101**, 083301 (2012).

[6] Y. Sugawara, Y. Kaji, K. Ogawa, R. Eguchi, S. Oikawa, H. Gohda, A. Fujiwara, and Y. Kubozono, Appl. Phys. Lett. **98**, 013303 (2011).

[7] N. Kawai, R. Eguchi, H. Goto, K. Akaike, Y. Kaji, T. Kambe, A. Fujiwara, and Y. Kubozono, J. Phys. Chem. C **116**, 7983(2012).

[8] D. V. Lang, X. Chi, T. Siegrist, A. M. Sergent, and A. P. Ramirez, Phys. Rev. Lett. **93**, 076601(2004).

[9] H. L. Gomes, P. Stallinga, M. Cölle, D. M. de Leeuw, and F. Biscarini, Appl. Phys. Lett. **88**, 082101 (2006).

[10] C. Goldmann, D. J. Gundlach, and B. Batlogg, Appl. Phys. Lett. **88**, 063501(2006).

[11] C. Goldmann, C. Krellner, K. P. Pernstich, S. Haas, D. J. Gundlach, and B. Batlogg, J. Appl. Phys. **99**, 034507 (2006).

[12] K. P. Pernstich, D. Oberhoff, C. Goldmann, and B. Batlogg, Appl. Phys. Lett. **89**, 213509 (2006).

[13] W. L. Kalb, T. Mathis, S. Haas, A. F. Stassen, and B. Batlogg, Appl. Phys. Lett. **90**, 092104 (2007).

[14] J. Takeya, T. Nishikawa, T. Takenobu, S. Kobayashi, Y. Iwasa, T. Mitani, C. Goldmann, C. Krellner, and B. Batlogg, Appl. Phys. Lett. 85, 5078 (2004).

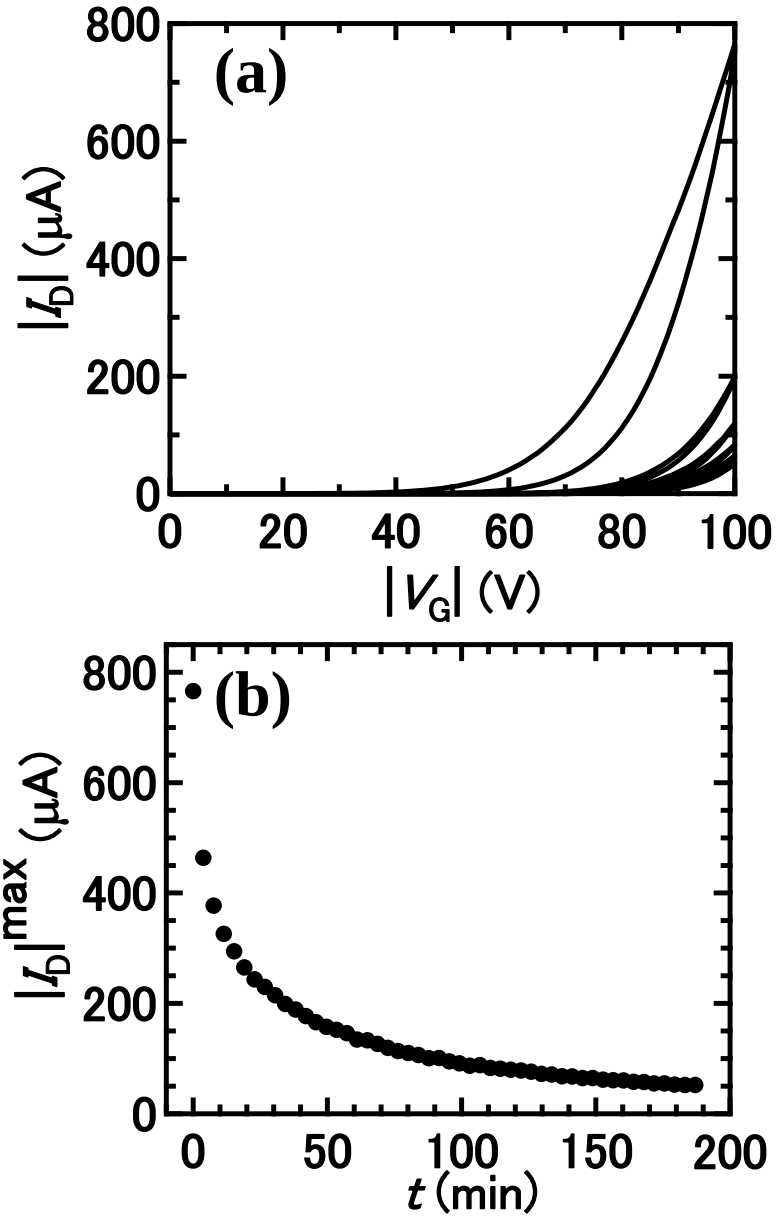

Figure 9-1. (a) Transfer curves and (b) time evolution of $|I_D|^{max}$ for [6]phenacene single crystal FET measured at 1 min interval. The numbers in (a) indicate the transfer curve measured at 1st, 5th, … and 30th cycle. Measurement time for one transfer curve is 2.8 min.

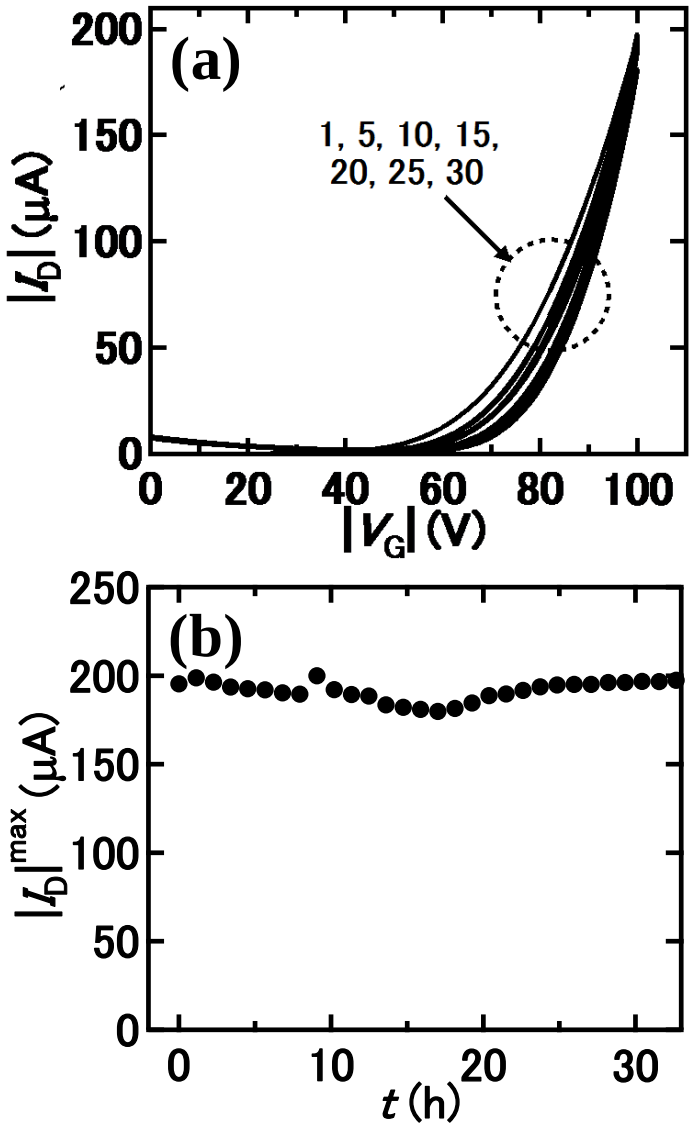

Figure 9-2. (a) Transfer curves and (b) time evolution of $|I_D|^{max}$ for [6]phenacene single crystal FET measured at 1 h interval. The numbers in (a) indicate the transfer curve measured at 1st, 5th, … and 30th cycle. Measurement time for one transfer curve is 8.1 min

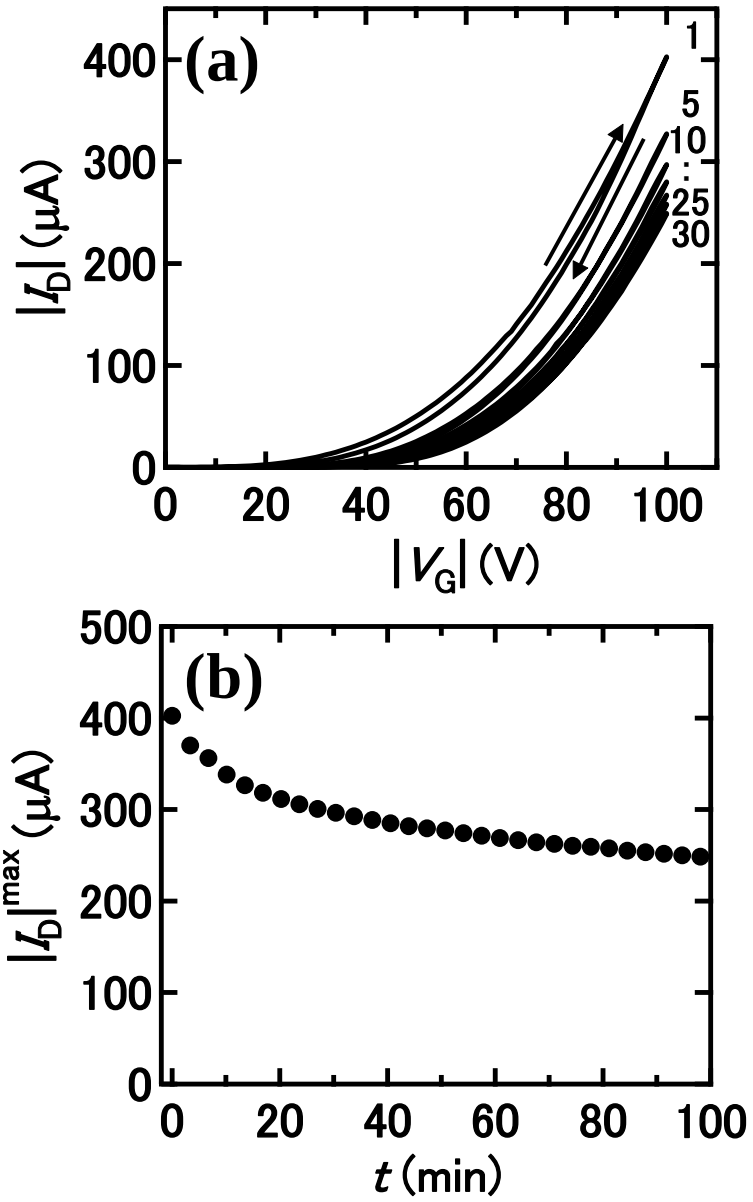

Figure 9-3. (a) Transfer curves and (b) time evolution of $|I_D|^{max}$ for [7]phenacene single crystal FET measured at 1 min interval. The numbers in (a) indicate the transfer curve measured at 1st, 5th, … and 30th cycle. Measurement time for one transfer curve is 2.4 min.

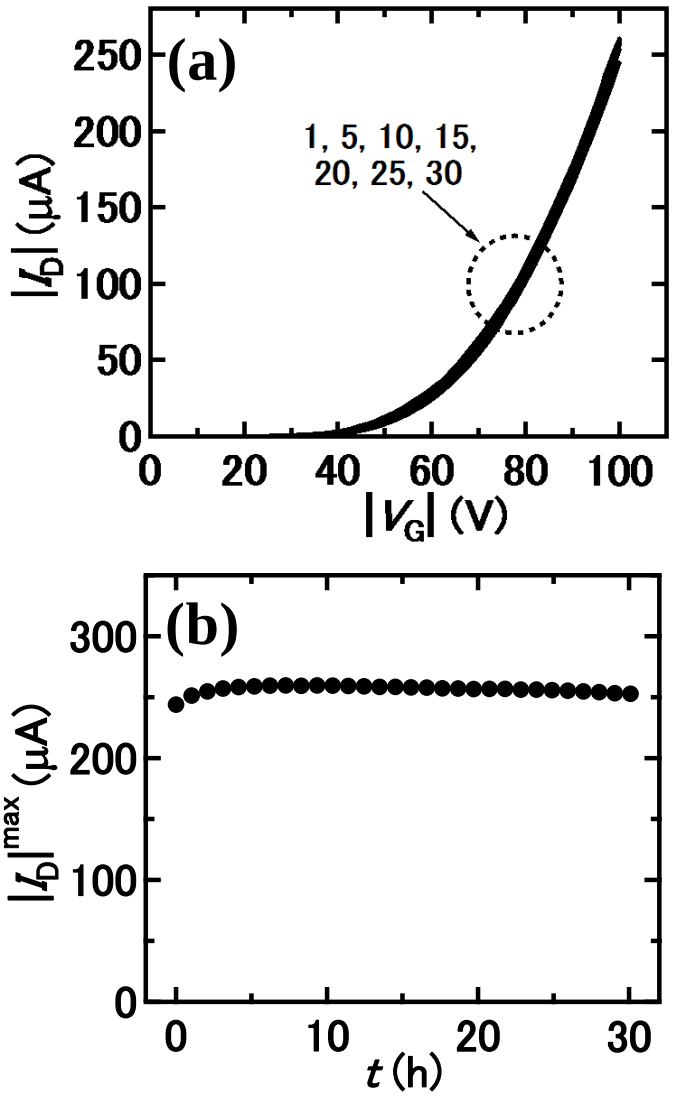

Figure 9-4. (a) Transfer curves and (b) time evolution of $|I_D|^{max}$ for [7]phenacene single crystal FET measured at 1 h interval. The numbers in (a) indicate the transfer curve measured at 1st, 5th, … and 30th cycle. Measurement time for one transfer curve is 2.2 min.

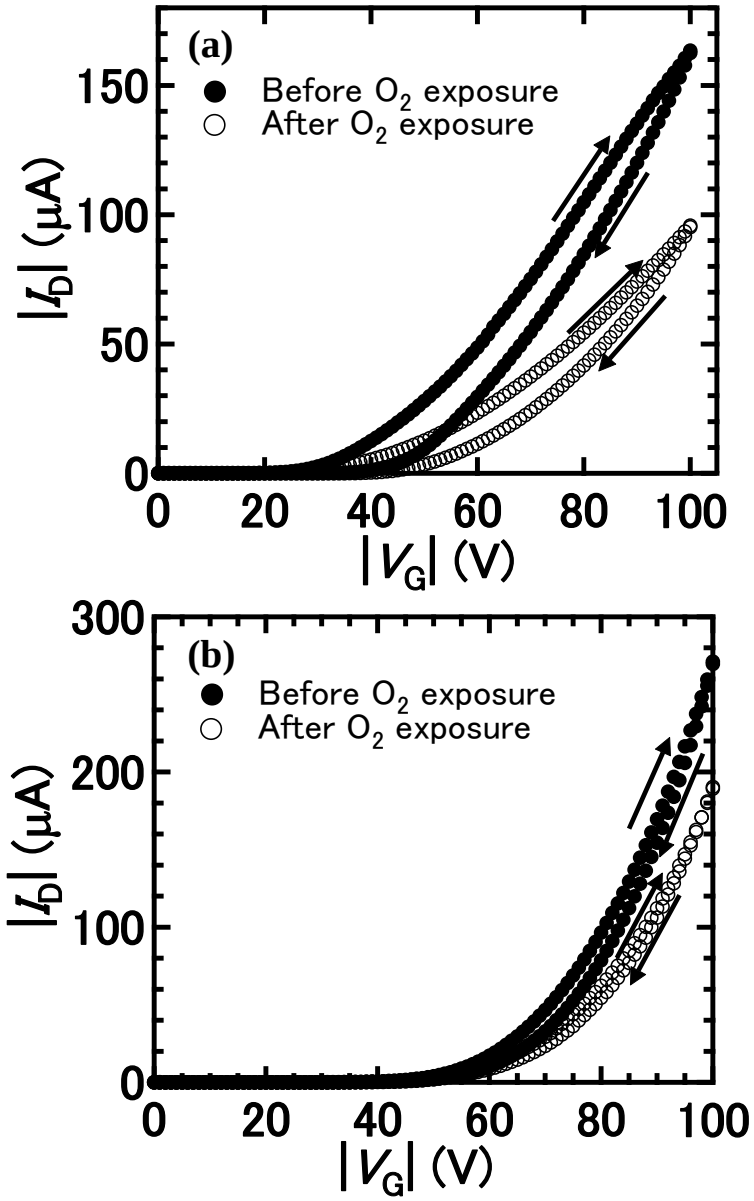

Figure 9-5. (a) Transfer curves for [6]phenacene single crystal FET before and after O_2 exposure. (b) Transfer curves for [7]phenacene single crystal FET before and after O_2 exposure.

Chapter 10. FET characteristics of [7]phenacene single crystal electric-double-layer (EDL) FETs

The high density accumulation of holes and electrons by field-effect may control physical properties of organic materials. Recently, the superconductivity is observed in inorganic materials such as $SrTiO_3$ [1], ZrNCl [2] and $KTaO_3$ [3] by an application of field-effect with electric-double-layer (EDL) capacitor. In other words, the superconductivity of two-dimensional materials is realised by fabricating their EDL FETs with ionic liquid gate dielectrics. Since electron accumulation into picene [4], phenanthrene [5] and DBP [6] solids by chemical doping with alkaline and alkaline-earth atoms can produce superconductivity, the superconducting transition may be expected by effective electron accumulation; actually the accumulation of three electrons per molecule is indispensable. The EDL FETs can provide many advantages from the point of view of an improvement of FET characteristics. The low voltage operation is expected because of a high capacitance of the EDL capacitor, *i.e.*, the effective high-carrier accumulation may be realised by an application of small bias voltage. Furthermore, high carrier accumulation may lower the contact resistance between single crystal and source / drain electrodes. We are also interested in the behaviour of μ value under high carrier accumulation or under high capacitance. The FET characteristics of [7]phenacene thin film FET were reported by our group [7]. In this case, the penetration of ions in ionic liquid into [7]phenacene thin films was observed, and the FET operation was not based on electrostatic but electrochemical process. In this study, we have used [7]phenacene single crystal for the EDL FETs. This should change the operation process because of a difficulty in ion penetration into the single crystal.

In this chapter, the author describes the characteristics of [7]phenacene single crystal EDL FETs using gel and sheet of ionic liquid gate dielectrics. This study aims for improvement of FET characteristics such as low-gate voltage operation and lowering of contact resistance. Also we have fully observed the FET operation processes in single crystal EDL FETs.

10-1. Introduction

Solid gate dielectrics such as SiO_2, Ta_2O_5 and HfO_2 have been extensively used as capacitor for organic FETs [8-16]. Except for this chapter, we used only solid gate dielectrics for the phenacene single crystal FETs. Owing to a small ε of SiO_2, the V_D and V_G required for device operation was too high. For solving this problem, in chapter 8, the FET characteristics of phenacene single crystal FETs with high-*k* gate dielectrics (Ta_2O_5 and HfO_2) have been studied. The usage of high-*k* gate dielectrics led to the lowering of V_D and V_G.

Another approach using ionic liquids as gate capacitor has recently attracted much interest from view of an improvement of FET performance of organic and polymer FETs [17-26] as well as high density carrier accumulation for control of physical properties of inorganic layered materials [1-3, 27-30]. The electric-double-layers (EDLs) are formed at the interfaces of electrode / ionic liquid and channel / ionic liquid when bias-voltage (V_G in FET device) is applied to ionic liquid, as seen from Figure 10-1. The ions with different charges can move each other towards opposite sides (the gate electrode and the channel), when the V_G is applied to the gate electrode. Finally, the ions are stabilised near the gate electrode and the channel (active layer of FET) which is called Helmholtz plane [31]; this plane produces EDL capacitor. The EDL is thin (typically ~ 1 nm) enough to result in the large capacitance. This EDL FET technique is useful also for inorganic semiconductors [1-3, 27-30]. Because of no penetration of ions in inorganic materials, this is understood as the electrostatic process.

In this chapter, we have investigated the FET characteristics of [7]phenacene EDL single crystal FET. The purpose of this study is to know the FET characteristics of EDL FET with single crystal of phenacene-type molecule. The device structure is shown in Figure 10-2. The low-voltage operation or a low-contact resistance is expected in the EDL FET. Two ionic liquids, [1-butyl-3-methylimidazolium][hexafluorophosphate] (bmim[PF6]) and [1-ethyl-3-methylimidazolium]-[bis(trifluoromethylsulfonyl)imide] (emim[TFSI]) were used in this study. The chemical formulae of these ionic liquids are shown in Figure 10-3. Furthermore, two-types of capacitors with ionic liquid were

fabricated, *i.e.*, ionic liquid gel and ionic-liquid polymer-sheet. Here, it should be noticed that the penetration of ions into single crystal is absolutely ruled out for the ionic liquid sheet because the ions are confined in ionic liquid sheet. Therefore, the comparison of FET characteristics between gel and sheet is of interest because operation process may be different, *i.e.*, electrochemical for gel and electrostatic for sheet.

10-2. Experimental

The ionic liquid gel of bmim[PF6] was prepared by the method reported previously [32]. Details are as follows:

(1) Poly(styrene-*b*-ethylene oxide-*b*-styrene) [PS-PEO-PS] and bmim[PF6] were dissolved at weight ratio of 1 : 9 in CH_2Cl_2.

(2) The solution was stirred for 16 h at room temperature.

(3) The CH_2Cl_2 was removed by heating the solution at 343 K for 7 h under Ar atmosphere, and the ionic liquid gel was obtained.

The optical microscope image of a droplet of bmim[PF6] gel is shown in Figure 10-4.

The ionic-liquid polymer-sheet of emim[TFSI] was prepared by the method reported previously [33]. Details are as follows:

(1) 110 mg of poly (vinylidene fluorideco-hexafluoropropylene) (abbreviated as P(VDF-HFP)) was dissolved into 1.8 ml acetone at room temperature.

(2) The solution was stirrerred for 1 h at room temperature until a clear homogeneous solution was obtained.

(3) 500 mg emim[TFSI] was added into the above solution, and it was stirred for 2 h at room temperature.

(4) The ionic-liquid polymer-sheet was obtained by casting the solution on a Petri dish and evapourating the remaining acetone at room temperature for 24 h.

The photograph of ionic-liquid polymer-sheet is shown in Figure 10-5.

The Pt gate electrode was directly inserted into ionic liquid gel in [7]phencene single crystal FET as shown in Figure 10-6(a). On the other hand, the Pt electrode was contacted to ionic liquid sheet with two types of approaches. In the first approach, the Pt electrode was contacted directly to ionic liquid sheet, and in the second approach, the Pt electrode was contacted to the sheet through Au plate, as seen from Figures 10-6(b) and (c), respectively. 3 nm thick TCNQ was inserted into the space between single crystal and Au source / drain electrodes. The C_o of bmim[PF_6] was 9.7 μF cm^{-2}, while that of emim[TFSI] was also 9.7 μF cm^{-2}. The values were constant in gel and liquid sheet. All experimental setups are the same as that described in chapter 5, except for the facts that, the $|V_G| = |V_D| \leq 3$ V could be applied for the FET devices, owing to a chemical window of ionic liquids.

10-3. Results and Discussion

10-3-1. Characteristics of [7]phenacene single crystal FET with ionic liquid gels

Figures 10-7(a) and (b) show transfer and output curves in [7]phenacene single crystal FETs with ionic liquid gel of bmim[PF6] as a gate dielectric, exhibiting typical p-channel FET characteristics. The operation voltage is extremely low as expected from the high C_o. The high C_o originates from the formation of 1 nm thick EDL at the interface between the single crystals and the ionic liquid. The μ and $|V_{TH}|$ were determined to be 3.8×10^{-1} cm^2 V^{-1} s^{-1} and 2.3 V, respectively. The μ was lower by one order of magnitude than those (3.0 - 3.2 cm^2 V^{-1} s^{-1}) for the [7]phenacene single crystal FETs with high-*k* gate dielectrics, Ta_2O_5 (HfO_2) and TCNQ (F4TCNQ), studied for low-voltage operation (chapter 8). The $|V_{TH}|$ was smaller than 6.3 V in the [7]phenacene single crystal FET with Ta_2O_5 and TCNQ, and it was close to the value observed with HfO_2 and F4TCNQ ($|V_{th}|$ = 2.6 V). Thus, the operation voltage is significantly lowered in the [7]phenacene single crystal FET with an EDL capacitor.

The μ for the [7]phenacene EDL single crystal FET was higher by a factor of two than that, 1.8×10^{-1} cm^2 V^{-1} s^{-1}, reported on the picene single crystal EDL FET [14]; in

both FET devices, the same ionic liquid gate dielectric was used. Further, the μ value for the [7]phenacene single crystal EDL FET was slightly higher than that, 2.6×10^{-1} cm^2 V^{-1} s^{-1}, reported on the [7]phenacene thin film EDL FET [7], but no drastic change in FET performance was found by changing the active layer from thin film to single crystal.

As seen from Figure 10-7(b), linear output curves were observed in the low $|V_D|$ range without concave behaviour, indicating no hole-injection barrier between single crystal and source / drain electrodes, or the formation of Ohmic contact. Such an Ohmic contact between single crystal and source / drain electrodes was also observed in the picene single crystal EDL FET [14]. Thus, this can be interpreted by considering that high density of holes near the source / drain electrodes can reduce the depletion region producing the Schottky barrier between single crystal and source / drain electrodes. In chapter 7, we discussed the V_G dependence of $<\phi_h^{eff}>$ in [7]phenacene single crystal FET with F4TCNQ, showing a slow decrease in $<\phi_h^{eff}>$ with an increase in $|V_G|$ (Figure 7-7(b)). Therefore, in [7]phenacene single crystal with source / drain electrodes modified by electron acceptor, such a behaviour that potential barrier height is lowered by accumulation of holes in channel region is observed. Actually, the picene single crystal EDL FET even without the insertion of TCNQ did not show any concave behaviour in the low $|V_D|$ range [14]. Therefore, if a high density of holes are effectively accumulated near the electrodes by EDL capacitor, electron-acceptor molecules (or charge transfer molecules) such as TCNQ and F4TCNQ may not be required to reduce the hole-injection barrier height.

As described in the first part of this chapter, the accumulation of high density of holes or electrons by electrostatic effect may control physical properties of organic materials. As the superconductivity is actually induced in $SrTiO_3$, ZrNCl and $KTaO_3$ by the electrostatic carrier doping technique with EDL capacitors [1-3], the observation of superconducting transition may be observed even in phenacene single crystal EDL FETs because the superconductivity by chemical doping with alkali metal is found in picene [4], phenanthrene [5] and DBP [6]. Actually, three electrons per molecule are required for the emergence of superconductivity [4-6]. Presently, only holes are accumulated in [7]phenacene single crystal EDL FET. The mobile hole density is 4.2×10^{13} cm^{-2} and ~

0.11 per [7]phenacene molecule by replacing V_G in Eq. 8-2 by $|V_G|$ - $|V_{TH}|$, indicating that the accumulation of more holes is indispensable for the control of physical properties. Finally, we must consider the reason why the μ value in the [7]phenacene EDL single crystal FET is lower by one order of magnitude than those, ~ 3 $cm^2 V^{-1} s^{-1}$, with solid gate dielectrics. One suggestion is that the scattering of holes by PF_6^- ions in bmim[PF6] may suppress smooth hole transport, as has been discussed for graphene transistors with liquid gate dielectrics [34].

10-3-2. Characteristics of [7]phenacene single crystal EDL FET with ionic - liquid polymer-sheet

Figures 10-8(a) and (b) show transfer and output curves of [7]phenacene single crystal EDL FET using emim[TFSI] polymer-sheet as the gate dielectric, which provide typical p-channel FET characteristics. In this measurement, the Pt gate electrode was directly contacted to polymer-sheet. The μ and $|V_{TH}|$ were determined to be 3.8×10^{-2} $cm^2 V^{-1} s^{-1}$ and 2.8 V, respectively. The μ is lower by one order of magnitude than that, 3.8×10^{-1} $cm^2 V^{-1} s^{-1}$, for the [7]phenacene single crystal EDL FET with bmim[PF6] gel as a gate dielectric. The $|V_{TH}|$ was slightly higher than, 2.3 V, in the [7]phenacene EDL FET with bmim[PF6] gel. As seen from the output curves shown in Figure 10-8(b), a large hysteresis is still observed together with a concave behaviour in low $|V_D|$ range.

To improve the FET characteristics, 100 μm thick Au plate was placed on the polymer-sheet and Pt gate electrode was contacted to the Au plate, as shown in Figure 10-6(c). The application of V_G through Au plate may enable ones to produce a homogeneous carrier accumulation in channel region. Figures 10-9(a) and (b) show transfer and output curves of [7]phenacene single crystal EDL FET with emim[TFSI] polymer-sheet, in which the V_G is applied through Au plate. The μ and $|V_{TH}|$ were determined to be 1.4×10^{-1} $cm^2 V^{-1} s^{-1}$ and 2.0 V, respectively. The μ value rapidly increases from 3.8×10^{-2} $cm^2 V^{-1} s^{-1}$ recorded in direct contact of Pt electrode to polymer-sheet. The $|V_{TH}|$ also reduces to 2.0 V from 2.8 V in direct contact. As seen from the output curves (Figure 10-9(b)), the concave behaviour disappears in low $|V_D|$ region.

The μ value is still lower than that, 3.8×10^{-1} cm^2 V^{-1} s^{-1}, for EDL FET with bmim[PF6] gel. Comparison of the FET characteristics between gel and polymer-sheet using the same ionic liquid have not yet been performed. Therefore, it is unclear whether the difference in μ value can be assigned to that between gel and polymer-sheet; the difference in ionic liquids may cause the difference in μ. The usage of polymer-sheet should provide an advantage to know the operation process because the possibility of electrochemical doping can be ruled out. Therefore, we have to advance the study on FET characteristics of [7]phenacene single crystal FET with ionic-liquid polymer-sheet. This is now in progress.

10-4. Conclusion

The low-voltage operation in [7]phenacene single crystal FETs has been achieved with ionic liquid gate dielectrics. The $|V_{TH}|$ was lower than those with high-k gate dielectrics. Furthermore, the FET characteristics in [7]phenacene single crystal FETs with ionic liquid gel and polymer-sheet have been compared and discussed. The μ in [7]phenacene single crystal FET with polymer-sheet was still lower than that with ionic liquid gel although the polymer-sheet should provide a merit that the electrochemical process is excluded. However, the study should be further developed since we have never investigated the difference in FET characteristics between gel and sheet using the same ionic liquid. To control physical properties, more carriers than the present density must be accumulated. If possible, the accumulation of electrons is necessary because only electron donation to hydrocarbon molecules produces the superconductivity [4-6].

References

[1] K. Ueno, S. Nakamura, H. Shimotani, A. Ohtomo, N. Kimura, T. Nojima, H. Aoki, Y. Iwasa, and M. Kawasaki. Nature Mater. **7**, 855 (2008).

[2] J. T. Ye, S. Inoue, K. Kobayashi, Y. Kasahara, H. T. Yuan, H. Shimotani, and Y. Iwasa, Nature Mater. **9**,125 (2010).

[3] K. Ueno, S. Nakamura, H. Shimotani, H. T. Yuan, N. Kimura, T. Nojima, H. Aoki, Y. Iwasa, and M. Kawasaki, Nature Nanotech. **6**, 408 (2011).

[4] R. Mitsuhashi, Y. Suzuki, Y. Yamanari, H. Mitamura, T. Kambe, N. Ikeda, H. Okamoto, A. Fujiwara, M. Yamaji, N. Kawasaki, Y. Maniwa, and Y. Kubozono, Nature **464**, 76 (2010).

[5] X. F. Wang, R. H. Liu, Z. Gui, Y. L. Xie, Y. J. Yan, J. J. Ying, X. G. Luo, and X. H. Chen, Nature Commun. **2**, 507 (2011).

[6] M. Xue, T. Cao, D. Wang, Y. Wu, H. Yang, X. Dong, J. He, F. Li, and G. F. Chen, Sci. Rep. **2**, 389 (2012).

[7] Y. Sugawara, Y. Kaji, K. Ogawa, R. Eguchi, S. Oikawa, H. Gohda, A. Fujiwara, and Y. Kubozono, Appl. Phys. Lett. **98**, 013303 (2011).

[8] R. W. I. de Boer, M. E. Gershenson, A. F. Morpurgo, and V. Podzorov, Phys. Stat. Sol. A **201**, 1302 (2004).

[9] A. Facchetti, M. -H. Yoon, and T. J. Marks, Adv. Mater. **17**, 1705 (2005).

[10] M. Halik, H. Klauk, U. Zschieschang, G. Schmid, C. Dehm, M. Schütz, S. Maisch, F. Effenberger, M. Brunnbauer, and F. Stellacci, Nature **431**, 963 (2004).

[11] Y. Kubozono, T. Nagano, Y. Haruyama, E. Kuwahara, T. Takayanagi, K. Ochi, and A. Fujiwara, Appl. Phys. Lett. **87**, 143506 (2005).

[12] G. D. Wilk and R. M. Wallace, Appl. Phys. Lett. **76**, 112 (2000).

[13] G. D. Wilk and R. M. Wallace, Appl. Phys. Lett. **74**, 2854 (1999).

[14] N. Kawai, R. Eguchi, H. Goto, K. Akaike, Y. Kaji, T. Kambe, A. Fujiwara, and Y. Kubozono, J. Phys. Chem. C **116**, 7983(2012).

[15] R. P. Ortiz, A. Facchetti, and T. J. Marks, Chem. Rev. **110**, 205 (2010).

[16] A. Facchetti, M. -H. Yoon, and T. J. Marks, Adv. Mater. **17**, 1705 (2005).

[17] W. Lu, A. G. Fadeev, B. Qi, E. Smela, B. R. Mattes, J. Ding, G. M. Spinks, J. Mazurkiewicz, D. Zhou, G. G. Wallace, D. R. MacFarlane, S. A. Forsyth, and M. Forsyth, Science **297**, 983(2002).

[18] Z. Wu, Z. Chen, X. Du, J. M. Logan, J. Sippel, M. Nikolou, K. Kamaras, J. R. Reynolds, D. B. Tanner, A. F. Hebard, and A. G. Rinzler, Science **305**, 1273 (2004).

[19] J. Takeya, K. Yamada, K. Hara, K. Shigeto, K. Tsukagoshi, S. Ikehata, and Y. Aoyagi, Appl. Phys. Lett. **88**, 112102 (2006).

[20] T. Uemura, M. Yamagishi, S. Ono, and J. Takeya, Appl. Phys. Lett. **95**, 103301 (2009).

[21] H. Shimotani, H. Asanuma, J. Takeya, and Y. Iwasa, Appl. Phys. Lett. **89**, 203501 (2006).

[22] M. J. Panzer and C. D. Frisbie, Adv. Mater. **20**, 3177 (2008).

[23] J. Lee, M. J. Panzer, Y. He, T. P. Lodge, and C. D. Frisbie, J. Am. Chem. Soc. **129**, 4532 (2007).

[24] J. H. Cho, J. Lee, Y. He, B. Kim, T. P. Lodge, and C. D. Frisbie, Adv. Mater. **20**, 686 (2008).

[25] N. Komura, H. Goto, X. He, H. Mitamura, R. Eguchi, Y. Kaji, H. Okamoto, Y. Sugawara, S. Gohda, K. Sato, and Y. Kubozono, Appl. Phys. Lett. **101**, 083301 (2012).

[26] T. Fujimoto and K. Awaga, Phys.Chem. Chem. Phys. **15**, 8983 (2013).

[27] M. Krüger, M. R. Buitelaar, T. Nussbaumer, C. Schönenberger, and L. Forró, Appl. Phys. Lett. **78**, 1291(2001).

[28] H. Shimotani, T. Kanbara, Y. Iwasa, K. Tsukagoshi, Y. Aoyagi, and H. Kataura, Appl. Phys. Lett. **88**, 073104 (2006).

[29] H. Shimotani, G. Diguet, and Y. Iwasa, Appl. Phys. Lett. **86**, 022104 (2005).

[30] R. Eguchi, M. Senda, E. Uesugi, H. Goto, T. Kambe, T. Noji, Y. Koike, A. Fujiwara, and Y. Kubozono. Appl. Phys. Lett. **102**, 103506 (2013).

[31] R. Kötz and M. Carlen, Electrochim. Acta **45**, 2483 (2000).

[32] Y. Kaji, K. Ogawa, R. Eguchi, H. Goto, Y. Sugawara, T. Kambe, K. Akaike, S. Gohda, A. Fujiwara, and Y. Kubozono, Org. Electron. **12**, 2076 (2011).

[33] J. C. Jansen, K. Friess, G. Clarizia, J. Schauer, and P. Izák, Macromolecules **44**, 39 (2011).

[34] A. Das, S. Pisana, B. Chakraborty, S. Piscanec, S. K. Saha, U. V. Waghmare, K. S. Novoselov, H. R. Krishinamurthy, A. K. Geim, A. C. Ferrari, and A. K. Sood, Narure Nanotech. **3**, 210 (2008).

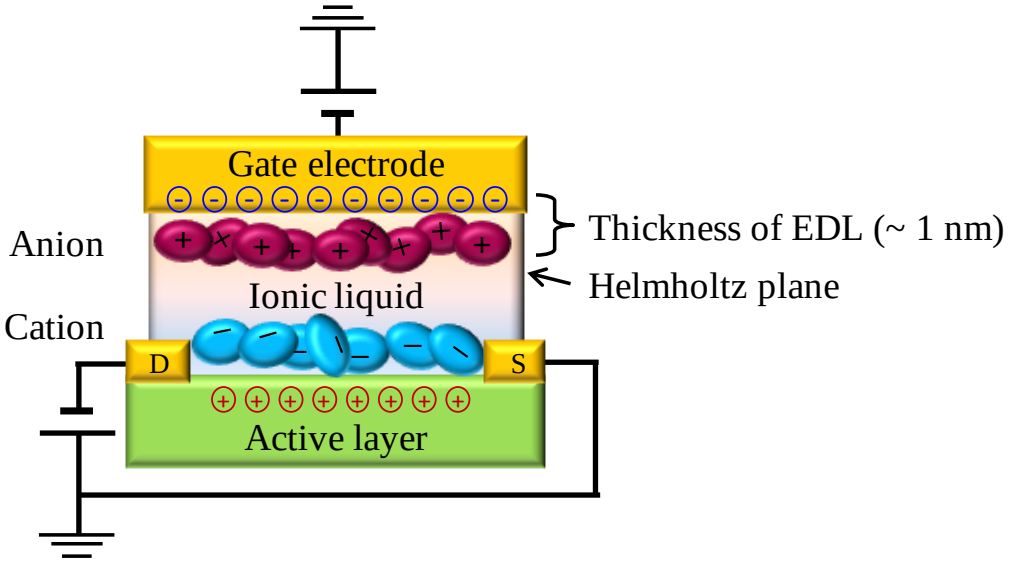

Figure 10-1. Schematic of an EDL capacitor using an ionic liquid. In this schematic, the negative gate voltage is applied to ionic liquid.

.

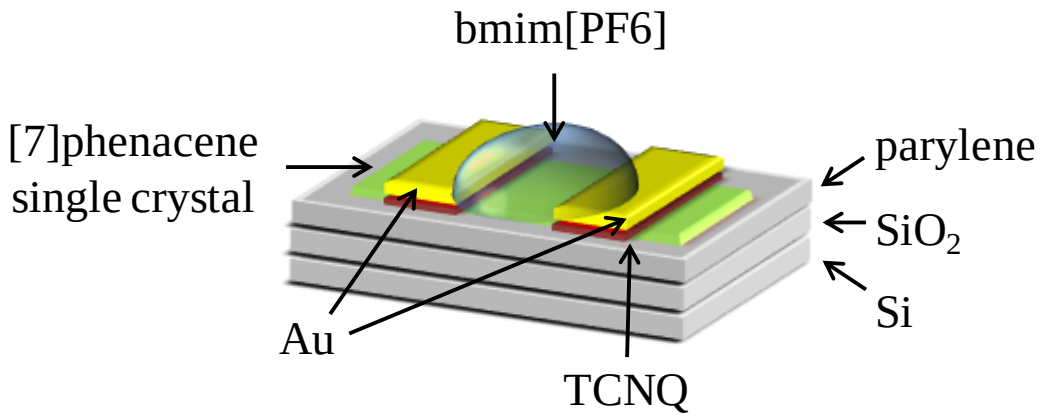

Figure 10-2. Device structure of a [7]phenacene single crystal EDL FET with bmim[PF6] as a gate dielectric.

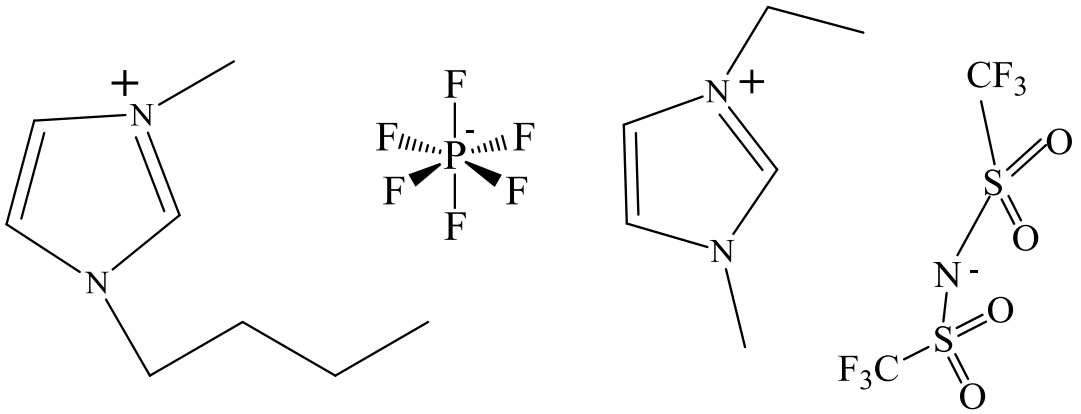

Figure 10-3. Molecular structures of bmim[PF6] and emim[TFSI].

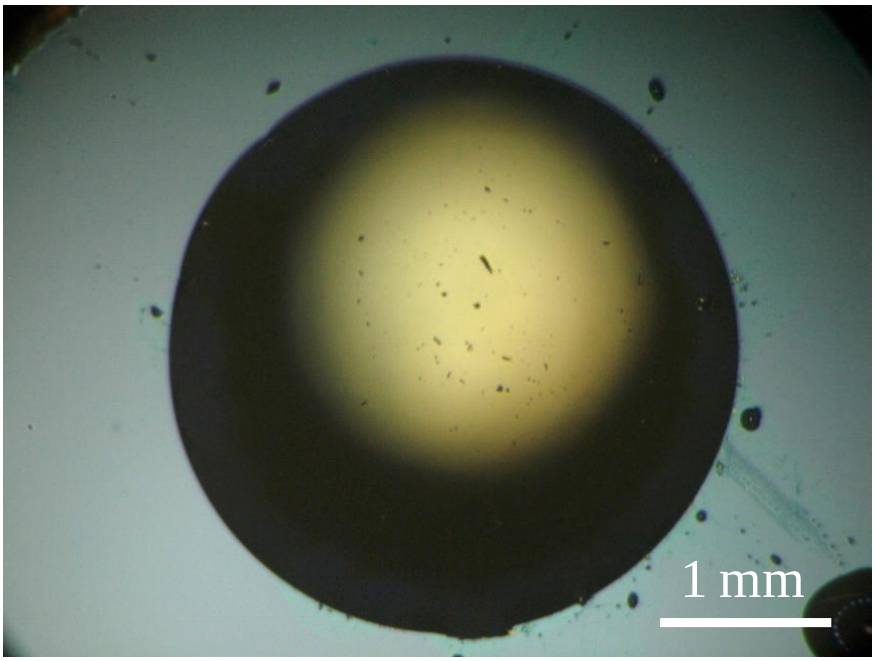

Figure 10-4. Optical microscope image of a droplet of bmim[PF6] gel on a SiO_2 / Si substrate.

Figure 10-5. Photograph of emim[TFSI] ionic liquid polymer sheet.

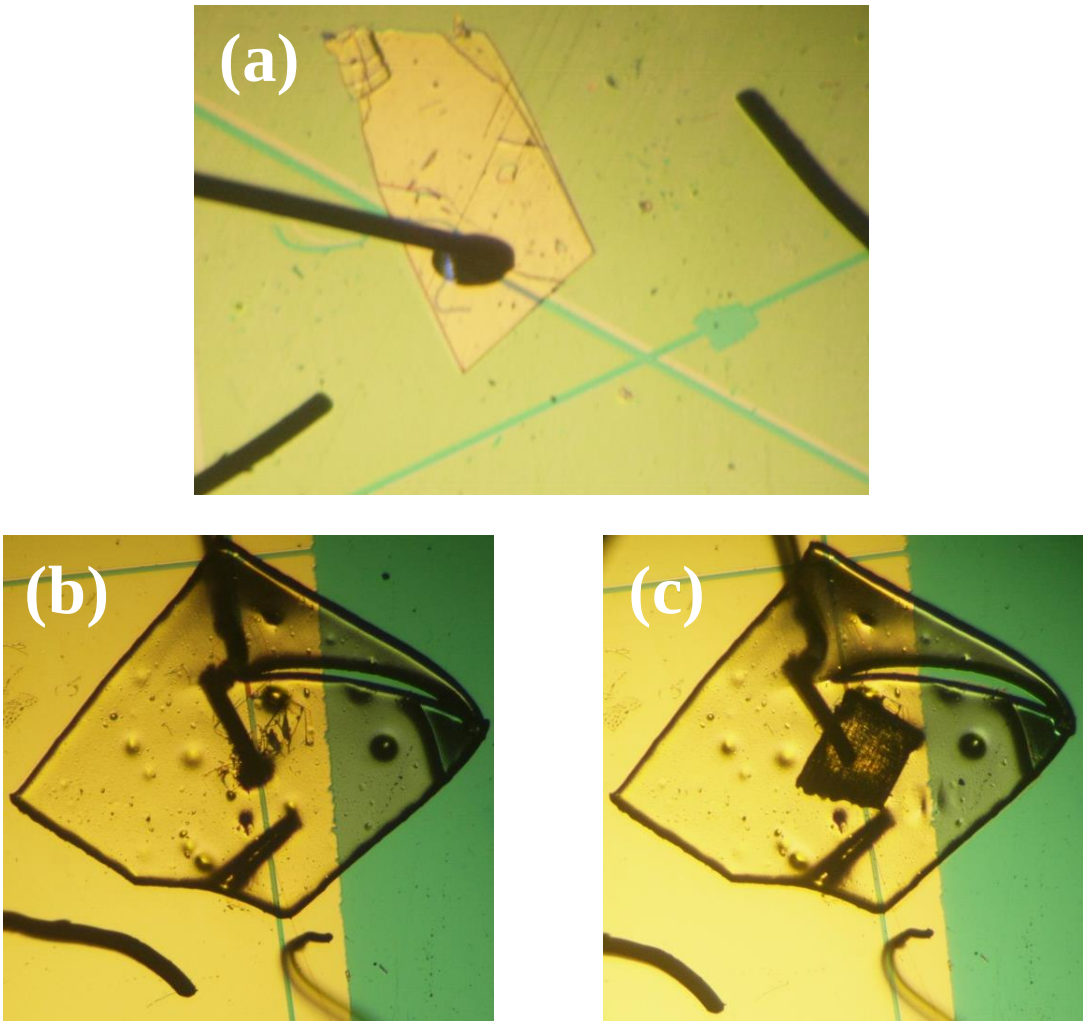

Figure 10-6. Optical microscope images of [7]phenacene single crystal EDL FET. (a) The Pt gate electrode is directly inserted into ionic liquid gel. (b) The Pt gate electrode is directly contacted to the emim[TFSI] sheet. (c) The Pt gate electrode is contacted to Au plate on the emim[TFSI] sheet.

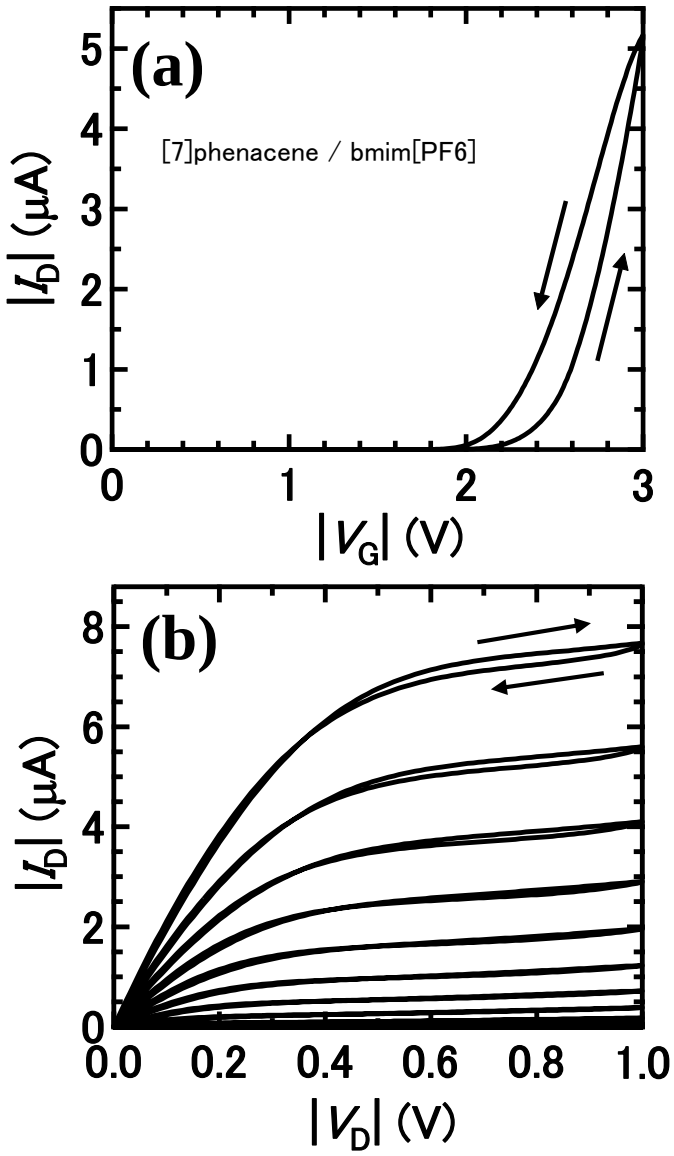

Figure 10-7. (a) Transfer and (b) output curves of [7]phenacene single crystal EDL FET with bmim[PF6] as a gate dielectric.

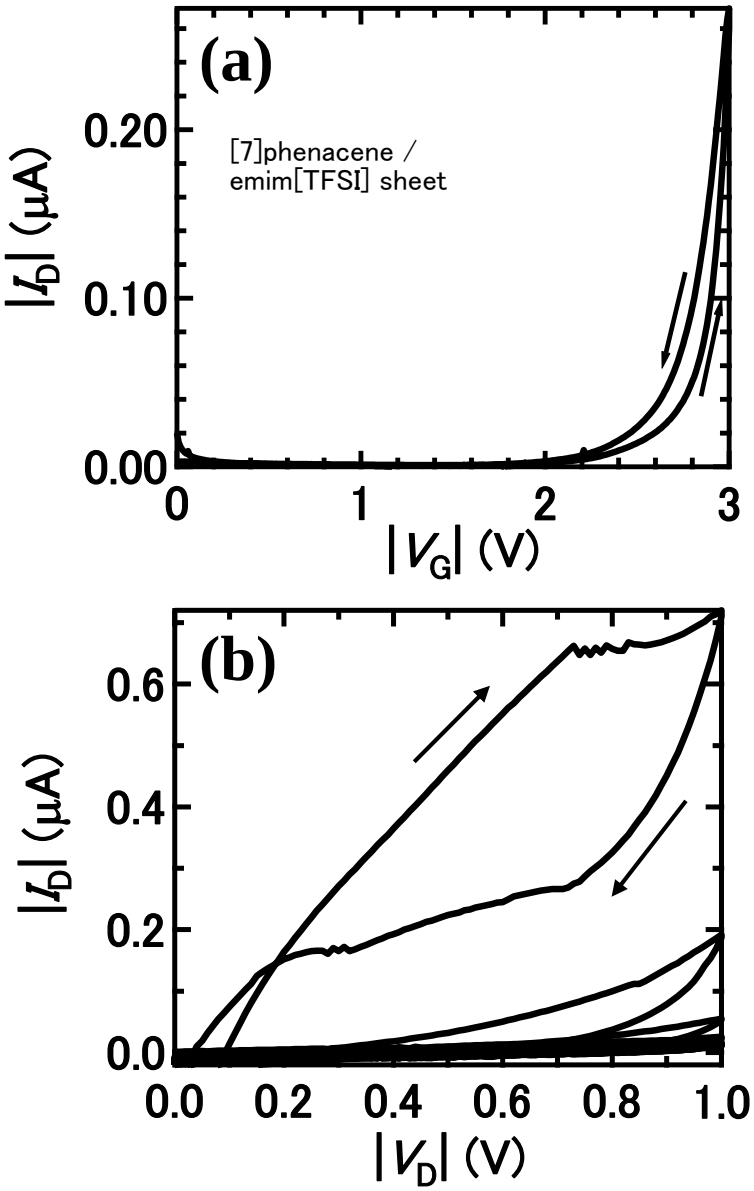

Figure 10-8. (a) Transfer and (b) output curves of [7]phenacene single crystal EDL FET with emim[TFSI] sheet as a gate dielectric.

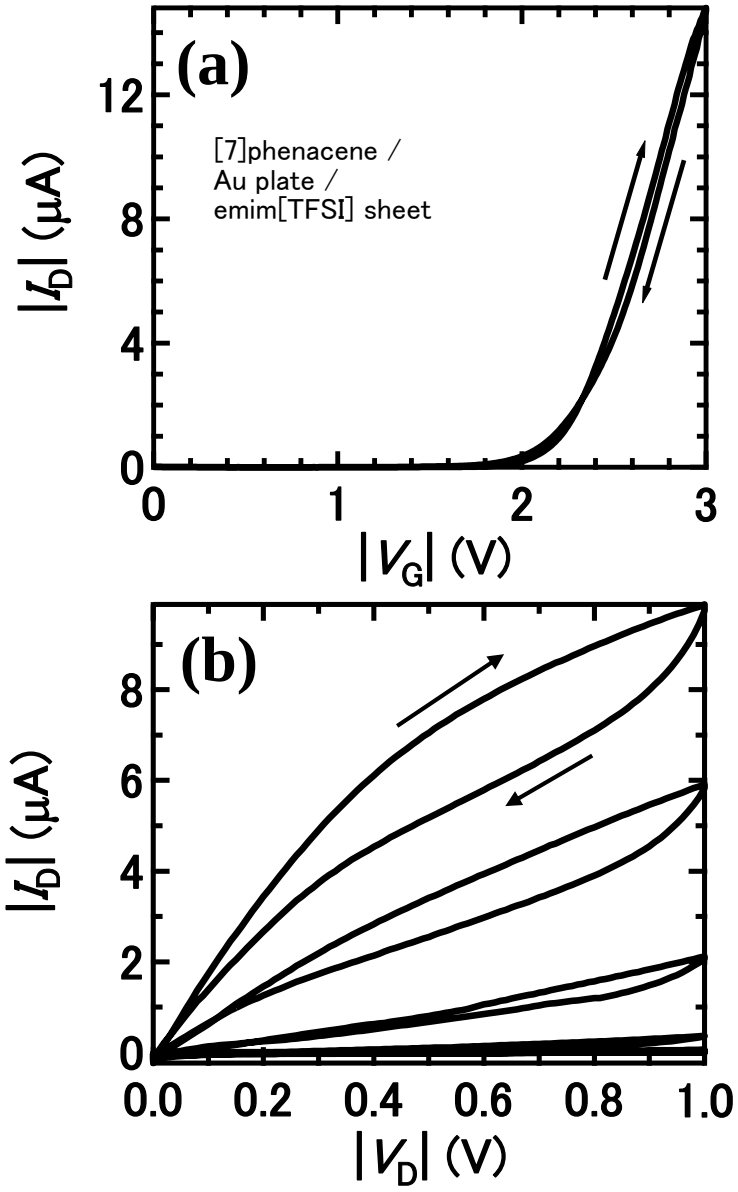

Figure 10-9. (a) Transfer and (b) output curves of [7]phenacene single crystal EDL FET with emim[TFSI] sheet as a gate dielectric. The Pt gate electrode is contacted to Au plate that is put on the surface of emim[TFSI] sheet.

Chapter 11. Temperature dependence of FET characteristics in [7]phenacene single crystal FETs

The fundamental FET characteristics of phenacene single crystal FETs were described in chapters 5 - 10. However, the transport mechanism has not yet been discussed in phenacene single crystal FET. In chapter 11, the author describes on the transport mechanism in [7]phenacene single crystal FET, *i.e.*, the channel conduction in single FET is clarified. In order to elucidate the transport mechanism, the temperature dependence of channel transport is investigated for [7]phenacene single crystal FETs. From the temperature dependence of the FET parameters (μ and $|I_D|$), the fundamental transport mechanism can be well understood, *i.e.*, band transport or hopping transport. In the band transport, the μ should increase with decreasing temperature owing to a decrease of scattering of the charge carriers by phonons, while in the hopping transport, the μ decreases with decreasing temperature owing to the thermally activated charge carriers. In this chapter, she discusses the transport mechanism based on the temperature dependence of the μ in [7]phenacene single crystal FET.

11-1. Introduction

Organic FETs have attracted much attention from technological as well as scientific perspectives [1-5]. The μ values reported in the rubrene single crystal FETs are as high as 18 $cm^2\ V^{-1}\ s^{-1}$ in the two-terminal measurement mode and 40 $cm^2\ V^{-1}\ s^{-1}$ in the four terminal measurement mode [6]. Clarifying the transport mechanism of carriers in organic single crystal FETs showing such a high μ value is an interesting research issue. The inorganic semiconductors show that the μ increases with decreasing temperature, *i.e.*, the μ - T plot follows the relation, $\mu \propto T^{-1.5}$ [7], because the scattering of the charge carriers by thermal phonons should be suppressed with a decrease in temperature. The transport implies band transport that carriers moves in band. At very low temperature, the scattering of the charge carriers by ionized impurities may affect the μ, resulting in a decrease in μ with decreasing temperature, which follows the relation, $\mu \propto T^{1.5}$ [7]. In

highly purified organic single crystals, the typical temperature dependence of μ shows a similar behaviour to that in inorganic semiconductors described above [8].

The charge carriers are localised on the molecules / atoms in disordered solids such as organic thin films. Such charge carriers can be thermally jumped among the localised states. In this case, the μ decreases with decreasing temperature. The μ - T plot follows Arrhenius-like relationship, $\mu \propto \exp(-\frac{E_A}{k_B T})$, where E_A is the activation energy that corresponds to the potential barrier height between the discrete trap states. The μ - T plots which could be fitted by Arrhenius model were reported for the thin film FETs with N,N'-dipentyl-3,4,9,10-perylene tetracarboxylic dimide [9], poly(9,9-dioctylfluorene-*co*-bithiophene) [10] and cobalt-phthalocyanine [11].

On the other hand, the intermediate hopping mechanism that carriers are captured by trap states and released to the band responsible for carrier transport was presented. This is named as 'multiple shallow trap and release (MTR) model' [12-15]. The expression for hole transport based on MTR model is given by $\mu \propto \frac{1}{1+\frac{N_t}{N_V} exp\frac{(\varepsilon_t - \varepsilon_v)}{k_B T}}$ where N_t, N_v, ε_t and ε_v refer to total DOS for shallow trap states, total effective DOS of valence band, energy level of trap states and edge energy of valence band. The $\varepsilon_t - \varepsilon_v$ corresponds to trap depth. The temperature dependence of μ in picene and [6]phenacene thin film FETs was well fitted by MTR model [16,17].

We have measured FET characteristics for [7]phenacene single crystal FET with SiO_2 gate dielectric in a temperature range of 20 - 300 K. The μ values obtained from the transfer curves showed different temperature dependences in two temperature ranges. From the temperature dependences, the transport mechanism is fully discussed.

11-2. Experimental

The temperature-dependent FET characteristics were measured for [7]phenacene single crystal FET with 400 nm thick SiO_2 gate dielectric (C_o = 9.1 nF cm^{-2}), in which 3 nm thick F4TCNQ was inserted into the space between single crystal and source / drain

electrodes. The surface of SiO_2 was coated with 30 nm thick parylene. Device fabrication process is the same as that described in chapter 5. The temperature-dependent measurements were carried out using a vacuum micro-probe / chamber system equipped with a liquid He flow cryostat; the transport properties were measured in two-terminal measurement mode. The values of μ, $|V_{TH}|$ and $|I_D|^{max}$ were determined from the transfer curve at V_G = –100 V at each temperature. The measurement system was the same as that described in chapter 5.

11-3. Results and Discussion

Typical transfer curves measured at 300 K and 20 K are shown in Figures 11-1(a) and (b), respectively. The values of μ and $|V_{TH}|$ at 300 K were determined to be 5.9 cm^2 V^{-1} s^{-1} and 19 V, respectively (Figure 11-1(a)), while those at 20 K are 3.4 cm^2 V^{-1} s^{-1} and 67 V, respectively (Figure 11-1(b)). The μ value decreases and the $|V_{TH}|$ increases at 20 K, compared with those at 300 K. The hysteresis of the transfer curves at 20 K is smaller than that at 300 K, indicating that the trap density in the device would be low at low temperature. In order to compare the behaviours of hysteresis at various temperatures, the transfer curves measured at some temperatures are plotted in Figure 11-2. The hysteresis gradually decreases with decreasing temperature. In particular, the hysteresis is hardly observed at 200 K. With a further decrease in temperature from 200 K, the hysteresis slightly increases, but the hysteresis at 20 K is still smaller than that measured at 300 K. Another point to be seen from Figure 11-2 is that the $|I_D|^{max}$ gradually decreases with decreasing temperature. The temperature dependence of the $|I_D|^{max}$ is discussed later.

In order to elucidate the transport mechanism in [7]phenacene single crystal FET, the μ value was determined from the transfer curve measured at each temperature. The μ - T plot is shown in Figure 11-3(a). The temperature dependence of μ can be categorized into two behaviours. In range 1 (170 - 300 K), the μ increases with decreasing temperature. This behaviour corresponds to the band-like transport that the μ increases with decreasing temperature. The μ shows the maximum μ value (8.8 cm^2 V^{-1} s^{-1}) at 130

K; the transfer curves at 130 K is shown in Figure 11-3(b).

In range 2 (20 - 90 K), a decrease in μ is observed with decreasing temperature. This behaviour may be attributed to impurity scattering (scattering by ionized impurities). Similar temperature dependence of μ is observed in FETs with single crystals of anthracene [18], tetracene [19] and pentacene [20].This is discussed later.

In order to clarify the temperature dependence of μ in range 1, the plots of μ are fitted with expression, $\mu = AT^{\alpha}$, as shown in Figure 11-4. The experimental μ - T plot could be fitted with the simple relation, $\mu = AT^{-0.5}$. In the ideal band-transport, the μ follows the expression, $\mu = AT^{-1.5}$. The α of –0.5 determined for μ - T plot in [7]phenacene single crystal FET deviates from the ideal case (α = –1.5). Nevertheless, the transport mechanism in [7]phenacene single crystal can be regarded as a band-transport like in range 1.

The experimental μ - T plot in range 2 (the decrease in μ when decreasing temperature) can be concluded to be governed by impurity scattering. In order to check the presence of contact resistance, the output curves were measured at 300 K and 20 K (Figures 11-5(a) and (b)). The output curves at 20 K show large concave behaviors at $|V_D|$ range in comparison with those at 300 K, indicating the presence of large contact resistance at low temperatures, regardless of an interface modification with F4TCNQ. This implies that the suppression of μ by contact resistance also affect to the μ - T plot observed in range 2. The further study should be made for the clarification of impurity scattering in low temperature range.

The temperature dependence of $|V_{TH}|$ and $|I_D|^{max}$ are shown in Figures 11-6(a) and (b). The $|V_{TH}|$ increases with decreasing temperature. The carriers are thermally activated to trap states (inter-band states) at high temperature. If it is the case, the $|V_{TH}|$ may decrease when increasing temperature, because the $|V_G|$ required for filling the trap states (*i.e.*, $|V_{TH}|$) should become smaller. On the other hand, the $|I_D|^{max}$ monotonously decreases with decreasing temperature, as shown in Figure 11-6(b). The I_D in saturation range is given by $I_D = \mu C_{ox} W \frac{1}{L} \frac{(V_G - V_{TH})^2}{2}$, which is shown in Eq. 4-8 . Therefore, the $|I_D|^{max}$ is

proportional to $\mu \times (V_G - V_{TH})^2$. From the experimental results (Figure 11-3), the μ increases or decreases with an increase in temperature, while the $|V_{TH}|$ monotonously decreases with an increase in temperature, causing an increase in $(V_G - V_{TH})^2$. As seen from the numerical calculation with the μ - T plot (Figure 11-3(a)) and the $|V_{TH}|$ - T plot (Figure 11-6(a)), the $|I_D|^{max}$ drastically increases with an increase in temperature, in consistent with the experimental $|I_D|^{max}$ - T plot (Figure 11-6(b)).

11-4. Conclusion

In this chapter, we have investigated temperature dependence of μ in [7]phenacene single crystal FET in a temperature range of 20 - 300 K. The temperature dependence showed band transport-like behavior. Namely, the thermal phonon governs the transport in high temperature, and impurity scattering governs the transport in low temperature. Here, we could not rule out the influence of contact resistance for the behaviour of μ in low temperature. The μ was as high as 5.9 $cm^2\ V^{-1}\ s^{-1}$ at 300 K, and the highest μ was 8.8 $cm^2\ V^{-1}\ s^{-1}$ at 130 K. The temperature dependence of $|V_{TH}|$ and $|I_D|^{max}$ may be reasonably explained. For more clear understanding of transport mechanism, the study on temperature dependence of FET characteristics with four-terminal measurement mode is now in progress.

References

[1] S. Hotta and K. Waragai, Adv. Mater. **5**, 896 (1993).

[2] C. D. Dimitrakopoulos, A. R. Brown, and A. Pomp, J. Appl. Phys. **80**, 2501 (1996).

[3] D. J. Gundlach, Y. Y. Lin, T. N. Jackson, S. F. Nelson, and D. G. Schlom, IEEE Electron Device Lett. **18**, 87 (1997).

[4] M. M.-Torrent and C. Rovira, Chem. Soc. Rev. **37**, 827 (2008).

[5] L. Li, P. Gao, M. Baumgarten, K. Müllen, N. Lu, H. Fuchs, and L. Chi, Adv Mater. **25**, 3419 (2013).

[6] J. Takeya, M. Yamagishi, Y. Tominari, R. Hirahara, Y. Nakazawa, T. Nishikawa, T. Kawase, T. Shimoda, and S. Ogawa, Appl. Phys. Lett. **90**, 102120 (2007).

[7] S. M. Sze, Semiconductor devices: physics and tecnology (John Wiley & Sons. Inc., Hoboken, 1985).

[8] M. Schwoerer, Organic Molecular Solids, (Wiley-VCH, Weinheim, 2007).

[9] R. J. Chesterfield, J. C. McKeen, C. R. Newman, C. D. Frisbie, P. C. Ewbank, K. R. Mann, and L. L. Miller, J. Appl. Phys. **95**, 6396 (2004).

[10] M. C. Hamilton, S. Martin, and J. Kanicki, Chem. Mater. **16**, 4699 (2004).

[11] S. Samanta, D. K. Aswal, A. Singh, A. K. Debnath, M. S. Kumar, Y. Hayakawa, S. K. Gupta, and J. V. Yakhmi, Appl. Phys. Lett. **96**, 013305 (2010).

[12] S. Terao, T. Hirai, N. Morita, H. Maeda, K. Kojima, and M. Tachibana, J. Appl. Phys. **108**, 124511 (2010).

[13] D. Knipp, R. A. Street, and A. R. Volkel, Appl. Phys. Lett. **82**, 3907 (2003).

[14] R. W. I. de Boer, M. Jochemsen, T. M. Klapwijk, A. F. Morpurgo, J. Niemax, A. K. Tripathi, and J. Pflaum, J. Appl. Phys. **95**, 1196 (2004).

[15] R. J. Chesterfield, J. C. Mckeen, C. R. Newman, P. C. Ewbank, D. A. da S. Filho, J.-L. Brédas, L. L. Miller, K. R. Mann, and C. D. Frisbie, J. Phys. Chem. B **108**, 19281 (2004).

[16] N. Kawasaki, Y. Kubozono, H. Okamoto, A. Fujiwara, and M. Yamaji, Appl. Phys. Lett. **94**, 043310 (2009).

[17] R. Eguchi, X. He, S. Hamao, H. Goto, H. Okamoto, S. Gohda, K. Sato, and Y. Kubozono, unpublished data.

[18] A. N. Aleshin, J. Y. Lee, S. W. Chu, J. S. Kim, and Y. W. Park, Appl. Phys. Lett. **84**, 5383 (2004).

[19] R. W. I. de Boer, T. M. Klapwijk, and A. F. Morpurgo, Appl. Phys. Lett. **83**, 4345 (2003).

[20] T. Minari, T. Nemoto, and S. Isoda, J. Appl. Phys. **99**, 034506 (2006).

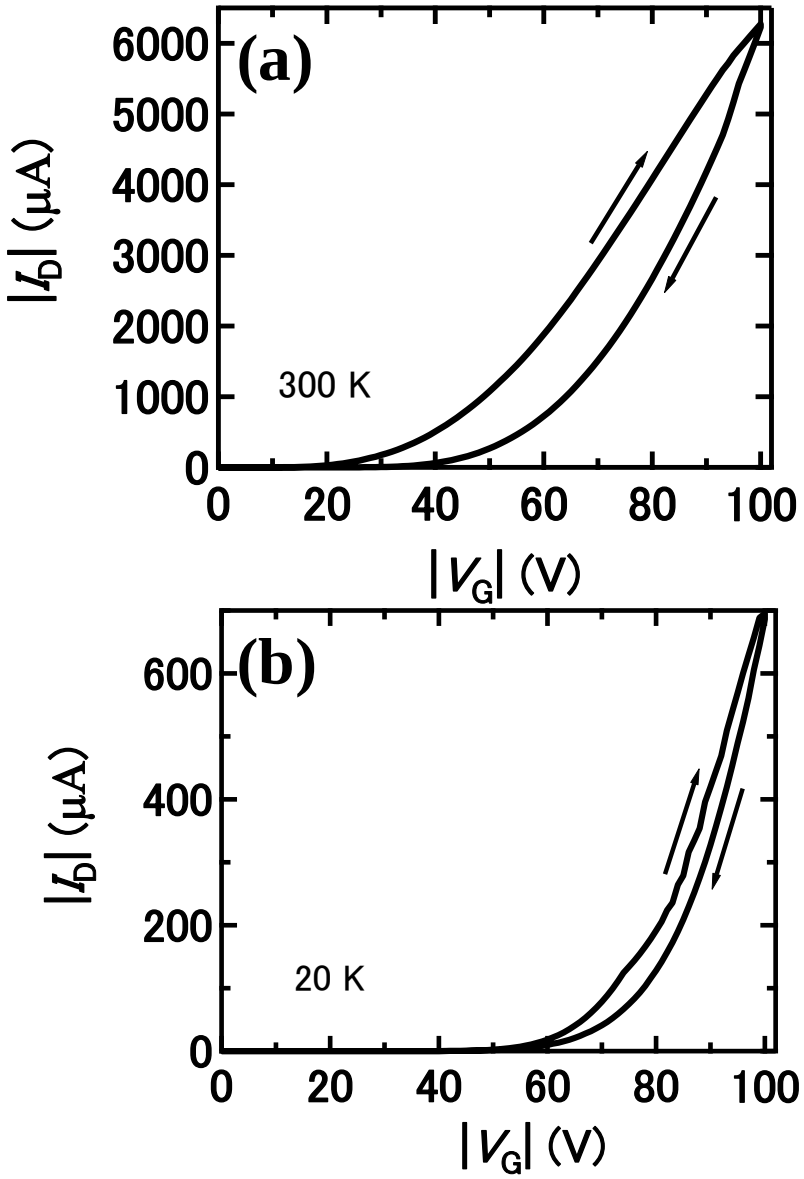

Figure 11-1. Transfer curves of [7]phenacene single crystal FET at (a) 300 K and (b) 20 K.

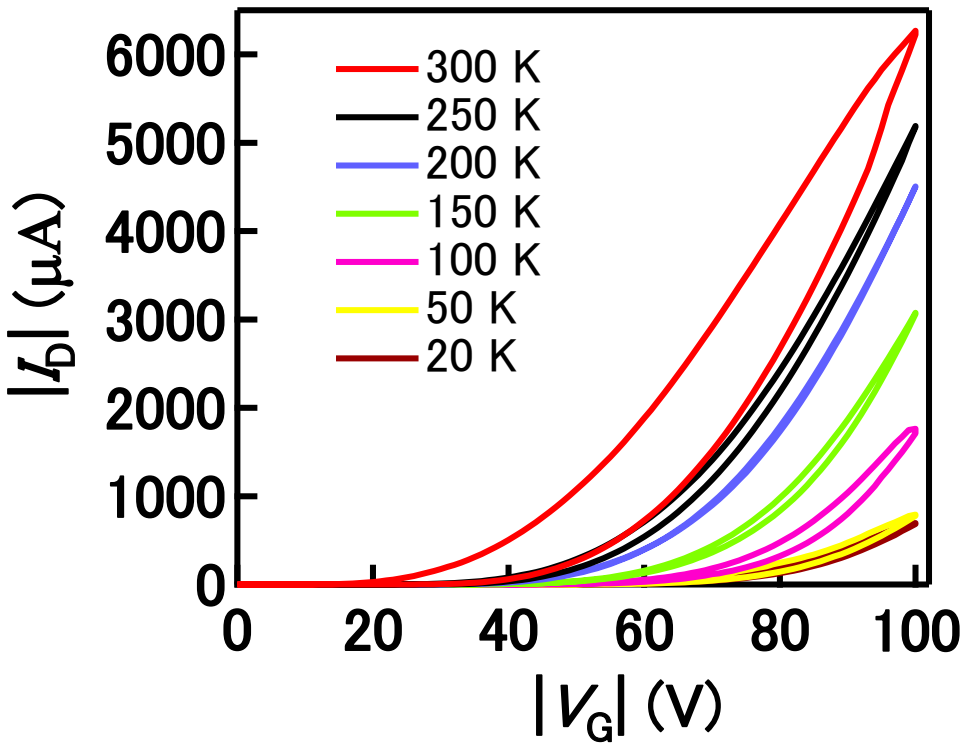

Figure 11-2. Transfer curves measured at different temperatures.

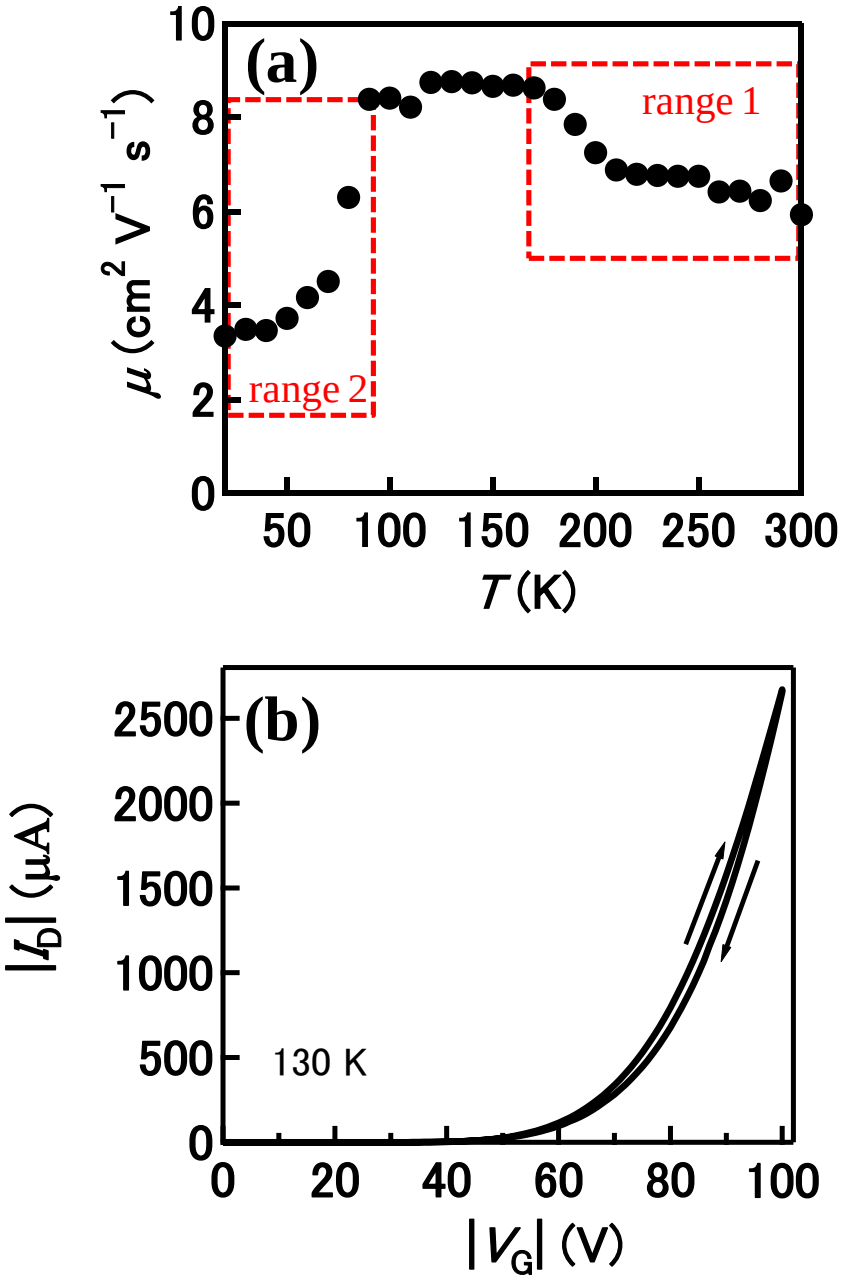

Figure 11-3. (a) Temperature dependence of μ in all temperature range from 300 K to 20 K. (b) Transfer curve of [7]phenacene single crystal FET at 130 K.

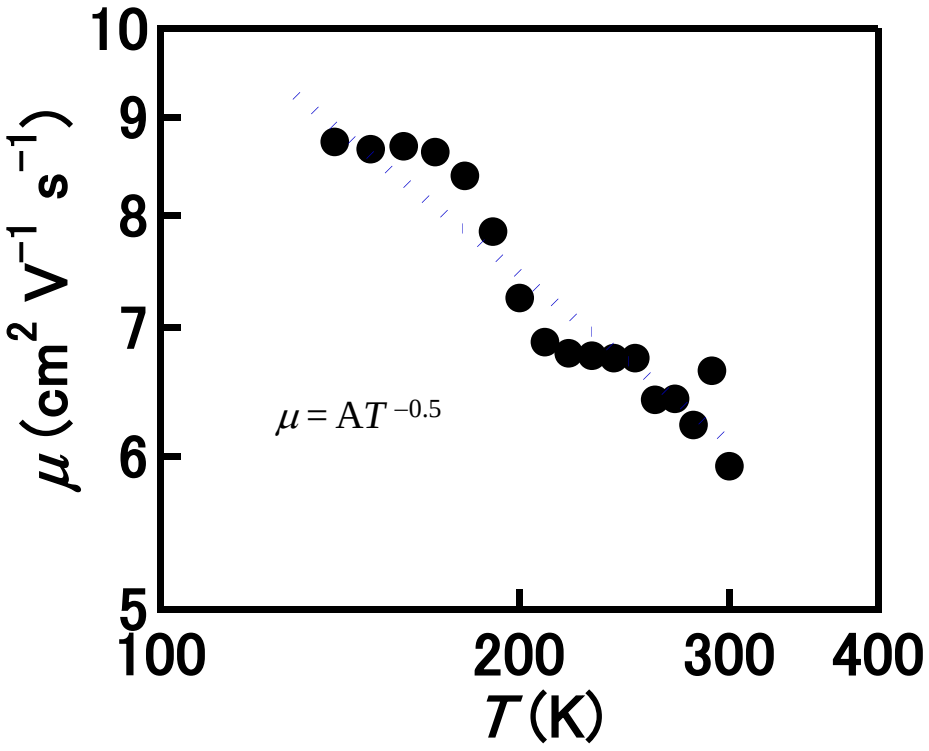

Figure 11-4. Temperature dependence of μ in range 1, which is fitted with the relation, $\mu = AT^{-0.5}$ (dotted line).

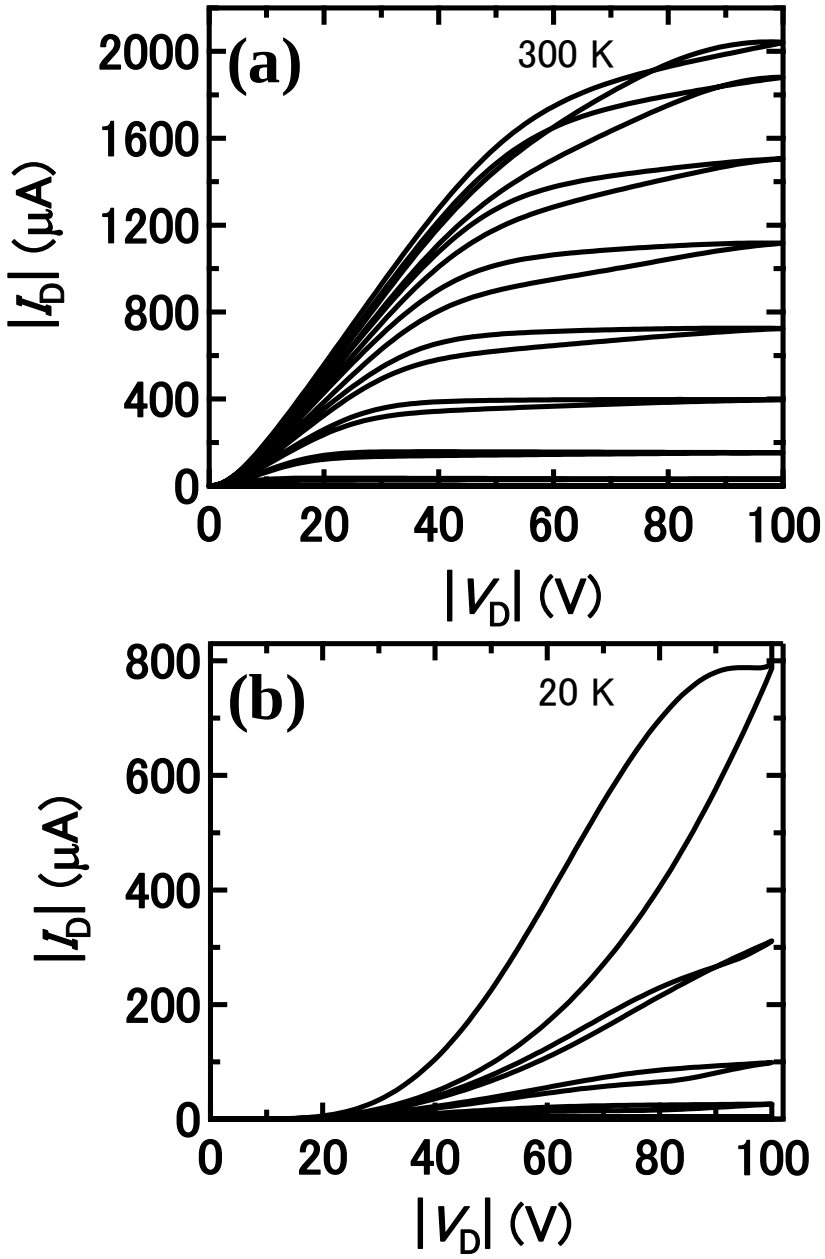

Figure 11-5. Output curves measured at (a) 300 K and (b) 20 K.

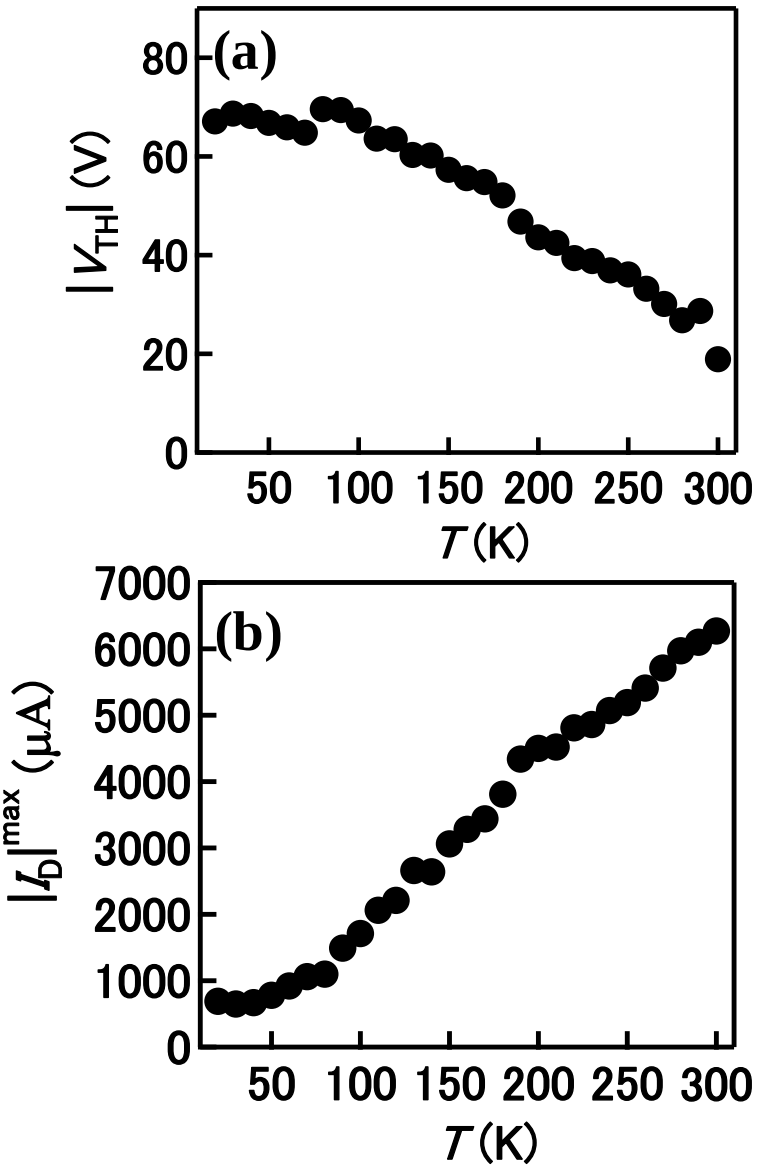

Figure 11-6. Temperature dependence of (a) $|V_{TH}|$ and (b) maximum of $|I_D|$.

Summary of FET work

Here, the author provides the summary of study on phenacene single crystal FETs. In this study, the FET properties of phenacene single crystal FETs are elucidated and the possible application of phenacene single crystal FETs towards future electronics are shown unambiguously. The details of her study are described in the following.

(1) Using the physical vapour transport method, we have succeeded in preparing high-quality single crystals of phenacene molecules. The optical microscope and AFM images clarified that the [7]phenacene single crystals possess wide and flat surfaces suitable for fabrication of FET devices. The crystal structures of phenacene molecules were determined with X-ray diffraction, and it is found that the stacking of *ab*-plane parallel to the substrate is formed, which is suitable for FET operation. The electronic structures of phenacene molecules were determined by photoelectron yield spectroscopy and optical absorption, and all phenacene molecules studied have the similar electronic structures to each other, with suitable for p-channel FET operation.

(2) Fundamental FET characteristics of phenacene single crystal FETs have been clarified, and an interface modification with electron donors / acceptors between single crystal and source / drain electrodes has been characterised in phenacene single crystal FETs. The FET properties are improved by the interface modification. Namely, it has been found that the concave behaviour in output curves disappears / reduces and the μ increases after modification. The potential barrier height between single crystal and source / drain electrodes is quantitatively evaluated based on double Schottky barrier model. The effect of electron acceptors / donors on potential barrier could be scaled by their redox potential. The relation between the FET parameters and redox potential has also been clarified. The maximum μ value in [7]phenacene single crystal FET reach 6.9 $cm^2\ V^{-1}\ s^{-1}$. The high-*k* gate dielectrics have been successfully applied to phenacene single crystal FETs to obtain low-voltage operation.

(3) The bias stress effect and O_2 gas-sensing properties investigated in phenacene single crystal FETs, and the bias stress effect is discussed based on the electric dipole of H_2O and formation of bias-induced trap states. In phenacene single crystal FETs, we have

never O_2 induced drain - current enhancement. Finally, we have tried to accumulate high density of holes into channel region of [7]phenacene single crystals FET with EDL gate capacitors, and the low-voltage operation is successfully achieved. The ionic liquid gel and ionic liquid sheets are successfully applied to [7]phenacene single crystal FET. In this study, the future perspective for a control of physical properties of phenacene crystals is also shown based on the evaluation of the accumulated carries.

(4) Temperature dependence of FET parameters in [7]phenacene single crystal FET has been fully investigated. It has shown that the band - transport is realised in the single crystal FET.

Through this study, the author has clarified potential application of phenacene molecules towards future practical FET devices. Moreover, she has unambiguously shown the significance of interface modification for a realisation high FET performance. In other words, the device modification can extract the potential ability of phenacene molecules for high-performance transistors. As a consequence, she can stress that her study on phenacene single crystal FETs will build up a new stage for fundamental physics and chemistry of FETs with phenacene molecules as well as an application of phenacene single crystal FETs towards future electronics.

Part 2

Chapter S-1. Introduction to superconducting metal-doped hydrocarbon solids

The author describes superconductivity of metal doped hydrocarbon solids in chapters S-1 and S-2. In chapter S-1, an introduction to newly discovered hydrocarbon superconductors is provided and the motivation of this study is clearly shown. The research on superconductivity of metal doped hydrocarbon solids closely relates to the transistor research with phenacene molecules reported in chapters 1 - 11. Namely, physics of carrier accumulation governs both the transistor operation and the superconductivity. However, the amount of accumulated carriers is conclusively different between a transistor operation and an emergence of superconductivity. The density of carriers required for transistor operation is 0.01 - 0.1 per molecule, while that of carriers required for emergence of superconductivity may be 3 per molecule. Therefore, physics emerging in higher density of carrier accumulation than that in transistor study (chapters 1 - 11) is discussed in chapters S-1 and S-2.

S-1-1. Organic superconductors and organic aromatic hydrocarbon superconductors

Superconductors with light elements such as B, C and Si (Light-element superconductors) are not only interesting for their fundamental physics and chemistry, but also important for future applications due to their abundance, low cost and lack of toxicity [1-5]. In particular, superconductivity in carbon-based materials such as fullerenes, organic molecular solids and graphites has attracted much attention because of their ease of design, flexibility and light weight in device application as well as inherent advantages of light elements superconductors [6-7]. Carbon-based superconductors were first discovered in graphite intercalation compounds [8], *i.e.*, alkali-metal doped AC_8 (A = K, Rb, Cs). These T_cs were less than 1 K. The T_c rapidly increased to 11.5 K by the discovery of CaC_6 [9]. In 1980, Jerome *et al*. discovered a superconductivity in di-(tetramethyltetraselenafulvalene)-hexafluorophosphate ($(TMTSF)_2PF_6$), which shows

T_c as high as 0.9 K at 12 kbar [10]. The $(TMTSF)_2PF_6$ solid was a quasi one dimensional (1D) organic conductor at ambient pressure. This was the first discovery of organic superconductors. Presently, the highest T_c in organic superconductors is 14.2 K at 8.2 GPa for β'-$(BEDT\text{-}TTF)_2ICl_2$ of a bis(ethylenedithio)tetrathiafulvalene (BEDT-TTF) family [11]. The first discovery of superconductivity in metal doped C_{60} was in K_3C_{60}, which showed the T_c as high as 18 K [12]. The T_c increased up to 33 K at ambient pressure in Cs_2RbC_{60} [13]. Presently, the highest T_c is 38 K for Cs_3C_{60} at 0.7 GPa [14].

S-1-2. The progress of organic hydrocarbon superconductors

In 2010, a new organic superconductor was discovered in aromatic molecules by our group [15]. The K doped picene solid, K_3picene, provided two different superconducting phases, T_c = 7 K and 18 K [15]; transistor study on picene was fully described in the former part (chapter 1 - 11) of this Doctor thesis. Subsequently, superconductivity of metal doped phenanthrene, $A_x$phenanthrene (A: alkali and alkali-earth metals), was reported by Chen's group [16-18]; the T_c is 5 - 6 K. The superconductivity is observed in stoichiometric molar ratio of 3 : 1 for metal atom to hydrocarbon molecule; the molar ratio is still nominal value. Phenanthrene molecule also has the same type of molecular structure as picene (W-shaped structure), and it consists of three benzene rings. Furthermore, the K doped 1,2:8,9-dibenzopentacene (DBP) solid showed superconductivity with T_c = 33 K [19], which was the highest in hydrocarbon superconductors. The molecular structures of picene, phenanthrene and DBP are shown in Figure S1-1.

S-1-3. The motivation of chapters S-1 and S-2

Conventional superconductors can be understood by Bardeen-Cooper-Schrieffer (BCS) theorem, and the superconductivity is produced by electron-electron pair (cooper pair) through electron-phonon coupling. The larger density of states on Fermi level, $N(\varepsilon_F)$, results in higher T_c, and the higher electron-phonon coupling constant, λ, results in higher

T_c. The molecular solid has narrow band width, W, to produce higher $N(\varepsilon_F)$ and T_c, and it has a higher phonon frequency due to molecular vibration to produce higher λ and T_c. However, the small W causes metal-insulator transition owing to the Coulomb repulsion, U. This picture emerges in C_{60} superconductors [20].

Unconventional superconductors cannot be explained by simple BCS theorem, and the electron-electron coupling is not mediated by phonon but by magnetic (spin) fluctuation or charge fluctuation. In BCS theorem, the T_c produced through the electron-phonon coupling is considered as approximately 0.1 × maximum phonon energy (E_D = 100 - 1000 K), *i.e.*, the T_c ~ 10 - 100 K. This is recognised as 'Limit of BCS'. On the other hand, Little presented the exciton-mediated high T_c superconductor in linear-chain polymer, in which the T_c can reach 1000 K because of 0.1 × exciton energy (E_E = 10000 K) [21]. However, it is still not realised. Cuprates [22-24] show the highest T_c (133 K in $HgBa_2Ca_2Cu_3O_8$ [24]) in superconductors reported so far, and the superconductivity is understood based on the spin-fluctuation model that the electron-electron pairing is produced by antiferromagnetic spin-fluctuation. Pnictides are also included in such unconventional superconductors [25-27]; the highest T_c is 55 K ($SmFeAsO_{1-x}F_x$ [27]). The T_c of unconventional superconductors is expressed with $k_BT_c = 0.01t$ in Hubbard model, where t is the hopping integral, and the T_cs of cuprates can be reasonably explained.

The discovery of organic hydrocarbon superconductors may open a new way for investigating high T_c superconductors, because of its high T_c of 18 K. The T_c is higher than organic superconductors (14 K in β'-$(BEDT\text{-}TTF)_2ICl_2$). However, even the superconducting phase of hydrocarbon superconductor is still unclear, and the parameters that characterise the superconductors are not experimentally obtained.

The purpose of this study is to identify the superconducting phase of picene superconductors, $K_x$picene and Rb_xpicene, *i.e.*, how many electrons are donated to picene molecule? What is the difference between 7 K phase and 18 K phase? Furthermore, the pressure dependence of 18 K phase is newly clarified in this study: the pressure dependence of 7 K phase was reported by our group [28]. Obtaining exact experimental data in the superconductors is of significance for clarifying the mechanism of

superconductivity. Finally, we have tried to make new superconductors with other hydrocarbon; the target molecule is coronene.

References

[1] M. I. Eremets, V. V. Struzhkin, H-K. Mao, and R. J. Hemley, Science **293**, 272, (2001).

[2] B. M. Klein and D. A. Papaconstantopoulos, Phys. Rev. Lett. **32**, 1193 (1974).

[3] I. T. Belash, O. V. Zharikov, and A. V. Palnichenko, Synthetic Metals **34**, 455 (1989).

[4] T. E. Weller, M. Ellerby, S. S. Saxena, R. P. Smith, and N. T. Skipper, Nature Phys. **1**, 39 (2005).

[5] V. L. Solozhenko, O. O. Kurakevych, D. Andrault, Y. L. Godec, and M. Mezouar, Phys. Rev. Lett. **102**, 015506 (2009).

[6] N. Murata, J. Haruyama, J. Reppert, A. M. Rao, T. Koretsune, S. Saito, M. Matsudaira, and Y. Yagi, Phys. Rev. Lett. **101**, 027002 (2008).

[7] S. P. Kelty, C-C. Chen, and C. M. Lieber, Nature **352**, 223 (1991).

[8] N. B. Hannay, T. H. Geballe, B. T. Matthias, K. Andres, P. Schmidt, and D. MacNair, Phys. Rev. Lett. **14**, 225 (1965).

[9] N. Emery, C. Hérold, M. Astuto, V. Garcia, Ch. Bellin, J. F. Marêché, P. Lagrange, and G. Loupias, Phys. Rev. Lett. **95**, 087003 (2005).

[10] D. Jérome, A. Mazaud, M. Ribault, and K. Bechgaard, J. Phys. Lett. **41**, 95 (1980).

[11] H. Taniguchi, M. Miyashita, K. Uchiyama, K. Satoh, N. Môri, H. Okamoto, K. Miyagawa, K. Kanoda, M. Hedo, and Y. Uwatoko, J. Phys. Soc. Jpn. **72**, 468 (2003).

[12] A. F. Hebard, M. J. Rosseinsky, R. C. Haddon, D. W. Murphy, S. H. Glarum, T. T. M. Palstra, A. P. Ramirez, and A. R. Kortan, Nature **350**, 600 (1991).

[13] K. Tanigaki, T. W. Ebbesen, S. Saito, J. Mizuki, J. S. Tsai, Y. Kubo, and S. Kuroshima, Nature **352**, 222 (1991).

[14] A. Y. Ganin, Y. Takabayashi, Y. Z. Khimyak, S. Margadonna, A. Tamai, M. J. Rosseinsky, and K. Prassides, Nature Mater. **7**, 367 (2008).

[15] R. Mitsuhashi, Y. Suzuki, Y. Yamanari, H. Mitamura, T. Kambe, N. Ikeda, H. Okamoto, A. Fujiwara, M. Yamaji, N. Kawasaki, Y. Maniwa, and Y. Kubozono, Nature **464**, 76 (2010).

[16] X. F. Wang, R. H. Liu, Z. Gui, Y. L. Xie, Y. J. Yan, J. J. Ying, X. G. Luo, and X. H. Chen, Nature Commun. **2**, 507 (2011).

[17] X. F. Wang, Y. J. Yan, Z. Gui, R. H. Liu, J. J. Ying, X. G. Luo, and X. H. Chen, Phys. Rev. B **84**, 214523 (2011).

[18] X. F. Wang, X. G. Luo, J. J. Ying, Z. J. Xiang, S. L. Zhang, R. R. Zhang, Y. H. Zhang, Y. J. Yan, A. F. Wang, P. Cheng, G. J. Ye, and X. H. Chen, J. Phys.: Condens. Matter. **24**, 345701 (2012).

[19] M. Xue, T. Cao, D. Wang, Y. Wu, H. Yang, X. Dong, J. He, F. Li, and G. F. Chen, Sci. Rep. **2**, 389 (2012).

[20] M. Schluter, M. Lannoo, M. Needels, G. A. Baraff, and D. Tománek Phys. Rev. Lett. **68**, 526 (1992).

[21] W. A. Little, Phys. Rev. **134**, A 1416 (1964).

[22] Y. Dalichaouch, M. C. de Andrade, and M. B. Maple, Physica C **218**, 309 (1993).

[23] J. G. Bednorz and K. A. Müller, Z. Phys. B **64**, 189 (1986).

[24] A. Schilling, M. Cantoni, J. D. Guo, and H. R. Ott, Nature **363,** 56 (1993).

[25] Y. Kamihara, H. Hiramatsu, M. Hirano, R. Kawamura, H. Yanagi, T. Kamiya, and H. Hosono, J. Am. Chem. Soc. **128**, 10012 (2006).

[26] Y. Kamihara, T. Watanabe, M. Hirano, and H. Hosono, J. Am. Chem. Soc. **130**, 3296 (2008).

[27] Z.-A. Ren, W. Lu, J. Yang, W. Yi, X.-L. Shen, Z.-C. Li, G.-C. Che, X.-L. Dong, L.-L. Sun, F. Zhou, and Z.-X. Zhao, Chin. Phys. Lett. **25**, 2215 (2008).

[28] T. Kambe, X. He**,** Y. Takahashi, Y. Yamanari, K. Teranishi, H. Mitamura, S. Shibasaki, K. Tomita, R. Eguchi, H. Goto, Y. Takabayashi, T. Kato, A. Fujiwara, T. Kariyado, H. Aoki, and Y. Kubozono, Phys. Rev. B **86**, 214507 (2012).

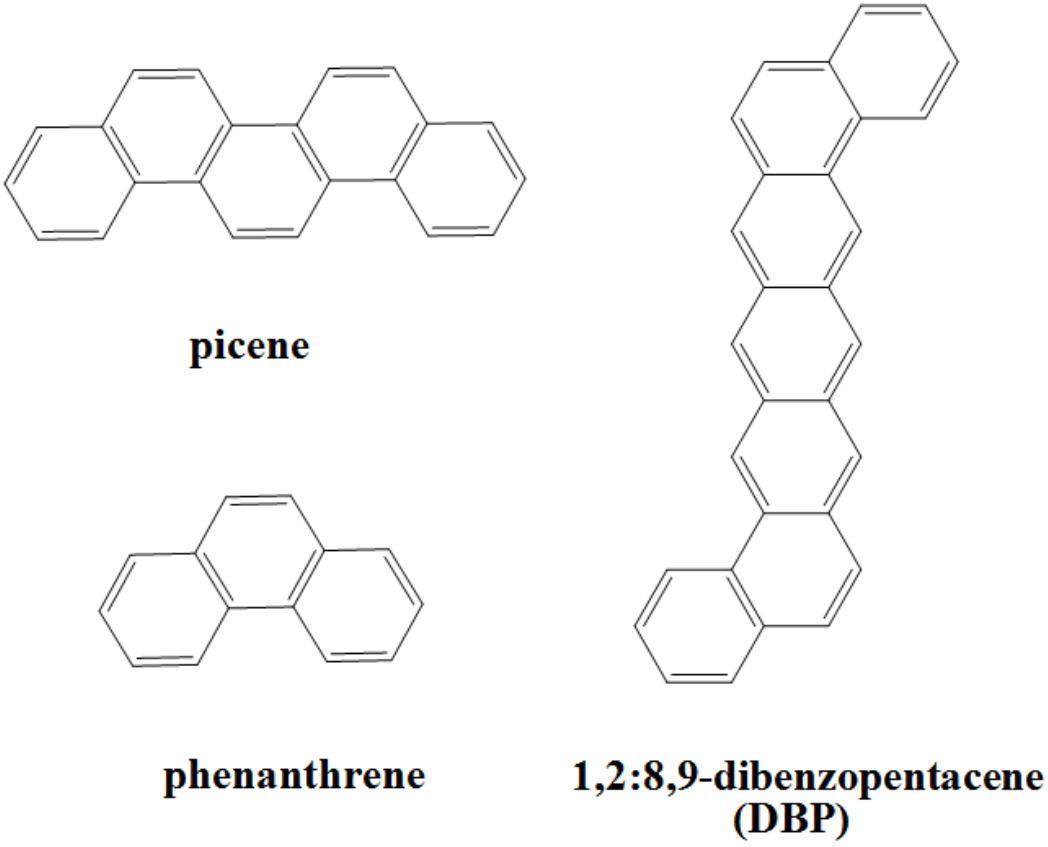

Figure S-1-1. Molecular structures of picene, phenanthrene and 1,2:8,9-dibenzopentacene (DBP).

Chapter S-2. Synthesis and physical properties of metal doped picene solids

In this chapter, the author describes the electronic structure and physical properties of solids of metal doped picene as well as selective synthesis of the 18 K phase. A clarification of physical properties and a discussion on the mechanism of superconductivity in picene superconductors are the research subjects in this study.

First, Raman scattering is used to characterise the number of electrons transferred from the dopants to a picene molecule; a softening of Raman scattering peaks enables ones to determine the number of transferred electrons. From this experiment, we have identified that three electrons are transferred to each picene molecule in the superconducting doped picene solids.

Second, the pressure dependence of T_c in 7 and 18 K phases of K_3picene is studied. The 7 K phase shows a negative pressure-dependence [1], while the 18 K phase exhibits a positive pressure-dependence which cannot be understood with a simple phonon mechanism of BCS theorem.

Third, a new synthesis method for superconducting K_3picene by a solution process with monomethylamine, CH_3NH_2, is also reported in this chapter. This method enables ones to prepare selectively the K_3picene sample exhibiting 18 K superconducting transition. The method for preparing K_3picene with T_c = 18 K may facilitate a clarification of the mechanism of superconductivity. Finally we shortly comment the new two-dimensional (2 D) molecular superconductor, $K_x$coronene.

The most of contents in this chapter are already published in Ref. 2 of the List of Publications (Style Kou 4-1).

S-2-1. Introduction

A new class of organic superconductor has been discovered in aromatic hydrocarbons. The superconductors are solids of hydrocarbons that include picene,

phenanthrene and DBP [1-6], doped with metal atoms. The first discovered superconductor is K_3picene, which possesses two different superconducting phases with T_c values as high as 7 and 18 K [6]. This has been followed by other studies, and the highest T_c in these hydrocarbon superconductors to date attains 33 K observed in $K_{3.45}$DBP [5], whose T_c is much higher than the highest T_c (14.2 K at 8.2 GPa in β'-(BEDT-TTF)$_2$ICl$_2$) in charge-transfer type organic superconductors [7]. The hydrocarbon superconductors are very attractive from viewpoints of development of new high-T_c superconductors as well as fundamental physics of superconductivity. Theoretical calculations for picene superconductors were also achieved, which suggests that the electron-phonon coupling is strong [8,9], the conduction band consists of four bands arising from two LUMO orbitals [10], and that strong hybridization between the dopants and molecules invalidates a rigid-band picture.

The departure from the rigid-band picture was experimentally evidenced by photoemission spectroscopy [11]. This photoemission study clearly showed a metallic ground state for $K_x$picene films. Our recent resistivity data also indicate a metallic behaviour for the K_3picene phase [12]. Further, a Pauli paramagnetic susceptibility was observed for a K_3picene bulk sample [6]. These results support metallic ground state for K_3picene. Donation of three electrons to an aromatic hydrocarbon molecule was reported to be a key for superconductivity [1-6]. While the nominal x value (number of metal atoms intercalated) in the superconducting samples of $A_x$hydrocarbon, (A: alkali metal atom) is 3, it is imperative to determine the real x value. Since single crystals cannot simply be obtained in the intercalation compounds, the Rietveld refinement is valuable. For the hydrocarbon superconductors, however, the Rietveld refinements have never been achieved because of its low crystal symmetry where the doped metal atoms do not occupy special symmetric sites [6].

On the other hand, Raman scattering is known to be a powerful tool for determining the x value in A_xC_{60} [13-15]. The A_g peak observed at 1469 cm^{-1} for pure C_{60} (with I_h symmetry), shifts to lower frequencies when alkaline metal atoms are doped into C_{60} solids. Actually, the peak shifts by 6 - 7 cm^{-1} for one electron donation to a C_{60} molecule, namely, the A_g peak is observed at 1452 cm^{-1} for K_3C_{60} [13], 1448 cm^{-1} for Rb_3C_{60} and

1447 cm^{-1} for Cs_3C_{60} [14,15], providing a good probe for determining the amount of doping or number of electrons on C_{60} molecule. We previously suggested that some of the peaks shift to lower frequencies with increasing the x value in $K_x$picene [1] in a similar manner as in A_xC_{60} [13-15], which indicates that the number of electrons on picene can be determined from the shift of Raman peak from that in pure picene. As previously suggested [1-6], three electron donations seem to be a key for superconductivity [3-5], but we have definitely to verify this. The first purpose of this study is to systematically investigate the Raman scattering for $A_x$picene (A: K and Rb) to correlate the number of electrons on the hydrocarbon molecules with the Raman frequency. The experimental Raman frequencies have been measured for a wide range of x = 0 - 5 in $A_x$picene, which is compared with theoretical frequencies for the Raman peaks. From this, we have evaluated the number of electrons per picene molecule to clearly determine the x value in the superconducting phases.

In characterising physical properties of picene superconductors, it is intriguing to compare the picene superconductors with superconducting solids of C_{60} and graphite; the highest at ambient pressure T_c is 33 K for $RbCs_2C_{60}$ in C_{60} superconductors [16], and 11.5 K for CaC_6 in graphite superconductors [17]. One probe for the physical properties is the pressure dependence of T_c: indeed, C_{60} and graphite superconductors have opposite tendencies; K_3C_{60} (T_c = 19.3 K) shows a large negative pressure coefficient (dT_c / dP = −7.8 K GPa^{-1}) [18], while CaC_6 has a positive one (dT_c / dP = 0.42 - 0.48 K GPa^{-1}) [19]. In the previous paper, we reported briefly the pressure dependence of T_c in 7 K phase of K_3picene [1], but the detailed analysis was not presented. Very recently, positive pressure dependence of T_c in A_3phenanthrene (A: K) [2] and $Ae_{1.5}$phenanthrene (Ae: Ba, Sr) [3] was reported, which cannot be understood with a simple phonon mechanism in conventional superconductor. Therefore, it is of significance to examine the pressure dependence of T_c in the T_c = 7 and 18 K phases of picene superconductors, which may provide an important key for investigating the mechanism of superconductivity. Thus the second purpose of this study is to explore the pressure dependence of 7 and 18 K phases of K_3picene, respectively. The pressure dependence is discussed from the viewpoints of crystal and electronic structures of picene superconductors.

The third purpose of this study is on the fabrication method for K_3picene samples. A still unclear question is why we have two phases with T_c = 7 and 18 K. The usual annealing method (or solid-reaction method) does not allow us to produce selectively 7 or 18 K phases. Even a precise control of nominal composition in $K_x$picene from x = 2.6 to 3.3 produced both 7 K and 18 K superconductors [1,6]. Here we have prepared K_3picene superconductor by a solution process with monomethylamine, CH_3NH_2, as a solvent, in order to search for a synthetic method for selectively preparing 7 K or 18 K phase. The solution process has successfully been used to control polymorphs of Cs_3C_{60}, which is a pressure-induced superconductor (T_c = 38 K (A15 phase) [20] and T_c = 40 K (face-centreed cubic phase) at 15 kbar) [21]. The author shows whether the solution process is applicable for picene superconductors.

S-2-2. Experimental.

Picene (purity: 99.9%) was purchased from NARD Co Ltd., which was used for the experiments without further purification. Alkali or alkali-earth metal was mixed with picene powder at nominal x value in a pyrex glass tube to fabricate $A_x$picene. In the annealing method, the pyrex tube was pumped and sealed at 10^{-5} Torr. The tubes were annealed at temperatures as high as ~443 K for ~10 days. The samples obtained after annealing were black in colour. The experimental procedures are shown in Figure S-2-1.

The Raman spectrum and magnetic susceptibility were measured for the samples treated in a glove box without any exposure to air. The Raman scattering was measured at 295 K with Raman spectrometer (JASCO NRS-3100) with an excitation energy having a wavelength λ = 785 nm, while magnetization, *M*, was measured with a SQUID magnetometer (Quantum Design MPMS2) in the temperature range > 2 K under ambient and high pressures. A magnetic field, *H*, of 20 Oe was applied in measuring *M* / *H*. For the measurement of pressure dependence of superconductivity, a Cu-Be piston-cylinder type pressure-cell was used. The hydrostatic pressure was mediated by Daphne oil. The applied pressure region was from 0.1 MPa to 1.2 GPa. A small piece of crystalline Sn or Pb was put inside the pressure cell along with the sample to monitor the exact pressure.

In the solution method for preparing $A_x$picene, on the other hand, CH_3NH_2 was introduced from the CH_3NH_2 gas bottle into the glass vessel containing picene powder and K metal at nominal stoichiometric molar ratio. The picene and K were completely dissolved in CH_3NH_2 by stirring at 223 K for 3 h. The colour of solution was dark-green. After complete dissolution, liquid CH_3NH_2 was removed at 300 K until the base pressure reaches 10^{-4} Torr. The black powder sample obtained after removing CH_3NH_2 was moved into quartz tube in an Ar filled glove box. The tube dynamically pumped and sealed at 10^{-6} Torr, was annealed at 443 K for 70 h to remove CH_3NH_2 completely. Special care was taken in the annealing procedure because high temperature annealing above 490 K for removal of CH_3NH_2 produces a very toxic material, KCN; actually even below 490 K, KCN may be produced. Powder X-ray diffractions for $K_x$picene were measured by RIGAKU RINT-TTR III and with synchrotron radiation (KEK-PF, SPring-8 and ESRF). The unit-cell parameters for $K_x$picene were determined by the LeBail analysis program in GSAS package [22]. Theoretical calculation of Raman frequencies and intensities for A_1, A_2, B_1 and B_2 modes for neutral picene and its anions, picene^{y-} (y = 0 - 5), with optimized structure (C_{2v} symmetry) was performed with B3LYP program based on hybrid Hartree-Fock (HF) / density functional theory (DFT) with the 6-31G* basis set [23-25].

S-2-3. Results and Discussions

S-2-3-1. Characterisation of the number of doped metal atoms in $K_x$picene and Rb_xpicene

Figures S-2-2(a) and S-2-3(a) show Raman spectra for samples of $K_x$picene and Rb_xpicene (x = 0 - 5), respectively, at 500 - 1800 cm^{-1}. A pronounced peak at 1378 cm^{-1} marked with an asterisk for pristine picene can be assigned to a superposition of ν_{20} and ν_{21} A_1 vibration modes of picene molecule, where ν_n stands for the nth A_1 vibration mode from the bottom. The ν_{20} and ν_{21} modes in picene^{y-} (y = 0 - 5) are schematically depicted in Figure S-2-4. These vibration modes are suggested to provide strong electron-phonon coupling [8]. In Figures S-2-2(b) and 3(b) the theoretical frequencies and intensities of Raman-active A_1, A_2, B_1 and B_2 vibration modes are shown along with the experimental

Raman spectra, where the experimental peaks agree well with the theoretical results. Figures S-2-2 and 3 also show that the pronounced peak observed at 1378 cm^{-1} for pristine picene shifts to lower frequencies with an increase in x for both $K_x$picene and Rb_xpicene samples.

The average values of ν_{20} and ν_{21} calculated theoretically are plotted for each picene molecule in Figures S-2-5(a) and (b). The experimental frequencies for the pronounced peak, which are ascribable to superposition of ν_{20} and ν_{21}, are plotted as a function of x for $K_x$picene and Rb_xpicene in Figures S-2-5(a) and (b), respectively. As seen from Figure S-2-5(a), the experimental frequencies in all the $K_x$picene samples basically fall on three discrete values, 1378, 1344 and 1313 cm^{-1}, which are consistent with those predicted theoretically for picene, picene^{2-} and picene^{3-} (respective dashed lines). This implies that only two phases, K_2picene and K_3picene, can be produced in doped $K_x$picene samples. As for K_1picene, this separates into two phases, picene and K_2picene, as seen from Figures S-2-2(b) and S-2-5(a). The same plots suggest that $K_{1.5}$picene and K_2picene samples decompose into three phases, picene, K_2picene and K_3picene.

Further, a Raman peak was observed in K_3picene samples at 1328 cm^{-1} in addition to those for K_2picene (1344 cm^{-1}) and K_3picene (1313 cm^{-1}), where the value (1328 cm^{-1}) is intermediate between the latter two. Thus the Raman peak at 1328 cm^{-1} may imply the presence of a phase with a fractional x ($K_{2.5}$picene), although the phase is not a main one. However, two Raman peaks should be observed at 1344 and 1313 cm^{-1} because Raman scattering reflects vibration of molecule even if the $K_{2.5}$picene phase appears as statistically averaged structure in this sample. Thus the origin of the Raman peak at 1328 cm^{-1} remains to be clarified. If a dynamic conversion of picene^{2-} and picene^{3-} produces the peak at 1328 cm^{-1}, the Raman scattering should be observed at low temperatures with the single peak splitting into peaks at 1344 and 1313 cm^{-1}. When nominal x value was increased above 3, only K_2picene and K_3picene were observed, while K_4picene and K_5picene phases could not be fabricated, which indicates that the maximum x value is three. From these plots, we conclude that only two phases, K_2picene and K_3picene, can be realised by an intercalation of K atoms into picene samples, while K_1picene is unstable.

In Figure S-2-5(a), the plots for phases with the same x value as the nominal x in the $K_x$picene sample is indicated in red (e.g., the Raman peak of K_3picene phase in the K_3picene sample).

Here, we should stress that the prepared individual $K_x$picene sample does not always contain all the crystal phases described above, but that some solid samples contain only one or two crystal phases. The number of appearance of the phases is given in parentheses in Figure S-2-5(a). The numbers then indicate the frequency with which the crystal phases appear. For example, all K_3picene samples (19 of them) contained the K_3picene crystal-phase, and 58% in 19 K_3picene samples showed only a peak ascribable to K_3picene crystal phase *i.e.*, a single phase of K_3picene. K_2picene samples produce a single phase of K_2picene (20%), picene+K_2picene+K_3picene phases (20%), a single phase of K_3picene (20%) and K_2picene+K_3picene (40%). K_1picene samples resulted in a single phase of K_2picene (25%) and picene+K_2picene phases (75%). $K_{1.5}$picene samples provided picene+K_2picene phases (20%), K_2picene+K_3picene (20%) and picene+K_2picene+K_3picene phases (40%) in which each fraction of phase (peak intensity) was almost the same. The $K_{1.5}$picene samples provided only a single phase of K_2picene (20%). It is suggested from these results that K metal in solid picene may not completely react in most of the samples except for those samples producing a single phase. Judging from the probability, 58%, of realisation of the single phase, it is suggested that K_3picene is more stable than K_2picene (25% for a single phase). Therefore, it is of interest to investigate theoretically the energetic stability of $K_x$picene phase.

As seen from Figures S-2-3(b) and S-2-5(b), the ν_{20}, ν_{21} Raman frequencies in Rb_xpicene samples also suggest presence of only three phases (picene, Rb_2picene and Rb_3picene) as in $K_x$picene. The observed frequencies, 1378, 1345 and 1313 cm^{-1}, can be assigned to picene, picene^{2-} and picene^{3-}, respectively; the values are consistent with those of $K_x$picene. It can be concluded from the plots (Figure S-2-5(b)) that Rb_1picene sample provides only two phases, picene and Rb_2picene, while Rb_2picene and Rb_3picene solid samples provide only three phases (picene, Rb_2picene and Rb_3picene). Thus, increasing nominal x leads to a realisation of phases with larger integer x values, in the same manner as in $K_x$picene (Figure S-2-5(a)). Increasing nominal x above 3 produces

Rb_3picene and picene as well as a new phase of $Rb_{2.5}$picene exhibiting a Raman frequency at 1323 cm^{-1}, this was also found in $K_x$picene. In the same manner as $K_x$picene, the stability of Rb_3picene is confirmed because of high probability, 44%, of formation of a single phase in the Rb_3picene samples.

The magnetic susceptibility has been measured for all the samples of $K_x$picene and Rb_xpicene. The $M / H - T$ curves for $K_x$picene samples that show the presence of K_3picene phase (with the Raman peak at ~ 1313 cm^{-1}) exhibit a clear drop at 7 or 18 K, indicating superconducting transitions. Conversely, all the samples that have no K_3picene phase exhibit no such behaviours. These results clearly indicate that superconducting phase in $K_x$picene relates closely to K_3picene phase. The M / H of Rb_xpicene samples also show the same behaviour, *i.e.*, the samples containing Rb_3picene phase have the superconducting transition, while the Rb_3picene samples that do not exhibit the Raman peak at ~ 1313 cm^{-1} exhibit no superconducting transitions, indicating that superconducting phase relates to Rb_3picene. Thus, we have identified that superconducting phases in $K_x$picene and Rb_xpicene can be closely associated with K_3picene and Rb_3picene crystal phases, respectively, from the M / H and Raman measurements.

S-2-3-2. Pressure dependence of T_c in 7 and 18 K phases

We now turn to the pressure effect of superconductivity in each phase. We first display the $M / H - T$ curves at various pressures for the 7 K phase of K_3picene. Figure S-2-6(a) shows that the T_c shifts downward with pressure, but only gradually. The midpoint of the superconducting transition, T_c^{mid}, shown in Figure S-2-6(b), decreases linearly with pressure up to 1 GPa, with $dT_c^{mid} / dP = -0.3$ K GPa^{-1}, which can be determined unambiguously because of the absence of any inhomogeneous broadening of the superconductive transition with increasing pressure. The dT_c / dP of the 7 K phase is negative as in K_3C_{60}, but the coefficient is an order of magnitude smaller. K_3C_{60} has a three-dimensional (3D) electronic band structure, so that pressure is expected to increase the bandwidth with a decreased $N(\varepsilon_F)$ [18], which in turn decreases T_c, regardless of a

softening of some C_{60} vibration modes [26]. The intercalated graphite, CaC_6, on the other hand, has a positive pressure dependence, where the electronic structure around the Fermi energy is shown to contain a large component of the so-called interlayer states, whose amplitudes reside in between the graphene layers, conferring a 3D character on the electronic structure [19,27]. In this compound, while the $N(\varepsilon_F)$ decreases with pressure, a large softening of an in-plane Ca vibration mode under pressure is shown to cause an increase in λ, which is considered to overcome the reduction of $N(\varepsilon_F)$ leading to an enhanced T_c.

Now we turn to the pressure dependence of T_c in the 18 K phase of K_3picene. Figure S-2-7(a) shows the M/H against T, normalized by the value at 50 K for clarity, for various pressures in the 18 K superconducting phase. We can immediately notice that the T_c^{onset}, shifts *upward*: The T_c^{onset}, shown in Figure S-2-7(b) against pressure, increases linearly with pressure up to 1.2 GPa, with dT_c^{onset}/dP = 12.5 K GPa^{-1}. The large positive pressure dependence found here contrasts sharply with the negative pressure dependence in the 7 K phase. The positive pressure dependence has also observed in A_3phenanthrene, and $Ae_{1.5}$phenanthrene [2-3]. However, the size of the coefficient, dT_c^{onset}/dP, is an order of magnitude larger than that, ~ 1 K GPa^{-1}, of phenanthrene superconductor. Since a reduced volume usually implies a smaller density of states at ε_F, this behaviour cannot be understood with a simple phonon mechanism of BCS superconductivity.

S-2-3-3. A selective preparation of 18 K superconducting phase in K_3picene

Figure S-2-8(a) shows the $M/H - T$ curve in zero-field cooling (ZFC) for $K_{3.1}$picene sample (nominal x = 3.1) that was prepared by the solution process. This data was reported and briefly discussed in Ref. 1. Before annealing the sample or removing CH_3NH_2 from the precursor, the M/H shows a Pauli-like, temperature-independent behaviour with a weak increase below 10 K. After the sample is annealed at 443 K for 70 h, the M/H begins to show an abrupt decrease with the T_c^{onset} = 18 K and the T_c^{mid} = 17 K. This superconducting transition coincides with that for the 18 K phase of K_3picene superconductor prepared by solid-reaction method, or annealing method [1,6]. The

maximum shielding fraction is still as low as 0.1%, a value lower by an order of magnitude than that, 1.2 %, for 18 K superconductor prepared by annealing method [6]. However, we notice that the solution-reaction method can produce 18 K superconducting phase more effectively than the solid-state method. In fact, all the K_3picene samples prepared by the solution method show a clear decrease in M/H at 18 K. The nominal x value for producing the superconducting phase with the solution process is confined to 2.9 – 3.1, suggesting that three K atoms per picene molecule is a key doping level.

Figure S-2-8(b) shows Raman scattering spectra for the K_3picene samples prepared by the solution method. One sample (curve A in Figure S-2-8(b)) was annealed at 443 K for 70 h in vacuum to remove CH_3NH_2, while the other (curve B) was not annealed. For comparison, the spectra for the K_3picene sample prepared by the solid-reaction method (curve C) as well as for pristine picene (curve D) are also shown. We can see that the Raman spectrum for the $K_{3.1}$picene sample prepared by the solution method (A) coincides with that for the $K_{3.0}$picene prepared by the solid-reaction method (C), where the peak shifts to a lower frequency by 67 cm^{-1} from 1378 cm^{-1} for pristine picene, which suggests that these samples possess the same number of electrons per picene molecule, *i.e.*, these can be represented as K_3picene. This result indicates the effectiveness of annealing at 443 K in vacuum for the removal of CH_3NH_2, and that CH_3NH_2 molecules are scarcely left in $K_{3.1}$picene sample (A). On the other hand, the peak for the $(CH_3NH_2)K_{3.0}$picene sample (B), which was prepared by solution method without annealing, shifts to a lower frequency by 48 cm^{-1}, showing that 2.5 electrons are transferred to picene molecule from K atoms. This implies that the remaining CH_3NH_2 molecule may capture 0.5 electrons from a picene molecule, *i.e.*, a back-electron transfer from picene molecule.

Figures S-2-9(a) and (b) show X-ray diffraction patterns for the $(CH_3NH_2)_zK_3$picene and K_3picene samples, respectively. The former was prepared by the solution method without annealing, while the latter was prepared by the solution method with annealing at 443 K for 70 h. The lattice parameters for the two samples obtained from the LeBail fit to X-ray diffraction patterns (Figure S-2-9) are listed in Table S-2-1; the space group was assumed to be $P2_1$ in these samples, in the same manner as picene and K_3picene prepared

by solid reaction method [1,6]. We can see from this Table that the lattice parameters, *a* and *c*, for the K_3picene sample prepared by the solution method without annealing, increase from those in pristine picene. Specifically, the *c* axis expands markedly, suggesting that CH_3NH_2 molecules are mainly intercalated into the space between the herringbones (*ab*-plane) layers of picene molecules.

The values of *a* and *c* in the K_3picene sample, prepared by the solution method with annealing, are smaller than those in the sample without annealing, which indicates that CH_3NH_2 was basically removed in the sample annealed at 443 K in vacuum, as consistent with the results obtained from the Raman scattering. The K_3picene sample prepared by the solid reaction (C in Figure S-2-8(b)) showed T_c of 7 K, while the K_3picene sample (A in Figure S-2-8(b)) prepared by the solution method with annealing showed T_c of 18 K. All the lattice parameters in the K_3picene sample prepared by the solution method with annealing are larger than those in pure picene, especially the *c* expands, suggesting that the crystal structure of K_3picene phase prepared by solution method is different from that (7 K phase) prepared by the solid reaction, *i.e.*, some K atoms in K_3picene prepared by the solution method may be intercalated into the space between *ab*-layers.

In fact, the theoretical calculation [10,28,29] (as summarized in Table S-2-2 for the structure parameters) shows a presence of two kinds of doping structures: (i) the one (denoted as K_3picene) with the dopants inserted within the herringbone-arranged picene layer (*ab*-layer), and (ii) another with some dopants intercalated in the interlayer regions as well, where the latter is meta-stable but does exhibit a local energy minimum. The structure is denoted as K_2K_1picene by Aoki group [1,10], where two K atoms are inserted into the *ab*-layer while one K atom is intercalated into the space between *ab*-layers. The lattice constants determined by X-ray diffraction indicate the expansion of *a*-axis and shrinkage of *c*-axis in the 7 K phase prepared by solid reaction, suggesting the intercalation of K atoms into the picene layer (*ab*-layer), which is consistent with the location of K atoms with intralayer insertion obtained theoretically [10]. On the other hand, some of the K atoms in K_3picene prepared by solution method may be intercalated into the space between *ab*-layers, which is consistent with the theoretical prediction that the structure with both intralayer and interlayer dopants is a meta-stable structure

[10,28,29]. Thus the theoretical structure (K_2K_1picene with two intra-layer and one inter-layer picene molecules) may possibly be related to the 18 K phase prepared by solution method, but this definitely requires further confirmation.

Superconducting mechanism and the symmetry of the gap function have yet to be known. The previous theoretical calculation suggests that the electron-phonon coupling is sufficiently strong to roughly account the size of T_c in doped picene [8,9,30]. At the same time, however, a possible relevance of the strong electron-electron correlation is pointed out in other theoretical works [31-33]. The multiple structures, found here to be dependent on the sample fabrication method, is consistent with the previous theoretical suggestion that there are multiple meta-stable structures in the doped picene [10,28,29]. More importantly, if the identification of the 18 K phase of the superconductivity to be the structure with the intra-layer plus inter-layer insertion of dopants is correct, this implies the superconductivity is dominated by details in the doping structure, and this may give a crucial clue in exploring the superconductivity mechanism, including some unconventional ones. We find that the 7 and 18 K phases react in opposite manners against the applied pressure, which may provide an important test in sorting the mechanism.

S-2-3-4. A discovery of new superconductor other than phenacene moleculs

In this section, the author describes on new organic hydrocarbon superconductor other than picene, phenathrene and DBP reported so far [1-6]. That is, we have newly discovered superconductivity of K doped coronene, $K_x$coronene. The coronene molecule does not take a phenacene-type molecular structure but a 2D-extended structure. Therefore, the discovery of superconductivity in $K_x$coronene implies that the superconductivity in metal doped hydrocarbon is not confined in phenacene-type molecules. This is a significant indication for a diversity of hydrocarbon superconductors. The diversity may be a key for higher-T_c superconductors.

The synthesis procedures are the same as those described in section S-2-2. Coronene powder (97% in purity) was purchased from Tokyo Chemical Industry, and the coronene

was sublimed for purification. The K metal was mixed with coronene powder at nominal molar ratio of 0.5 : 1 and annealed at 573 K.

The molecular structure of coronene is shown in Figure S-2-10(a), The solid comprises a stacking of layers (*ab*-plane) along *c* (Figure S-2-10(b)). Figure S-2-11 shows M / H versus T, for $K_{0.5}$coronene at ZFC and FC measurements, suggesting superconductivity at 7 K; exact amount of K in $K_{0.5}$coronene sample is unclear. The fact that $K_x$coronene shows superconductivity may be important because the superconductivity is observed in 2D extended molecule for the first time, suggesting that many superconductors can be realised in metal intercalated hydrocarbon solids.

S-2-4. Conclusion

The conclusion of the present paper is three-fold: (1) We have performed a characterisation of the number of electrons on picene molecule using Raman scattering, and two different phases of A_2picene and A_3picene were found in the $A_x$picene samples, indicating the absence of A_1picene phase. From the Raman scattering of superconducting $A_x$picene samples, it has been found that the A_3picene phase relates closely to superconducting phase. (2) The pressure study reveals that the 18 K phase has a positive dT_c^{mid} / dP as in superconducting phenanthrene [2-4], while the 7 K phase has a negative coefficient. The latter is understandable from the BCS picture, while the former does not fit with simple phonon-mechanism BCS superconductivity. (3) The preparation of K_3picene by a solution method led selectively to 18 K superconducting phase, which is different from the preparation by annealing method which produces 7 or 18 K phase. The K_3picene sample prepared by the solution method showed longer *c* axis than in K_3picene with the annealing method, indicating that a K atom may be intercalated into the space between the herringbone (*ab*) layers, *i.e.* two K atoms in intra-layer and one K atom in inter-layer. Finally, we showed that new 2D superconductor, $K_x$coronene, could be realised. This may be important for future development of superconductors with higher T_c because it verifies that superconductivity is not confined in phenacene molecules.

References

[1] T. Kambe, X. He, Y. Takahashi, Y. Yamanari, K. Teranishi, H. Mitamura, S. Shibasaki, K. Tomita, R. Eguchi, H. Goto, Y. Takabayashi, T. Kato, A. Fujiwara, T. Kariyado, H. Aoki, and Y. Kubozono, Phys. Rev. B **86**, 214507 (2012).

[2] X. F. Wang, R. H. Liu, Z. Gui, Y. L. Xie, Y. J. Yan, J. J. Ying, X. G. Luo, and X. H. Chen, Nature Commun. **2**, 507 (2011).

[3] X. F. Wang, Y. J. Yan, Z. Gui, R. H. Liu, J. J. Ying, X. G. Luo, and X. H. Chen, Phys. Rev. B **84**, 214523 (2011).

[4] X. F. Wang, X. G. Luo, J. J. Ying, Z. J. Xiang, S. L. Zhang, R. R. Zhang, Y. H. Zhang, Y. J. Yan, A. F. Wang, P. Cheng, G. J. Ye, and X. H. Chen, J.Phys.: Condens. Matter **24**, 345701 (2012).

[5] M. Xue, T. Cao, D. Wang, Y. Wu, H. Yang, X. Dong, J. He, F. Li, and G. F. Chen, Sci. Rep. **2**, 389 (2012).

[6] R. Mitsuhashi, Y. Suzuki, Y. Yamanari, H. Mitamura, T. Kambe, N. Ikeda, H. Okamoto, A. Fujiwara, M. Yamaji, N. Kawasaki, Y. Maniwa, and Y. Kubozono, Nature **464**, 76 (2010).

[7] H. Taniguchi, M. Miyashita, K. Uchiyama, K. Satoh, N. Môri, H. Okamoto, K. Miyagawa, K. Kanoda, M. Hedo, and Y. Uwatoko, J. Phys. Soc. Jpn. **72**, 468 (2003).

[8] T. Kato, T. Kambe, and Y. Kubozono, Phys. Rev. Lett. **107**, 077001 (2011).

[9] M. Casula, M. Calandra, G. Profeta, and F. Mauri, Phys. Rev. Lett. **107**, 137006 (2011).

[10] Y. Kubozono, H. Mitamura, X. Lee, X. He, Y. Yamanari, Y. Takahashi, Y. Suzuki, Y. Kaji, R. Eguchi, K. Akaike, T. Kambe, H. Okamoto, A. Fujiwara, T. Kato, T. Kosugi, and H. Aoki, Phys. Chem. Chem. Phys. **13**, 16476 (2011).

[11] H. Okazaki, T. Wakita, T. Muro, Y. Kaji, X. Lee, H. Mitamura, N. Kawasaki, Y. Kubozono, Y. Yamanari, T. Kambe, T. Kato, M. Hirai, Y. Muraoka, and T. Yokoya, Phys. Rev. B **82**, 195114 (2010).

[12] K. Teranishi, X. He, Y. Sakai, M. Izumi, H. Goto, R. Eguchi, Y. Takabayashi, T. Kambe, and Y. Kubozono, Phys. Rev. B **87**, 060505 (R)(2013).

[13] M. Schluter, M. Lannoo, M. Needels, G. A. Baraff, and D. Tománek, Phys. Rev. Lett. **68**, 526 (1992).

[14] M. S. Dresselhaus, G. Dresselhaus, and P. C. Eklund, J. Raman Spectros. **27**, 351 (1996).

[15] S. Fujiki, Y. Kubozono, S. Emura, Y. Takabayashi, S. Kashino, A. Fujiwara, K. Ishii, H. Suematsu, Y. Murakami, Y. Iwasa, T. Mitani, and H. Ogata, Phys. Rev. B **62**, 5366 (2000).

[16] K. Tanigaki, T. W. Ebbesen, S. Saito, J. Mizuki, J. S. Tsai, Y. Kubo, and S. Kuroshima, Nature **352**, 222 (1991).

[17] N. Emery, C. Hérold, M. d'Astuto, V. Garcia, Ch. Bellin, J. F. Marêché, P. Lagrange, G. Loupias, Phys. Rev. Lett. **95**, 087003 (2005).

[18] G. Sparn, J. D. Thompson, S.-M. Huang, R. B. Kaner, F. Diederich, R. L. Whetten, G. Grüner, and K. Holczer, Science **252**, 1829 (1991).

[19] J. S. Kim, L. Boeri, R. K. Kremer, and F. S. Razavi, Phys. Rev. B **74**, 214513 (2006).

[20] Y. Takabayashi, A. Y. Ganin, P. Jeglič, D. Arčon, T. Takano, Y. Iwasa, Y. Ohishi, M. Takata, N. Takeshita, K. Prassides, and M. J. Rosseinsky, Science **323**, 1585 (2009).

[21] T. T. M. Palstra, O. Zhou, Y. Iwasa, P. E. Sulewski, R. M. Fleming, and B. R. Zegarski, Solid State Commun. **93**, 327 (1995).

[22] A. C. Larson and R. B. Von Dreele, "General Structure Analysis System (GSAS)", Los Alamos National Laboratory Report LAUR 86-748 (2004).

[23] A. D. Becke, Phys. Rev. A **38**, 3098 (1988).

[24] C. Lee, W. Yang, and R. G. Parr, Phys. Rev. B **37**, 785 (1988).

[25] R. Ditchfield, W. J. Hehre, and J. A. Pople, J. Chem. Phys. **54**, 724 (1971).

[26] D. W. Snoke, Y. S. Raptis, and K. Syassen, Phys. Rev. B **45**, 14419 (1992).

[27] G. Csányi, P. B. Littlewood, A. H. Nevidomskyy, C. J. Pickard, and B. D. Simons, Nature Phys. **1**, 42 (2005).

[28] T. Kosugi, T. Miyake, S. Ishibashi, R. Arita, and H. Aoki, Phys. Rev. B **84**, 214506 (2011).

[29] T. Kosugi, T. Miyake, S. Ishibashi, R. Arita, and H. Aoki, Phys. Rev. B **84**, 020507(R) (2011).

[30] A. Subedi and L. Boeri, Phys. Rev. B **84**, 020508(R) (2011).

[31] G. Giovannetti and M. Capone, Phys. Rev. B **83**, 134508 (2011).

[32] M. Kim, B. I. Min, G. Lee, H. J. Kwon, Y. M. Rhee, and J. H. Shim, Phys. Rev. B **83**, 214510 (2011).

[33] Y. Nomura, K. Nakamura, and R. Arita, Phys. Rev. B **85**, 155452 (2012).

Table S-2-1. Experimentally obtained lattice parameters for picene and K-doped picene.

	a (Å)	*b* (Å)	*c* (Å)	*β* (°)	*V*(Å^3)
Pristine picene[a)]	8.472(2)	6.170(2)	13.538(7)	90.81(4)	708
K_3picene[b)]	8.707(7)	5.912(4)	12.97(1)	92.77(5)	667
$(CH_3NH_2)_zK_3$picene[c)]	8.927(5)	6.151(1)	14.476(4)	94.16(3)	793
K_3picene[d)]	8.571(5)	6.270(2)	14.001(3)	91.68(3)	752

a) Taken from Ref. 6.

b) Taken from Ref. 6, where the sample was prepared by solid reaction method.

c) Sample prepared by solution method without annealing.

d) Sample prepared by solution method with annealing.

Table S-2-2. Theoretically obtained lattice parameters for K-doped picene.

	a (Å)	*b* (Å)	*c* (Å)	β(°)	*V* (Å^3)
K_2K_1picene	8.776	6.394	13.346	94.03	747.069
K_3picene (A)	7.421	7.213	14.028	104.53	726.848
K_3picene (B)	7.408	7.223	14.116	105.93	726.328

Theoretically obtained lattice parameters for K-doped picene [28]. K_3picene stands for a structure where all the three K atoms are inserted within the picene layer (with two possible structures A and B), while K_2K_1picene a structure with two intralayer atoms and one interlayer one.

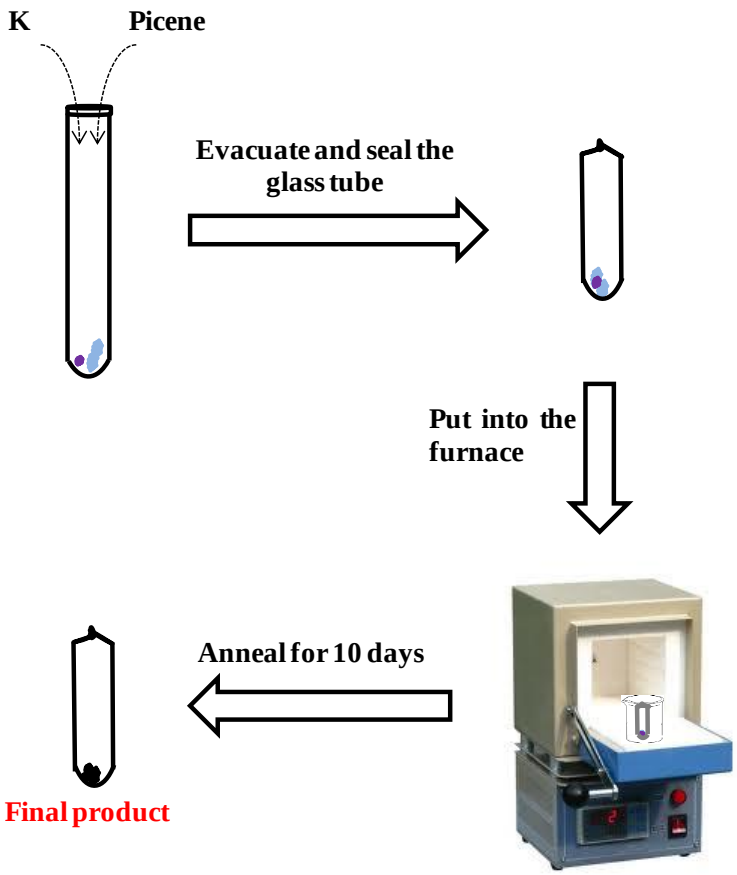

Figure S-2-1. Experimental procedure for obtaining aromatic hydrocarbon superconductors by the annealing method.

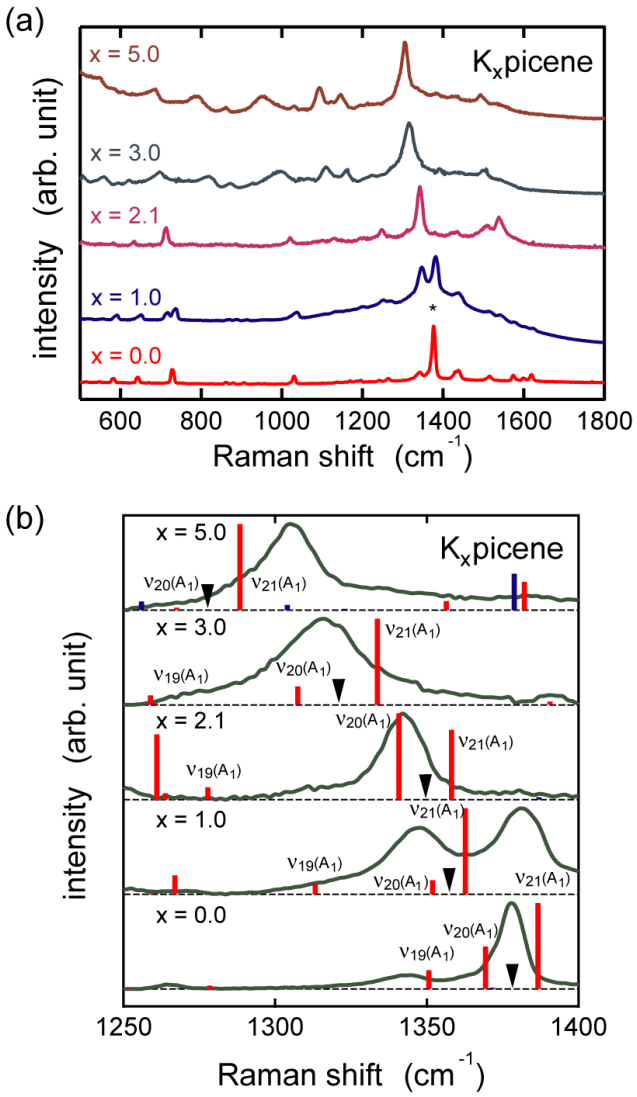

Figure S-2-2. Raman scattering spectra in $K_x$picene (x = 0 - 5) at (a) 500 - 1800 cm^{-1} and (b) 1250 - 1400 cm^{-1}. Raman peaks calculated theoretically are indicated with bars in (b) with A_1 (B_2) mode in red (blue). The height of the red bars represents the relative intensities of the Raman peak. All the theoretical results are shifted downward by 27 cm^{-1} so that the theoretical average value of n_{20} and n_{21} A_1 modes in neutral picene fits to its experimental average value, 1378 cm^{-1}. The arrows indicate averaged values of theoretical n_{20} and n_{21} A_1 modes. The explanation of notation, n_n, is described in text.

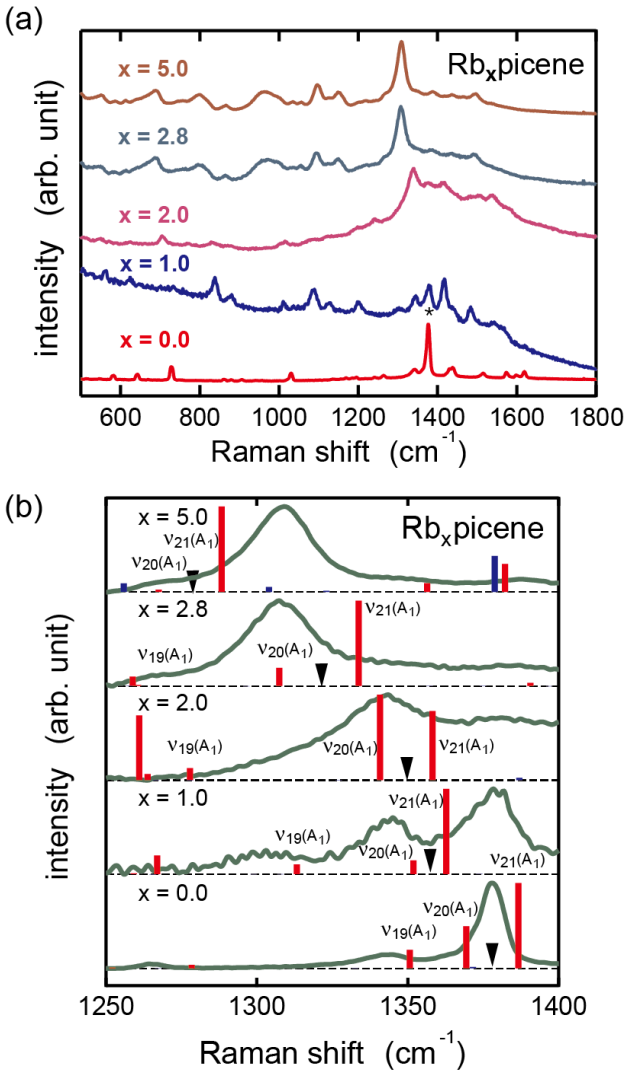

Figure S-2-3. A similar plot as in Figure S-2-2 for Rb$_x$picene (x = 0 - 5).

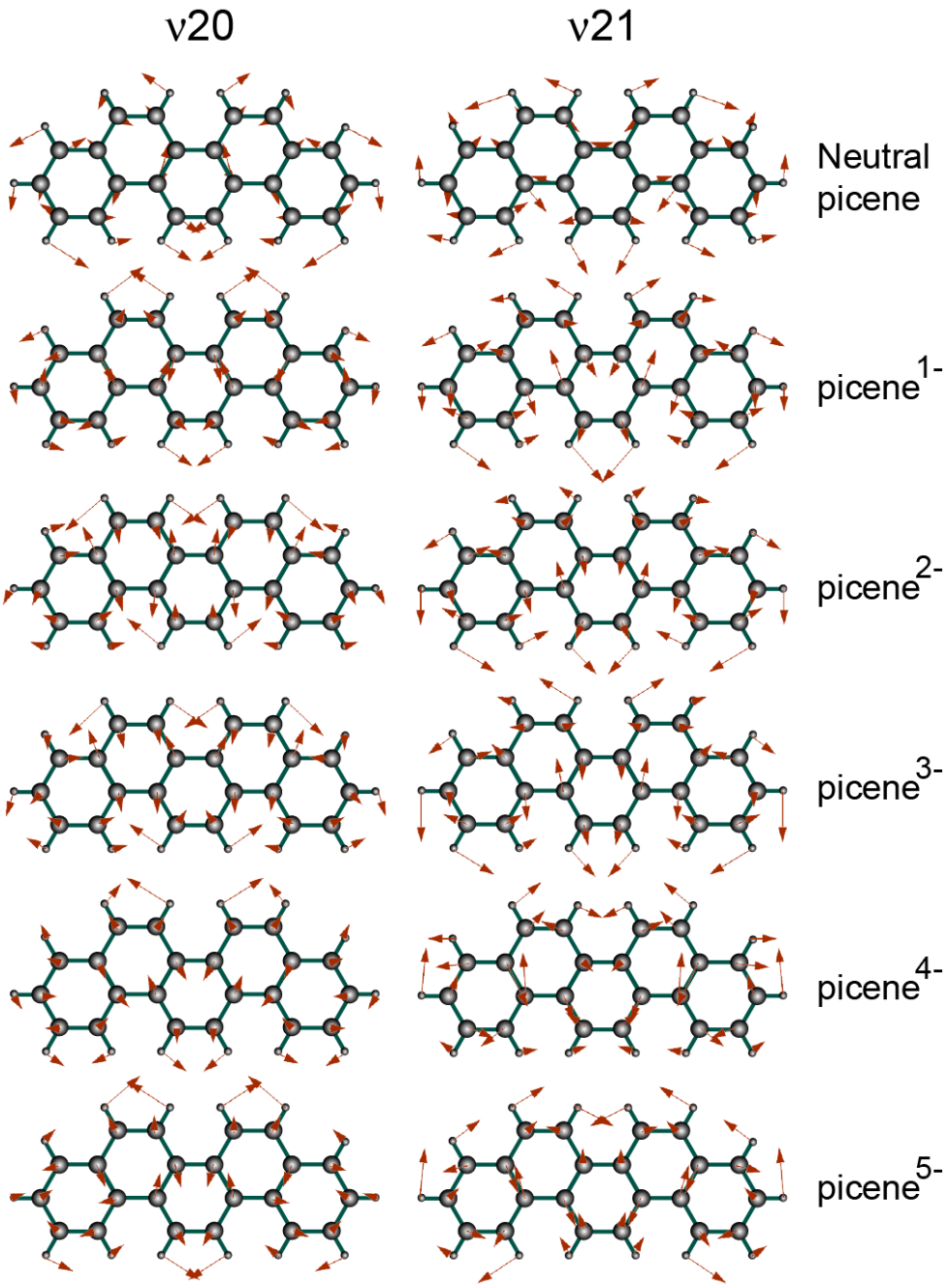

Figure S-2-4. ν_{20} and ν_{21} A_1 modes schematically shown for picene^{y-} (y = 0 - 5).

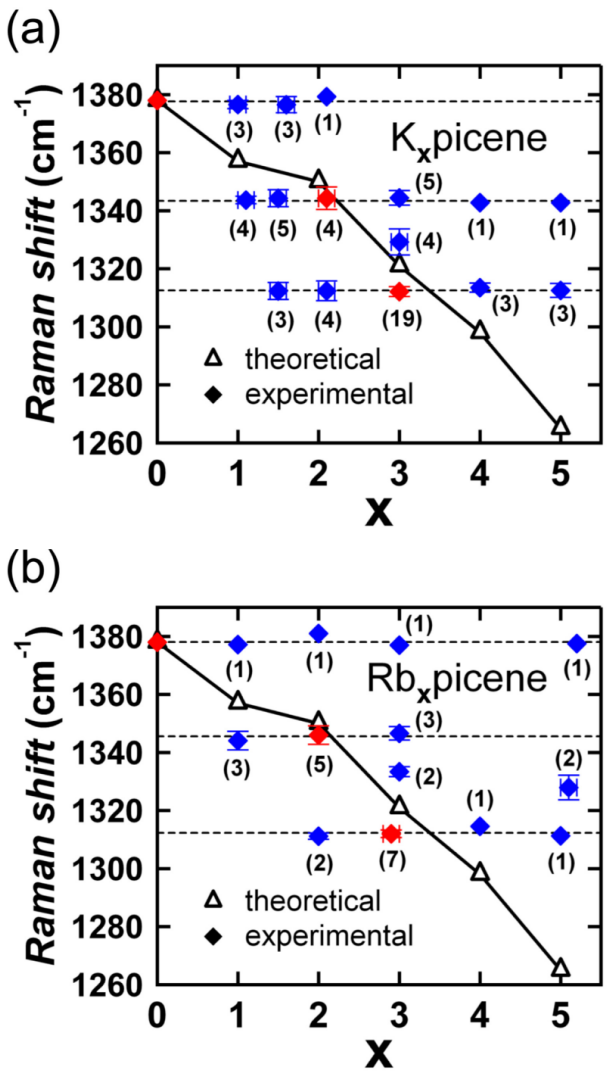

Figure S-2-5. Plots of frequency of experimental and theoretical Raman peaks against the nominal value, x, in (a) $K_x$picene and (b) Rb_xpicene (x = 0 - 5). Frequency of the theoretical Raman peak corresponds to the average value of frequencies for n_{20} and n_{21} A_1modes. The theoretical plots are shifted by 27 cm^{-1} so that the theoretical average value of n_{20} and n_{21} A_1 modes in neutral picene fits to its experimental average value, 1378 cm^{-1}. The experimental plots in red refer to the $K_x$picene (Rb_xpicene) phase produced in the $K_x$picene (Rb_xpicene) sample (see text). The numerical value in parenthesis stands for the number of times the phase appeared in each sample.

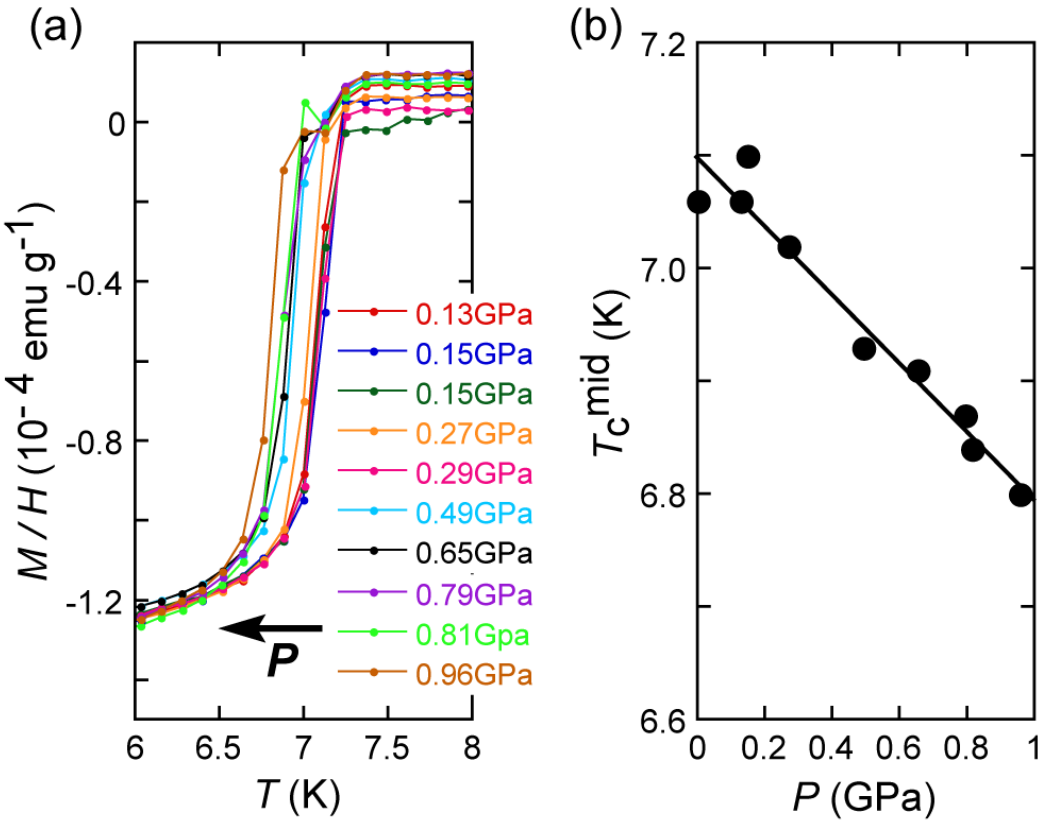

Figure S-2-6. (a) M / H - T curves for various pressures, and (b) pressure dependence of T_c^{mid} in the 7 K superconducting phase of $K_{3.3}$picene. dT_c^{mid} / dP is determined by a linear fitting in T_c^{mid} -P plot.

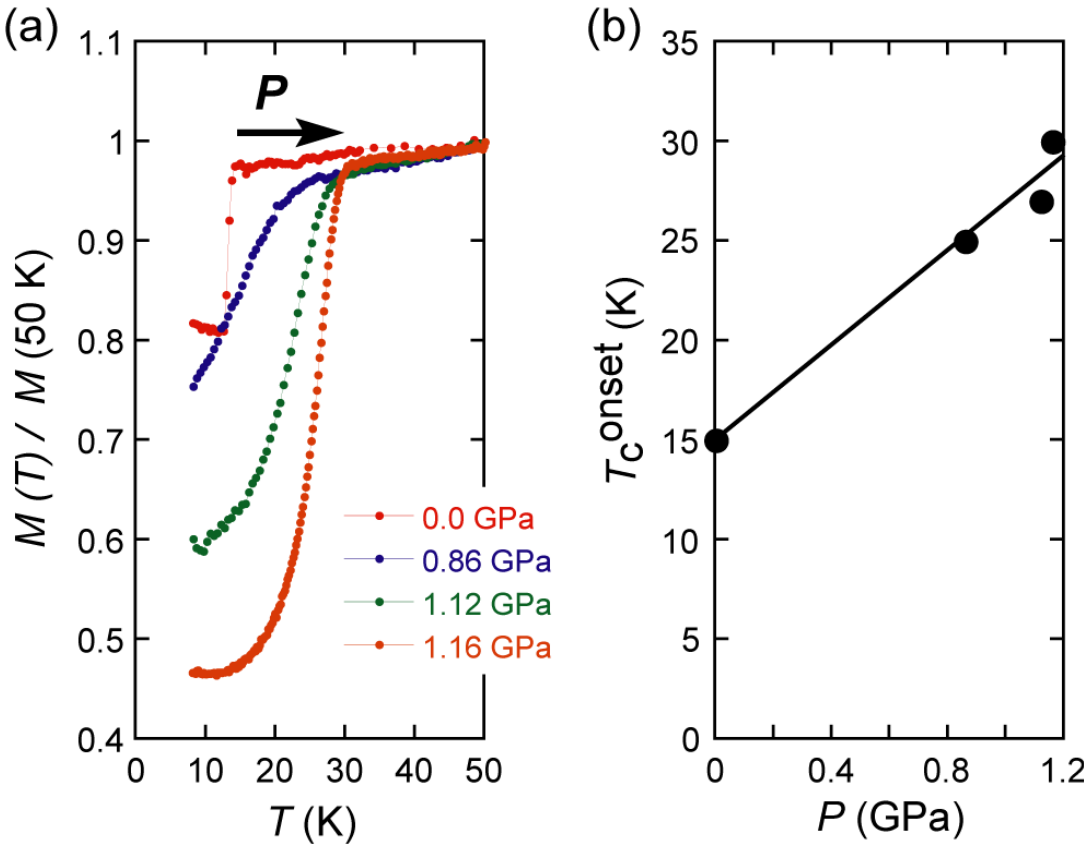

Figure S-2-7. Similar plot as in Figure S-2-6 for the 18 K superconducting phase of $K_{3.3}$picene

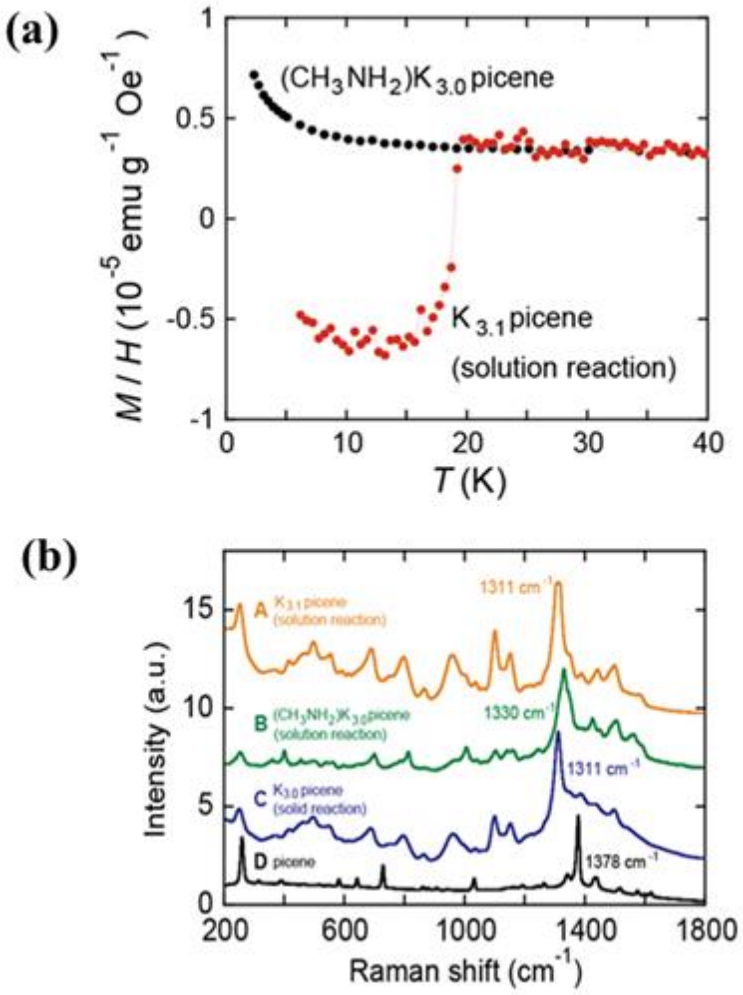

Figure S-2-8. (a) M / H - T curve in zero-field cooling (ZFC) for $(CH_3NH_2)K_3$picene and $K_{3.1}$picene samples, which were prepared by the solution process (see text). This data was reported and briefly discussed in Ref. 10. (b) Raman scattering spectra for the K_3picene samples which were prepared by the solution method (curve A), $(CH_3NH_2)K_3$picene (curve B), K_3picene sample prepared by the solid-reaction method (curve C), and pristine picene (curve D).

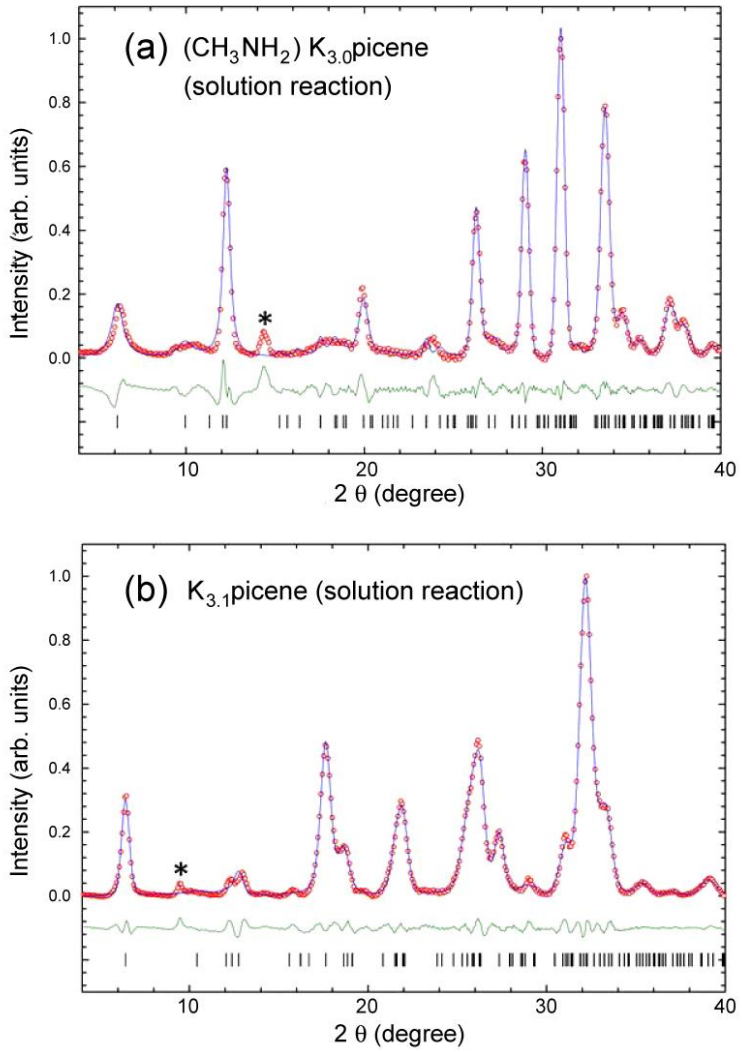

Figure S-2-9. X-ray diffraction patterns for (a) $(CH_3NH_2)K_3$picene and (b) K_3picene samples. Red circles (blue lines) represent the observed (calculated) diffraction patterns. The green line shows the difference between the observed and calculated patterns. Black vertical bars correspond to the predicted peak positions. The lattice parameters for two samples, $(CH_3NH_2)K_3$picene and K_3picene, obtained from the LeBail fit to X-ray diffraction patterns are listed in Table S-2-1.

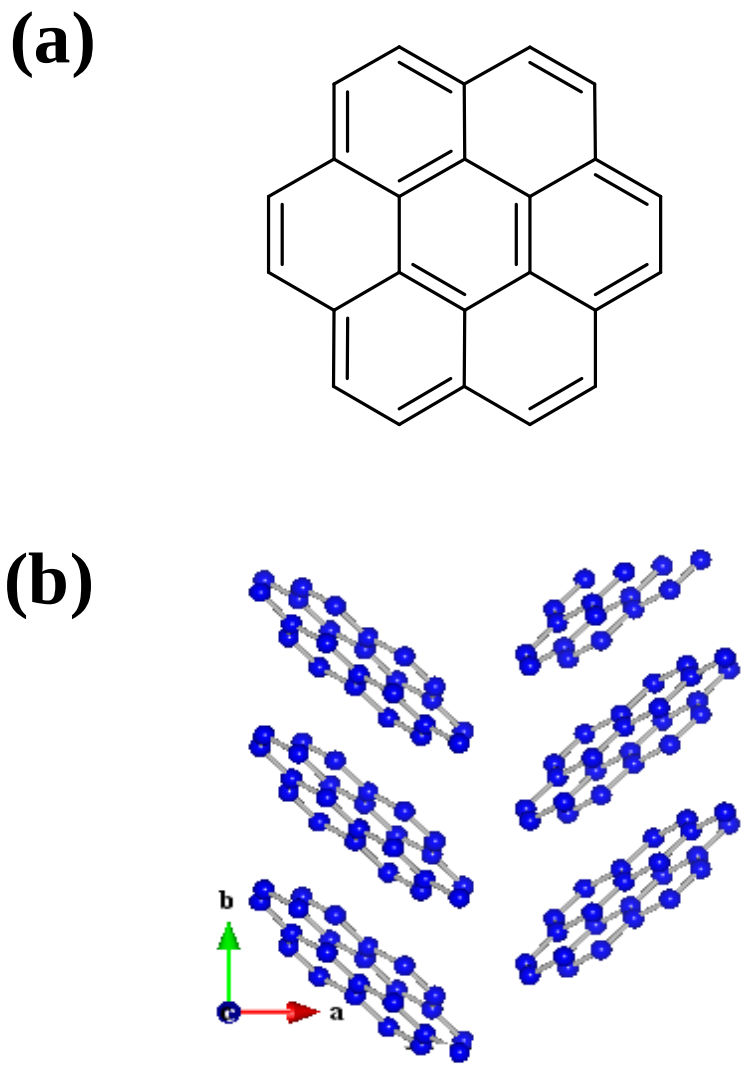

Figure S-2-10. (a) Molecular structure of coronene. (b) Crystal structure of coronene viewed from *c*-direction.

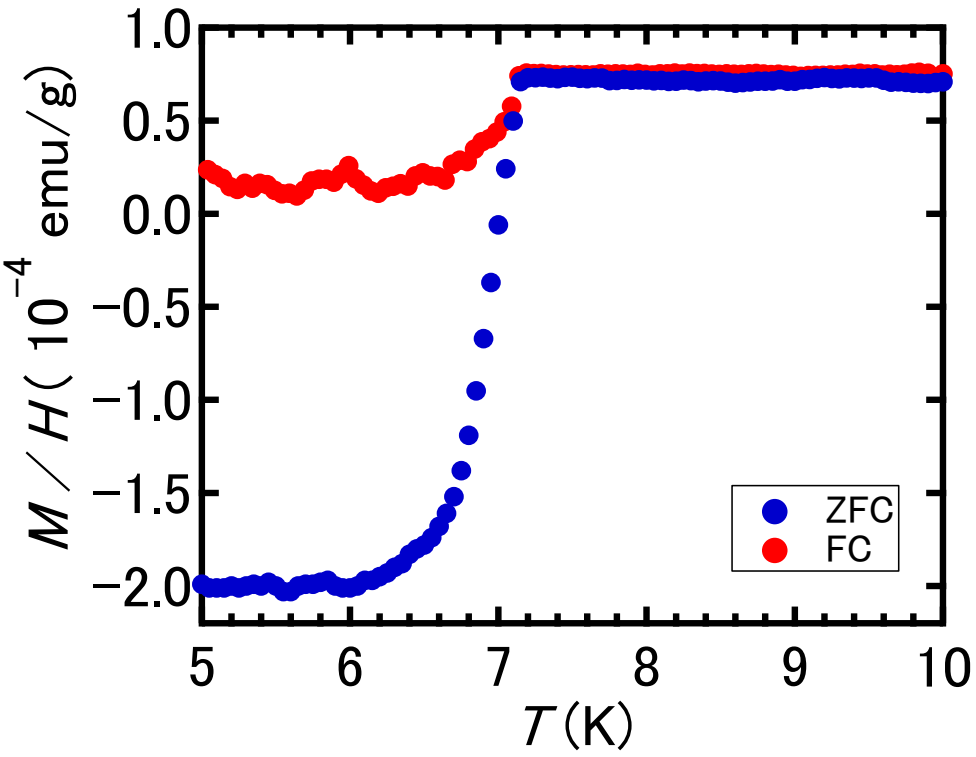

Figure S-2-11. Temperature dependence of M / H for $K_x$coronene.

Acknowledgements

First of all, I am much grateful to Prof. Yoshihiro Kubozono of Research Laboratory for Surface Science and Research Centre of New Functional Materials for Energy Production, Storage and Transport, Okayama University, for his valuable guidance for my study during Doctor's Course and his warmhearted / continuous encouragement. I would like to appreciate him for my building up scientific background in physics and chemistry of transistors and superconductors based on his educational direction. Also, I greatly thank him for providing me the opportunity to work in a talented research team in Japan.

I am also thankful to Dr. Ritsuko Eguchi in Research Laboratory for Surface Science for her excellent guidance that she has provided me as a successful female physicist. In the past three years, I enjoyed the work with Dr. Ritsuko Eguchi and obtained her valuable suggestions. I am much indebted to Dr. Hidenori Goto in the Laboratory for his valuable and kind suggestions during my Doctor's Course and I could learn how to do research. Special thanks will be provided to Prof. Takashi Kambe of Physics Department for his excellent guidance and suggestions in my superconductor study. I wish to greatly thank Prof. Hideki Okamoto for his valuable collaboration and guidance for my study. I also thank Mr. Yasuyuki Sugawara of Kuramoto Co. Ltd., and Mr. Shin Gohda of NARD Institute, Ltd. for their valuable assistance to FET works. I also thank Prof. Hideo Aoki and Prof. Yoshihiro Iwasa of Tokyo University for their valuable suggestions for my study. Further, I would like to thank Prof. Takashi Kato of Nagasaki institute of applied science for his valuable suggestion based on theoretical chemistry. I wish to appreciate Dr. Yukihiro Yoshida and Prof. Gunzi Saito of Meijo University for their kindly providing me samples of electron donors and acceptors, which fascinated my research on contact resistance in organic transistors. Furthermore, I wish to thank Prof. Kosmas Prassides for his providing me the chance to work in University of Durham, UK. Finally I wish to thank Prof. Akihiko Fujiwara of JASRI-SPring-8 for his valuable suggestions for all my study.

I am indebted to Prof. Yasushi Nishihara for his kind assistance and support for my study in Okayama University. I wish to greatly acknowledge to friendships as well as valuable advice / collaboration of the Laboratory members, Dr. Koki Akaike and Dr. Yasuhiro Takabayashi, Mses. Shino Hamao, Yumiko Kaji, Noriko Komura, Lu Zheng, Eri Uesugi, Megumi Senda and Keiko Ogawa, and Messrs. Hiroki Mitamura, Xuesong Lee, Nobuyuki Kawai, Kazuya Teranishi, Yusuke Sakai, Masanari Izumi and Hidehiko Akiyoshi. Also I wish to say special thanks to Ms. Michie Sasaki for her kind / warmhearted assistance in my life at Laboratory during Doctor's Course. In addition, I also thank to my friends, Mses. Jiao Jiao, Jing Li, Xia Lan, Juan Dai, Ting Li, Meng Mao, Li Qiu and Haiyan Dang, and Messrs. Ninghui Chang and Qiang Ma for their providing me supports and friendships when I needed them the most.

I would like to greatly thank my family for their supports and encouragement. In particular, my parents have supported continuously me during not only my Doctor's Course but also all my life. Finally, I wish to provide special thanks to my husband, Mr. Peng Hu, for his encouraging and kind supports for my life as well as his deep understanding for my research life.

The X-ray diffraction measurements with synchrotron radiation were carried out under the proposals of SPring-8 (2011B1496 and 2011A1938), KEK-PF (2011G109) and ESRF (HS-4556); the measurements at ESRF were done at proposal of KEK-PF (2011G109)

Xuexia He

28 July, 2013, in Okayama University